Stony Brook University

Structural Study of Layered Oxides and Oxysulfides as Positive Electrode Materials for Rechargeable Lithium Ion Batteries

A Dissertation Presented

by

Dongli Zeng

to

The Graduate School

in Partial Fulfillment of the Requirements

for the Degree of

Doctor of Philosophy

in

Chemistry

Stony Brook University

May 2010

Stony Brook University

Dongli Zeng

We, the dissertation committee for the above candidate for the **Doctor of Philosophy** degree, hereby recommend acceptance of this dissertation.

Clare P. Grey, D. Phil., Advisor
Professor, Department of Chemistry

John B. Parise, Ph. D., Chairperson
Professor, Department of Geosciences

Stephen Koch, Ph. D., Third Member
Professor, Department of Chemistry

Jason Graetz, Ph. D., Outside Member
Materials Scientist, Energy Sciences and Technology Department,
Brookhaven National Laboratory

This dissertation is accepted by the Graduate School.

Lawrence Martin
Dean of the Graduate School

Abstract of the Dissertation

Structural Study of Layered Oxides and Oxysulfides as Positive Electrode Materials for Rechargeable Lithium Ion Batteries

by

Dongli Zeng

Doctor of Philosophy

in

Chemistry

Stony Brook University

2010

As one of the most advanced energy storage systems, lithium ion batteries have become a necessity of today's information-rich mobile society. Layered oxide $LiCoO_2$ is the positive electrode material used in most of the present commercial rechargeable

lithium ion batteries, but the high cost, toxicity and structural limitations of $LiCoO_2$ limit its applications, especially for large-scale appliances, therefore alternative materials are needed.

The work described in this dissertation focuses on studies of the electrochemistry and structures of layered oxides and oxysulfides as the positive electrode materials in rechargeable lithium ion batteries. A combination of techniques has been applied to characterize the structures, including the X-ray/neutron diffraction (XRD/ND), X-ray Absorption Near Edge Spectroscopy (XANES), Pair Distribution Function (PDF) analysis along with the reverse Monte Carlo (RMC) simulations, and solid state $^{6/7}$Li Magic angle spinning (MAS) Nuclear Magnetic Resonance (NMR).

The series of layered oxides $Li[Ni_yMn_yCo_{(1-2y)}]O_2$ ($0 < y \leq 1/2$), with Ni and Mn substitution of partial or all of the Co in $LiCoO_2$, have shown promising electrochemical behavior and triggered a large amount of research. Nonetheless, there is still lack of understanding from the fundamental point of view of the structure-property relationships. Therefore, a systematic study has been performed on this series to investigate their structures and cation orderings. The XRD results confirm the presence of the layered α-$NaFeO_2$-type structure while XANES experiments verify the presence of Ni^{2+}, Mn^{4+} and Co^{3+}. The ^{6}Li MAS NMR spectra of compounds with low Ni/Mn contents ($x \leq 0.10$) show several well resolved resonances, which start to merge when the amount of Ni and Mn increases, finally forming a broad resonance at high Ni/Mn contents. Analysis of both the ^{6}Li MAS NMR $^6Li[Ni_{0.02}Mn_{0.02}Co_{0.96}]O_2$ spectrum and neutron PDF data of $Li[Ni_{1/3}Mn_{1/3}Co_{1/3}]O_2$ reveals a non-random distribution of the transition metal (TM)

cations in the TM layers, where Ni and Mn have a strong tendency to associate and form Ni/Mn clusters.

Following the studies of the pristine materials, a systematic study has been performed to investigate the structural changes of $Li[Ni_{0.05}Mn_{0.05}Co_{0.90}]O_2$ (the $y = 0.05$ member) upon electrochemical lithium deintercalation. By using a combination of techniques, including XRD, X-ray absorption near edge spectroscopy and solid state NMR, a complete picture of the whole delithiation processes has been revealed. The results show that the non-random cation distribution has large effects on the order of Li removal. The ions located closest to Mn^{4+} are extracted first, and the oxidation of not only Ni^{2+} but also some Co^{3+}, is seen in the beginning of Li extraction (less than 0.15 mole is removed). Further deintercalation (additional 0.2 mole of Li removal) induces an insulator to metal transition that is similar to that reported for $LiCoO_2$. When half of the Li ions are extracted, the electrochemical signature for lithium vacancy ordering in the host framework is observed. The NMR results for deintercalation of more than 50% Li were compared to those for Li_xCoO_2 at similar stages of charge, which are reported here for the first time; they indicate that the behavior of these two phases at these potentials is very similar. When the batteries are charged to voltages higher than 4.6 V, very few lithium ions remain in the structure and the O3 to O1 phase transition occurs.

Layered $Sr_2MnO_2Cu_{2m-\delta}S_{m+1}$ (m = 1, 2 and 3, $\delta \sim 0.5$) are a novel family of oxysulfides that have been synthesized recently. They consist of alternating Perovskite-type $[Sr_2MnO_2]$ layer and various thicknesses of antifluorite-type $[Cu_2S]$ layers. They operate by a displacement mechanism of their electrochemical reactions towards Li,

where most of the inserted Li replaces Cu and forms Li_2S-like environment and extrudes Cu out of the framework as metallic particles. The reversible (de)lithiation processes of the m = 2 member have been investigated intensively. The results show that the Li insertion and deintercalation occur via different processes, and the involved active redox species are both Cu from the sulfide layer and Mn from the Perovskite oxide layer. Variations of the sulfur framework are observed upon the insertion/removal of Li, and the results indicate that the properties of the sulfur framework strongly affect the electrochemical behavior and cycling performance of the studied material.

Table of Content

List of Figures

List of Tables

Acknowledgments

I would like to express my sincere thanks to many people, since this would never be accomplished without their support and encouragement.

First and foremost, I would like to thank my dear advisor, Prof. Clare P. Grey, for her providing me this great chance doing so interesting and exciting research in this group, and for her guidance and support over all these years. She has been always so intelligent and full of creativity, and she is also so patient and caring for people. I am deeply impressed by her attitude to science, research, and to students and other people. Her dedication to science and her enthusiasm to life will always inspire me, both in my future career and life. I am forever grateful to have her being my advisor,

I would like to thank my committee members, Prof. John B. Parise, Prof. Stephen Koch, and Prof. Peter Khalifah, for their help and advices. Special thanks to Dr. Jason Graetz for being the outside member for my defense. I also want to thank Prof. Brain Phillips, for his insightful comments during our joint group meetings.

I want to thank Dr. Jordi Cabana Jiménez, who taught me almost everything when I first entered the lab. He has been so generous and kind all the time. His help, patience, assistance, and insightful suggestions, are truly appreciated.

I thank Dr. Won-Sub Yoon for his big help in conducting synchrotron experiments and data processing. I am thankful to the assistance from the researchers and beamline scientists from Brookhaven National Laboratory: Dr. Syed Khalid, Dr. Nebojsa Marinkovic, Dr. Xiao-Qing Yang, and Dr. Key-Wan Nam.

I also wish to acknowledge Ekaterina Pomerantseva from Lomonosov Moscow State University for bringing the interesting project and working with me in the basement. Natasha Chernova and Stanley Whittingham from SUNY Binghamton, Alex I. Smirnov from North Carolina State University, and Simon J. Clarke from University of Oxford, are acknowledged for fruitful discussions and collaborations. The US Department of Energy, Office of FreedomCAR and Vehicle Technologies, and Petroleum Research Found from American Chemical Society have provided the financial support.

I would like to thank all the past and present group members: Julien Bréger, Meng Jiang, Lesley Holmes, Hailong Chen, Kenneth Rosina, for being the best officemates ever; Nicole Trease, for bringing in so much fun stuff and always willing to proof read my non-native words without any complaint; Hua Huo, for always being so considerate and caring; Lucienne Buannic, for sharing with me lots of the summer school fun; Jongsik Kim, for the coffee candies and all the relax conversations; Kellie Morgan, for always bring me the best peanut brittles from the west coast; Sylvio Indris and Rosa Robert, for helping a lot during the beamtime we spent together; Riza Dervisoglu and Gunwoo Kim, for always remembering to take shots of those precious moments; Baris Key and Fulya Dogan, for carrying my poster all the way to Hawaii; Luming Peng, Paul Sideris, and Stephen Boyd, for your encouragement and support for all the time… Rangeet Bhattacharyya, Ulla Gro Nielsen, Frédéric Blanc, Derek Middlemiss, Lin-shu Du, Olivera Zivkovic, John Palumbo, Ben (Yunxu) Zhu, Lina Zhou, Xiao Hua, Hao Wang, Frédérique Pourpoint, Pavel Rehak, James Pastore, and our visitors, Adam Best, Naoko Yamakawa, Junichi Shirakawa, and from Phillips' group, Jian Feng, Wei Li, Harris

Mason, and Stacey Cochiar, I do appreciate all the unforgettable moments with everyone of you. Special thanks go to Zhouguang Lu and Toyoki Okumura, for the joyful days during the conferences and the very useful information and the inspiring discussions you provided that helped me get through my exam meetings. Lauretta Passanant and Deborah Murphy are also thanked for their kindness and help.

I also wish to acknowledge Prof. Nancy Goroff, the director of my program, and Katherine Hughes, Norma Reyes, Lizandia Perez, Heidi Ciolfi, and Charmine Yapchin from the main office, for their miscellaneous help all along my studies.

I especially cherish the friendship I gained, without which my life would be much less colorful. Many thanks to all my friends, in Stony Brook: Xinxin Yang, Huaning Zhang, Jing Zhou, Xiaohui Peng, Lu Gan, Hongjun Zhou, Qi Chen, Qi Wu, Yuanzhi Tang, Li Li, Fangyu Ding, Howard (Hao) Lu, Yimin Mao, Fanlin Meng, Liang Luo, Zhou Dai, Airong Song, Nina Liu, Pan Pan, Yuehu Ou, Lily Wang, Yuan Bi, Jin Gao, Jung-Eun Yeo, Sushi Yang, and Pittsburgh: Xiaomi Xu, Taehoon Choi, Benjamin Kabagambe, Patrick Rodgers, Bin Sui, Wangyang Tu, and Fangyong Yan.

Last but not the least, I want to express my deepest appreciation to my family. I am grateful to my grandpa, Xianying Zeng, who was always so proud of me. And my parents, Yi'an Zeng and Aifang Jiang, my sister, Yan Zeng, my parents-in-law, Jiasong Wang and Lifang Zhang, and of course my dear husband, Zhihui Wang, and my most beautiful and adorable sweetheart, Vanessa Xibin Wang, they have always been the greatest support for me. I could never have accomplished this work without their tremendous love and help! Thank you and I love you all!

Chapter 1 Introduction

1.1 General Background and Motivations

1.1.1 Energy Crisis and Environmental Concerns

Our modern economy is a petroleum-based economy, as its development heavily depends on the utilization of fossil fuels, such as oil, natural gas and coal. In fact, statistical data shows that over 80% of the total world energy consumption is derived from the combustion of fossil fuels (see Figure 1.1a) [1], and the projected world total energy consumption in 2030 will be increased by over 40% of that in 2006 (see Figure 1.1b) [2]. The critical issues faced by the whole world is not only the limited reserves of these non-sustainable energy sources, but also the environmental concerns, such as the global warming caused by the greenhouse gas emissions.

Energy-related CO_2 emissions contribute the major part of the greenhouse gas emissions. As shown in Figure 1.2, in 2008, over 80% of the total U.S. greenhouse gas emissions are energy-related CO_2, among which the largest sector is contributed from the combustion of fossil fuels to generate electricity (40.6%), and the second largest sector is transportations (33.1%) [3]. To alleviate the present dilemma, new technologies need to

be developed to generate electricity from "clean" sources that do not generate CO_2, such as solar, wind, water and nuclear. Meanwhile, the advent of electric vehicles (EVs), including hybrid electric vehicles (HEVs), plug-in HEVs and all-electric vehicles, also provides the potential of altering the current situation, since the EVs have much higher engine efficiencies and much lower, or even zero, CO_2 emissions than conventional vehicles using internal combustion engines.

However, a major challenge in turning both of these strategies into practice is the development of effective electrical energy storage (EES) systems. It is easy to understand the necessity of high performance EES systems in EVs for transportation. For the utilization of alternative energy sources, EES systems are also required to insure around-the-clock delivery of electricity generated from the "clean" sources, as some of them are only available during certain time periods or within certain regions, such as the solar and wind sources. Also, EES systems are necessary to mediate fluctuations during electrical power supply and reduce or diminish the loss that would be caused by an unexpected power outage.

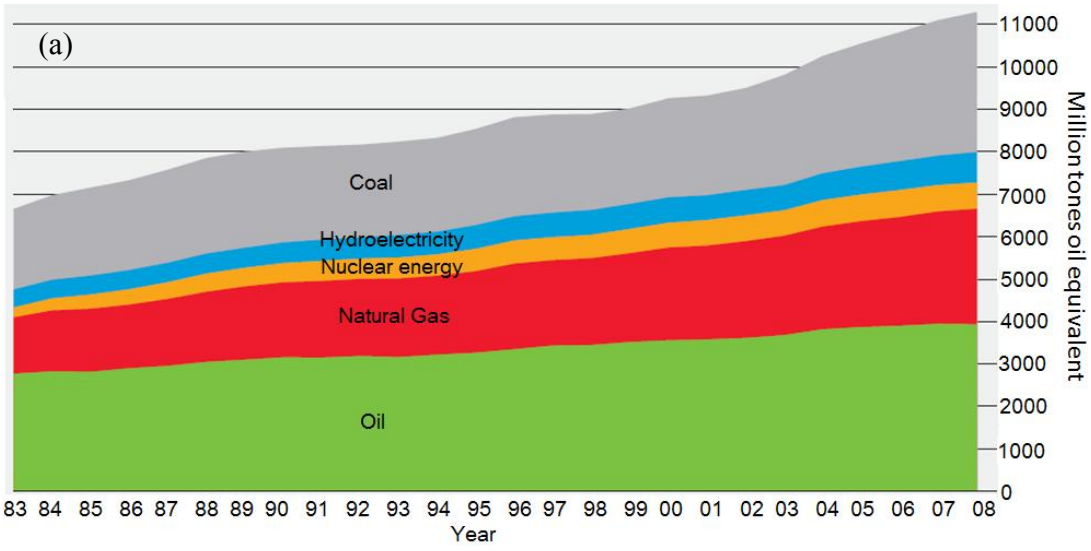

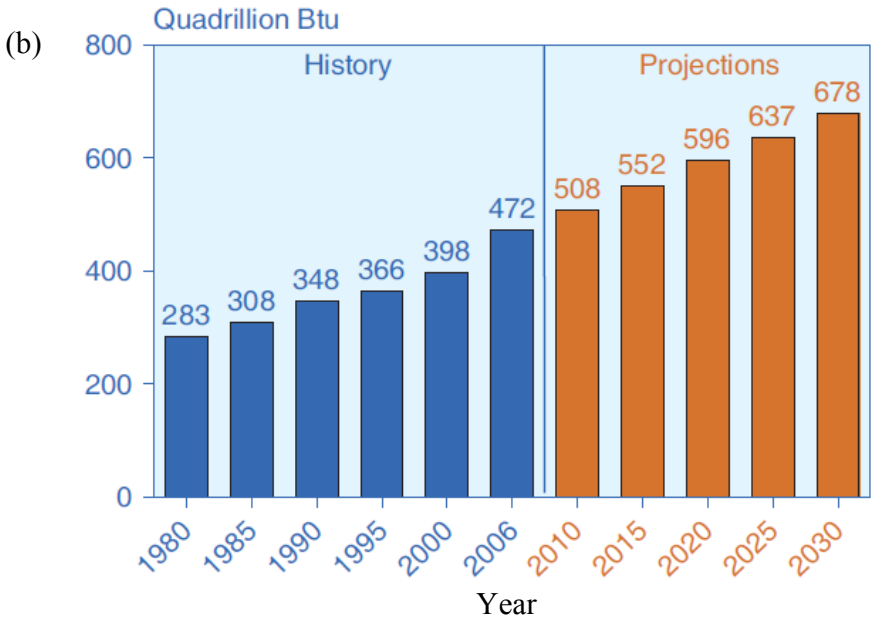

Figure 1.1. Statistical data for the world's total energy consumption, (a) by major sources, 1983 – 2008 (after ref. [1]) and (b) history: 1980 – 2006, and projections: 2010 – 2030 (after ref. [2]).

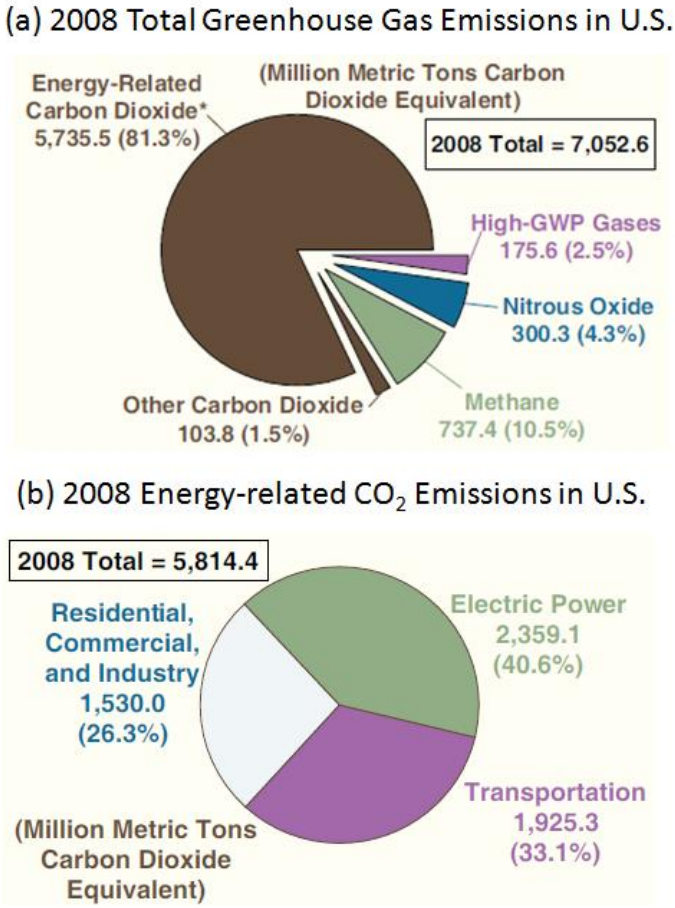

Figure 1.2. (a) The U.S. total greenhouse gas emissions, 2008. (b) The U.S. energy-related CO_2 emissions by end-use sector, 2008. (Figures after ref. [3].)

1.1.2 Electrical Energy Storage Systems

The EES devices used today include batteries, fuel cells and electrochemical capacitors (ECs) [4]. These systems operate based on different fundamentals: batteries and fuel cells store the energy by converting the electrical energy into chemical form using redox reactants, while ECs store the energy directly as it is. Despite the different operating mechanisms, these systems have common features in their compositions: they all have two electrodes separated by the electrolyte, and the energy storage or conversion reactions take place at the electrode/electrolyte boundary interface.

Schematics of the three systems are shown in Figure 1.3. Batteries are closed systems that provide electrical energy to external applicators, and the energy is generated by the redox reactions occurring at the electrodes. During this process, the negative electrode material, also known as the anode, is oxidized and gives out electrons, and the positive electrode material, known as cathode as well, is reduced. Different from batteries, fuel cells are open systems and the reactants, for example, O_2 and H_2, are delivered from outside the cell. The electrodes are charge-transfer media where the redox reactions take place but they are not the active materials. In batteries and fuel cells, the terms positive and negative electrode are often used, as the redox reactions at one electrode usually occur at higher electrode potentials than the reactions that occur at the other electrode. In ECs, the energy storage/delivery processes may not involve the redox reactions but via the formation/release of the electrical double layers (EDL), although the terms positive and negative electrode are still in common use [4].

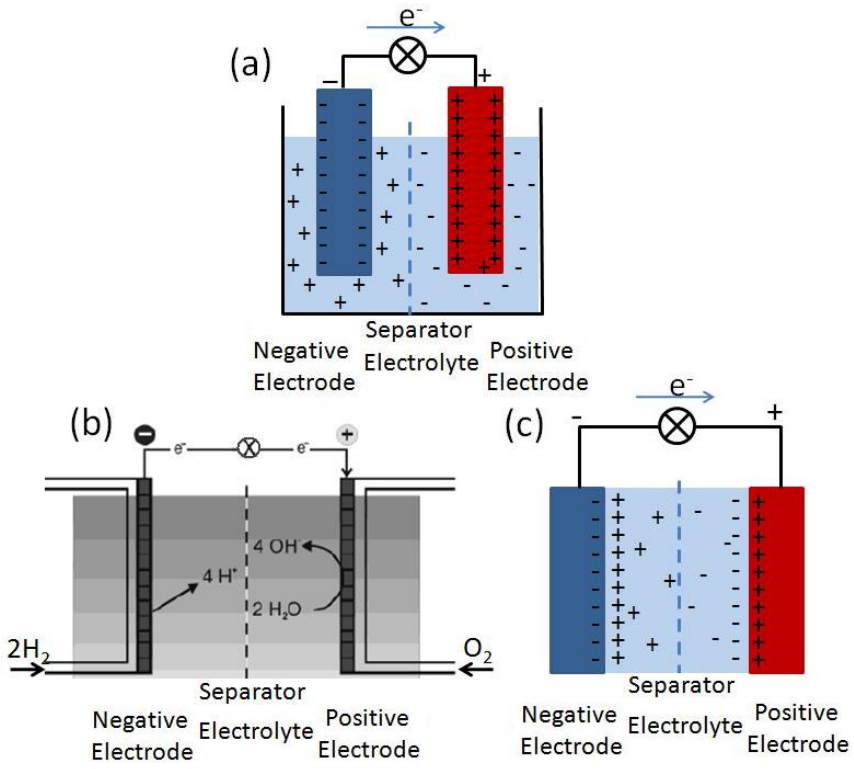

Figure 1.3. Schematic representations of three types of EES systems showing their key components. (a) A battery in use, (b) a fuel cell showing continuous flow of reactants and the redox reactions inside, and (c) an electrochemical capacitor showing the energy storage at the electrode/electrolyte interface. (Figures modified after ref. [4].)

Among these EES devices, so far batteries are found in the most market applications. Batteries can be classified as two types: primary and secondary. A primary battery is assembled in its charged state and can be used only once before it is exhausted and discarded. Secondary batteries, also called the rechargeable batteries, can be restored to the charged condition after being discharged by applying an opposite direction electric current in the opposite direction through the external circuit [4].

The term "specific energy" or "energy density" (unit in Wh/L or Wh/kg) is used to evaluate how much energy a battery is able to store or deliver in different systems. It is a function of the cell potential (V) and the specific capacity (Ah/kg) [5]. The cell potential is determined by the difference between the chemical potentials of the active materials in the two electrodes. Capacity is the amount of electrons involved in the electrochemical reaction in the cell and has the unit of coulombs (C) or ampere-hours (Ah). Below is the equation to calculate the theoretical specific capacity of a battery:

$$C_{th} = \frac{96500 \times \Delta x}{3.6 \times MW} \left(mAh / g \right) \qquad (1.1)$$

where Δx is the number of electrons produced in the charging/discharging process and MW is the molecular weight of the active material.

Figure 1.4 shows a comparison of the gravimetric and volumetric energy densities among different types of rechargeable battery technologies [5]. It clearly indicates that Li-based batteries occupy the highest energy density region so far. This is not surprising, since lithium is the most electropositive metal with a -3.04V potential versus the standard hydrogen electrode, and it is the lightest metal (ρ = 0.53 g/cm^3 or MW = 6.94 g/mol) as

well. These features motivated the use of lithium metal as negative electrode and the development of battery technologies based on the Li system.

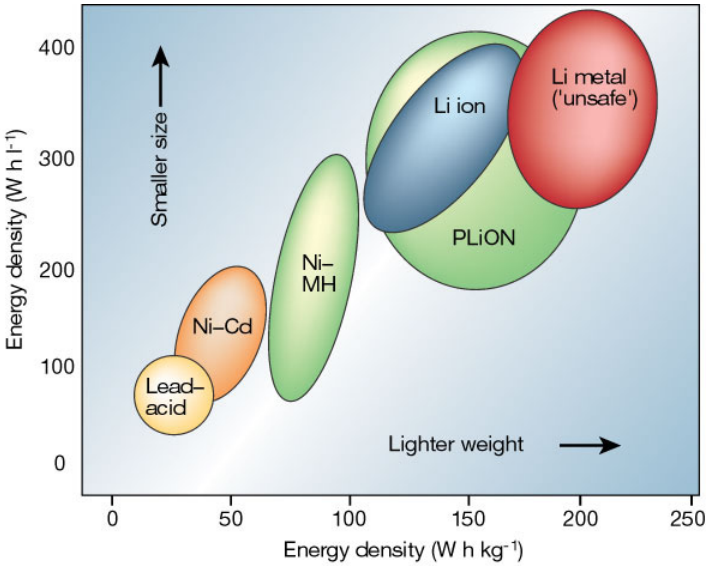

Figure 1.4. Comparison of gravimetric (Wh/kg) and volumetric (Wh/L) energy densities among common rechargeable battery systems. (Figure after ref. [5].)

1.2 Lithium Batteries

1.2.1 A Brief History and Commonly Used Positive Electrode Materials

In the 1970s, various inorganic compounds, identified later as intercalation compounds, were shown to reversibly react with alkali metals. This discovery plays a crucial role in the development of high energy rechargeable lithium battery systems. The first rechargeable lithium battery system was Li-metal based.

In the mid-1970s, Whittingham first proposed the possibility of using TiS_2, an inorganic layered compound, as the positive electrode material for secondary lithium batteries and successfully developed the Li/TiS_2 system at Exxon [6]. The use of Li metal directly as the negative electrode enables the high capacity and energy density of the battery system, but also has intrinsic limitations related to the safety issues. When Li metal is used with a liquid electrolyte solution, the formation of the lithium dendrites on the surface of the Li metal upon cycling is potentially hazardous, as growing dendrites may penetrate the separator and result in short circuit or even explosions due to thermal runaway.

Later, in the 1980s, carbonaceous materials, such as pyrolytic carbon and graphite, were recognized as potential negative electrode materials in lithium batteries as lithium can be reversibly inserted into the materials at low voltage [7]. Meanwhile, Goodenough showed that $LiCoO_2$ can be used as the positive electrode material in rechargeable lithium batteries as it has a similar layered structure to the layered dichalcogenides that are capable of reversible lithium (de)intercalation [8]. These developments, along with the

usage of appropriate organic electrolyte solvents, have been applied to the design of the first successfully commercialized lithium ion batteries (LIBs). The term "lithium ion battery" refers to the presence of Li in its ionic rather than the metallic state in the battery, and it is much safer than the Li-metal based battery as there is much less chance of the dendrite Li formation[9]. The first generation of the commercial rechargeable lithium ion batteries, developed by SONY in 1990 [10], consisted of $LiCoO_2$ and graphite as the positive and negative electrode respectively. The system is operated by a so called "rocking chair" mechanism as both of the $LiCoO_2$ and graphite have layered structure, and Li ions travel back and forth between the two electrodes upon cycling. During charging, Li ions are extracted from Li_xCoO_2 and intercalated into the carbon anode to form Li_xC_6, while during discharging, Li ions are extracted from the anode and re-inserted into the Li_xCoO_2 side. A schematic showing the principles during the charging/discharging processes is shown in Figure 1.5 [9].

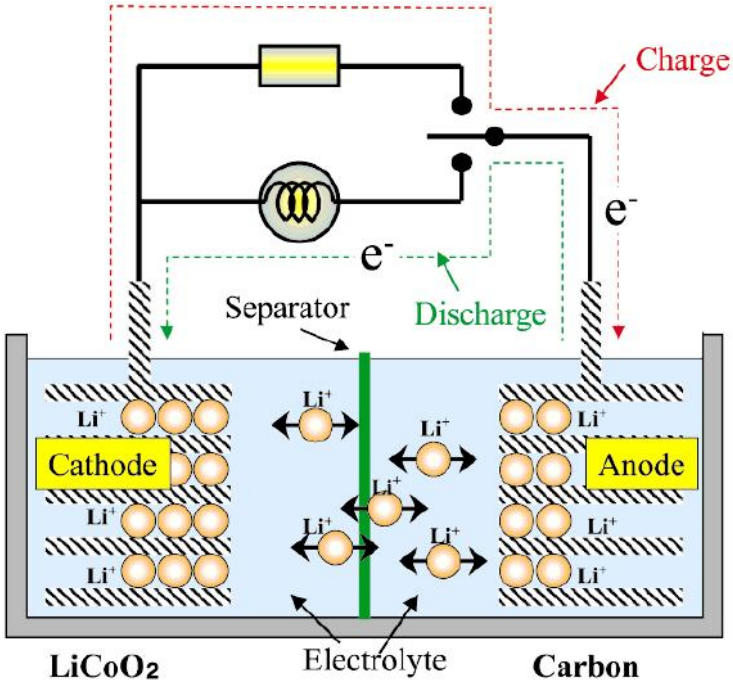

Figure 1.5. A schematic showing the charge/discharge principles of a lithium ion cell. (Figure after ref. [9].)

Today, rechargeable lithium ion batteries based on $LiCoO_2$ and graphite dominate the market, especially in powering small portable devices, such as cell phones, cameras, and laptop computers. However, $LiCoO_2$ based electrodes have disadvantages, for example, the instability of the delithiated phase $Li_{1-x}CoO_2$ (when x is beyond 0.5) limits the operating voltage range below 4.2 V and the practical capacity to ~140 mAh/g, which is approximately half of the theoretical capacity of $LiCoO_2$ (273 mAh/g). Also, $LiCoO_2$ is a relatively expensive material, as the Co availability on earth is limited. Alternative positive electrode materials are therefore needed, especially for large-scale applications, such as the HEVs and EVs. Layered transition metal oxides, $LiMO_2$, with a partial or complete substitution of Co with other transition metal cations, such as Mn and Ni, have then become one of the most studied materials as potential alternatives to $LiCoO_2$. Among them, compounds with the composition $LiNi_yMn_yCo_{1-2y}O_2$ ($0 < y \leq 1/2$), which can be considered as a solid solution of $LiCoO_2$ and $LiNi_{0.5}Mn_{0.5}O_2$, show very good electrochemical behavior and have inspired a large amount of researches on these compounds. More details in the research progress regarding this series compounds will be described in Section 1.3.1 in this chapter.

Other than the layered material, spinel-type $LiMn_2O_4$, first proposed by Thackeray et al. [11], is another promising positive electrode material because of its low cost and low toxicity. Its operating voltage is around 4 V, and it has better thermal stability than layered $LiCoO_2$. The disadvantages of this material, however, are the relatively low specific capacity (120 mAh/g for $LiMn_2O_4$) and the capacity fading upon cycling due to the dissolution of Mn^{3+} in the electrolyte [12]. Compared with the layered

materials, which have two-dimensional framework structures formed by edge-sharing MO_6 octahedra, spinel $LiMn_2O_4$ has a three-dimensional structure (see Figure 1.6). This 3-D network, however, is similar to the framework of the layered materials, as oxygens are cubic close packed in both systems and the MnO_6 octahedras in spinel are also edge-sharing. These similarities have inspired the development of a new concept in designing materials, the layered-spinel composite electrode, which are in fact a mixture of spinel $LiMn_2O_4$ or $Li_{1+x}Mn_{2-x}O_4$ and various layered compounds [13-15]. The electrochemical and thermal stability and cycling performance of these composite electrodes are strongly related to their compositions. The specific cases will not be discussed here since they are beyond the scope of this dissertation.

The most striking breakthrough in the progress of the positive electrode materials development is the utilizing of Olivine-type $LiFePO_4$ (structure shown in Figure 1.6). $LiFePO_4$ operates at a voltage around 3.4 V, and its capacity approaches the theoretical value 170 mAh/g, and with very good capacity retention upon hundreds of cycles. It is cheap, stable, and environmently benign, thus, it could have a major impact in EES systems. $LiFePO_4$ was first proposed by Goodenough in 1997 [16], but did not draw much attention due to the intrinsic low electronic conductivity of this material, resulting in a low rate performance in charge and discharge. To improve the electrochemical performance of $LiFePO_4$, many efforts have been made, including cation doping [17-18], carbon coating [19], reducing the particle size [20], and attempting different synthesis methods [21-23]. One of the most highlighted studies is by Chiang and co-workers, they discovered that the electronic conductivity of $LiFePO_4$ ($\sim 10^{-9}$ S/cm) can be significantly

increased by eight orders of magnitude to 10^{-1} S/cm by only 0.5% Nb^{5+} doping [17]. Although the origin of this conductivity enhancement is under debate, the fact that dramatically improved performance can be achieved for modified $LiFePO_4$ has enabled the possibility of using $LiFePO_4$ in systems requiring high power. In fact, the carbon coated and doped nano-structured $LiFePO_4$ materials developed by Chiang have been mass produced by A123Systems Inc. and successfully applied to industry products, such as power tools (DeWalt line) from Black & Decker and PHEVs (Chevrolet Volt) from General Motors [24].

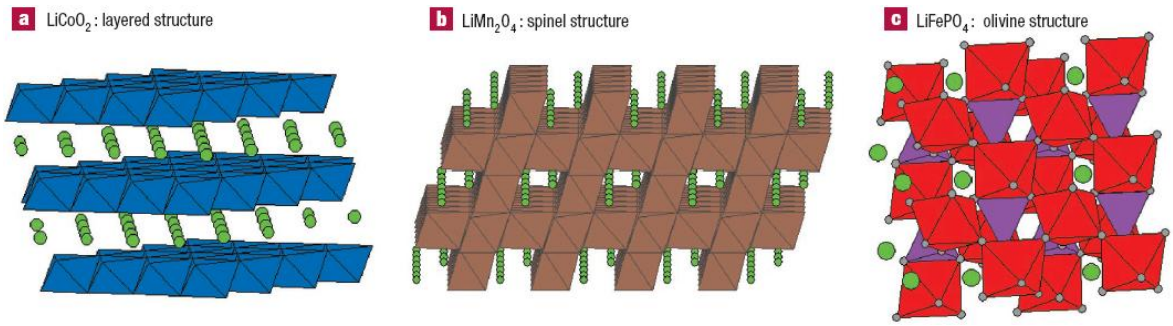

Figure 1.6. The crystal structure diagrams of (a) layered $LiCoO_2$, (b) spinel-type $LiMn_2O_4$, and (c) olivine-type $LiFePO_4$. Color keys: Li: green, Co: blue, Mn: brown, Fe: red, and P: purple. (Figure after ref. [25].)

1.2.2 Three Operation Mechanisms

There are three types of reaction mechanisms in describing the electrochemical reactions of the electrode materials towards Li: intercalation, conversion, and displacement (see Figure 1.7).

Most of the positive electrode materials used in today's rechargeable lithium batteries operate by the intercalation mechanism. The intercalation compounds, such as the three major types of materials described above, layered $LiCoO_2$, spinel type $LiMn_2O_4$, Olivine type $LiFePO_4$, and their doped variants, have one (or more) redox center (often the 3d transition metals) that functions as the charge reservoir and a stable framework structure that is capable of reversible lithium intercalation. During charge, when lithium is removed out of the structure, the transition metal will be oxidized to compensate the charge loss, and during discharge, the transition metal is reduced upon lithiation. The reversible (de)lithiation reactions of $LiCoO_2$ is shown here as a representative reaction.

$$LiCo^{3+}O_2 \leftrightarrow Li_{1-x}Co^{3+}_{(1-x)}Co^{4+}_{x}O_2 + xLi^{+} \qquad (1.2)$$

However, there exist intrinsic capacity limitations as lithium can only be inserted into the vacant sites in the framework structure, and the available charge in these systems is limited by the amount and the valence changes of the redox species, e.g., often only one electron per transition metal cation is available.

Conversion reactions, in contrast, offer the possibility of utilizing multiple electrons of the transition metal cations, since it involves Li-driven full reduction of the transition metals to the metallic state. The conversion reaction is often associated with 3d transition metal binary compounds M_xX_y (M = Fe, Co, Cu etc. and X = F, O, S, N, P etc.).

Upon lithiation, the fully reduced transition metals embed in Li_nX matrices and form the metallic particle/Li_nX nano-composites (see Figure 1.7b), and the redox reactions are repetitive during the following cycles. The general form of the conversion reaction is shown with Eq. 1.3.

$$M_xX_y + ny\ Li \leftrightarrow y\ Li_nX + x\ M \qquad (1.3)$$

The output voltage of the system is determined by the iconicity of the M-X bond, and a general trend of increased voltage through the metal nitrides and sulfides, to the metal oxides, and to the highly ionic metal fluorides is expected [26]. Therefore, the operation voltage of the system can be tuned over a wide range by changing the anions, and these materials can be used as either positive or negative electrode materials. Another advantage by the conversion mechanism is that much higher capacity can be obtained. For example, Tarascon and co-workers have demonstrated the specific capacity as high as 600 to 1000 mAh/g can be achieved for CoO with good cycling performance [27]. Amatucci et al. have reported the over 600 mAh/g and 400 mAh/g specific capacity for FeF_3 and NiF_2 respectively [28].

However, there are drawbacks with this mechanism. One is the large polarization due to the poor conductivities usually associated with the M_xX_y compounds, which are often insulators or poor conductors. This results in a large voltage difference between the discharge and charge, and therefore poor energy efficiency (see Figure 1.8). To address this problem, studies on both the chemistry and morphology of the material and the electrode configurations are needed. By using the conducting matrix technique, combined with the use of nanocomposite materials, Amatucci and co-workers have successfully

cycled BiF_3/C composite with a specific capacity of around 230 mAh/g [29], and obtained the near-theoretical capacity of CuF_2 of over 500 mAh/g [30].

As for the displacement reactions, also referred to as combination displacement/intercalation (CDI) reactions, they have features of both the intercalation and conversion reactions. Materials operated by this mechanism usually have an invariant part in the structure, but there also involve Li-driven metal extrusion/injection processes. The displacement reaction concept has been applied in describing the reactions of some the Cu-Sn and Cu-Sb intermetallic alloys that can function as the negative electrode materials in LIBs [31-33], and has been re-introduced to describe the reactions occur in the positive electrodes by Tarascon et al. very recently [34] [35].

$Cu_{2.33}V_4O_{11}$ is one of the successfully developed positive electrode materials that operates by the CDI mechanism [34]. It has a layered structure consisting of $[V_4O_{11}]_n$ layers, and Cu cations (Cu^+ and Cu^{2+}) distributed in between the layers (see the inset of Figure 1.9). When it electrochemically reacts with Li, a reversible Li-driven process leading to the growth and disappearance of Cu metal dendrites, with a concomitant decomposition and recrystallization of the initial phase, is observed. A sustainable reversible capacity of over 250 mAh/g at a voltage around 2.7 V is obtained.

So far, besides $Ag_2V_4O_{11}$, which has been successfully applied in primary lithium batteries for implantable medical devices [36-38], only a few systems operated by this mechanism have been examined in the rechargeable lithium ion battery systems, and they are all copper based materials [34, 39-42].

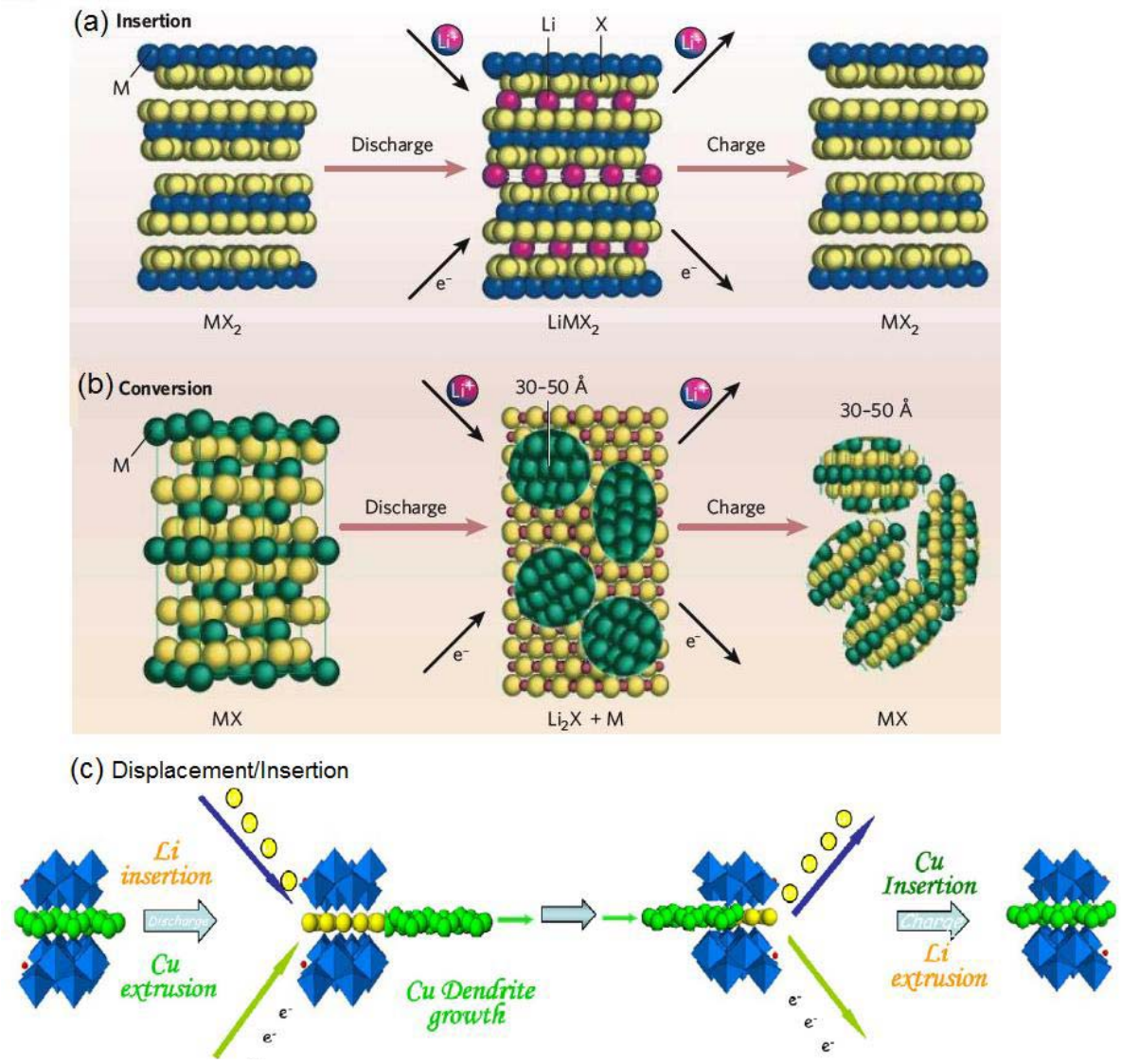

Figure 1.7. Schematic representations showing: (a) the intercalation, and (b) the conversion, and (c) displacement/insertion reaction mechanisms operated by the electrode materials of the electrochemical reactions towards Li. (Figures after ref. [28, 41, 43].)

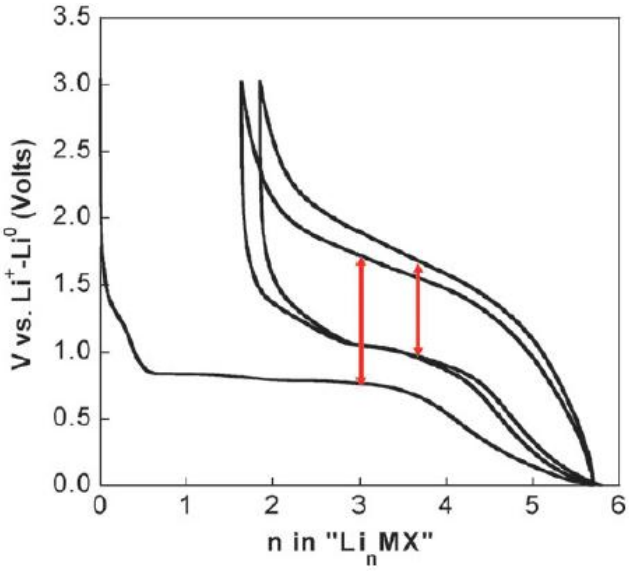

Figure 1.8. A typical voltage vs. composition profile for the conversion reaction materials. A large voltage hysteresis between the reduction and oxidation is clearly seen. (Figure after ref. [44].)

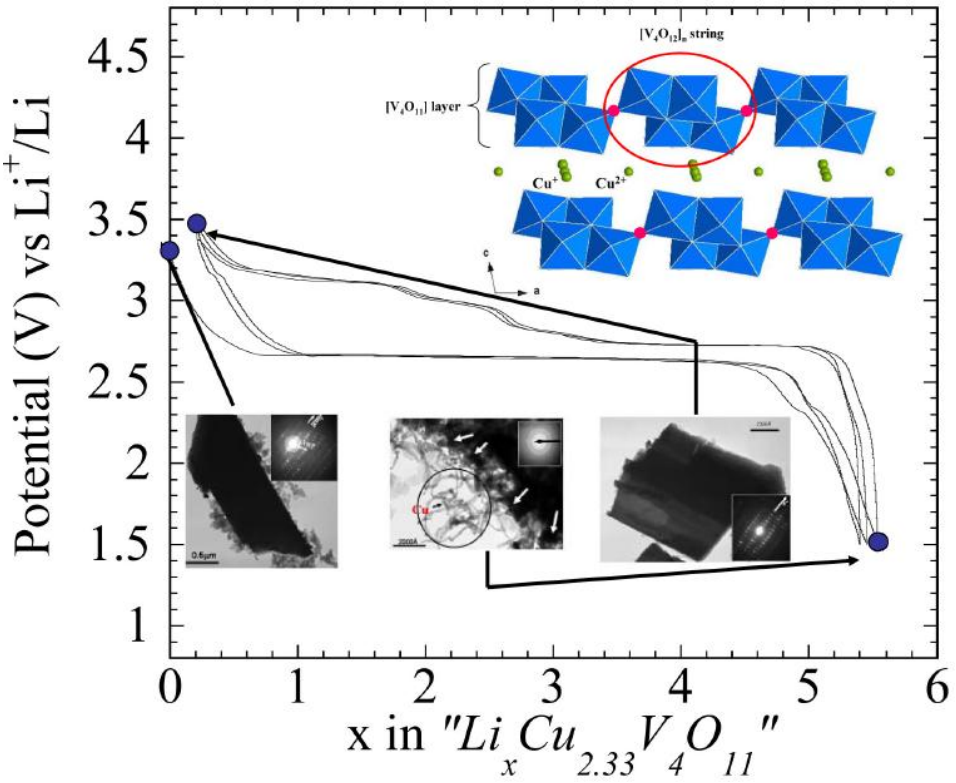

Figure 1.9. The voltage vs. composition profile of a $Cu_{2.33}V_4O_{11}$/Li cell. The TEM images for the positive electrode recorded for the pristine, at the end of 1st discharge, and at the end of the charge are shown to illustrate the reversibility of the copper extrusion process. The crystal structure of $Cu_{2.33}V_4O_{11}$ is shown in the inset at the up right corner. (Figure after ref. [38].)

1.3 Intercalation Compounds and CDI Compounds

1.3.1 Layered $LiCoO_2$ and $Li[Ni_yMn_yCo_{(1-2y)}]O_2$ $(0 < y \leq 1/2)$

Intercalation compounds have been considered as ideal electrode materials since they are capable of accommodating guest species, e.g. Li^+ ions, over certain concentration ranges. Layered transition metal oxides, with the general formula of $LiMO_2$ (M = transition metals), are one important family of the intercalation compounds, and have drawn great attention due to their relatively high potentials.

$LiCoO_2$ adopts a layered framework corresponding to the α-$NaFeO_2$ structure (space group $R\bar{3}m$, No. 166) with the oxygen ions close packed in a cubic arrangement, and the transition metal (TM) and lithium ions occupying the octahedral sites in alternating layers (Figure 1.10) [8]. As mentioned in the previous section, the CoO_6 octahedra are edge-sharing and form 2-D layers, and lithium can diffuse in between the layers. The $LiCoO_2$/Li cell exhibits high potentials with the open circuit voltage (OCV) of Li_xCoO_2 varies from 3.9 to 4.7 V as x changes from 0.07 to 1 [45]. However, not the whole range of the delithiation process is reversible, the Li_xCoO_2 phase becomes unstable when there is more than 50% of Li removal ($x < 0.5$). Further delithiation will result in the shearing of the CoO_2 layers, and induce an irreversible phase transition to form the O1 phase at high voltages (see Figure 1.11) [46-48]. The O1 phase has a reduced inter layer space compared with the O3 phase adopted by the pristine compound, which causes difficulties of Li re-insertion during the following discharge. Therefore, despite a

theoretical capacity of 273 mAh/g, only around half of it, e.g., around 140 mAh/g, can be achieved for practical use during cycling.

The structural changes of $LiCoO_2$ during the 1st charge have been investigated intensively, and the *in situ* and *ex situ* XRD studies have demonstrated that several distinct phase transitions occur upon lithium removal [46, 49-50]. As shown in Figure 1.11, when x decreases in Li_xCoO_2, the first transition occurs shortly after the charge starts, leading to the co-existence of two phases (R_1 and R_2) over the range $0.93 < x < 0.75$. This transition is associated with an insulator-to-metal (MIT) transition reported by Ménétrier et al. [51]. When x approaches 0.5, the order/disorder of Li in the structure results in two transitions in the regions slightly above and below the $x = 0.5$. The phase transition to the lithium ordered $x = 0.5$ phase is associated with a distortion of the phase from hexagonal (R_2) to monoclinic (M) symmetry. At high voltages, during the range of $1/3 < x < 0.87$, there exists another two-phase region and the O1 phase is formed when the voltage exceeds 4.5 V.

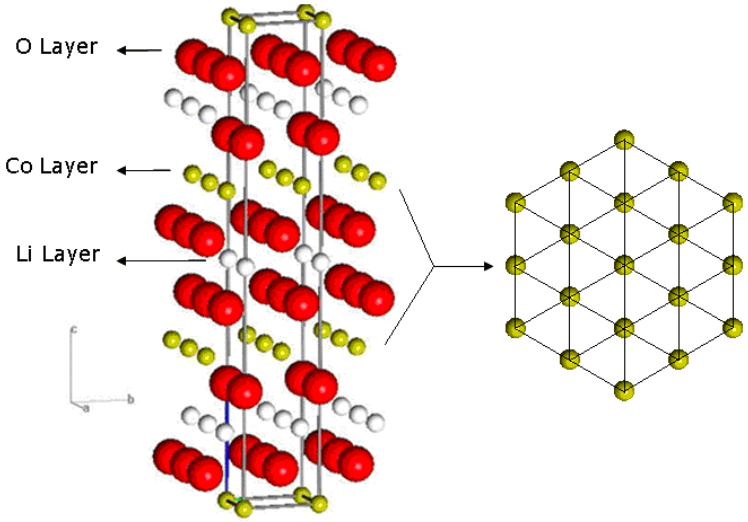

Figure 1.10. α-$NaFeO_2$-type structure ($R\bar{3}m$) of layered material $LiCoO_2$. The trigonal lattice of the TM layer (Co layer here) is shown on the right.

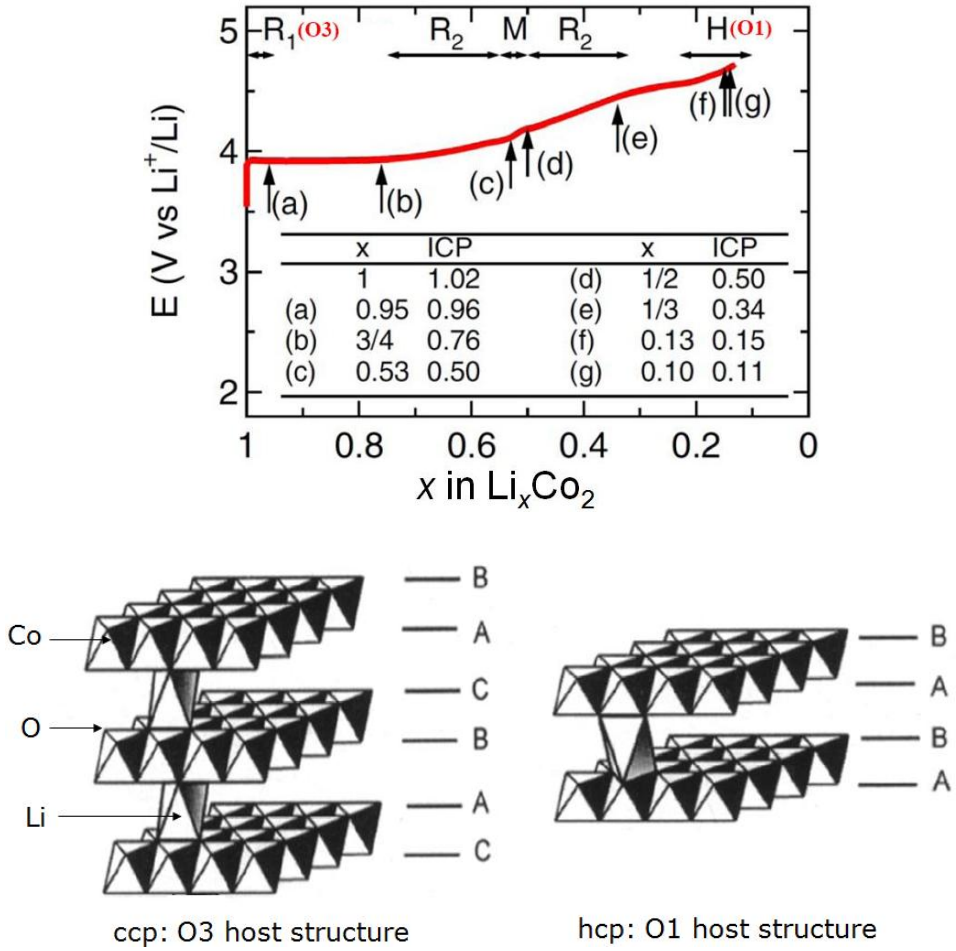

Figure 1.11. Top: a typical voltage vs. composition profile of a Li_xCoO_2/Li cell. The major phases are represented with symbols R (rhombohedral), M (monoclinic), and H (hexagonal), and points at different stages are indicated with letters (a) to (g). The corresponding compositions are listed in the table included in the figure. The O3 phase refers to the pristine phase with the CoO_2 layers forming ABCABC stacking sequence, and the O1 phase refers to the sheared structure with CoO_2 layers stacking with an ABAB sequence. Bottom: illustrations of the ABCABC stacking sequence in the O3 phase (left) and the ABAB stacking sequence in the O1 phase (right). (Figures after ref. [52] (top) and ref. [53] (bottom).)

$LiCoO_2$ exhibits relatively long cycle life when the delithiated Li is less than 50%. To improve its electrochemical performance, e.g., achieve higher capacity and increase the stability of the delithiated phase, strategies including doping, Co-substitution, and surface coating, etc., have been attempted. Studies have shown that a small amount of certain inactive main group elements, such as B [54], Mg [55-56], and Al[57-58], can be beneficial to the cycleability of $LiCoO_2$. Also, it has been reported that upon cycling, a passivation layer forms on the surface of $LiCoO_2$ particles, and this layer would isolate the active material from other particles and the current collector, causing capacity fading [59]. Therefore, an extensive research of surface coating the cathode materials has also been conducted, aiming at avoiding unwanted surface reactions and to protect the bulk material. Most of the studies are focused on metal oxide coatings, such as Al_2O_3 [60-62], ZrO_2 [63-65], MgO [66-67], TiO_2 [65]. The Al_2O_3 and MgO coating has been demonstrated to improve the cycleability of commercial $LiCoO_2$, significantly. A recent study reported by Sun et al. shows that coating the $LiCoO_2$ particles with a uniform 10 nm coating of AlF_3 also largely improves the capacity retention in the 3 to 4.5 V range [68].

In addition to improving the electrochemical performance of $LiCoO_2$, using materials with less or no Co content is another motivation to study the materials with partially or completely substituted Co, such as $LiNiO_2$[69], $LiNi_{1-y}Co_yO_2$ [70], $LiMnO_2$ [71], $LiNi_{1-y}Mn_yO_2$ [72-73] and $LiNi_{1-y-z}Mn_yCo_zO_2$ [74-75]. Among them, layered materials with the compositions $Li[Ni_yMn_yCo_{1-2y}]O_2$, first synthesized by Ohzuku and

Makimuru [76] and Lu et. al. [77], show very good electrochemical behavior and, consequently, have triggered a large amount of research on these and related compounds.

The electrochemical properties of $Li[Ni_yMn_yCo_{(1-2y)}]O_2$ ($0 < y \leq 1/2$) have been extensively studied by several groups [78-82]. Dahn's group published several papers discussing the crystal structures, morphology, thermal stability and electrochemical properties of $Li[Ni_yMn_yCo_{(1-2y)}]O_2$ as y increases from 0 to 0.5 [83-84]. According to their study, these compounds show specific capacities around 110 mAh/g to 130 mAh/g in a voltage window between 3.0 V and 4.2 V (see Figure 1.12), and they display very good capacity retentions in this voltage range (see Figure 1.13). With a higher cutoff voltage (e. g., 4.4 V), the specific capacity can be increased by approximately 30 mAh/g.

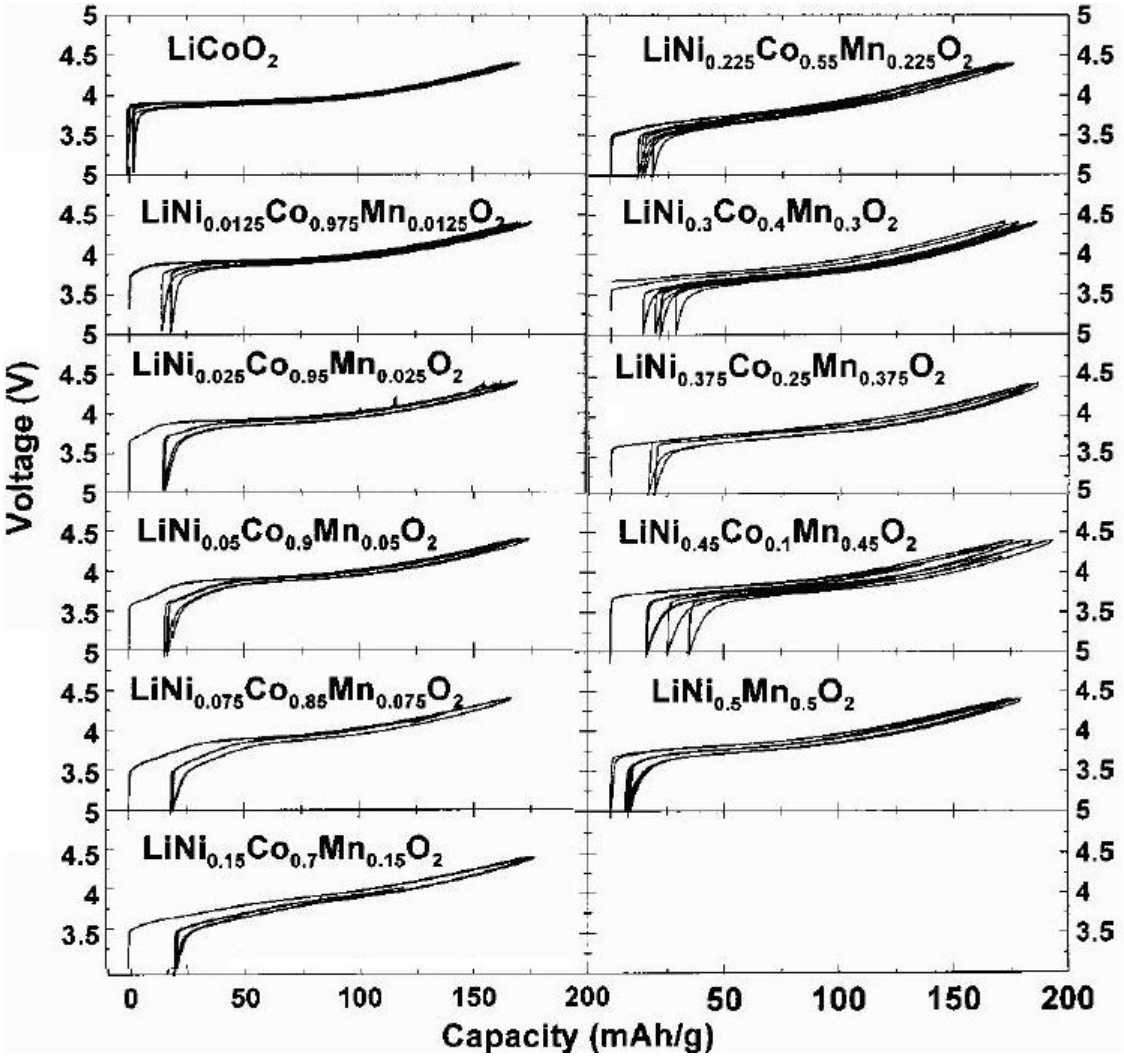

Figure 1.12. First few cycles of $Li[Ni_yMn_yCo_{(1-2y)}]O_2$ ($0 \leq y \leq 0.5$) between 3.0 to 4.4 V using a specific current of 5 mA/g (current rate approximately equivalent to a C/60 regime). (Figure after ref. [83].)

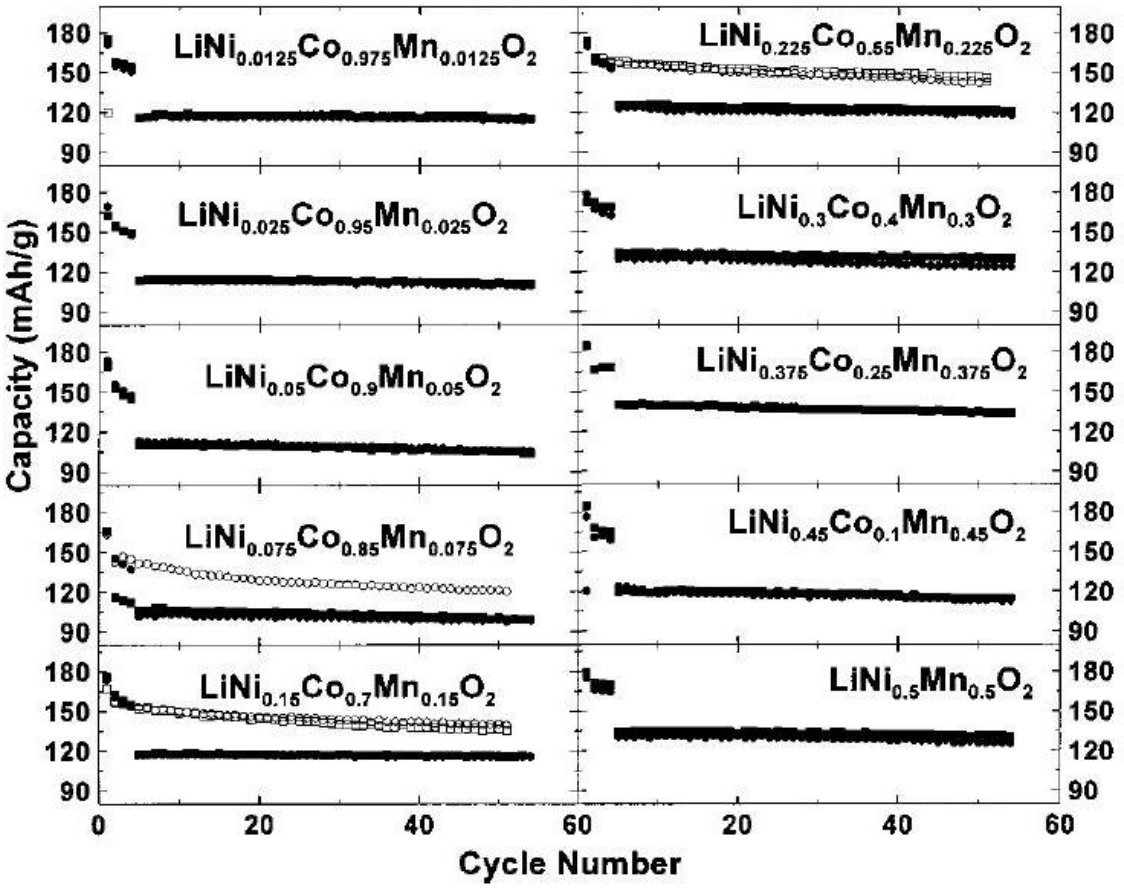

Figure 1.13. Capacity retention for $Li[Ni_yMn_yCo_{(1-2y)}]O_2$ ($0 < y \leq 0.5$) cycling between 3.0 to 4.2 V (solid symbols) and between 3.0 to 4.4 V (open symbols) using a specific current of 30 mA/g (approximately equivalent to a C/10 current rate). (Figure after ref. [83].)

The two most attractive members from this series are the y = 1/3 member, $Li[Ni_{1/3}Mn_{1/3}Co_{1/3}]O_2$ (denoted as NMC333), and the y = 1/2 member, $Li[Ni_{0.5}Mn_{0.5}]O_2$ (denoted as NMC550), since they both exhibit very promising electrochemical properties. Specifically, $Li[Ni_{1/3}Mn_{1/3}Co_{1/3}]O_2$ shows a stable capacity of around 150 mAh/g in the voltage window at 3.5 to 4.2 V and a capacity of over 200 mAh/g on cycling to 5.0 V [76]. $Li[Ni_{0.5}Mn_{0.5}]O_2$ has a stable structure and gives a stable capacity of 200 mAh/g between 2.5 and 4.5 V after 30 cycles [73].

Much work has been devoted to these compounds to understand the structure-properties relationship. For the NMC333 material, the first-principle calculations, backed by experimental XANES results, demonstrated that the oxidation states of Ni, Mn and Co in the pristine compound are +2, +4 and +3 respectively [79]. Based on these methods it is also proposed that, upon charging, Ni^{2+} is oxidized first, then Co^{3+} is oxidized only on charging up to high potentials in the 4.88-5.2 V range. Ni^{2+}/Ni^{3+} are thought to be present for lithium contents (x) in $Li_x[Ni_{1/3}Mn_{1/3}Co_{1/3}]O_2$ of $2/3 \leq x \leq 1$, Ni^{3+}/Ni^{4+} for $1/3 \leq x \leq 2/3$, and Co^{3+}/Co^{4+} for $0 \leq x \leq 1/3$. The oxidation state of Mn^{4+} remains unchanged through the charging process [78-79]. Yoon and co-workers used *in situ* metal K-edge and O K-edge X-ray absorption spectroscopy (XAS) and ^6Li MAS NMR spectroscopy to probe the local environment and electronic structural changes, and their results show that in the range of $2/3 \leq x \leq 1$, the oxidation of Ni^{2+} ions represents the major charge compensation mechanism [85-86]. This is consistent with the theoretical calculations.

As for the NMC550 material, Ni^{2+} co-exists with Mn^{4+} in the transition metal layers and the Jahn-Teller species Ni^{3+} and Mn^{3+} are consequently absent, and this allows

for the stabilization of the framework [72, 87]. Upon cycling, Ni^{2+} is the active redox center and it is oxidized to Ni^{4+} in a fully oxidized (delithiated) phase. In contrast, Mn^{4+} stays unchanged throughout the whole oxidation process. Therefore, the stability of NMC550 has been attributed to the fact that half of the transition metals (Mn^{4+}) inside the framework remain inactive upon delithiation.

Although NMC550 shows a good stability over a large range of the lithium concentration, the rate capability of this material is not as good as $LiCoO_2$. Recent NMR studies have demonstrated that the electrochemical behavior of NMC550 material is largely affected by the cation orderings/exchange both in the transition metal layers and between the transition metal and lithium layers [82, 88-89]. A greatly improved rate performance was observed in an "ideal" layered NMC550 material prepared via an ion-exchanging method [82].

Despite much work on the $Li[Ni_yMn_yCo_{(1-2y)}]O_2$ system, it still remains unclear as to how Ni/Mn ordering is disrupted by Co^{3+} doping, how the ordering and oxidation state of the three cations changes across the series and as a function of the processing conditions, and most importantly, how this affects the electrochemical performance. Therefore, a systematic and intensive study has been conducted to investigate the structure of the pristine materials, and the results are presented in Chapter 2. Following this study, Chapter 3 discusses the study of the delithiation processes of a representative member $Li[Ni_{0.05}Mn_{0.05}Co_{0.90}]O_2$ (denoted as **90Co**).

1.3.2 CDI compounds

As mentioned in Section 1.2.2, the combination displacement insertion (CDI) mechanism is a relatively new concept in describing the reactions of the electrodes for LIBs. So far, there are not many CDI compounds have been developed. Intrigued by the success of $Cu_{2.33}V_4O_{11}$ described earlier, a systematic study has been conducted on several other Cu-V-O and Cu-V-S systems. This study revealed that the dimensionality and flexibility of the framework structure and the Cu mobility in the material play important roles in governing the CDI reactions [41].

In addition, as the Cu is known to be mobile in the spinel structure, the CDI reactions have also been examined in a Cu-based thiospinel, $CuTi_2S_4$ [39]. As $CuTi_2S_4$ is a cation mixed-valance system ($Cu^{+}Ti^{3+}Ti^{4+}S_4^{2-}$), another Cu-based thiospinels, $CuCr_2S_4$, an anion mixed system ($Cu^{+}Cr_2^{3+}S_3^{2-}S^{-\bullet}$), was chosen and studied as a comparative case[34, 39]. The results suggest that the $CuTi_2S_4$ system goes through a CDI reaction in the initial stage of the first discharge (not beyond 2 Li insertion), where Li intercalation into the Ti_2S_4 framework is associated with fully reduced Cu extrusion and reduction of Ti^{4+} to Ti^{3+}. This process is fully reversible upon re-oxidation (charging). As for $CuCr_2S_4$, its electrochemical reactivity towards Li initially also occurs through a CDI reaction, with the reduction of Cu and $S^{-\bullet}$, but Cu cannot be totally reduced and extruded (the end of the discharge phase is $Li_{1.75}Cu_{0.25}Cr_2S_4$), and the reaction is partially reversible. The differences between these two thiospinels have been ascribed to the larger Cu mobility in $CuTi_2S_4$ than in $CuCr_2S_4$[34].

Another class of compounds that shows the CDI reactions towards Li is a novel class of oxysulfides, $Sr_2MnO_2Cu_{2m-\delta}S_{m+1}$ (m = 1, 2 and 3, $\delta \sim 0.5$), that has been successfully synthesized very recently [90-91]. These materials consist of alternating Perovskite-type [Sr_2MnO_2] sheets and various thicknesses of antifluorite-type [Cu_2S] sheets (see Figure 1.14). Previous studies have shown that Li can be both chemically [92] and electrochemically [40] inserted into the structure, and these reactions are reversible. The neutron diffraction data for the chemical lithiated phases [92] and Li NMR data for the electrochemical lithiated phases [40] have confirmed that the inserted Li ions, in both cases, replace the Cu in the MS_4 tetrahedral sites in the framework structure, and the elemental Cu is extruded. The electrochemical capacity of the oxysulfides is proportional to the thickness of the sulfide layers (see Figure 1.15), where the m=3 member has the largest capacity, indicating that the Perovskite-type oxide layers seem inert in electrochemical reactions. The cycleability of these materials in LIBs has been tested within a voltage window of 1.1 to 2.7 V. The results show that the capacity retentions of these oxysulfides largely depend on the thickness of the Cu_2S layer in each member as well, where higher capacity retentions were observed for the ones with thinner sulfide layers. This indicates that the rigid Perovskite-type [Sr_2MnO_2] layers in the structure, although seem with no capacity contribution, provide the structural stability and are beneficial to the cycleability.

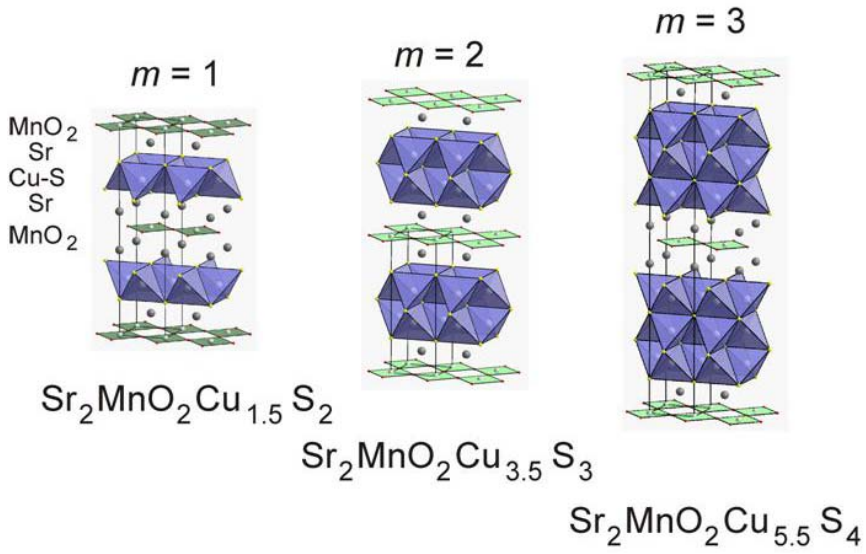

Figure 1.14. Structure of the series oxysulfides $Sr_2MnO_2Cu_{2m-\delta}S_{m+1}$ with m = 1, 2 and 3. (Figure after ref. [40].)

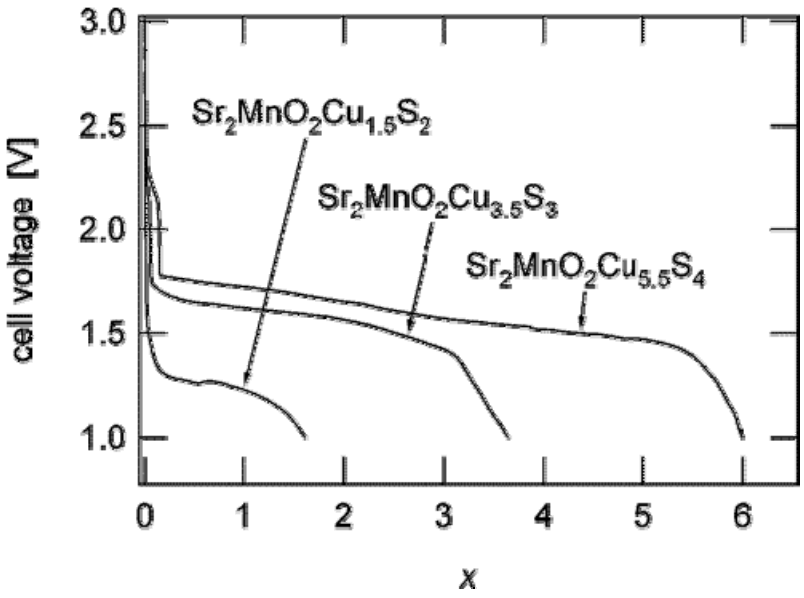

Figure 1.15. The first discharge of $Sr_2MnO_2Cu_{2m-\delta}S_{m+1}$ with m = 1, 2 and 3, vs. a Li metal negative electrode, with a discharge rate of C/20. x denotes the number of Li insertion per formula unit. (Figure after ref. [40].)

Understanding the reactions and phase transitions involved in the electrochemical processes from a fundamental point of view can provide valuable insight in recognizing the structure-properties relationship of the material and help design or search for new functional systems with desired performance features. The studies summarized above have provided valuable information in understanding the CDI reactions and some of the crucial parameters in determining the electrochemical performance. However, there still remain pieces of the puzzle to fully understand the CDI mechanism. To pursue a deeper understanding of the CDI reactions in the oxysulfide systems, the $m = 2$ member has been chosen as a representative case and its electrochemical behavior and the structural changes during the (dis)charge processes are investigated intensively (Chapter 4).

1.4 Solid State NMR

Solid-state NMR has been a very useful tool in studying the structures and electronic properties of the electrode materials for LIBs. Different from diffraction techniques that probe the long range structures (average), solid state NMR provides valuable information regarding the short range structures (local), , even in disordered systems [93]. NMR is element specific, and by using different nuclei as probes the local environment of different species can be distinguished. Lithium ions are directly involved in the electrochemical processes occurring in the LIB systems. Fortunately, the two naturally occuring Li nuclei (^{6}Li and ^{7}Li) are both NMR active species. Thus, they are commonly used as probes in the electrode materials for LIBs. Moreover, NMR spectra are quantitative and the integrated area (intensity) of a particular resonance is

proportional to the amount of the equivalent nuclei contributing to it. For the positive electrode materials, as the charge / discharge processes are associated with the removal / insertion of Li, the changes of the Li amount at certain sites can be evaluated by performing quantitative analysis of the NMR spectra. In the following sections, basic concepts such as the magic angle spinning (MAS), Fermi-contact interactions, dipolar coupling, and others, will be introduced briefly [93-96].

1.4.1 Magic Angle Spinning (MAS) NMR

In liquid static NMR, molecules in the solution tumble very fast (10^{-9} to 10^{-12} s) and the anisotropic interactions are all averaged out on the NMR spectral time scale (10^{-3} to 10^{-6} s). This results in narrow resonance lineshapes in the NMR spectra. In solid-state NMR, however, molecules are relatively fixed compared with in solution, and this lack of molecular motion results in a broadening of the lineshape in the spectra. Nevertheless, it has been shown that the NMR spectrum can be influenced by mechanical rotation of the whole sample [97]. Specifically, when the sample is rotated at a "magic angle" of 54.736° with respect to the external magnetic field (B_0) (Figure 1.16), the anisotropic interactions such as chemical shielding interaction, heteronuclear dipolar interaction, and first order quadrupole coupling (for nuclei with spin $I > 1/2$), can be eliminated. When the spinning frequency of the rotor is faster than the size of the anisotropic interaction, only a single resonance is observed; otherwise, the powder pattern is split into an isotropic resonance with spinning sidebands separated at intervals of the spinning frequency. The theory behind the MAS technique will not be discussed here, but is given

in detail in reference [94]. By applying the MAS technique, high resolution NMR spectra can be obtained.

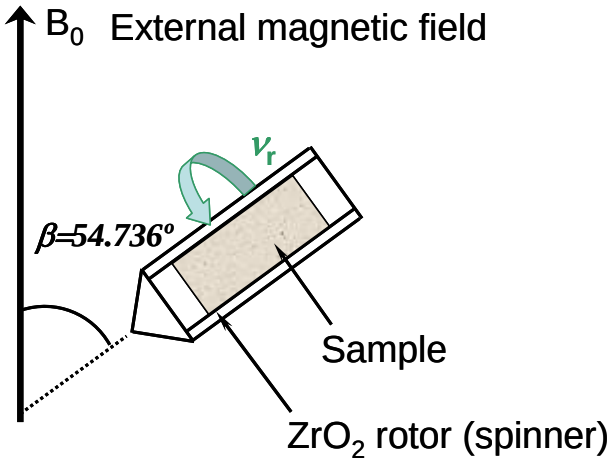

Figure 1.16. Schematic representation of the Magic Angle Spinning (MAS) technique. The angle between the external magnetic field B_0 and the rotor axis is the magic angle, β = 54.736°, and ν_r is the spinning speed frequency of the rotor.

1.4.2 NMR Spectra of Paramagnetic Materials

Most of the battery materials proposed up to date have paramagnetic ions (with unpaired electrons) in the charged or discharged state, for example, Ni^{2+} (d^8), Ni^{3+} (d^7), Co^{4+} (d^{5+}), Mn^{3+} (d^4), and Mn^{4+} (d^3). Therefore, NMR spectra of the battery materials are often dominated by the interactions between Li nuclear spins and electronic spins on the paramagnetic ions.

Paramagnetic ions with electronic spin *S* are associated with magnetic moments, μ_e, which are randomly distributed when there is no field present (Figure 1.17a). The electronic spin number *S* is determined by the number of unpaired electrons of the ion, for example, $S = 1/2$ for Ni^{3+} (d^7), $S = 1$ for Ni^{2+} (d^8), and $S = 3/2$ for Mn^{4+} (d^3). By applying an external magnetic field (B_0), the originally random distribution of magnetic moments, μ_e, of the paramagnetic ions tend to align along the external magnetic field, defined as the *z*-direction, and the energy levels are split into $2S+1$ energy states, as shown in Figure 1.17b for the case of $S = 1/2$. This is referred to as the Zeeman splitting. Since the electrons are negatively charged, the energy level of the $|-1/2\rangle$ state is lower than the $|+1/2\rangle$ state. Since the lifetime of an ion in a particular electronic state is very short compared with the time scale probed by NMR, only the average overall magnetic moment ($\overline{\mu}_e$) at the local magnetic field can be detected by NMR (Figure 1.17c), and be sensed by the nearby nucleus (*I*) on the NMR timescale (Figure 1.17d).

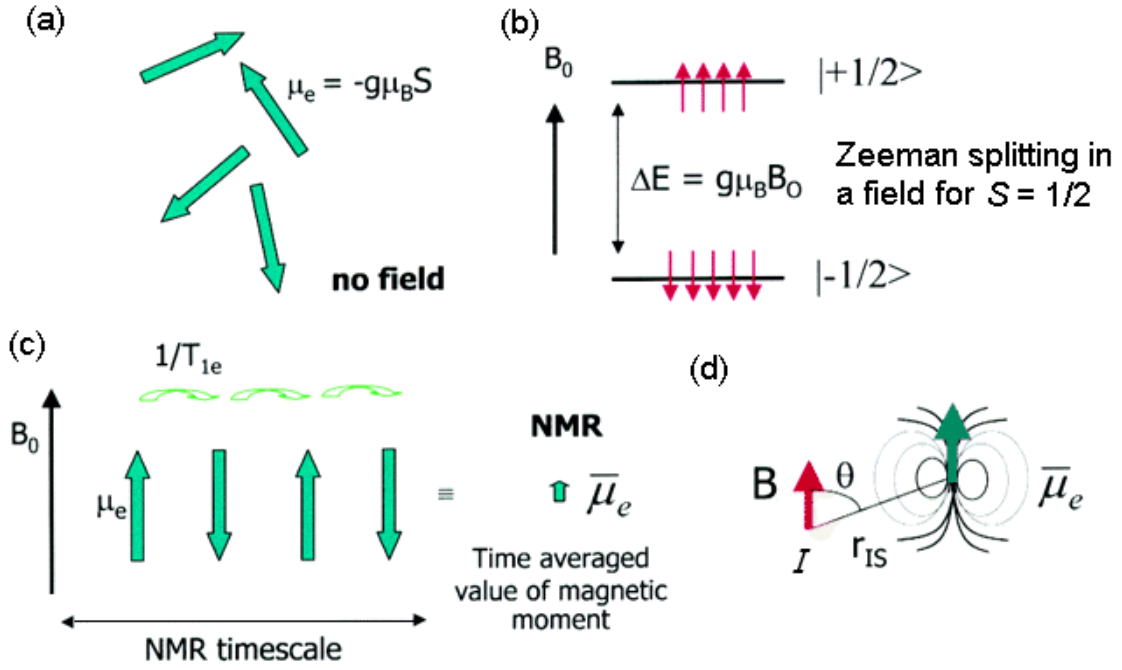

Figure 1.17. Representations of how the applied external magnetic field (B_0) affects the local magnetic field on the nuclei of intereste. (a) Random distribution of magnetic moments of paramagnetic ions with unpaired electrons with no field applied. (b) Effect of an applied static magnetic field on a paramagnet with electron magnetic moment μ_e and electronic spin $S = 1/2$. The magnetic moment tends to align with the direction of B_0, and the energy level are split into |-1/2> and |+1/2> states. (c) Spins in different states transit (e.g. |+1/2>↔|-1/2>) at the rate $1/T_{1e}$, which is typically much shorter than the NMR timescale, and the NMR is only able to probe the time averaged magnetic moment value $\overline{\mu}_e$. (d) The averaged magnetic moment on the local magnetic field $\overline{\mu}_e$ affects its nearby nucleus *I*. (Figures modified from ref. [93].)

When studying the nuclear-electron spin (*I*-*S*) system, in principle two resonances in the NMR spectrum are expected, since *I* can couple with magnetic moments associated with two electron spin states |-1/2> and |+1/2> (in the case of $S = 1/2$). However, in reality, as the relaxation of the electrons are much faster (very short T_{1e}) compared with the NMR timescale, the nucleus *I* cannot respond to each electronic state but only with the time-average of the two electronic spin states, $\overline{\mu}_e$, and only a single resonance at the average frequency is observed. This average $\overline{\mu}_e$ is proportional to the time average value of the paramagnetic electron spins along the *z* axis, $\langle S_z \rangle$, which is given by:

$$\langle S_z \rangle = -\frac{B_0}{\mu_0 g N_0 \mu_B} \chi_M \qquad (1.4)$$

where μ_0 is the permeability, *g* the electron *g*-factor, N_0 the Avogadoro's number, μ_B the Bohr magneton, and χ_M the magnetic molar susceptibility in m^3/mol [95, 98].

The electron-nuclear interactions can occur either through chemical bonds (Fermi-contact interaction) or through space (dipolar coupling). In the $^{6/7}$Li MAS NMR spectra for most of the battery materials, the NMR shifts are induced by the Fermi-contact interaction, and the spread of the sidebands is the result of the dipolar coupling. Figure 1.18 shows a ^{6}Li MAS NMR spectrum of Li_2MnO_3 with the effects of different interactions illustrated as an example.

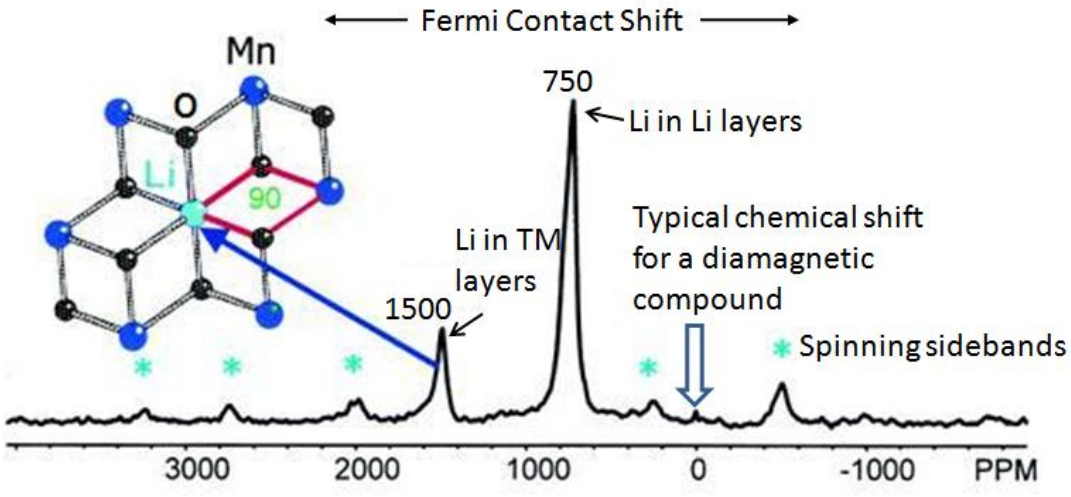

Figure 1.18 ^{6}Li MAS NMR spectrum of the layered compound Li_2MnO_3. Two resonances are observed: one at 750 ppm coming from Li in Li layers, the other one at 1500 ppm coming from Li surrounded by 6 Mn in the transition metal layers. The isotropic resonances and spinning sidebands are marked with their shifts and asterisks, respectively.

1.4.2.1 Fermi Contact Interaction

The Fermi-contact interaction, also called the hyperfine interaction, arises from the transfer of unpaired electron spin density from the paramagnetic ions to the nuclear spin. This density can be transferred directly from the paramagnets or via intermediate atoms. The Fermi-contact interaction is a function of the unpaired electron density on the paramagnetic ions. The Hamiltonian equation for Fermi-contact (H_c) can be written as below:

$$H_c = A_c \cdot I_z \cdot \langle S_z \rangle \qquad (1.5)$$

where A_c is the hyperfine coupling constant, I_z is the nuclear spin and $\langle S_z \rangle$ is the time average electronic spin of unpaired electrons as described in Eq. 1.3.

The NMR shift, δ, induced by the Fermi-contact interaction is proportional to the electron density at the observed nucleus, $\langle S_z \rangle$, and can be written as:

$$\delta = \frac{\Delta\omega}{\omega_0} = -\frac{A_c}{\omega_0 h}\langle S_z \rangle \qquad (1.6)$$

where ω_0 is the observed Larmor frequency, and $\Delta\omega = \omega - \omega_0$.

The size and direction of the shift, δ, is determined by the hyperfine constant A_c in the above equation, and A_c/h can be expressed as:

$$\frac{A_c}{h} = \frac{g\mu_B\gamma_N\rho(r=0)\mu_0}{3S} \qquad (1.7)$$

where γ_N is the gyromagnetic ratio for the nucleus, and $\rho(r = 0)$ is the electron spin density at the nucleus I. Only the s-orbital electrons on the nucleus of interest will be considered since only s-orbital electrons have non-zero probabilities of showing up at the

nuclear region ($\rho(r) \neq 0$, where $r \rightarrow 0$). Depending on the connectivity between the orbitals on the paramagnetic ions and the orbitals on the studied nucleus, the $^{6/7}$Li hyperfine shift can be very large for the paramagnetic systems, while the typical resonance range for diamagnetic species is very narrow (0 ± 5 ppm).

Electron spin density can be transferred from the paramagnet to the nucleus of interest directly or indirectly via intermediate atoms, for example, oxygen. When the electron density is transferred via the indirect way (which is a common situation when studying the Li NMR of battery materials), the transferred electron spin density largely depends on the bondings, such as the geometry (bond distances and angles) and ionicity, involving the paramagnetic ions, Li, and intervening atoms. The Fermi contact shift induced by each magnetic ion is additive, and the observed shift is the sum of each individual interaction and reflects the total spin density that is transferred to the studied nucleus.

In the layered $LiMO_2$ (M = transition metal, TM) structure, there are two types of interactions between lithium ions and the unpaired electrons on the transition metals. One is the 90° M-O-Li interaction, and the other one is the 180° M-O-Li interaction, which occurs between the lithium ions and the transition metal ions located in the first and second coordination shells, respectively (Figure 1.19). The electron spin on the transition metal cation M can be transferred to the *s* orbital of Li via the oxygen atoms in between, but merely depends on the M-O-Li bond angles, the effective transferred electron density can be very different, even for the same TM cation, for example, Mn^{4+} (d^3).

Figure 1.20 shows the possible mechanism for the transfer of d-electron spin density of Mn^{4+} ($t_{2g}^{3}e_{g}^{0}$) to the 2s orbital of Li via the 2p orbital of oxygen in these two types of interactions. In the 90° interaction situation, a half filled t_{2g} orbital induces an orientation of the spins, thus, a magnetic moment of the oxygen 2p-orbital electrons. This results in a paralleled magnetic moment transfer to the empty 2s-orbital on Li yielding a positive shift (around 120-150 ppm) in the NMR spectrum. When it comes to the 180° case, the empty e_g orbital tends to transfer electron density with the same sign as the t_{2g} orbital due to the exchange coupling between e_g and t_{2g} of the same atom. This results in the opposite situation on the empty Li 2s-orbital and a positive shift appears in the NMR spectrum (approximately -60 ppm) [99].

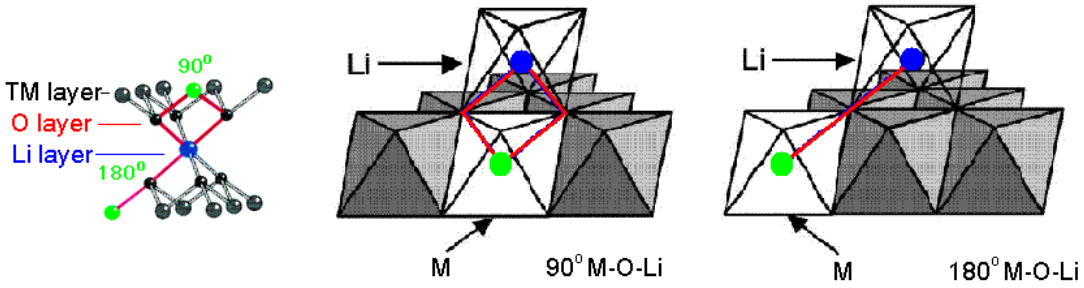

Figure 1.19. Illustrations of the two types of interactions (90° and 180° M-O-Li interactions) between Li in Li layer of a $LiMO_2$-type structure, and transition metals (TM) in TM layers (M=Ni, Mn or Co). The interactions occur via the oxygen as intermediate atoms. A representation of the geometric environment of lithium is also depicted. (Figure modified after ref. [100].)

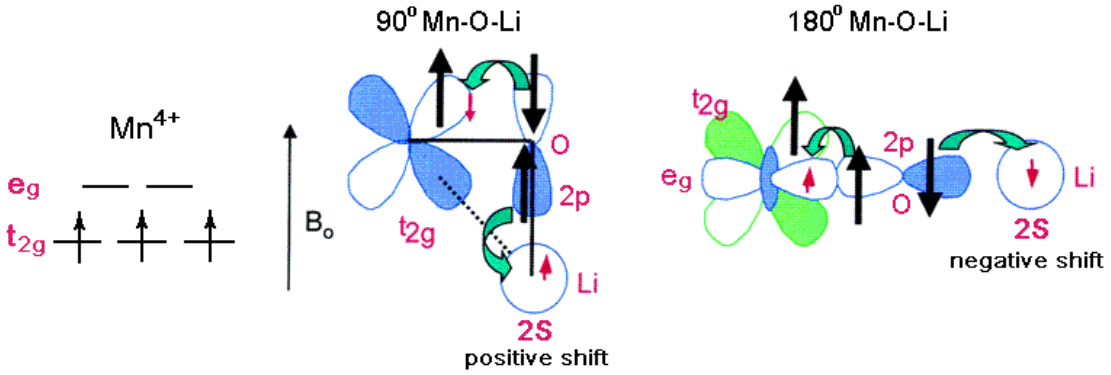

Figure 1.20. Diagrams showing the possible mechanisms for how the transfer of electron spin density on Mn^{4+} to Li^{+}, these depend on the type of M-O-Li environment. Left: electron configuration of Mn^{4+} in an octahedral field. Center: the 90° Mn-O-Li interaction. Right: the 180° Mn-O-Li interaction. (Figure after ref. [93])

1.4.2.2 Dipolar Coupling

As mentioned in the earlier part, the dipolar interaction is a through-space interaction between the magnetic moment μ_e (or time-averaged $\overline{\mu}_e$) and the studied nucleus *I*. As illustrated in Figure 1.17d, *I* is affected by the local magnetic field of the nearby electronic spin *S*, and the Hamiltonian for this electron-nuclear interaction is given by:

$$H_{en} = \frac{\mu_0}{4\pi} \overline{\mu}_e \widetilde{D}_{en} \mu_N \qquad (1.8)$$

where μ_N is the nuclear magnetic moment of *I* ($\mu_N = \gamma_N (h/2\pi) I_z$), and $\widetilde{D}_{en}$ is the dipolar coupling tensor between the nucleus and unpaired electron. The matrix elements of $\widetilde{D}_{en}$ is defined as:

$$D_{ij} = \frac{1}{r^3}\left(\delta_{ij} - 3e_i e_j\right) \qquad (1.9)$$

where *r* is the distance between the nuclear and electronic spins, δ_{ij} is the Kronecker delta ($\delta_{ij} = 1$ for $i = j$ and $\delta_{ij} = 0$ for $i \neq j$), and e_i and e_j are the *x, y, z* components of a unit vector point from the nuclear spin (*I*) to the electron spin (*S*) in a chosen coordinate system.

Clearly, the dipolar coupling is angular dependent. Since the dipolar vectors in solids are randomly orientated with respect to the magnetic field, the dipole-dipole interaction causes a distribution of resonance frequencies and line broadening of the NMR signal. The angular dependence of the dipolar coupling includes a term of ($3 \cos^2 \beta$

– 1), and this interaction is equal to zero when the angle between the dipolar vector and the external magnetic field β satisfied the equation:

$$3\cos^2\beta - 1 = 0. \qquad (1.10)$$

The solution of this equation is the *magic angle*: $\beta = 54.736°$. Therefore, as mentioned in the earlier section, by applying the MAS technique, the dipolar coupling can be averaged out and the broad line of the spectrum is split into relatively narrow lines (the sidebands) spaced at integer multiples of the MAS frequency v_r. If the MAS frequency is large enough, in principle there will be only a single resonance that can be observed.

As shown in Eq. 1.8, the size of the dipolar coupling depends on both $\overline{\mu}_e$ and μ_N. Since $\overline{\mu}_e$ is proportional to $\langle S_z \rangle$, and they are both proportional to the external magnetic field strength B_0. On the other hand, μ_N is determined by the gyromagnetic ratio γ_N, and therefore, nucleus with a larger γ_N usually has larger dipolar couplings and results in larger spinning sideband manifolds in the MAS spectra. In the case of Li MAS NMR, ^{7}Li with its much higher gyromagnetic ratio than ^{6}Li ($\gamma^7\text{Li}/\gamma^6\text{Li} = 2.6$) results in much larger dipolar interactions, and the spectra with much larger spinning sidebands (see Figure 1.21 for an example). Thus, relatively weak resonances in the ^{7}Li MAS NMR spectra may be difficult to resolve since they are obscured by overlapping of the spinning sidebands from more intense resonances. Therefore, to minimize the effect of the dipolar interaction and simplify the spectra, the MAS experiments are preferred to be performed under low magnetic field, using low γ_N nuclei, and with fast MAS.

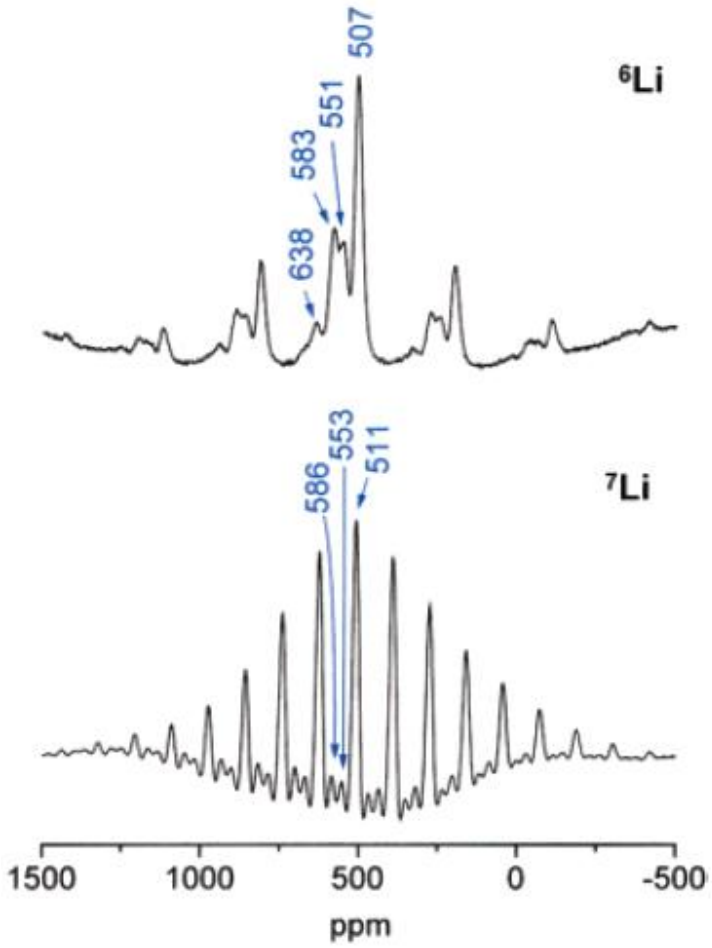

Figure 1.21. Comparison of the ^{6}Li and ^{7}Li MAS NMR spectra of a $LiMn_2O_4$ sample obtained of a MAS spinning speed of 10.5 kHz and a magnetic field strength of 4.7 T (200 MHz for ^{1}H). (Figure after ref. [93])

References

1. *BP Statistical Review of World Energy (June 2009)*. 2009.

2. *International Energy Outlook 2009*. 2009, Energy Information Administration, U.S. Department of Energy.

3. *Emissions of Greenhouse Gases in the United States 2008*, U.S.E.I. Administration, Editor. 2009, U.S. Department of Energy.

4. Winter, M. and R.J. Brodd, What Are Batteries, Fuel Cells, and Supercapacitors? *Chem. Rev.*, 2004. **104**: p. 4245-4269.

5. Tarascon, J.-M. and M. Armand, Issues and challenges facing rechargeable lithium batteries. *Nature*, 2001. **414**: p. 359-367.

6. Whittingham, M.S., Electrical Energy-storage and intercalation chemistry. *Science*, 1976. **192**(4244): p. 1126-1127.

7. Mohri, M., N. Yanagisawa, Y. Tajima, H. Tanaka, T. Mitate, S. Nakajima, M. Yoshida, Y. Yoshimoto, T. Suzuki, and H. Wada, Rechargeable lithium battery based pyrolytic carbon as a negative electrode. *J. Power Sources*, 1989. **26**(3-4): p. 545-551.

8. Mizushima, K., P.C. Jones, P.J. Wiseman, and J.B. Goodenough, Li_xCoO_2(0<x<-1): A new cathode material for batteries of high energy density. *Mater. Res. Bull.*, 1980. **15**(6): p. 783.

9. Nishi, Y., The Development of Lithium Ion Secondary Batteries. *Chem. Rec.*, 2001. **1**(5): p. 406-413.

10. Nagaura, T. and K. Tozawa, Lithium ion rechargeable battery. *Prog. Batteries Solar Cells*, 1990. **9**: p. 209-217.

11. Thackeray, M.M., W.I.F. David, P.G. Bruce, and J.B. Goodenough, Lithium insertion into manganese spinels. *Mat. Res. Bull.*, 1983. **18**(4): p. 461-472.

12. Amatucci, G. and J.M. Tarascon, Optimization of insertion compounds such as $LiMn_2O_4$ for Li-ion batteries. *J. Electrochem. Soc.*, 2002. **149**(12): p. K31-K46.

13. Johnson, C.S., J.S. Kim, C. Lefief, N. Li, J.T. Vaughey, and M.M. Thackeray, The significance of the Li_2MnO_3 component in 'composite' xLi_2MnO_3 •(1-x)$LiMn_{0.5}Ni_{0.5}O_2$ electrodes. *Electrochem. Commun.*, 2004. **6**(10): p. 1085-1091.

14. Johnson, C.S., N. Li, J.T. Vaughey, S.A. Hackney, and M.M. Thackeray, Lithium-manganese oxide electrodes with layered-spinel composite structures $xLi_2MnO_3 \bullet (1-x)Li_{1+y}Mn_{2-y}O_4$ ($0 < x < 1$, $0 <= y <= 0.33$) for lithium batteries. *Electrochem. Commun.*, 2005. **7**(5): p. 528-536.

15. Thackeray, M.M., C.S. Johnson, J.T. Vaughey, N. Li, and S.A. Hackney, Advances in manganese-oxide 'composite' electrodes for lithium-ion batteries. *J. Mater. Chem.*, 2005. **15**(23): p. 2257-2267.

16. Padhi, A.K., K.S. Nanjundaswamy, and J.B. Goodenough, Phospho-olivines as positive-electrode materials for rechargeable lithium batteries. *J. Electrochem.Soc.*, 1997. **144**(4): p. 1188-1194.

17. Chung, S.Y., J.T. Bloking, and Y.M. Chiang, Electronically conductive phospho-olivines as lithium storage electrodes. *Nat. Mater.*, 2002. **1**(2): p. 123-128.

18. Herle, P.S., B. Ellis, N. Coombs, and L.F. Nazar, Nano-network electronic conduction in iron and nickel olivine phosphates. *Nat. Mater.*, 2004. **3**(3): p. 147-152.

19. Ravet, N., Y. Chouinard, J.F. Magnan, S. Besner, M. Gauthier, and M. Armand, Electroactivity of natural and synthetic triphylite. *J. Power Sources*, 2001. **97-8**: p. 503-507.

20. Yamada, A., S.C. Chung, and K. Hinokuma, Optimized $LiFePO_4$ for lithium battery cathodes. *J. Electrochem. Soc.*, 2001. **148**(3): p. A224-A229.

21. Arnold, G., J. Garche, R. Hemmer, S. Strobele, C. Vogler, and A. Wohlfahrt-Mehrens, Fine-particle lithium iron phosphate $LiFePO_4$ synthesized by a new low-cost aqueous precipitation technique. *J. Power Sources*, 2003. **119**: p. 247-251.

22. Kwon, S.J., C.W. Kim, W.T. Jeong, and K.S. Lee, Synthesis and electrochemical properties of olivine $LiFePO_4$ as a cathode material prepared by mechanical alloying. *J.Power Sources*, 2004. **137**(1): p. 93-99.

23. Dominko, R., J.M. Goupil, M. Bele, M. Gaberscek, M. Remskar, D. Hanzel, and J. Jamnik, Impact of $LiFePO_4$/C composites porosity on their electrochemical performance. *J. Electrochem. Soc.*, 2005. **152**(5): p. A858-A863.

24. http://www.a123systems.com/.

25. Thackeray, M., Lithium-ion batteries - An unexpected conductor. *Nat. Mater.*, 2002. **1**(2): p. 81-82.

26. Malini, R., U. Uma, T. Sheela, M. Ganesan, and N.G. Renganathan, Conversion reactions: a new pathway to realise energy in lithium-ion battery-review. *Ionics*, 2009. **15**(3): p. 301-307.

27. Poizot, P., S. Laruelle, S. Grugeon, L. Dupont, and J.M. Tarascon, Nano-sized transition-metaloxides as negative-electrode materials for lithium-ion batteries. *Nature*, 2000. **407**(6803): p. 496-499.

28. Amatucci, G.G. and N. Pereira, Fluoride based electrode materials for advanced energy storage devices. *J. Fluorine Chem.*, 2007. **128**(4): p. 243-262.

29. Bervas, M., F. Badway, L.C. Klein, and G.G. Amatucci, Bismuth fluoride nanocomposite as a positive electrode material for rechargeable lithium batteries. *Electrochem. Solid State Lett.*, 2005. **8**(4): p. A179-A183.

30. Badway, F., A.N. Mansour, N. Pereira, J.F. Al-Sharab, F. Cosandey, I. Plitz, and G.G. Amatucci, Structure and electrochemistry of copper fluoride nanocomposites utilizing mixed conducting matrices. *Chem. Mater.*, 2007. **19**(17): p. 4129-4141.

31. Kepler, K.D., J.T. Vaughey, and M.M. Thackeray, $Li_xCu_6Sn_5$ ($0 < x < 13$): An intermetallic insertion electrode for rechargeable lithium batteries. *Electrochem. Solid State Lett.*, 1999. **2**(7): p. 307-309.

32. Kepler, K.D., J.T. Vaughey, and M.M. Thackeray, Copper-tin anodes for rechargeable lithium batteries: an example of the matrix effect in an intermetallic system. *J.Power Sources*, 1999. **81**: p. 383-387.

33. Thackeray, M.M., J.T. Vaughey, C.S. Johnson, A.J. Kropf, R. Benedek, L.M.L. Fransson, and K. Edstrom, Structural considerations of intermetallic electrodes for lithium batteries. *J. Power Sources*, 2003. **113**(1): p. 124-130.

34. Morcrette, M., P. Rozier, L. Dupont, E. Mugnier, L. Sannier, J. Galy, and J.M. Tarascon, A reversible copper extrusion-insertion electrode for rechargeable Li batteries. *Nat. Mater.*, 2003. **2**(11): p. 755-761.

35. Tarascon, J.M., S. Grugeon, M. Morcrette, S. Laruelle, P. Rozier, and P. Piozot, New concepts for the search of better electrode materials for rechargeable lithium batteries. *Comptes Rendus Chimie*, 2005. **8**: p. 9-15.

36. Leising, R.A. and E.S. Takeuchi, Solid-state cathode materials for lithium batteries: effect of synthesis temperature on the physical and electrochemical properties of silver vanadium oxide. *Chem. Mater.*, 1993. **5**(5): p. 738-742.

37. Leising, R.A., W.C. Thiebolt, and E.S. Takeuchi, Solid-State Characterization of Reduced Silver Vanadium Oxide from the Li/SVO Discharge Reaction. *Inorg. Chem.*, 1994. **33**(25): p. 5733-5740.

38. Leising, R.A. and E.S. Takeuchi, Solid-State Synthesis and Characterization of Silver Vanadium Oxide for Use as a Cathode Material for Lithium Batteries. *Chem. Mater.*, 1994. **6**(4): p. 489-495.

39. Bodenez, V., L. Dupont, M. Morcrette, C. Surcin, D.W. Murphy, and J.M. Tarascon, Copper extrusion/reinjection in Cu-based thiospinels by electrochemical and chemical routes. *Chem. Mater.*, 2006. **18**(18): p. 4278-4287.

40. Indris, S., J. Cabana, O.J. Rutt, S.J. Clarke, and C.P. Grey, Layered Oxysulfides $Sr_2MnO_2Cu_{2m-0.5}S_{m+1}$ (m=1, 2, and 3) as Insertion Hosts for Li ion batteries. *J. Am. Chem. Soc.*, 2006. **128**(41): p. 13354-13355.

41. Rozier, P., M. Morcrette, O. Szajwaj, V. Bodenez, M. Dolle, C. Surcin, L. Dupont, and J.M. Tarascon, Li-Driven Copper Extrusion/Re-injection in Various Cu-based Oxides and Sulfides. *Isr. J. Chem.*, 2008. **48**(3-4): p. 235-249.

42. Bodenez, V., L. Dupont, L. Laffont, A.R. Armstrong, K.M. Shaju, P.G. Bruce, and J.M. Tarascon, The reaction of lithium with $CuCr_2S_4$ - lithium intercalation and copper displacement/extrusion. *J. Mater. Chem.*, 2007. **17**(30): p. 3238-3247.

43. Armand, M. and J.M. Tarascon, Building better batteries. *Nature*, 2008. **451**(7179): p. 652-657.

44. Palacin, M.R., Recent advances in rechargeable battery materials: a chemist's perspective. *Chem. Soc. Rev.*, 2009. **38**(9): p. 2565-2575.

45. Winter, M., J.O. Besenhard, M.E. Spahr, and P. Novak, Insertion electrode materials for rechargeable lithium batteries. *Adv. Mater.*, 1998. **10**(10): p. 725-763.

46. Amatucci, G.G., J.-M. Tarascon, and L.C. Klein, CoO_2, The End Memeber of the Li_xCoO_2 Solid Solution. *J. Electrochem. Soc.*, 1996. **143**(3): p. 1114-1123.

47. Ozawa, K., Lithium-ion rechargeable batteries with $LiCoO_2$ and carbon electrodes - the $LiCoO_2$ C system. *Solid State Ionics*, 1994. **69**(3-4): p. 212-221.

48. Wang, H.F., Y.I. Jang, B.Y. Huang, D.R. Sadoway, and Y.T. Chiang, TEM study of electrochemical cycling-induced damage and disorder in $LiCoO_2$ cathodes for rechargeable lithium batteries. *J. Electrochem. Soc.*, 1999. **146**(2): p. 473-480.

49. Reimers, J.N. and J.R. Dahn, Electrochemical and *In situ* X-Ray Diffraction Studies of Lithium Intercalation in Li_xCoO_2. *J. Electrochem. Soc.*, 1992. **139**(8): p. 2091-2097.

50. Morcrette, M., Y. Chabre, G. Vaughan, G. Amatucci, J.-B. Leriche, S. Patous, C. Masquelier, and J.-M. Tarascon, In situ X-ray diffraction techniques as a powerful tool to study battery electrode materials. *Electrochimica Acta*, 2002. **47**: p. 3137-3149.

51. Ménétrier, M., I. Saadoune, S. Levasseur, and C. Delmas, The insulator-metal transition upon lithium deintercalation from $LiCoO_2$: electronic properties and ^7Li NMR study. *J. Mater. Chem.*, 1999. **9**: p. 1135-1140.

52. Mukai, K., Y. Ikedo, H. Nozaki, J. Sugiyama, K. Nishiyama, D. Andreica, A. Amato, P.L. Russo, E.J. Ansaldo, J.H. Brewer, K.H. Chow, K. Ariyoshi, and T. Ohzuku, Magnetic phase diagram of layered cobalt dioxide Li_xCoO_2. *Phys. Rev. Lett.*, 2007. **99**.

53. Van der Ven, A., M.K. Aydinol, and G. Ceder, First-Principles Evidence for Stage Ordering in Li_xCoO_2. *J. Electrochem. Soc.*, 1998. **145**(6): p. 2149-2155.

54. Alcántara, R., P. Lavela, J.L. Tirado, R. Stoyanova, and E. Zhecheva, Structure and electrochemical properties of boron-doped $LiCoO_2$. *J. Solid State Chem.*, 1997. **134**(2): p. 265-273.

55. Antonijevic, S. and S. Wimperis, Refocussing of chemical and paramagnetic shift anisotropies in H-2 NMR using the quadrupolar-echo experiment. *J. Magn. Reson.*, 2003. **164**(2): p. 343-350.

56. Levasseur, S., M. Ménétrier, and C. Delmas, On the $Li_xCo_{1-y}Mg_yO_2$ system upon deintercalation: electrochemical, electronic properties and Li-7 MAS NMR studies. *J. Power Sources*, 2002. **112**(2): p. 419-427.

57. Myung, S.T., N. Kumagai, S. Komaba, and H.T. Chung, Effects of Al doping on the microstructure of $LiCoO_2$ cathode materials. *Solid State Ionics*, 2001. **139**(1-2): p. 47-56.

58. Castro-Garcia, S., A. Castro-Couceiro, M.A. Senaris-Rodriguez, F. Soulette, and C. Julien, Influence of aluminum doping on the properties of $LiCoO_2$ and $LiNi_{0.5}Co_{0.5}O_2$ oxides. *Solid State Ionics*, 2003. **156**(1-2): p. 15-26.

59. Aurbach, D., B. Markovsky, A. Rodkin, E. Levi, Y.S. Cohen, H.J. Kim, and M. Schmidt, On the capacity fading of $LiCoO_2$ intercalation electrodes: the effect of cycling, storage, temperature, and surface film forming additives. *Electrochimica Acta*, 2002. **47**(27): p. 4291-4306.

60. Cho, J., Y.J. Kim, and B. Park, Novel $LiCoO_2$ cathode material with Al_2O_3 coating for a Li ion cell. *Chem. Mater.*, 2000. **12**(12): p. 3788-3791.

61. Cho, J., Y.J. Kim, and B. Park, $LiCoO_2$ cathode material that does not show a phase transition from hexagonal to monoclinic phase. *J. Electrochem. Soc.*, 2001. **148**(10): p. A1110-A1115.

62. Chen, Z.H. and J.R. Dahn, Studies of $LiCoO_2$ coated with metal oxides. *Electrochem. Solid State Lett.*, 2003. **6**(11): p. A221-A224.

63. Cho, J., T.J. Kim, Y.J. Kim, and B. Park, High-performance ZrO_2-coated $LiNiO_2$ cathode material. *Electrochem. Solid State Lett.*, 2001. **4**(10): p. A159-A161.

64. Chen, Z.H. and J.R. Dahn, Effect of a ZrO_2 coating on the structure and electrochemistry of Li_xCoO_2 when cycled to 4.5 V. *Electrochem. Solid State Lett.*, 2002. **5**(10): p. A213-A216.

65. Kannan, A.M., L. Rabenberg, and A. Manthiram, High capacity surface-modified $LiCoO_2$ cathodes for lithium-ion batteries. *Electrochem. Solid State Lett.*, 2003. **6**(1): p. A16-A18.

66. Mladenov, M., R. Stoyanova, E. Zhecheva, and S. Vassilev, Effect of Mg doping and MgO-surface modification on the cycling stability of $LiCoO_2$ electrodes. *Electrochem. Commun.*, 2001. **3**(8): p. 410-416.

67. Wang, Z.X., X.J. Huang, and L.Q. Chen, Performance improvement of surface-modified $LiCoO_2$ cathode materials - An infrared absorption and X-ray photoelectron spectroscopic investigation. *J. Electrochem. Soc.*, 2003. **150**(2): p. A199-A208.

68. Sun, Y.K., J.M. Han, S.T. Myung, S.W. Lee, and K. Amine, Significant improvement of high voltage cycling behavior AlF_3-coated $LiCoO_2$ cathode. *Electrochem. Commun.*, 2006. **8**(5): p. 821-826.

69. Dahn, J.R., U. von Sacken, and C.A. Michal, Structure and electrochemistry of $Li_{1\pm y}NiO_2$ and a new Li_2NiO_2 phase withe the $Ni(OH)_2$ structure *Solid State Ionics*, 1990. **44**(1-2): p. 87-97.

70. Saadoune, I. and C. Delmas, $LiNi_{1-y}Co_yO_2$ positive electrode materials: relationships between the structure, physical properties and electrochemical behaviour. *J. Mater. Chem.*, 1996. **6**: p. 193-199.

71. Capitaine, F., P. Gravereau, and C. Delmas, A new variety of $LiMnO_2$ with a layered structure. *Solid State Ionics*, 1996. **89**: p. 197-202.

72. Rossen, E., C.D.W. Jones, and J.R. Dahn, Structure and electrochemistry of $Li_xMn_yNi_{1-y}O_2$. *Solid State Ionics*, 1992. **57**(3-4): p. 311-318.

73. Ohzuku, T. and Y. Makimura, Layered Lithium Insertion Material of $LiNi_{1/2}Mn_{1/2}O_2$: A Possible Alternative to $LiCoO_2$ for Advanced Lithium-Ion Batteries. *Chem. Lett.*, 2001: p. 744-745.

74. Liu, Z., A. Yu, and J.Y. Lee, Synthesis and characterization of $LiNi_{1-x-y}Co_xMn_yO_2$ as the cathode materials of secondary lithium batteries. *J.Power Sources*, 1999. **81-82**: p. 416-419.

75. Yoshio, M., H. Noguchi, J.-i. Itoh, M. Okada, and T. Mouri, Preparation and properties of $LiCo_yMn_xNi_{1-x-y}O_2$ as a cathode for lithium ion batteries. *J. Power Sources*, 2000. **90**: p. 176-181.

76. Ohzuku, T. and Y. Makimura, Layered Lithium Insertion Material of $LiCo_{1/3}Ni_{1/3}Mn_{1/3}O_2$ for Lithium-Ion Batteries. *Chem. Lett.*, 2001: p. 642-643.

77. Lu, Z., D.D. MacNeil, and J.R. Dahn, Layered $Li[Ni_xCo_{1-2x}Mn_x]O_2$ Cathode Materials for Lithium Ion Batteries. *Electrochem. Solid-St. Lett.*, 2001. **4**(12): p. A200-A203.

78. Shaju, K.M., G.V.S. Rao, and B.V.R. Chowdari, Performance of layered $Li(Ni_{1/3}Co_{1/3}Mn_{1/3})O_2$ as cathode for Li-ion batteries. *Electrochimica Acta*, 2002. **48**: p. 145-151.

79. Hwang, B.J., Y.W. Tsai, D. Carlier, and G. Ceder, A Combined Computational/Experimental Study on $LiNi_{1/3}Co_{1/3}Mn_{1/3}O_2$. *Chem. Mater.*, 2003. **15**: p. 3676-3682.

80. Koyama, Y., I. Tanaka, H. Adachi, Y. Makimura, and T. Ohzuku, Crystal and electronic structures of superstructural $Li_{1-x}[Co_{1/3}Ni_{1/3}Mn_{1/3}]O_2$ ($0 \leqslant x \leqslant 1$). *J. Power Sources*, 2003. **119-121**: p. 644-648.

81. Koyama, Y., N. Yabuuchi, I. Tanaka, H. Adachi, and T. Ohzuku, Solid-State Chemistry and Electrochemistry of $LiCo_{1/3}Ni_{1/3}Mn_{1/3}O_2$ for Advanced Lithium-Ion Batteries. *J. Electrochem. Soc.*, 2004. **151**(10): p. A1545-A1551.

82. Kang, K., Y.S. Meng, J. Bréger, C.P. Grey, and G. Ceder, Electrodes with High Power and High Capacity for Rechargeable Lithium Batteries. *Science*, 2006. **311**: p. 977-980.

83. MacNeil, D.D., Z. Lu, and J.R. Dahn, Structure and electrochemistry of $Li[Ni_xCo_{1-2x}Mn_x]O_2$ ($0 <= x <= 1/2$). *J. Electrochem. Soc.*, 2002. **149**(10): p. A1332-A1336.

84. Jouanneau, S., D.D. MacNeil, Z. Lu, S.D. Beattie, G. Murphy, and J.R. Dahn, Morphology and Safety of $Li[Ni_xCo_{1-2x}Mn_x]O_2$ ($0 \leqslant x \leqslant 1/2$). *J. Electrochem. Soc.*, 2003. **150**(10): p. A1299-A1304.

85. Yoon, W.-S., C.P. Grey, M. Balasubramanian, X.-Q. Yang, D.A. Fischer, and J. McBreen, Combined NMR and XAS Study on Local Environments and Electronic Structures of Electrochemcally Li-Ion Deintercalated $Li_{1-x}Co_{1/3}Ni_{1/3}Mn_{1/3}O_2$ Electrode System. *Electrochem. Solid-St. Lett.*, 2004. **7**(3): p. A53-A55.

86. Yoon, W.-S., M. Balasubramanian, K.Y. Chung, X.-Q. Yang, J. McBreen, C.P. Grey, and D.A. Fischer, Investigation of the Charge Compensation Mechanism on the Electrochemically Li-Ion Deintercalated $Li_{1-x}Co_{1/3}Ni_{1/3}Mn_{1/3}O_2$ Electrode System by Combination of Soft and Hard X-ray Absorption Spectroscopy. *J. Am. Chem. Soc.*, 2005. **127**: p. 17479-17487.

87. Spahr, M.E., P. Novak, B. Schnyder, O. Haas, and R. Nesper, Characterization of layered lithium nickel manganese oxides synthesized by a novel oxidative coprecipitation method and their electrochemical performance as lithium insertion electrode materials. *J. Electrochem. Soc.*, 1998. **145**(4): p. 1113-1121.

88. Bréger, J., N. Dupré, P.J. Chupas, P.L. Lee, T. Proffen, J.B. Parise, and C.P. Grey, Short- and Long-Range Order in the Positive Electrode Material, $Li(NiMn)_{0.5}O_2$: A Joint X-ray and Neutron Diffraction Pair Distribution Function Analysis and NMR Study. *J. Am. Chem. Soc.*, 2005. **127**: p. 7529-7537.

89. Bréger, J., K. Kang, J. Cabana, G. Ceder, and C.P. Grey, NMR, PDF and RMC study of the positive electrode material $Li(Ni_{0.5}Mn_{0.5})O_2$ synthesized by ion-exchage methods. *J. Mater. Chem.*, 2007. **17**: p. 3167-3174.

90. Zhu, W.J. and P.H. Hor, Unusual layered transition-metal oxysulfides: $Sr_2Cu_2MO_2S_2$ (M=Mn, Zn). *J. Solid State Chem.*, 1997. **130**(2): p. 319-321.

91. Gal, Z.A., O.J. Rutt, C.F. Smura, T.P. Overton, N. Barrier, S.J. Clarke, and J. Hadermann, Structural chemistry and metamagnetism of an homologous series of layered manganese oxysulfides. *J. Am. Chem. Soc.*, 2006. **128**(26): p. 8530-8540.

92. Rutt, O.J., G.R. Williams, and S.J. Clarke, Reversible lithium insertion and copper extrusion in layered oxysulfides. *Chem. Commun.*, 2006(27): p. 2869-2871.

93. Grey, C.P. and N. Dupré, NMR Studies of Cathode Materials for Lithium-Ion Rechargeable Batteries. *Chem. Rev.*, 2004. **104**: p. 4493-4512.

94. Levitt, M.H., *Spin dynamics: basics of nuclear magnetic resonance* 2001: John Wiley & Sons Ltd.

95. Kittel, C., *Introduction to Solid State Physics*. 6th ed. 1986: John Wiley & Sons, New York.

96. Carrington, A. and A.D. McLachlan, *Introduction to Magnetic Resonance*. 1967, Harper and Row: New York.

97. Andrew, E.R., A. Bradbury, and R.G. Eades, Nuclear Magnetic Resonance Spectra from a Crystal Roatated at High Speed. *Nature*, 1958. **182**(4650): p. 1659-1659.

98. Yoon, W.-S., Y. Paik, X.-Q. Yang, M. Balasubramanian, J. McBreen, and C.P. Grey, Investigation of the Local Structure of the $LiNi_{0.5}Mn_{0.5}O_2$ Cathode Material during Electrochemical Cycling by X-Ray Absorption and NMR Spectroscopy. *Electrochem. Solid-St. Lett.*, 2002. **5**(11): p. A263-A266.

99. Pan, C., Y.J. Lee, B. Ammundsen, and C.P. Grey, ^{6}Li MAS NMR Studies of the Local Structure and Electrochemical Properties of Cr-doped Lithium Manganese and Lithium Cobalt Oxide Cathode Materials for Lithium-Ion Batteries. *Chem. Mater.*, 2002. **14**: p. 2289-2299.

100. Carlier, D., M. Ménétrier, C.P. Grey, C. Delmas, and G. Ceder, Understanding the NMR shifts in paramagnetic transition metal oxides using density functional theory calculations. *Phys. Rev. B*, 2003. **67**: p. 174103.

Chapter 2 Cation Ordering in $Li[Ni_xMn_xCo_{(1-2x)}]O_2$ Layered Cathode Materials; An NMR, Pair Distribution Function, X-ray Absorption Spectroscopy and Electrochemical Study

2.1 Introduction

Lithium ion batteries occupy a very large portion of the portable battery market because of their high energy density and design flexibility. $LiCoO_2$ currently represents the most widely used positive electrode in most commercial rechargeable lithium batteries. It has a layered framework corresponding to the α-$NaFeO_2$ structure (space group $R\bar{3}m$, No. 166) with the oxygen ions close packed in a cubic arrangement, and the transition metal (TM) and lithium ions occupying the octahedral sites in alternating layers (Figure 2.1). Unfortunately, the safety issues associated with $LiCoO_2$, its poor rate performance, and the toxicity of cobalt limit its use in large-scale applications. This has motivated the study of other layered compounds that contain less or no cobalt at all, such as $LiNiO_2$ [1], $LiNi_{1-y}Co_yO_2$ [2], $LiMnO_2$ [3], $LiNi_{1-y}Mn_yO_2$ [4-5] and $LiNi_{1-y-z}Mn_yCo_zO_2$ [6-7]. Among them, the members of the compositional series $Li[Ni_xMn_xCo_{1-2x}]O_2$, first synthesized by Ohzuku and Makimura[8] and Lu et al. [9], show very good electrochemical behavior and, consequently, have triggered a large amount of research on

these and related compounds. In particular, $Li[Ni_{1/3}Mn_{1/3}Co_{1/3}]O_2$, shows a stable capacity of around 150 mAh/g in the voltage window 3.5 to 4.2 V and a capacity of over 200 mAh/g on cycling to 5.0 V [8]. First-principle calculations, backed by experimental X-ray Absorption Spectroscopy (XAS) results, demonstrated that the oxidation states of Ni, Mn and Co in the pristine compound are +2, +4 and +3 respectively [10], even though both $LiMnO_2$ and $LiNiO_2$ contain trivalent transition metal ions [3, 11]. These methods, along with ^6Li Magic Angle Spinning (MAS) Nuclear Magnetic Resonance (NMR) spectroscopy, were used to probe the local environments of the different ions and the changes in the electronic structure of the compounds upon charging. Based on these methods, and detailed electrochemical measurements [12], Ni^{2+} was shown to oxidize at the lowest potential and represent the major charge compensation site [10, 13], [14-15]. Ni^2 and $/Ni^{3+}$ are thought to be present for lithium contents (x) in $Li_x[Ni_{1/3}Mn_{1/3}Co_{1/3}]O_2$ of $2/3 \leq x \leq 1$, and Ni^{3+} and Ni^{4+} for $1/3 \leq x \leq 2/3$. Co^{3+} is oxidized to Co^{4+} for $0 \leq x \leq 1/3$, in the 4.88-5.2 V range, the oxidation state of Mn^{4+} remaining unchanged through the charging process.

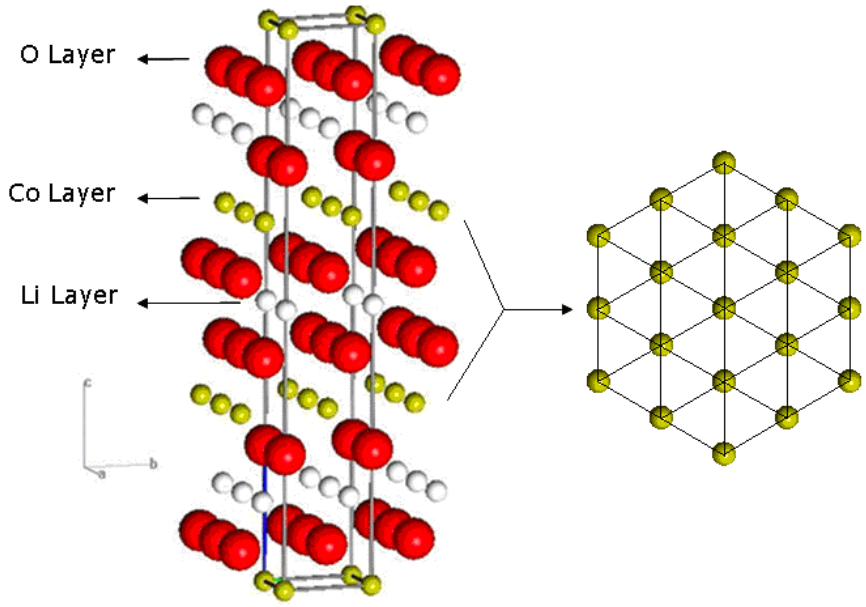

Figure 2.1 α-$NaFeO_2$-type structure ($R\bar{3}m$) of cathode material $LiCoO_2$. The trigonal lattice of the TM layer (Co layer here) is shown on the right.

Despite the considerable amount of work devoted, to date, to the $Li[Ni_xMn_xCo_{(1-2x)}]O_2$ system, it still remains unclear as to how Ni/Mn ordering is disrupted by Co^{3+} doping, how the ordering and oxidation state of the three cations change across the series and as a function of the processing conditions, and most importantly, how this affects the electrochemical performance. For the related system, $Li[Li_{(1-2x)/3}Ni_xMn_{(2-x)/3}]O_2$, both first-principle calculations and experimental data from techniques that probe the local structure have provided clear evidence for strong interactions between Ni^{2+} and Mn^{4+} ions [16]. More specifically, it has already been reported that these ions tend to be next to each other in the TM layers in $Li[Ni_{0.5}Mn_{0.5}]O_2$ (x = 0.5 in both series) resulting in a non-random distribution of cations [17]. Furthermore, in the "ideal" layered material, with limited Li/Ni exchange between the layers, the Ni and Mn ions show a tendency to order in zig-zags, as opposed to chains [18]. In the case of $Li[Ni_{1/3}Mn_{1/3}Co_{1/3}]O_2$, recent ^6Li MAS NMR results from Cahill and co-workers are consistent with a non-random distribution of cations in the TM layers [19], and the authors propose a model whereby the TM ions order so as to maintain local charge balance. However, their analysis only considered the (Fermi contact) interactions between Li and its 1st coordination shell of TM ions. The interactions involving the 2nd coordination shell were ignored, although these interactions can be quite large [20-21]. Nonetheless, their NMR data and analysis do provide compelling evidence for local TM clustering.

The nature of the cation ordering will also be linked to the oxidation states of the Ni and Mn ions in the $Li[Ni_xMn_xCo_{(1-2x)}]O_2$ series. Two extreme scenarios can be envisaged as x decreases and the Co^{3+} concentration increases. In the first scenario,

Ni/Mn clustering is assumed. Here, the pair of cations (Ni^{2+} + Mn^{4+}) is likely to be more stable than (Ni^{3+} + Mn^{3+}). In the second case, a random distribution of the three ions on the α-$NaFeO_2$ trigonal lattice (Figure 2.1) is assumed. Now, as the average Ni^{2+}-Mn^{4+} separation increases, the energy penalty associated with charge separation, i.e. the cost to convert (Ni^{3+} + Mn^{3+}) to (Ni^{2+} + Mn^{4+}), increases and, in the limit of infinite dilution, the oxidation state of these two cations is likely 3+. The most likely scenario will depend on the balance between entropic factors, which favor random distributions, and the energy penalty associated with the formation of two 3+ cations, and will presumably be affected by the synthetic methods used to prepare the materials.

The work presented here uses a combination of techniques including X-ray and neutron diffraction, X-ray Absorption Near Edge Spectroscopy (XANES), ^{6}Li Magic Angle Spinning (MAS) NMR spectroscopy and neutron Pair Distribution Function (PDF) analysis along with Reverse Monte Carlo (RMC) calculations, to investigate the local and long range structure for this series of compounds. These techniques are sensitive to either the oxidation state (XANES) or the local structure surrounding the element under investigation (NMR/PDF). In particular, the cation ordering in the TM layers for the compounds with x = 0.02 and x = 1/3 were studied intensively. The effect of the synthesis conditions on slight off-stoichiometry samples are also discussed for the former.

2.2 Experimental

2.2.1 Synthesis of the compounds.

All the compounds prepared in the $Li[Ni_xMn_xCo_{(1-2x)}]O_2$ series (x = 0.01, 0.0125, 0.02, 0.025, 0.05, 0.075, 0.10, 0.125, 0.15, 0.20, 0.25, 0.30, 1/3) were synthesized following the procedure from Lu et al. [9], using a mixed transition metal hydroxide as a reagent to improve the mixing and the purity of the final products [22]. To prepare this hydroxide, stoichiometric amounts of $Mn(NO_3)_2 \cdot 4H_2O$ (>97.0%, Fluka), $Ni(NO_3)_2 \cdot 6H_2O$ (>98.0%, Fluka), and $Co(NO_3)_2 \cdot 6H_2O$ (98+%, Aldrich) were dissolved in 50mL distilled water and added dropwise into a 400 mL $LiOH \cdot H_2O$ (purified, crystal, Fisher) solution with around twice a molar amount excess to maintain a highly basic pH. The resulting precipitates, $Ni_xMn_xCo_{(1-2x)}(OH)_2 \cdot nH_2O$, were filtered and washed thoroughly with distilled water and, then, dried overnight at 180°C. For the natural abundance samples, the resulting powder was ground with a stoichiometric amount of $LiOH \cdot H_2O$, made into pellets, heated first at 480°C for 3 hours, reground, repelletized, and heated at 900°C for another 3 hours. Finally, the pellets were quenched with liquid nitrogen. In the case of the ^6Li enriched samples (x = 0.02) or the ^7Li enriched sample (x = 1/3) also described in this study, either $^6LiOH \cdot H_2O$ (90-95% ^6Li, FW=41.1, Cambridge Isotope Laboratories, Inc.) (referred to as $Li[Ni_{0.02}Mn_{0.02}Co_{1.96}]O_2$ "sample 1"), $^6Li_2CO_3$ (90-95% ^6Li, FW=72.11, Cambridge Isotope Laboratories, Inc. "sample 2") or $^7LiOH \cdot H_2O$ (97% ^7Li, FW=42.04, Sigma-Aldrich) was used instead.

Several compounds were prepared as references for the XANES experiments. $Li[Ni_{0.2}Co_{0.8}]O_2$ was synthesized as reported [23] by using stoichiometric amounts of Li_2CO_3 (99%, Fisher), NiO (99%, Aldrich), and Co_3O_4 (Aldrich) heated, in air, at 600°C for 15 hours, quenched, and re-heated at 900°C for 24 hours, followed by a final quenching in liquid nitrogen. $Li_{0.9}[Ni_{0.45}Ti_{0.55}]O_2$ was prepared by ion-exchange from its sodium precursor in hexanol. A full description of the synthesis procedure is reported elsewhere [24]. Li_2MnO_3 was prepared by heating, in air, stoichiometric amounts of Li_2CO_3 and Mn_2O_3 at 650°C for 12 hours, following by quenching, and re-heating at 850°C for 24 hours, with a final slow cooling in air [25]. The other reference compounds used in the study, commercial NiO (99%, Aldrich) and Mn_2O_3 (99%, Aldrich), were used without further purification.

2.2.2 X-ray Diffraction (XRD).

XRD was carried out on a Rigaku Miniflex powder diffractometer. The 2θ range used for data collection was from 20º to 120º (chromium tube with CrK_α: $\lambda = 2.2909$ Å). A step scan of 2θ = 0.02º/step size was used for all samples and the scan speed was 1º/min. Cell parameter refinements were performed by using the program JADE XRD pattern processing 6.5 (Materials Data, Inc.).

2.2.3 Solid-State NMR.

The ^6Li MAS NMR experiments were performed at 29.39 MHz on a Chemagnetics CMX-200 spectrometer (B_0 = 4.7 T) by using a double resonance 1.8 mm probe. Silicon nitride (Si_3N_4) rotors were used and spun at a speed of 38 kHz. All the

spectra were acquired following a rotor-synchronized Hahn echo sequence (90°-τ-180°-τ-acquisition). The spectra were referenced to a standard 1M ^{6}LiCl solution at 0 ppm. π/2 pulses of 3.5 μs were used, with a delay time of 0.2 s. A pulse delay array was performed for the sample $Li[Ni_{0.02}Mn_{0.02}Co_{0.96}]O_2$ and fully-relaxed, quantitative spectra could be obtained with a pulse delay of 0.2 s, presumably due to presence of the paramagnetic ions in the sample.

2.2.4 X-ray Absorption Near-Edge Spectroscopy (XANES).

The XANES spectra were collected on beamline X19A at the National Synchrotron Light Source (NSLS) in the Brookhaven National Laboratory. The measurements were performed in transmission or fluorescence mode using a Si (111) double-crystal monochromator detuned to 35-45% of its original intensity to eliminate the high order harmonics. Energy calibration was carried out using the first inflection point of the spectrum of Mn and Ni metal foil as a reference (Mn K-edge = 6539 eV, Co K-edge = 7709 eV, and Ni K-edge = 8333 eV).

2.2.5 Neutron Diffraction (ND) and Pair Distribution Function (PDF) analysis.

Neutron diffraction experiments were performed on the General Purpose Powder Diffractometer (GPPD) at the Intense Pulsed Neutron Source (IPNS, Argonne National Laboratory, USA) for $^{7}Li[Ni_{1/3}Mn_{1/3}Co_{1/3}]O_2$. The sample (around 500 mg) was packed into ¼-inch inside-diameter thin-walled vanadium cans. The exposure time was around 12 hours. The data was corrected for instrument background, sample and background absorption and multiple scattering. Data up to Q_{max} = 25 Å^{-1} were used in the Fourier

transform. Rietveld [26] refinement of the structure was performed with GSAS-EXPGUI [27-28], with this neutron diffraction data. The Pair Distribution Function (PDF) data obtained from this neutron experiment was processed by using PDFgetN [29].

2.2.6 Electrochemistry.

Cathodes were prepared by mixing 80 wt% of the active material, 10 wt% of acetylene black, and 10 wt% of poly-vinylidene fluoride (PVDF) binder in N-methyl pyrrolidone (NMP). The slurry was deposited on an aluminium foil and dried at 80°C until the solvent had evaporated completely. Coin cells (CR2032, Hohsen corp.) were assembled in an argon-filled glove box. Each cell contains typically about 15 mg of active material, separated from a Li disk by two pieces of Celgard separator (Celgard Inc, USA). A 1M solution of $LiPF_6$ in ethylene carbonate:dimethyl carbonate (1:1) has been used as the electrolyte. Electrochemical experiments were carried out on a battery cycler (Arbin Instruments, College Station, Texas) in galvanostatic mode at a C/50 rate.

2.3 Results and Discussion

2.3.1 X-ray Diffraction.

The XRD patterns of $Li[Ni_xMn_xCo_{(1-2x)}]O_2$ with different values of x show similar features, and are consistent with a single phase with a α-$NaFeO_2$ structure. A representative pattern for the x = 0.15 sample is shown in Figure 2.2. The clearly-resolved 006/012 and 108/110 pairs of reflections indicate a well-developed layered structure [30]. Refinements using these data show an increase of the cell parameters c and a with increasing x. This is due to the increasing amount of Ni^{2+}, which is larger than Co^{3+} ($r(Ni^{2+})$ = 0.69 Å compared to $r(Co^{3+})$ = 0.55 Å and $r(Mn^{4+})$ = 0.53 Å) [12]. The actual refined values are listed in Table 2.1, and the results are plotted in Figure 2.3. These results are consistent with the previous study by MacNeil et al.[12].

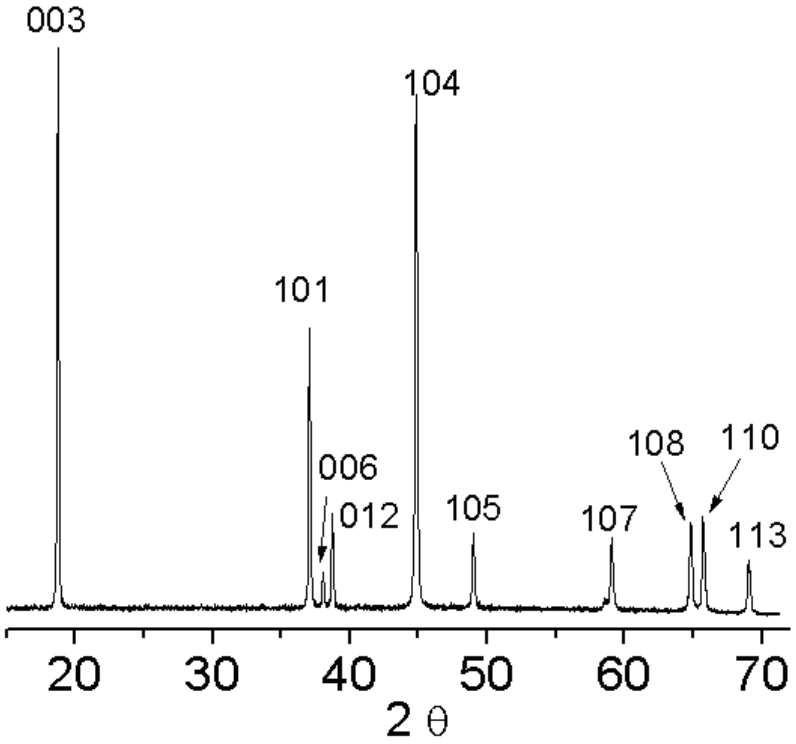

Figure 2.2**.** XRD pattern of $Li[Ni_{0.15}Mn_{0.15}Co_{0.70}]O_2$ and Miller indices corresponding to a unit cell with $R\bar{3}m$ space group. The 2θ values correspond to copper radiation ($K_{\alpha 1}$: λ = 1.54178 Å).

Table 2.1. Cell parameters of the samples in the $Li[Ni_xMn_xCo_{(1-2x)}]O_2$ series as refined from the patterns shown in Figure S1.

x	Co content (%)	a (Å)	c (Å)
0.01	98	2.8140±0.0009	14.064±0.004
0.0125	97.5	2.8165±0.0006	14.069±0.003
0.02	96	2.8154±0.0009	14.066±0.006
0.025	95	2.81596±0.0005	14.078±0.003
0.05	90	2.8204±0.0005	14.085±0.003
0.075	85	2.8232±0.0005	14.124±0.002
0.10	80	2.8278±0.0009	14.125±0.002
0.15	70	2.8395±0.0007	14.170±0.003
0.20	60	2.8457±0.0004	14.194±0.002
0.25	50	2.8535±0.0006	14.214±0.003
0.30	40	2.8593±0.0007	14.230±0.004
0.33	33	2.8617±0.0006	14.234±0.003

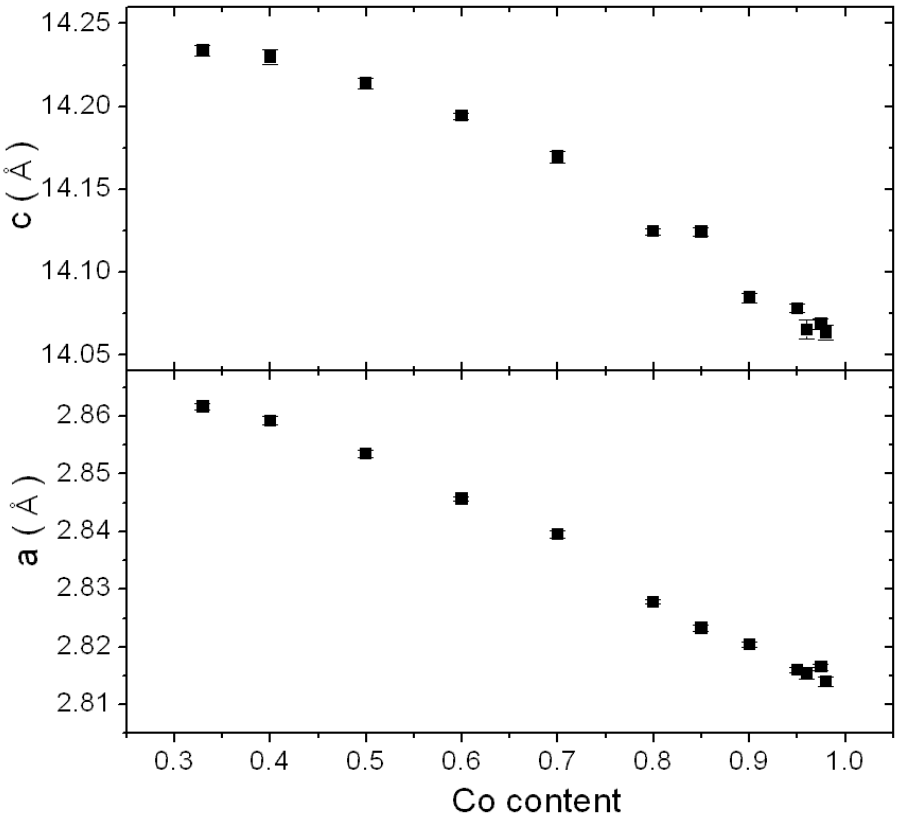

Figure 2.3. Evolution of the cell parameters along the $Li[Ni_xMn_xCo_{(1-2x)}]O_2$ series against the Co content, as obtained from the refinement of the XRD patterns. The error values shown in Table 2.1 are also included as error bars.

2.3.2 XANES Spectroscopy.

Figure 2.4(a) shows selected normalized Ni K-edge XANES spectra of the $Li[Ni_xMn_xCo_{(1-2x)}]O_2$ series with different x values. Those of the reference compounds with either Ni^{2+} (NiO and $Li_{0.9}[Ni_{0.45}Ti_{0.55}]O_2$) or Ni^{3+} ($Li[Ni_{0.2}Co_{0.8}]O_2$) are also included. All the $Li[Ni_xMn_xCo_{(1-2x)}]O_2$ compounds, even with very low x (e.g., $x = 0.0125$ and 0.025), have very similar absorption edge energy positions, close to those of NiO and $Li_{0.9}[Ni_{0.45}Ti_{0.55}]O_2$ and noticeably shifted away from that of layered $Li[Ni_{0.20}Co_{0.80}]O_2$, suggesting the existence of Ni^{2+} in our samples. This can be more clearly seen in the first derivative of the spectra (Figure 2.4(b)), where the peaks corresponding to the Ni absorption edge for our samples and for the Ni^{2+} reference compounds are in the same position, and at a lower energy than that for Ni^{3+} in $Li[Ni_{0.20}Co_{0.80}]O_2$.

Figure 2.5 and Figure 2.6 correspond to the normalized Mn and Co K-edge XANES spectra, respectively. The energy of the absorption edge of the former is the same for all the studied compounds and exhibits a clear Mn^{4+} character as in Li_2MnO_3. For Co, the energy of the absorption edge for the studied compounds is the same as that of the reference compound $Li[Ni_{0.20}Co_{0.80}]O_2$, indicating the presence of Co^{3+}.

A previous study of $Li[Ni_{1/3}Mn_{1/3}Co_{1/3}]O_2$ shows that the oxidation states for Ni, Mn and Co are +2, +4 and +3 respectively [14]. The results presented here indicate that the compounds in the $Li[Ni_xMn_xCo_{(1-2x)}]O_2$ series ($0.01 \leq x \leq 0.30$) also consist of divalent Ni ions (Ni^{2+}), tetravalent Mn ions (Mn^{4+}) and trivalent Co ions (Co^{3+}) throughout the whole range.

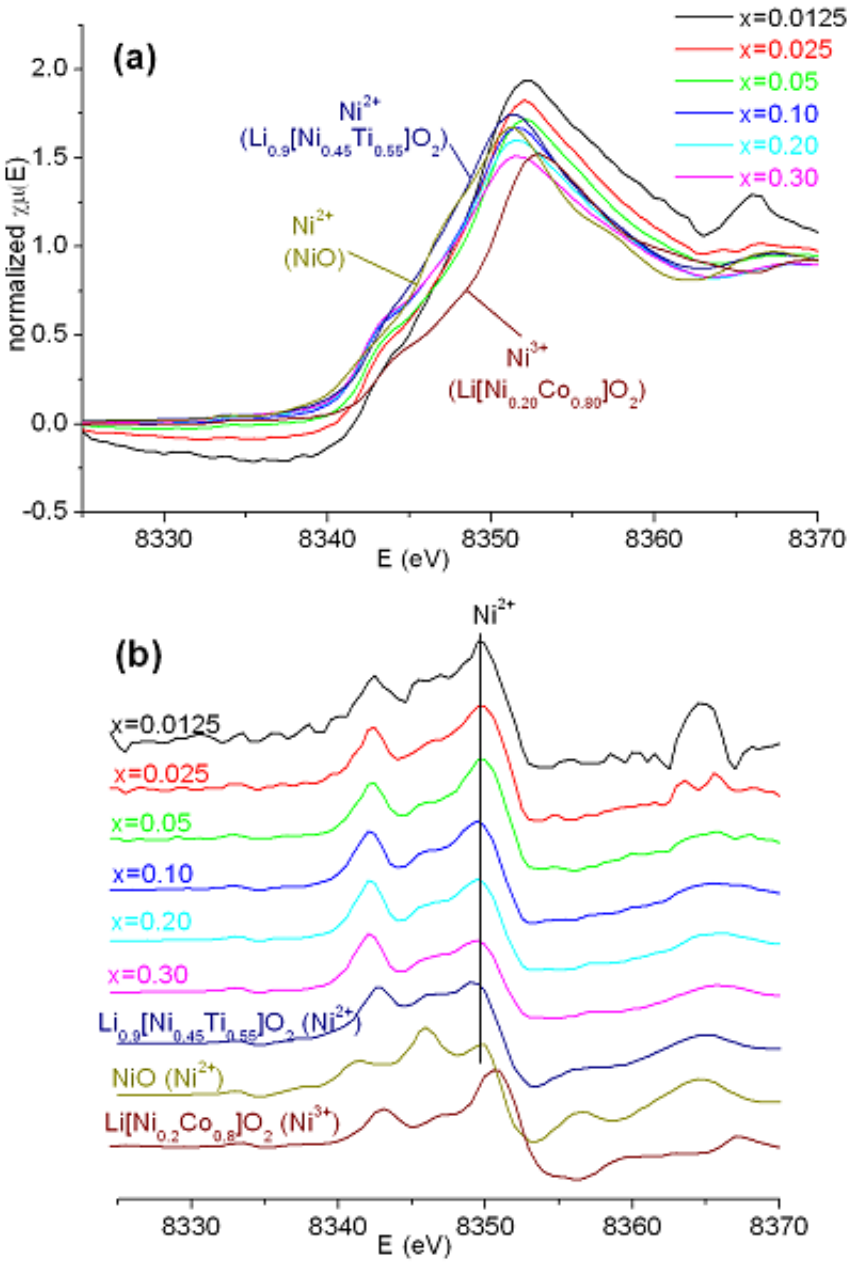

Figure 2.4. **(a)** Normalized Ni K-edge XANES spectra of selected compounds in the $Li[Ni_xMn_xCo_{(1-2x)}]O_2$ series at room temperature. Other Ni^{2+} and Ni^{3+} compounds are also included as references. **(b)** First derivative of the normalized Ni K-edge XANES spectra shown in **(a)**.

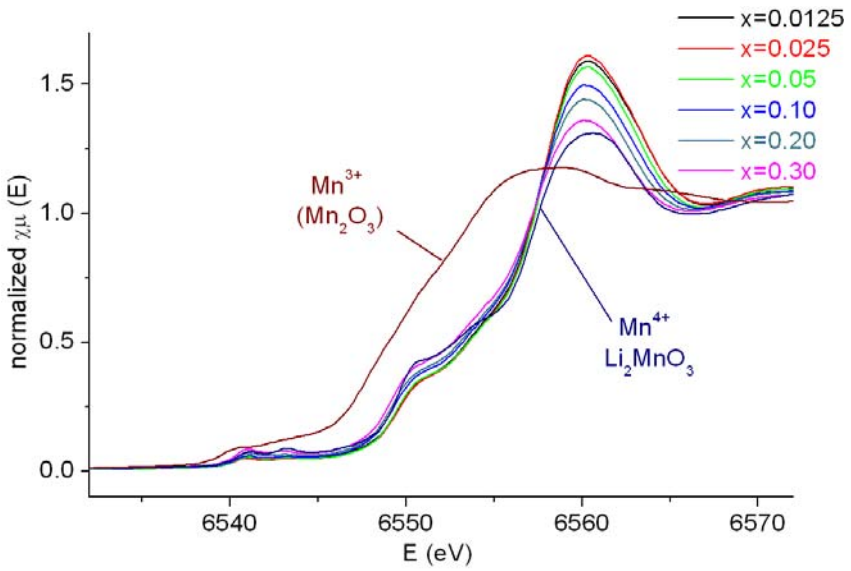

Figure 2.5. Normalized Mn K-edge XANES spectra of selected compounds in the $Li[Ni_xMn_xCo_{(1-2x)}]O_2$ series at room temperature, together with the Mn^{3+} and Mn^{4+} reference compounds.

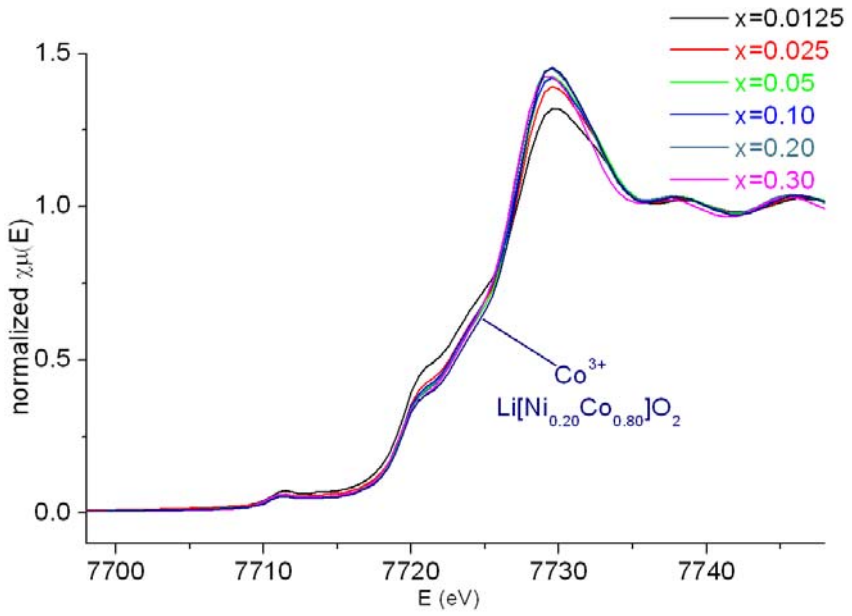

Figure 2.6. Normalized Co K-edge XANES spectra of selected compounds in the $Li[Ni_xMn_xCo_{(1-2x)}]O_2$ series at room temperature, together with $Li[Ni_{0.20}Co_{0.80}]O_2$, a Co^{3+} reference compound.

2.3.3 ^{6}Li MAS NMR

2.3.3.1 Evolution of the spectra along the $Li[Ni_xMn_xCo_{(1-2x)}]O_2$ series.

Figure 2.7 shows the ^{6}Li MAS NMR spectra of the natural abundance $Li[Ni_xMn_xCo_{(1-2x)}]O_2$ samples, with x varying from 0.01 to 1/3. Each spectrum is normalized with respect to the sample mass and the number of spectral acquisitions. The spectrum of the sample with $x = 0.01$ is dominated by a sharp 0 ppm peak, but the spectra evolve noticeably as x increases. As x varies from 0.01 to 0.10, the spectra show three major differences. The first change is a decrease of the intensity of the 0 ppm resonance as the Ni/Mn amount in the compound increases. This corresponds to a decreasing presence of a $LiCoO_2$-like local environment, in which lithium is surrounded by six Co^{3+} ions in both its first and second coordination shells. The second and third changes occur in the positive and negative shift regions, where several resonances (at 390, 250, 140 and -55 ppm, among others) start to appear and become more evident. However, no significant change in the shift of these signals is observed with increasing x. The local environments that give rise to these resonances will be discussed in detail later. In the samples with higher x, *i.e.*, with even higher amounts of Ni/Mn, the well resolved resonances observed in the compounds with low Ni/Mn contents start to merge and form a broad resonance with center of gravity at around 300 ppm. Additionally, the intensity of the resonance at 0 ppm significantly decreases and is ultimately buried under the broad resonance when x reaches 0.25. As a result of this, the center of gravity of the spectrum shifts to higher shift values (around 440 ppm).

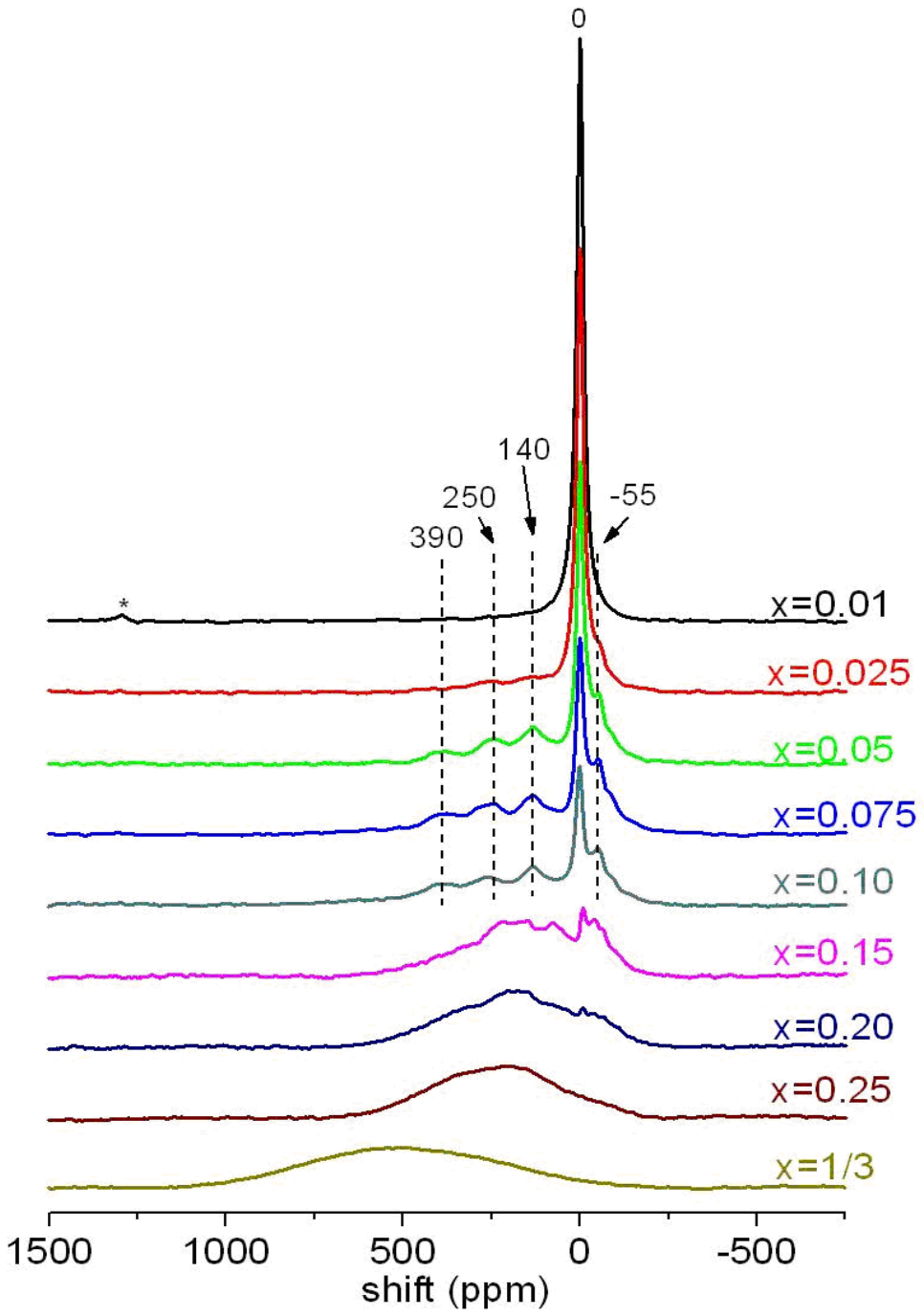

Figure 2.7. Evolution of the ^{6}Li MAS NMR spectra of the samples prepared in the $Li[Ni_xMn_xCo_{(1-2x)}]O_2$ series with a spinning speed of 38kHz. The *x* values are shown and range from 0.01 to 1/3. The most intense well-resolved isotropic resonances are indicated. The asterisk indicates a spinning side band originating from the 0 ppm resonance.

To investigate the chemical environment that leads to each resonance in further detail, the ^{6}Li MAS NMR spectrum of enriched $^6Li[Ni_{0.02}Mn_{0.02}Co_{0.96}]O_2$ (x = 0.02) was acquired and studied more extensively.

2.3.3.2 $^6Li[Ni_{0.02}Mn_{0.02}Co_{0.96}]O_2$: implications for the local structure.

Before analyzing the spectrum of this compound in detail, we need to describe the possible local environments for lithium in this type of material. Each of these environments will result in a characteristic NMR signal, due to the interactions between Li and the nearby paramagnetic ions.

In the ideal layered $LiMO_2$ (M = transition metal) structure (Figure 2.8), each Li^+ ion has 12 neighboring transition metal cations, six in the 1st cation coordination shell and six in the 2nd cation coordination shell. There are two types of interactions between lithium ions and the unpaired electrons on the transition metals: one forming 90° M-O-Li angle (between lithium and a TM in its 1st cation coordination shell) and leading to a so-called 90° M-O-Li interaction and one with a 180° M-O-Li angle (between lithium and a TM in the Li's 2nd cation coordination shell) and a 180° M-O-Li interaction. Similarly, each transition metal cation interacts with six lithium ions the layer below (or above).

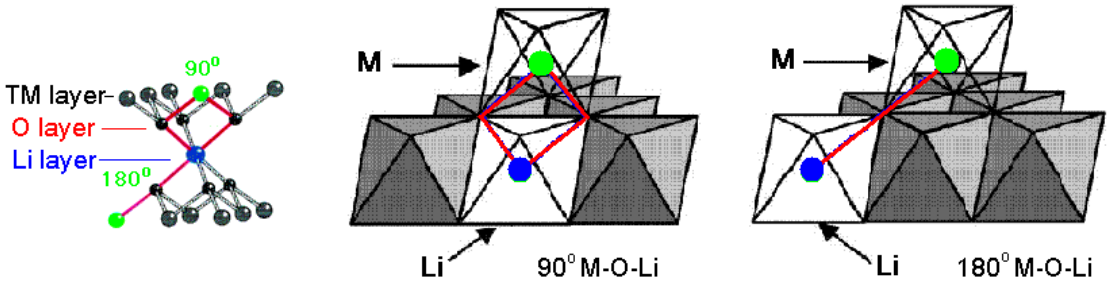

Figure 2.8. Graphic representation of the two possible types of interactions between the lithium ions in the lithium layer of a $LiMO_2$-type structure, and the transition metal TM=Ni, Mn, Co, in this case) ions in the TM layer. The interactions occur via the oxygen as intermediate atoms. A representation of the geometric environment of lithium is also depicted. (Figures modified after ref.[20].)

Li/Ni exchange [14, 31] may occur in $LiMO_2$-type compounds with high amounts of Ni, due to the similar ionic radius of Li^+(0.74 Å) and Ni^{2+} (0.69 Å). However, previous XRD refinements showed that this exchange is extremely limited for this series of compounds when the Co content is higher than 85% [12]. For this reason, an ideal situation with no lithium/transition metal exchange was assumed here.

Once the environments are defined, we need to assign a shift for each of them. Previous ^{6}Li NMR studies in other layered-type systems, such as Li_2MnO_3, $Li[Ni_xMn_{(2-x)/3}Li_{(1-2x)/3}]O_2$ and $Li[Ti_xNi_{1-x}]O_2$, have allowed us to estimate the values associated with the presence of a given transition metal in a given oxidation state in the 1st or 2nd coordination shell of a central lithium. As a result, we established that the hyperfine shift induced by a single Mn^{4+} ion *via* two intervening oxygen atom(s) is around +250 ppm for one Mn^{4+} in the 1st coordination shell (i.e., two 90° Mn^{4+}-O-Li bonds), and -60 ppm for one Mn^{4+} in the 2nd coordination shell (i.e., via one 180° Mn^{4+}-O-Li bond) [20, 32]. In the case of Ni^{2+}, the corresponding values are *ca.* -30 ppm and +170 ppm, respectively [33]. Finally, for Ni^{3+}, we would expect a shift of *ca.* -15 ppm for the presence of two 90º Ni^{3+}-O-Li interactions (one Ni^{3+} in the 1st coordination shell), and +110 ppm for one 180º Ni^{3+}-O-Li interaction (one Ni^{3+} in the 2nd coordination shell) [34-35]. The shifts induced by Ni^{3+} have the same sign as those of Ni^{2+}, but they are smaller in magnitude.

Figure 2.9 shows a zoom of the ^{6}Li MAS NMR spectrum of $^6Li[Ni_{0.02}Mn_{0.02}Co_{0.96}]O_2$ (sample 1). The deconvolution shows that there are eight major resonances: 390, 258, 140, 0, -24, -53, -77 and -135 ppm, which can be assigned to specific chemical environments labeled based on the fact that all the M-O-Li interactions

are additive, and consistent with the presence of Ni^{2+} and Mn^{4+} as observed in the XANES spectra (Table 2.2). The resonance at 390 ppm is then assigned to Li^{+} with one Mn^{4+} in its 1st coordination shell and one Ni^{2+} in its 2nd coordination shell. Two environments are assigned to the resonance at 258 ppm: Li^{+} with one Mn^{4+} and (i) zero or (ii) one Ni^{2+} in its 1st coordination shell. The calculated hyperfine shifts for these two environments differ by only 24 ppm and are, most likely, not resolvable. The -77 ppm resonance is assigned to Li^{+} with one Ni^{2+} in the 1st coordination shell and one Mn^{4+} in the 2nd coordination shell (sum of -24 and -53 ppm). The weak resonance at -135 ppm, is assigned to a Li^{+} located in an environment with one Ni^{2+} in its 1st coordination shell and two Mn^{4+} in its 2nd coordination shell. The shift caused by Ni^{2+} ions in the 2nd coordination shell (140 ppm) is somewhat smaller than observed in isostructural material $Li_{0.9}[Ni_{0.45}Ti_{0.55}]O_2$ (approx. +170 ppm). The hyperfine interaction is, however, known to be very sensitive to the Li-O-M bond angle, the degree of orbital overlap (covalency), and the coordination environment of the oxygen atoms. A smaller shift is quite likely for the current system Mn^{4+} (and Co^{3+}) system since the more covalent Mn^{4+} (and Co^{3+}) ions may compete effectively for binding to the nearby oxygen atoms.

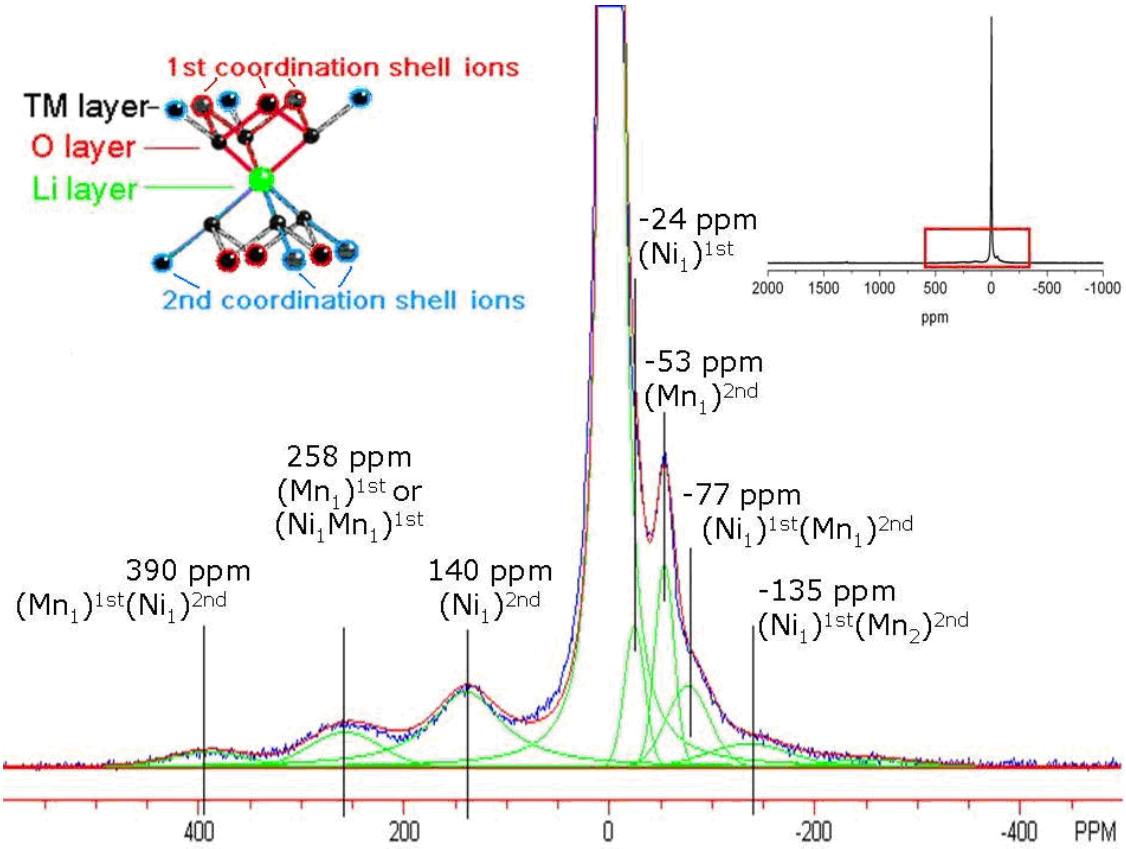

Figure 2.9. A zoom of the ^{6}Li MAS NMR spectrum of $^{6}Li[Ni_{0.02}Mn_{0.02}Co_{0.96}]O_2$ (sample1) acquired at 38 kHz, with its corresponding deconvolution (green peaks and red line (sum)) and proposed signal assignments. **Upper right corner inset:** full spectrum; red rectangular box indicates the zoomed region. **Upper left corner inset:** arrangement of the twelve neighboring atoms around a central lithium. $(Ni_{x1}Mn_{y1})^{1st}(Ni_{x2}Mn_{y2})^{2nd}$ represents the composition of the two coordination shells for each lithium, where x and y, along with the subscript 1 (for the 1st coordination shell) and 2 (for the 2nd coordination shell), indicate the Ni^{2+} and Mn^{4+} contents respectively. The other neighboring cations are all Co^{3+}, and are omitted for clarity.

Table 2.2. Summary of the probabilities resulting from the two models described in the text, and normalized peak areas resulting from the deconvolution of the experimental spectra for the two samples of $^{6}Li[Ni_{0.02}Mn_{0.02}Co_{0.96}]O_2$

Index No.	Configuration	Shift (ppm)	Model				Spectra Deconvolution	
			Random		Clustered		Sample 1	Sample 2
			Calculation	P_{random}	Calculation	$P_{cluster}$	Norm. Area	Norm. Area
1	$(Co_6)^{1st}(Co_6)^{2nd}$	0	1×0.96^{12}	0.613	(50-9)/50	0.82	0.7605*	0.8236*
2	$(Ni_1Co_5)^{1st}(Co_6)^{2nd}$	-24	$6\times0.02\times0.96^{11}$	0.077	1/50	0.02	0.0309	0.0225
3	$(Mn_1Co_5)^{1st}(Co_6)^{2nd}$	+258	$6\times0.02\times0.96^{11}$	0.077	1/50	0.02	0.0269	0.0233
4	$(Co_6)^{1st}(Ni_1Co_5)^{2nd}$	+140	$6\times0.02\times0.96^{11}$	0.077	2/50	0.04	0.0607	0.0533
5	$(Co_6)^{1st}(Mn_1Co_5)^{2nd}$	-53	$6\times0.02\times0.96^{11}$	0.077	2/50	0.04	0.0424	0.0281
6	$(Ni_1Co_5)^{1st}(Mn_1Co_5)^{2nd}$	-77	$6\times6\times0.02^2\times0.96^{10}$	0.009	1/50	0.02	0.0379	0.0298
7	$(Mn_1Co_5)^{1st}(Ni_1Co_5)^{2nd}$	+398	$6\times6\times0.02^2\times0.96^{10}$	0.009	1/50	0.02	0.0125	0.0078
8	$(Ni_1Mn_1Co_4)^{1st}(Co_6)^{2nd}$	+234	$6\times5\times0.02^2\times0.96^{10}$	0.009	1/50	0.02	-	-
9	$(Co_6)^{1st}(Ni_1Mn_1Co_4)^{2nd}$	+87	$6\times5\times0.02^2\times0.96^{10}$	0.009	-	-	-	-
10	$(Ni_1Co_5)^{1st}(Ni_1Co_5)^{2nd}$	+116	$6\times6\times0.02^2\times0.96^{10}$	0.009	-	-	-	-
11	$(Mn_1Co_5)^{1st}(Mn_1Co_5)^{2nd}$	+205	$6\times6\times0.02^2\times0.96^{10}$	0.009	-	-	-	-
12	$(Ni_2Co_4)^{1st}(Co_6)^{2nd}$	-48	$1/2\times6\times5\times0.02^2\times0.96^{10}$	0.004	-	-	-	-
13	$(Mn_2Co_4)^{1st}(Co_6)^{2nd}$	+516	$1/2\times6\times5\times0.02^2\times0.96^{10}$	0.004	-	-	-	-
14	$(Co_6)^{1st}(Ni_2Co_4)^{2nd}$	+280	$1/2\times6\times5\times0.02^2\times0.96^{10}$	0.004	-	-	-	-
15	$(Co_6)^{1st}(Mn_2Co_4)^{2nd}$	-106	$1/2\times6\times5\times0.02^2\times0.96^{10}$	0.004	-	-	-	-
16	$(Ni_1Co_5)^{1st}(Mn_2Co_4)^{2nd}$	-135	-	-	-	-	0.0209	0.0104
17		-250	-	-	-	-	0.0072	0.0015
				total 0.991		1	1	1

* The area of spinning sidebands has been included in the intensity of the 0 ppm peak.

While the peak positions (shift values) provide information about the cation arrangements around the lithium ions, the intensity (peak area) will provide quantitative information on the number of such Li environments existing in the structure. In the situation here, with 96% of Co in the transition metal layers, noticeable differences in the distributions of the possible local environments (and, thus, the NMR spectrum) should be seen between a random Ni/Mn distribution and a model in which $Ni^{2+}$and Mn^{4+} are clustered. This will be demonstrated as follows: the chemical environment (shifts) distribution prediction in these two models (random and clustered) will be obtained using the probabilities for every environment *via* calculation or simulation. The two prediction patterns will then be compared with the real spectrum. A view of the layered structure resulting from the two possible transition metal cation distributions considered here is shown in Figure 2.10.

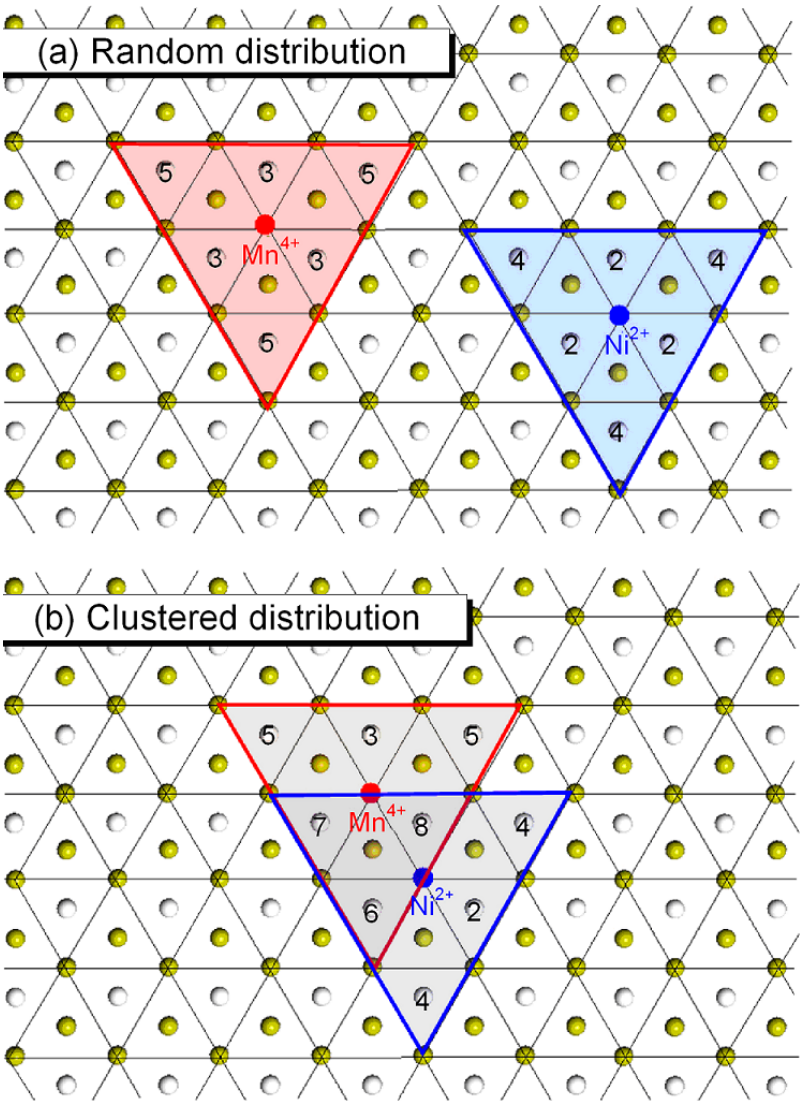

Figure 2.10. Graphic representation of the two possible cation distributions in a layered O3 structure. Only one of the possible distributions for the random model is shown. White balls correspond to lithium ions, and yellow balls correspond to cobalt lying in the transition metal layers above (crossed by the solid lines of the triangular lattice) and below (in the centers of the small triangles) the lithium layer. Red and blue balls in the diagram represent Mn^{4+} and Ni^{2+}, respectively, and the red and blue large triangles indicate the region in which lithium ions interact with these ions, either through a 180º or a 90º interaction, with Mn^{4+} and Ni^{2+}, respectively. Oxygen atoms are omitted for clarity. The numbers refer to the different possible configurations in each model, as shown in Table 2.2. When the same environment is observed in both models, the same number is used (e.g., configuration "3" refers to the local environment for lithium $(Mn_1Co_5)^{1st}(Co_6)^{2nd}$ in both models). All the unlabeled lithium ions correspond to the $(Co_6)^{1st}(Co_6)^{2nd}$ local environment and correspond to configuration 1 in Table 2.2.

The positions of the Ni^{2+}, Mn^{4+} and Co^{3+} ions are independent in the random model and the probability that they are located at a given cation position in the TM layers is 0.02, 0.02 and 0.96 respectively. To simplify the analysis, only configurations with up to two Ni or Mn in the two coordination shells are considered (accounting for more than 99% of all the possible local environments, as seen in Table 2.2). These possible configurations and their corresponding chemical shifts and probabilities are listed in Table 2.2. The normalized area of each peak in the spectra of two samples (sample 1 and sample 2) from different batches of $^6Li[Ni_{0.02}Mn_{0.02}Co_{0.96}]O_2$, prepared to examine the variations between samples with the same nominal compositions, are listed in the table as well.

The probability calculation for the cluster model is not as straightforward and hence a simulation method is used (Figure 2.10(b)). In a unit cell with 50 lithium ions, the simplest situation with one Ni^{2+} and Mn^{4+} next to each other (i.e., clustered) in the same transition metal layer is considered. This Ni^{2+}/Mn^{4+} pair generates seven more possible chemical environments apart from the Co-only one, and nine (out of fifty) lithium ions fall into this region. The population of lithium in each chemical environment can be easily deduced by counting them. This model has oversimplified the real situation by ignoring the possibility that there may be another Ni^{2+}/Mn^{4+} pair in the layer below and that more extended clusters may be present. This would affect some (if not all) of the nine lithium ions that are already affected by the Ni^{2+}/Mn^{4+} pair. However, this representation depicts the most likely cluster for very dilute systems and results in noticeable differences in the populations of the different Li ions in comparison to the

random model, and this should already allow us to monitor the presence of ordering in the compound.

The experimental and calculated intensities for each local environment are plotted as a function of the corresponding hyperfine shift in a histogram, for the random (Figure 2.11(a)) and the cluster (Figure 2.11(b)) models. Based on these calculations, the structure with a random $Ni^{2+}/Mn^{4+}/Co^{3+}$ distribution is expected to have a relatively strong resonance at 0 ppm along with four weak peaks with comparable intensities at approximately +258, +140, -24 and -53 ppm. With the "cluster" constraint, the NMR spectrum is predicted to have a more intense 0 ppm peak, two weaker peaks at around +140 and -53 ppm, and three even weaker, but still observable, peaks at -77, +390 and +258 ppm. By comparing the experimental data and the two models, it is clear that the cluster model provides a better fit to the experimental data, the fit being particularly good for sample 2.

Some peaks in the experimental spectrum, such as at that at +140 ppm, have slightly higher intensities than predicted with the cluster model, and there are also additional resonances due to local environments not generated with this cluster. Some of these differences arise from difficulties in resolving the different local environments. For example, the resonance due to configuration 8, $Li(Ni_1Mn_1Co_4)^{1st}$, most likely is contained within the resonance ascribed to configuration 3, $Li(Mn_1Co_5)^{1st}$. However, it must be pointed out that the resonance at -135 ppm has to arise from three paramagnetic ions in close proximity (the lithium local environment $Li(Ni_1Co_5)^{1st}(Mn_2Co_4)^{2nd}$). The Mn-Ni-Mn cluster, where the three cations are in a linear chain, in the same layer, will give rise

to this new local environment, in addition to local environments already described in Table 2.2, suggesting that this resonance is a signature for more extended clustering. The three cations could also be in two different layers. The resonance at -250 ppm must also be associated with extended clustering, and is consistent with an environment with three Ni^{2+} and three Mn^{4+} in the 1^{st} and 2^{nd} Li^{+} cation coordination shells respectively. Again, although the cations can be in more than one layer, this environment also arises from the extended cluster formed from a triangle of three adjacent Ni^{2+} ions, capped by three adjacent Mn^{4+} to form a larger triangle. Sample 1 appears to contain more extended clustering. It also contains a weaker 0 ppm resonance, suggesting that there are also regions or domains in the sample containing less clustering.

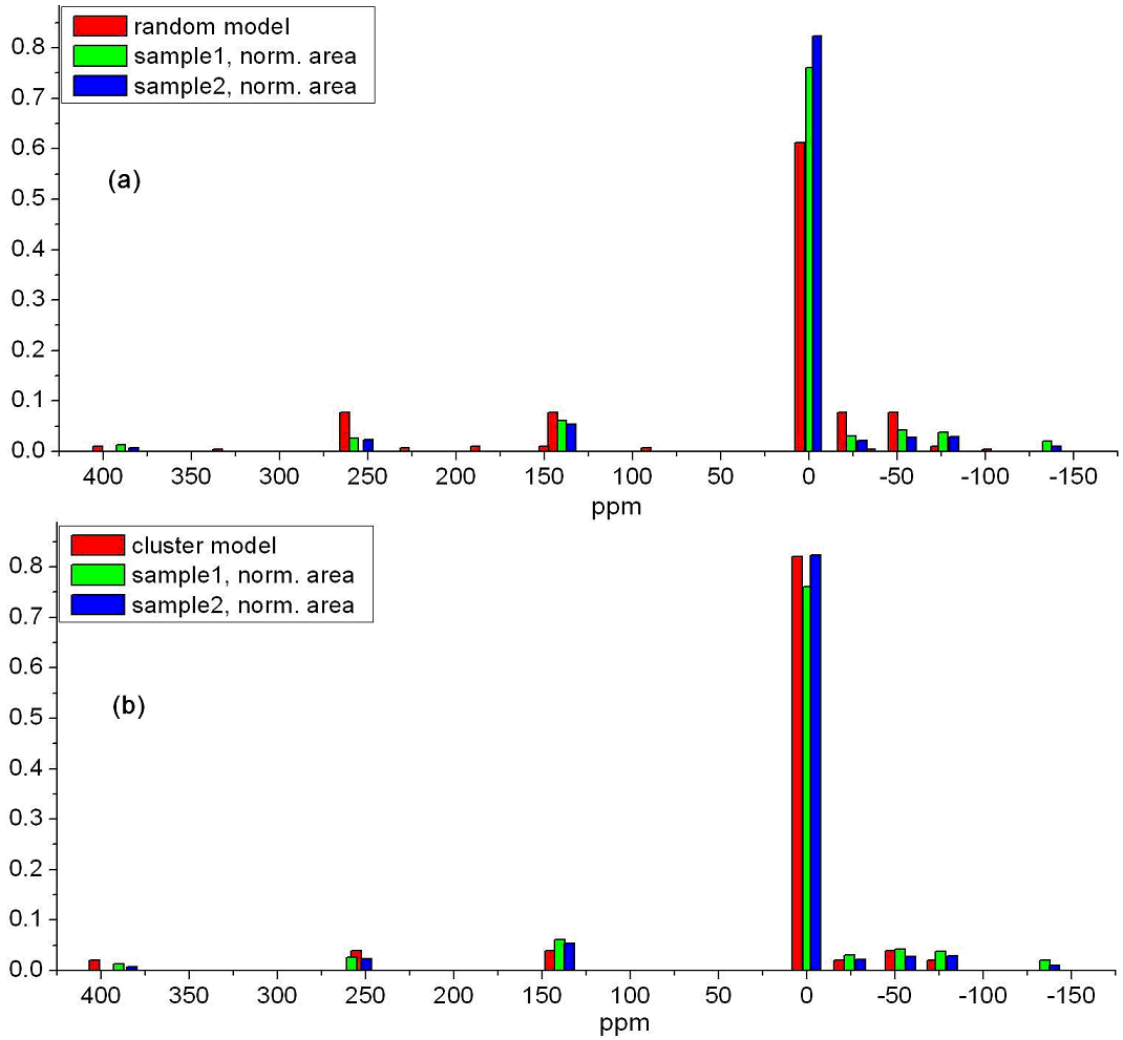

Figure 2.11. Comparison of the probabilities resulting from **(a)** the random and **(b)** the cluster model with the normalized experimental peak intensities obtained from the deconvolution of the spectra of the two $^{6}Li[Ni_{0.02}Mn_{0.02}Co_{0.96}]O_2$ samples.

2.3.3.3 Investigation of the effect of doping level on the local structure.

As seen in Figure 2.7, the intensity of the 0 ppm peak, which is correlated with the amount of Li^+ in a $LiCoO_2$-like local environment, decreases as the doping level of Ni/Mn in the compound increases. The normalized experimental 0 ppm peak intensities obtained from the deconvolution of the spectra were compared with the probabilities of the $LiCoO_2$-like environment ($Li(Co_6)^{1st}(Co_6)^{2nd}$) in both the random and the cluster model (Figure 2.12). In the random model, for a compound $Li[Ni_xMn_xCo_{(1-2x)}]O_2$ with a given x, the probability for one Co to be located in a given position in the TM layers is $(1-2x)$, and thus, the probability of the $Li(Co_6)^{1st}(Co_6)^{2nd}$ environment is $(1-2x)^{12}$. In the cluster model, an approximation is made here to calculate the probability of the $Li(Co_6)^{1st}(Co_6)^{2nd}$ environment: instead of considering the three cations individually (Ni, Mn and Co with concentrations x, x and $(1-2x)$, respectively), only two random species, Ni/Mn pairs and Co cations, with concentrations x and $(1-2x)$ respectively, are considered. The probability for one Co to be located in a given position is then $(1-2x)/[x+(1-2x)]$, which simplifies to $(1-2x)/(1-x)$, and the probability of the $Li(Co_6)^{1st}(Co_6)^{2nd}$ environment under this approximation is then $[(1-2x)/(1-x)]^{12}$. However, since the Ni/Mn pair is the species that is considered, this approximation underestimates the total configuration numbers by excluding possible configurations where only one cation from the Ni/Mn pair affects the Li environment (*i.e.*, the Ni or Mn cation is in its 1st or 2nd coordination shell) while the other cation of the pair is in the 3rd coordination shell, *e.g.,* configurations $Li(Co_6)^{1st}(Ni_1Co_5)^{2nd}$ and $Li(Co_6)^{1st}(Mn_1Co_5)^{2nd}$. Thus, the calculated probability $[(1-2x)/(1-x)]^{12}$ is over estimated. In spite of this, the

comparison of the experimental data with the calculated probabilities in the two models clearly shows that the normalized experimental 0 ppm peak intensities are higher than the calculated probabilities in the random model. The calculated probabilities in the cluster model with the approximation are very close to the experimental data in the low Ni/Mn component samples. As the doping level of Ni/Mn increases, the concentrations predicted based on the pair model are higher than those seen experimentally. This is due to the fact that more possible configurations are excluded when there are more Ni/Mn in the TM layers, and is likely due to the limitations of the model. In conclusion, the data show clear evidence for a degree of clustering in these samples, consistent with result presented above for $x = 0.02$.

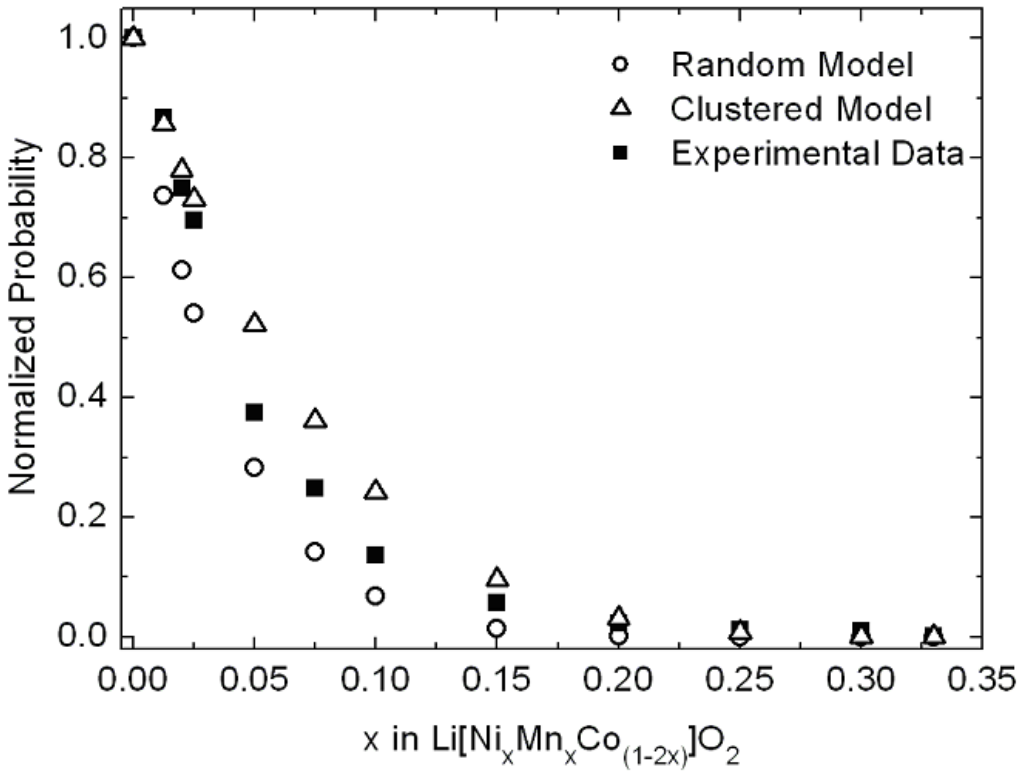

Figure 2.12. Comparison of the normalized 0 ppm peak intensity obtained from the deconvolution of the spectra of the Li[$Ni_xMn_xCo_{(1-2x)}$] series with the calculated probabilities in the random and clustered model.

2.3.3.4 Effect of the starting lithium stoichiometry on the TM cation ordering

The effect of the initial Li:TM ratio in the starting materials used to prepare the sample with 2% Ni and 2% Mn doping on the ^{6}Li NMR results was explored, in order to determine whether this affects the cation ordering of the compound. Figure 2.13 shows an expansion of the ^{6}Li NMR spectra of three samples with stoichiometry $^6Li_{x_0}[Ni_{0.02}Mn_{0.02}Co_{0.96}]O_2$, where x_0 = 0.95, 1.00 and 1.05, respectively. Although the spectra of all three samples are qualitively similar, the resonance at 140 ppm, assigned to Ni in the 2nd coordination shell, is clearly shifted to a lower value of approximately 120 ppm in the lithium-overstoichiometric sample, $^6Li_{1.05}(Ni_{0.02}Mn_{0.02}Co_{0.96})O_2$. This is ascribed to the substitution of some of the excess Li^+ in the transition metal layers, and the associated oxidation of some of the Ni ions to Ni^{3+}, which is required for charge compensation. Because of the presence of some Ni^{3+}, the Ni/Mn clustering may not be as prevalent. This may result in some isolated Mn cations which are likely present as Mn^{3+}. We tentatively assign the resonance at -43 ppm to the local environments containing this ion in the 2nd coordination shell. Finally, no significant changes are observed for the resonances at 250 and -55 ppm, generated by the presence of Mn^{4+}, indicating that those environments remain the same for both compositions. The spectra of the stoichiometric sample, $^6Li_{1.00}[Ni_{0.02}Mn_{0.02}Co_{0.96}]O_2$, and the lithium deficient sample, $^6Li_{0.95}[Ni_{0.02}Mn_{0.02}Co_{0.96}]O_2$, are similar, but the intensities of the resonances nearby the paramagnetic ions are weaker. In addition, the lineshapes of the -55, 140 and 250 ppm resonances are slightly different. The changes are ascribed to Li^+ vacancies in the Li layers. These vacancies will also result in the formation of some Ni^{3+}, but presumably,

these cations will not be detected because they are nearby Li-ion vacancies (in the Ni^{3+} 2nd coordination shell) and not Li^{+}.

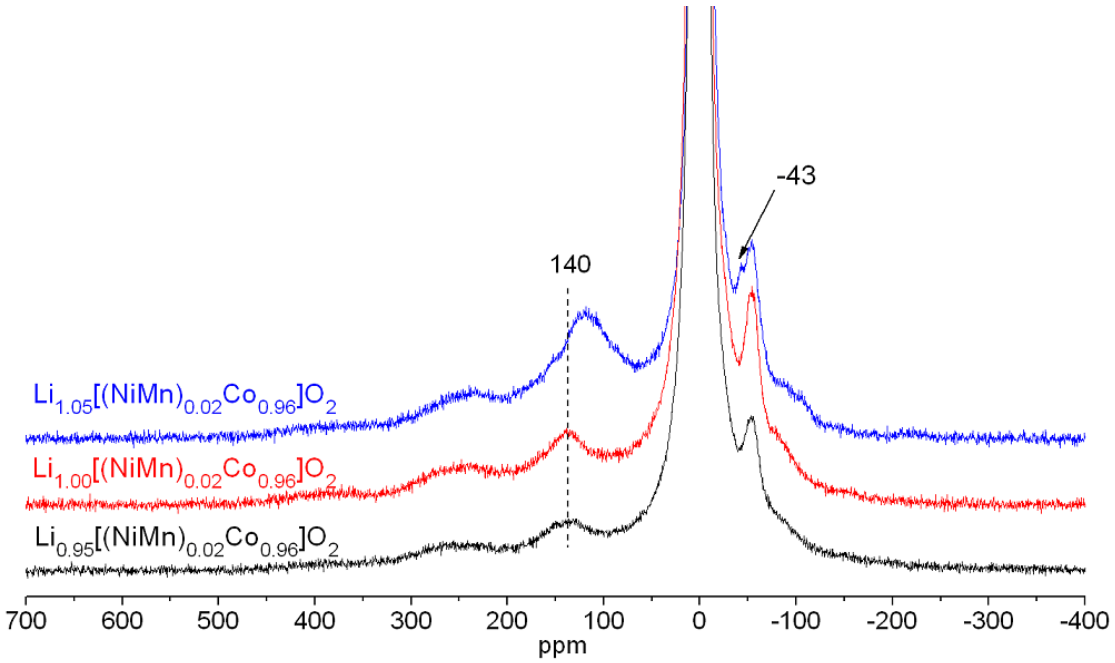

Figure 2.13. Expansion of the ^{6}Li MAS NMR spectra of (black) $^{6}Li_{0.95}[Ni_{0.02}Mn_{0.02}Co_{0.96}]O_2$, (red) $^{6}Li_{1.00}[Ni_{0.02}Mn_{0.02}Co_{0.96}]O_2$ and (blue) $^{6}Li_{1.05}[Ni_{0.02}Mn_{0.02}Co_{0.96}]O_2$, acquired at 38 kHz. The shifts of select key resonances are indicated (see text).

2.3.4 Neutron scattering studies of $^{7}Li[Ni_{1/3}Mn_{1/3}Co_{1/3}]O_2$

2.3.4.1 Powder neutron diffraction.

Figure 2.14 shows the neutron diffraction pattern of $^{7}Li[Ni_{1/3}Mn_{1/3}Co_{1/3}]O_2$, together with the calculated and difference curves obtained by Rietveld refinement. The resulting structural parameters are shown in Table 2.3.

Good agreements are seen between the experimental data and patterns calculated with the $LiCoO_2$ structural model (space group $R\bar{3}m$). Close examination of the diffraction patterns revealed weaker peaks, which could not be indexed with the $R\bar{3}m$ space group. These peaks can, however, be ascribed to impurities in the material, corresponding to oxides containing Ni, Co and/or Mn. Allowing Li/Ni exchange between the TM and Li layers of $Li[Ni_{1/3}Mn_{1/3}Co_{1/3}]O_2$, yields a small occupancy (< 2 %) of Ni in the Li layer. This refinement led to the following cell parameters: c = 14.2235(1) Å and a = 2.85939(1) Å. These results are consistent with a previous Rietveld refinement of $Li[Ni_{1/3}Mn_{1/3}Co_{1/3}]O_2$ pattern from ND data, which gave c = 14.227(8) Å and a = 2.860(2) Å, with R_{wp} = 2.95 % [36], and with previous NMR data on a similar material which indicated a 2-4% Li/Ni exchange between the Li and TM layers [14, 19].

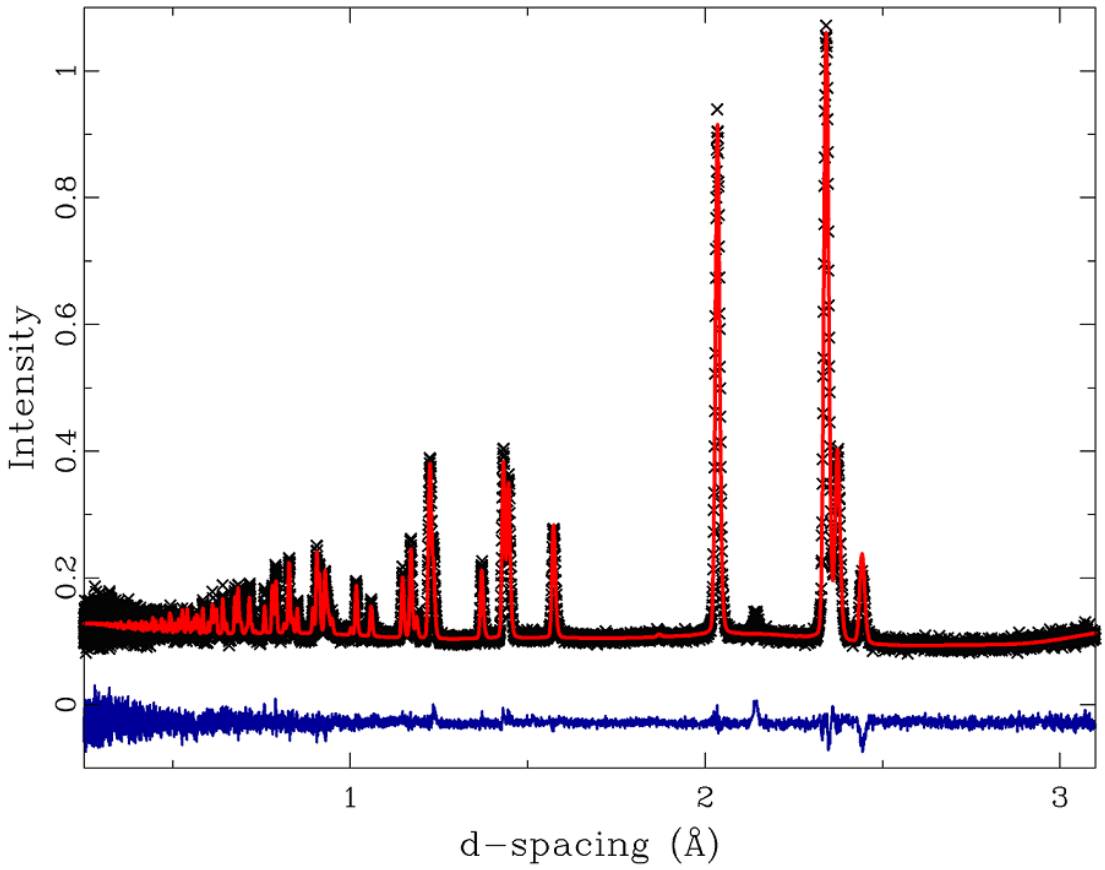

Figure 2.14. Results of the Rietveld refinement of $^{7}Li[Ni_{1/3}Mn_{1/3}Co_{1/3}]O_2$ using neutron diffraction data (bank 4, ± 90°, of the GPPD detector). The crosses and the solid red line represent the experimental data and the calculated pattern, respectively. The difference between the calculated and experimental patterns is shown in blue below the data. The resulting structural parameters are given in Table 2.3.

Table 2.3. Structural parameters resulting from the Rietveld refinement of $^{7}Li[Ni_{1/3}Mn_{1/3}Co_{1/3}]O_2$ using neutron diffraction data. Simultaneous refinement with the same parameters of four different histograms was performed, corresponding to banks 2,3, 4 and 5 of the GPPD detector.

	$^{7}Li[Ni_{1/3}Mn_{1/3}Co_{1/3}]O_2$
Space group	R-3m
a (Å)	2.85939(1)
c (Å)	14.2235(1)
V (Å^3)	100.713(1)
z(O)	0.24091(2)
Li/Ni Exchange	1.9(1) %
100**Uiso* (Å^2) Li/Ni (3a) Ni/Co/Mn/Li (3b) O (6c)	 3.18(4) 1.57(2) 0.500(7)
Bank 2 (± 125°) Bank 3 (± 107°) Bank 4 (± 90°) Bank 5 (± 53°)	5.49 % 5.20 % 5.30 % 5.89 %

Table 2.4. Coherent neutron scattering lengths b_i (fm) of the different isotopes [37].

^{7}Li	Co	Ni	Mn	O
-2.22	2.49	10.3	-3.73	5.80

2.3.4.2 PDF analysis and RMC calculations.

The neutron Pair Distribution Function (PDF) was calculated from the neutron diffraction data for $^{7}Li[Ni_{1/3}Mn_{1/3}Co_{1/3}]O_2$ (Figure 2.15). This calculation consists of a Fourier transform of all the scattering data (both Bragg and diffuse scatterings) and is not dependent on the model used to describe the diffraction data. The first correlation distance at around 2 Å corresponds to a superposition of the M-O distances, where M = Li, Ni, Co and Mn. The intensity of this peak is positive, as the contribution from the positive coherent scattering lengths of Ni and Co atoms (see Table 2.4) are larger than those from elements with negative scattering lengths (^{7}Li and Mn). The second peak at around 2.9 Å is ascribed to the M-M and O-O bonds, where M can be Li, Ni, Mn or Co. Peaks below 1.9 Å are termination ripples due to the cutoff of the Fourier transform at a finite Q and do not correspond to any real correlations in the structural model. All the other peaks (above 3 Å) are a superposition of numerous environments, and therefore, are too complicated to assign.

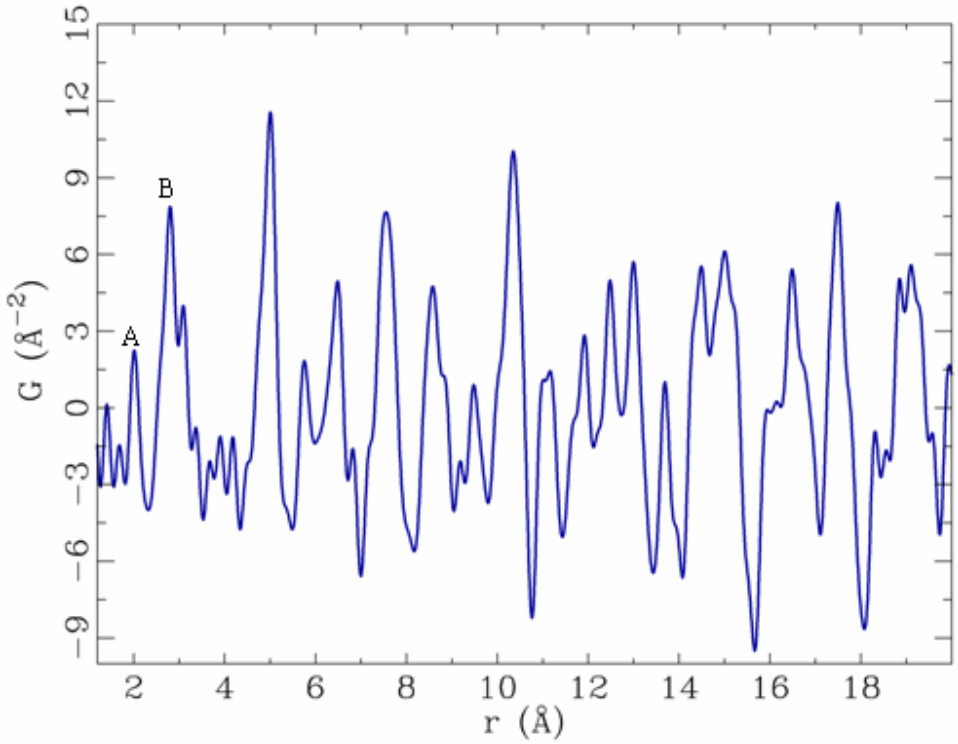

Figure 2.15. Pair distribution function (PDF, *G(r) vs. distance –r-*) for $^{7}Li[Ni_{1/3}Mn_{1/3}Co_{1/3}]O_2$. The peaks assignments are: A: M-O distances and B: M-M and O-O distances, where M is Li, Ni, Co or Mn.

A fit of the experimental data using Reverse Monte Carlo (RMC) calculations [38-39] was performed in order to explore a possible ordering of the Ni/Co/Mn atoms in $^{7}Li[Ni_{1/3}Mn_{1/3}Co_{1/3}]O_2$, in a similar approach to the one used for $^{7}Li(NiMn)_{0.5}O_2$ as previously reported [17-18]. The cell parameters determined from the Rietveld refinement of the neutron data were used in the RMC calculations, which were performed with the DISCUS program [40]. Initially, a cluster comprising 10×10×2 (a×a×c) unit cells (2400 atoms), was built. Given the low amount (<2%) of Li/Ni site exchange obtained from the Rietveld refinement of the diffraction data, 0% exchange was assumed. The Ni, Co and Mn atoms were placed in a random arrangement on the TM layers. Given their relatively small concentration, the impurities were not introduced as a second phase in the calculations. The difference between the resulting calculated PDF and the experimental data is shown in Figure 2.16(a). The match is clearly quite poor, and, thus, further structural refinement is needed. To accomplish this, RMC calculations were carried out as follows: Ni, Co and Mn atoms were swapped randomly and all the atoms were allowed to relax in the *ab* plane; if a generated move improved the fit, the move was accepted. The final calculated PDF is shown in Figure 2.16(b), and a clear improvement to the fit of the experimental data over that calculated from the ideal $LiCoO_2$ model was obtained and most of the major features appear to be captured.

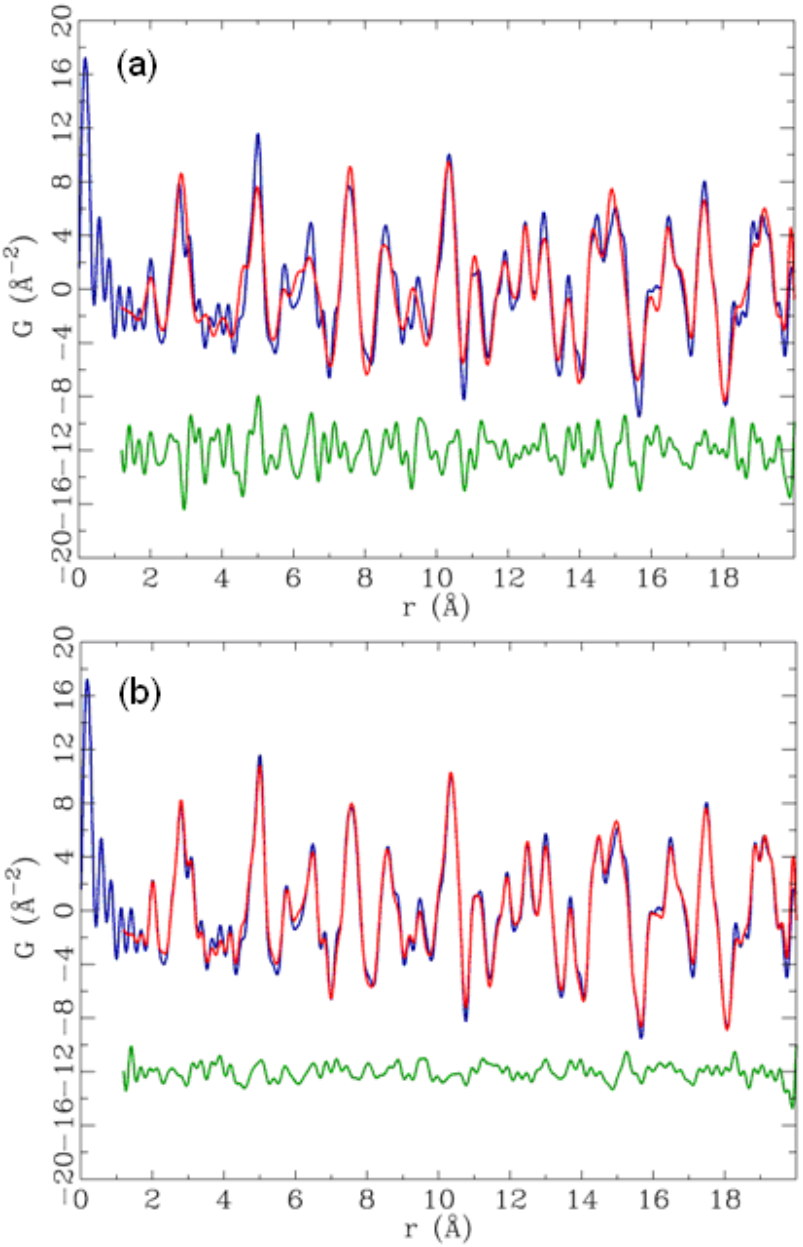

Figure 2.16. Fit of the experimental NPDF data for $^{7}Li[Ni_{1/3}Mn_{1/3}Co_{1/3}]O_2$ with the calculated structural model **(a)** before (random ordering), and **(b)** after the Reverse Monte Carlo (RMC) calculations. The blue line represents the experimental data and the solid red line, the calculated PDF. The difference between the calculated and experimental patterns is shown in green.

The number of each different cation pair before and after the RMC calculations is reported in Table 2.5. The ordering of the Ni and Mn cations in the TM layers is clearly non-random, with Ni closer to more Mn in the 1st coordination shell and to more Ni in the 2nd coordination shell than would be expected for such an arrangement, as indicated by the negative and positive Ni/Mn occupational correlations for the 1st and 2nd coordination shells, respectively. In contrast, the Ni/Co and Mn/Co occupational correlations are much closer to zero indicating a close to random distribution for these cations. Only a very slight tendency for Co to be surrounded more by Ni or Mn than by Co can be observed for the 1st coordination shell. We note, however, that given the much smaller (positive) neutron scattering factor of Co (in comparison to Ni), the sensitivity of this method to correlations involving Co will lower, which may lead to an *underestimation* of the cation ordering, particularly that involving Co. Based on these results, the Ni atoms are, on average, surrounded by 1.6 Ni, 1.8 Co and 2.5 Mn ions in the 1st coordination shell, and by 2.8 Ni, 1.2 Co and 2.0 Mn ions in the 2nd coordination shell.

The results were compared with three different possible cation ordering schemes shown in Figure 2.17 derived from the α-$NaFeO_2$ lattice. The first scheme (Figure 2.17(a)) is the so-called $\left[\sqrt{3}\times\sqrt{3}\right]$ R30º-type superlattice [41-43], in which all three metal cations order on a triangular lattice to maintain the three-fold symmetry. The second ordering scheme (Figure 2.17(b)), in which the three cations order in parallel chains, was assumed in the theoretical work of Hwang et al. [10]. Finally, since a zig-zag arrangement of the Ni and Mn ions represents the ground state for $Li[Ni_{0.5}Mn_{0.5}]O_2$ [16], a third scheme was constructed which comprises zig-zag chains of the three cations

(Figure 2.17(c)). The three ordering schemes show different correlations in the 1st coordination shell. Total avoidance between the same cations (0% for the Ni-Ni, Mn-Mn and Co-Co pairs) is seen for the $\left[\sqrt{3}\times\sqrt{3}\right]$ R30º-type superlattice structure. The parallel chain arrangement shows an equal concentration of all the different pairings (16.7% for all the pairs), while the zig-zag arrangement is associated with the highest preference for clustering of like cations (22.2% for the Ni-Ni, Mn-Mn and Co-Co pairs). For the 2nd coordination shell (Table 2.5(b)), total avoidance between different cations (0% for Ni-Mn, Mn-Co and Co-Ni pairs) is seen for the $\left[\sqrt{3}\times\sqrt{3}\right]$ R30º-type superlattice structure, while a high preference is observed for the same cations (33.3% for Ni-Ni, Mn-Mn and Co-Co pairs). In contrast, the parallel chain arrangement shows high preference for Ni-Mn, Mn-Co and Co-Ni pairs (33.3%). Finally, the zigzag arrangement results in equal amount of all the pairs.

When the RMC calculation results are compared with the four structural models (random, $\left[\sqrt{3}\times\sqrt{3}\right]$ R30º-type superlattice, parallel chains and zigzag arrangement), the cation arrangements in the TM layers in $Li[Ni_{1/3}Mn_{1/3}Co_{1/3}]O_2$ fit two models to some degree. On one hand, the increase in the number of Ni-Mn pairs in the 1st coordination shell but decrease in the 2nd coordination shell is consistent with the $\left[\sqrt{3}\times\sqrt{3}\right]$ R30º-type superlattice, while the number of Ni-Co, Mn-Co and Co-Co pairs in both shells are closer to those resulting from the random model.

The ^{6}Li NMR spectrum of $Li[Ni_{1/3}Mn_{1/3}Co_{1/3}]O_2$ reinforces this analysis. The absence of discrete peaks and the broad features of the resonance [14, 19] are consistent

with a lack of complete ordering of the cations in the TM layers, even at a local level. The tendency for $\left[\sqrt{3}\times\sqrt{3}\right]$-type ordering is consistent with the model of Cahill et. al.[19]. where local charge balance is proposed (comprising triangles of Co^{3+}, Ni^{2+} and Mn^{4+}), and also suggests that more long-range ordering may be present in small domains in some samples, consistent with the TEM data for this material [43].

Local ordering schemes that resemble the $\left[\sqrt{3}\times\sqrt{3}\right]$ superlattice presumably represent the most stable ordered configuration, because this scheme maximizes the favorable Ni-Mn contacts, while minimizing high energy Mn^{4+}-Mn^{4+} coulombic interactions. However, the driving force for ordering involving Co^{3+} in the α-$NaFeO_2$ sub-lattice is much weaker due to the 3+ charge on this cation, and entropic factors will favor the disruption of the Ni-Mn ordering by Co^{3+}. Furthermore, there are no energy penalties associated with Co-Co pair formation, and the presence of these pairs (or more extended chains) will not prevent the formation of longer chains of Ni-Mn arrangements, but it will well prevent the long-range ordering of the $\left[\sqrt{3}\times\sqrt{3}\right]$ superlattice. NMR analysis of the low doping levels, which clearly shows the formation of Ni^{2+}-Mn^{4+} pairs and some tendency for larger cluster formation, is clearly consistent with this model of strong Ni-Mn ordering disrupted by the Co^{3+} ions. A schematic of this ordering is shown in Figure 2.18.

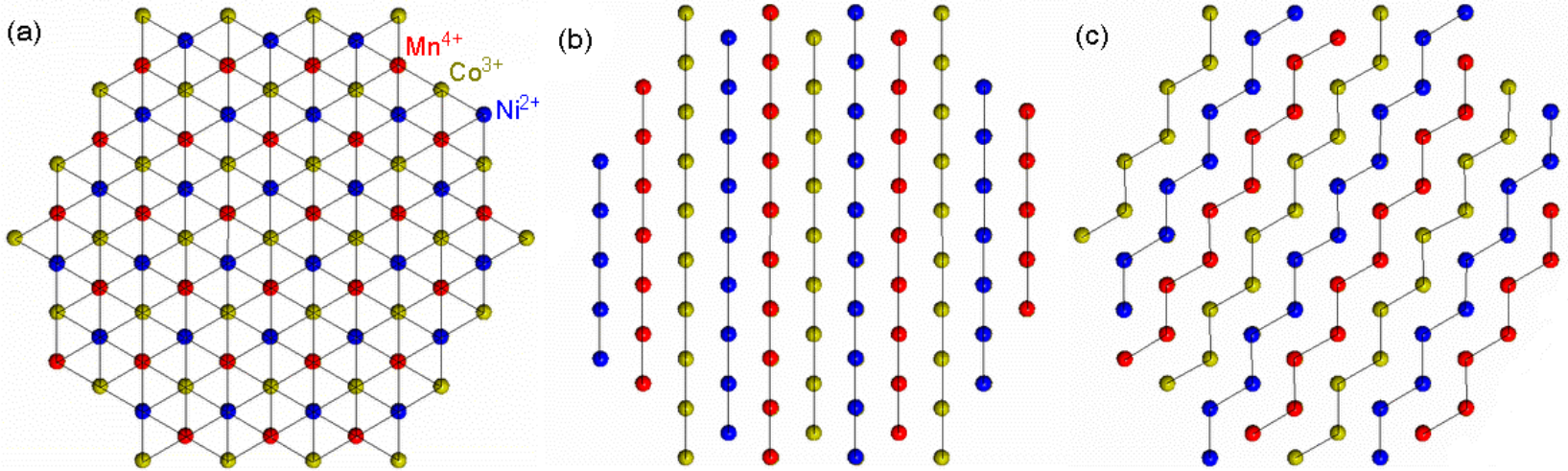

Figure 2.17. Schematic illustrations of the three ordered models proposed in the text for one TM layer in $Li[Ni_{1/3}Mn_{1/3}Co_{1/3}]O_2$: **(a)** $\left[\sqrt{3}\times\sqrt{3}\right]$ R30º-type superlattice; **(b)** parallel and **(c)** zigzag arrangements.

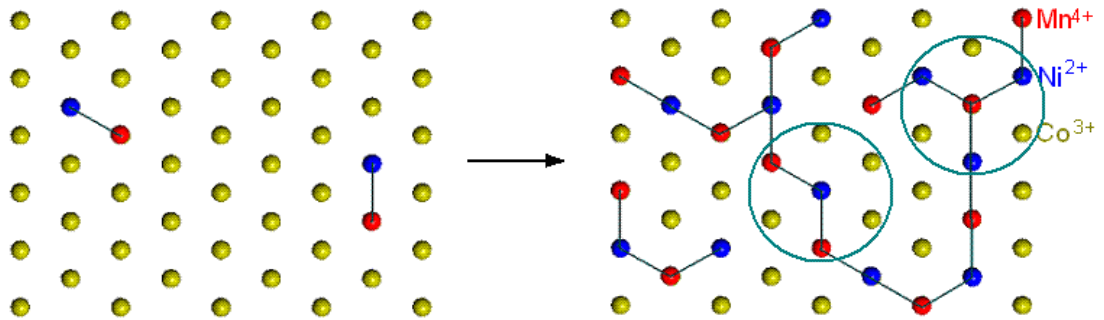

Figure 2.18. A schematic illustration of **(left)** isolated Ni/Mn pairing in low doping level and **(right)** the formation of longer chains of Ni-Mn arrangements in increasing doping level. Some $\left[\sqrt{3}\times\sqrt{3}\right]$ superlattice motifs are illustrated in green circles.

Table 2.5. Number of Ni/Mn/Co pairs in the transition metal layers (*ab* plane) of $^{7}Li[Ni_{1/3}Mn_{1/3}Co_{1/3}]O_2$ and occupational correlation results before and after the RMC calculations and comparison with the number of cation pairs in the four models. A 10×10×2 cluster size was used, and only the first and second coordination shells are considered. (* The correlation coefficient c_{ij} between a pair of sites i and j is given by the statistical definition [44] of the correlation: $c_{ij} = (Pij - \theta 2)/(\theta(1-\theta))$, where P_{ij} is the probability that both sites i and j are occupied by the same atom type and θ is its overall occupancy. Negative values of c_{ij} indicate that the sites i and j tend to be occupied by different atom types.)

(a) 1st coord. shell	RMC results		Possible Models			
	Before (Random)	After	Random	[√3 ×√3]R30º-Superlattice	Parallel cation chains	Zigzag arrangement
%Ni-Ni pairs	11.8 % (212 p.)	9.1 % (164 p.)	11.1%	0	16.7%	22.2%
%Ni-Mn pairs	24.4 % (439 p.)	28.4 % (512 p.)	22.2%	33.3%	16.7%	11.1%
%Mn-Mn pairs	12.0 % (216 p.)	9.6 % (172 p.)	11.1%	0	16.7%	22.2%
%Ni-Co pairs	20.4 % (367 p.)	21.7 % (390 p.)	22.2%	33.3%	16.7%	11.1%
%Mn-Co pairs	20.3 % (365 p.)	21.1 % (380 p.)	22.2%	33.3%	16.7%	11.1%
%Co-Co pairs	11.2 % (201 p.)	10.1 % (182 p.)	11.1%	0	16.7%	22.2%
Total	100 %	100 %	100%	100%	100%	100%
Correlation c_{NiMn}*	-0.012	-0.211				
Correlation c_{NiCo}*	+0.067	-0.064				
Correlation c_{MnCo}*	+0.058	-0.035				

(b) 2nd coord. shell	RMC results		Possible Models			
	Before (Random)	After	Random	[√3 ×√3]R30º-Superlattice	Parallel cation chains	Zigzag arrangement
%Ni-Ni pairs	12.2 % (220 p.)	15.8 % (285 p.)	11.1%	33.3%	0	16.7%
%Ni-Mn pairs	21.4 % (386 p.)	14.1 % (254 p.)	22.2%	0	33.3%	16.7%
%Mn-Mn pairs	13.1 % (236 p.)	16.8 % (302 p.)	11.1%	33.3%	0	16.7%
%Ni-Co pairs	22.4 % (404 p.)	22.6 % (406 p.)	22.2%	0	33.3%	16.7%
%Mn-Co pairs	21.0 % (378 p.)	21.0 % (378 p.)	22.2%	0	33.3%	16.7%
%Co-Co pairs	9.8 % (176 p.)	9.7 % (175 p.)	11.1%	33.3%	0	16.7%
Total	100%	100%	100%	100%	100%	100%
Correlation c_{NiMn}*	+0.076	+0.400				
Correlation c_{NiCo}*	-0.018	+0.045				
Correlation c_{MnCo}*	+0.035	+0.096				

2.3.5 Consequences of cation ordering for the electrochemical behavior.

Figure 2.19 shows the electrochemical profiles, and the corresponding derivatives (dx_0/dV), for representative members of the $Li[Ni_xMn_xCo_{(1-2x)}]O_2$ series tested as electrodes in a lithium battery. A shoulder that extends from *ca.* 3.6 to 3.8 V (left dashed line) is observed in the voltage profile (see also the small peak in the derivative plot) in the initial stages of deintercalation for $0.01 \leq x \leq 0.15$. The amount of extracted lithium correlates with the Ni content and as a consequence, this process was previously ascribed to the oxidation of nickel from Ni^{2+} to Ni^{4+} [12]. A second process is seen, again for $0.01 \leq x \leq 0.15$, at 3.9 V. The voltage value corresponds to the insulator to metal transition of $LiCoO_2$, which has been reported to result in a biphasic region (from approx. $x_0 = 0.95 – 0.75$) for the undoped material [45-46], consistent with the presence of a voltage *plateau* in the profile (and a corresponding sharp peak in the derivative). The higher voltage (4 V and onwards) processes, noticeable only at low Ni and Mn contents, are associated with a series of phase transitions that occur in $LiCoO_2$ on removal of 50% or more of the lithium ions [45-46]. The fact that these transitions also take place in samples that contain Ni and Mn indicates that, especially at low contents of these ions, the sample has a considerable $LiCoO_2$-like character. In all the cases, almost complete removal of the lithium ions from the compound can be achieved at 5 V.

Noticeable changes in the electrochemical profile are seen as Ni doping increases. The most significant is the gradual broadening and finally disappearance for the $x = 0.20$ sample of the peak in the derivative associated with the 3.9 V *plateau*. This can be ascribed to a change in the mechanism of lithium deintercalation, which is no longer two-

phase. Instead of showing the 3.9 V *plateau*, when $x \geq 0.20$, the voltage increases gradually with decreasing lithium content to around 4.2 V. This is now associated with a broad peak at around 3.7 V in the derivative curve, due to a single phase process that results in the extraction of 50% of the lithium. After this reaction, a new process centered around 4.4 V, followed by a gradual increase of the voltage up to 4.7 V, accounting for additional 40% of extracted lithium, is observed.

These changes in the electrochemical behavior of the samples are strongly correlated with our observations, by ^{6}Li MAS NMR, of the changes in the local structure of the compounds. With increasing Ni and Mn contents, the gradual loss of intensity of the resonance at 0 ppm, resulting from the presence of $Li(Co_6)^{1st}(Co_6)^{2nd}$ local environments, can be associated with the loss of Co-rich domains, and is correlated with the gradual broadening and then loss of the peak due to the insulator to metal transition seen in the electrochemical profiles. This loss of contact between cobalt ions is likely to interrupt the cooperative effect required for an insulator to metallic transition. Once there are no longer any isolated Co^{3+} clusters, a change in the mechanism of the lithium deintercalation is observed. *In situ* XRD and *ex situ* NMR experiments are in progress to provide further insights into the changes in the behavior of compounds in the $Li[Ni_xMn_xCo_{(1-2x)}]O_2$ ($0.01 \leq x \leq 1/3$) series upon oxidation, and to fully characterize all the electrochemical processes.

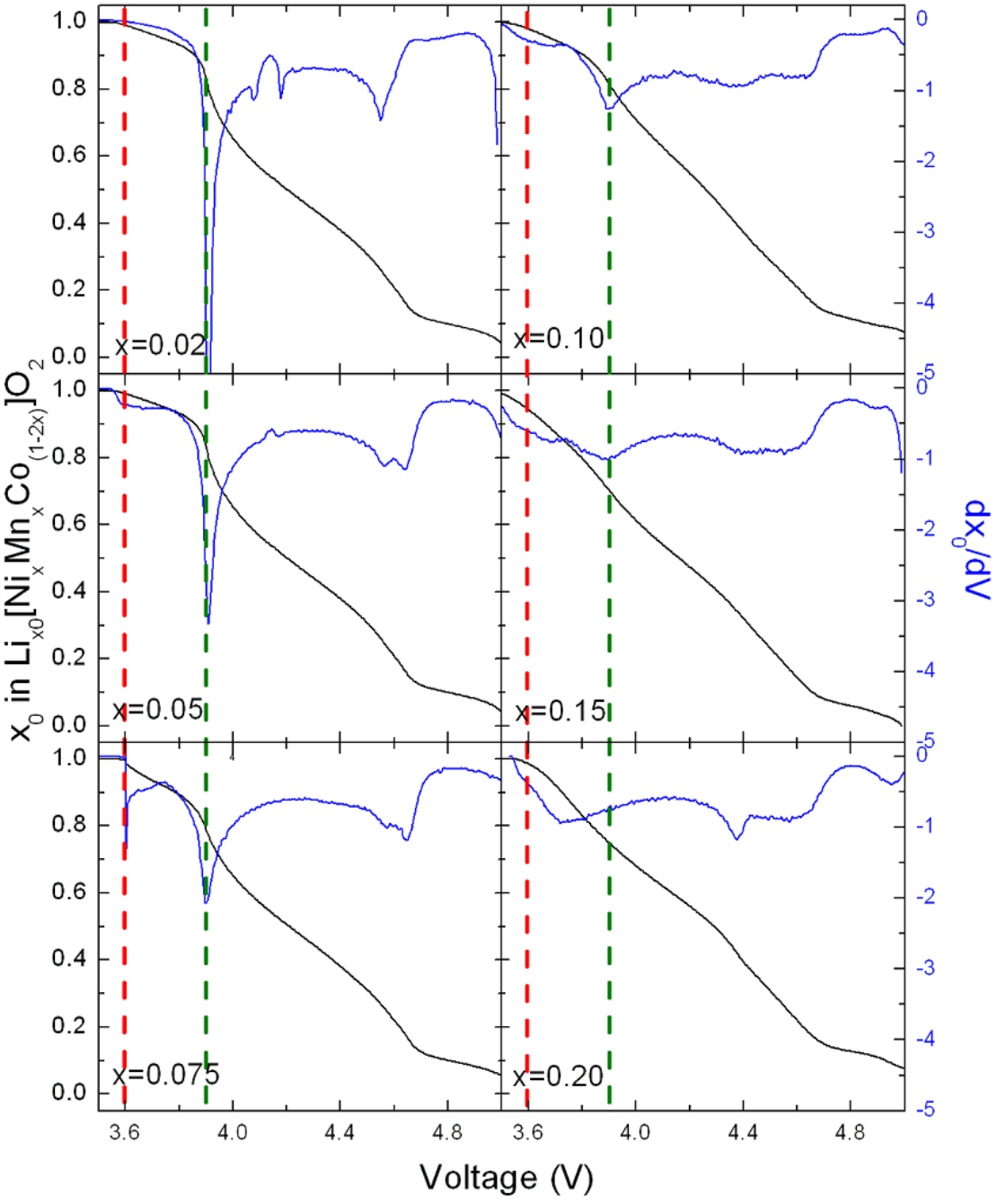

Figure 2.19. Plot of the voltage vs. Li content (x_0 in $Li_{x0}[Ni_xMn_xCo_{(1-2x)}]O_2$) (black lines) and derivative dx_0/dV (blue lines) of a $Li[Ni_xMn_xCo_{(1-2x)}]O_2$ (x = 0.02 to 0.20) electrode charged against lithium metal at a C/50 rate.

2.4 Conclusions

Several members of the $Li[Ni_xMn_xCo_{(1-2x)}]O_2$ ($0.01 \leq x \leq 1/3$) series, isostructural with layered $LiCoO_2$ (space group $R\bar{3}m$, No. 166), were synthesized. The XANES measurements show that these compounds contain Ni^{2+}, Mn^{4+} and Co^{3+} ions. The ^6Li MAS NMR spectra of the compounds show some common features. Several well resolved resonances can be observed in the compounds with low Ni/Mn contents, and when the amount of Ni and Mn increases, those resonances start to merge and finally form a broad resonance. The chemical environments of the resonances in the spectra for low Ni/Mn contents ($x \leq 0.10$) were assigned using prior NMR analyses of paramagnetic materials, based in the hyperfine shift due to each type of transition metal cation in the 1st and 2nd coordination shells.

In the very dilute sample, $^6Li[Ni_{0.02}Mn_{0.02}Co_{0.96}]O_2$, analysis of the ^6Li MAS NMR spectra indicates the formation of Ni^{2+}/Mn^{4+} clusters in the predominantly Co^{3+} TM layers. Moreover, it has been found that the oxidation state of Ni in this high Co content sample is highly dependent on the starting Li/Transition Metal ratio, the NMR spectrum of a sample containing 5% Li excess showing peaks associated to the presence of Ni^{3+}. Neutron PDF analysis of $Li[Ni_{1/3}Mn_{1/3}Co_{1/3}]O_2$ shows a non-random distribution of Ni and Mn cations in the TM layers, with Ni closer to Mn in the 1st coordination shell (resembling the $\left[\sqrt{3}\times\sqrt{3}\right]$ R30º-type superlattice structure model) but a more random distribution of Co. The ^6Li NMR spectrum of this compound and an analysis of the resonance due to Co^{3+} rich regions, for the whole $Li[Ni_xMn_xCo_{(1-2x)}]$ series, is also consistent with the PDF results, indicating a non-random distribution of transition metal

cations in the TM layers. The local ordering was correlated with variations in the mechanism of lithium intercalation with increased Ni/Mn content. The most significant change was the conversion of two-phase reaction due to an insulator to metal transition, as reported for stoichiometric $LiCoO_2$, first into a broader process and then the total disappearance of this process for $x \geq 0.20$. The decrease in the concentration of Co-rich clusters in the pristine materials as seen by NMR, tracked closely with these changes.

These results suggest that Ni and Mn show a strong tendency for clustering in the TM layers all along the $Li[Ni_xMn_xCo_{(1-2x)}]O_2$ ($0.01 \leq x \leq 1/3$) series. The results provide further insight into the structural features of these compounds, which are currently of high interest as positive electrodes in lithium-ion batteries.

References

1. Dahn, J.R., U. von Sacken, and C.A. Michal, Structure and electrochemistry of $Li_{1\pm y}NiO_2$ and a new Li_2NiO_2 phase withe the $Ni(OH)_2$ structure *Solid State Ionics*, 1990. **44**(1-2): p. 87-97.

2. Saadoune, I. and C. Delmas, $LiNi_{1-y}Co_yO_2$ positive electrode materials: relationships between the structure, physical properties and electrochemical behaviour. *J. Mater. Chem.*, 1996. **6**: p. 193-199.

3. Capitaine, F., P. Gravereau, and C. Delmas, A new variety of $LiMnO_2$ with a layered structure. *Solid State Ionics*, 1996. **89**: p. 197-202.

4. Rossen, E., C.D.W. Jones, and J.R. Dahn, Structure and electrochemistry of $Li_xMn_yNi_{1-y}O_2$. *Solid State Ionics*, 1992. **57**(3-4): p. 311-318.

5. Ohzuku, T. and Y. Makimura, Layered Lithium Insertion Material of $LiNi_{1/2}Mn_{1/2}O_2$: A Possible Alternative to $LiCoO_2$ for Advanced Lithium-Ion Batteries. *Chem. Lett.*, 2001: p. 744-745.

6. Liu, Z., A. Yu, and J.Y. Lee, Synthesis and characterization of $LiNi_{1-x-y}Co_xMn_yO_2$ as the cathode materials of secondary lithium batteries. *J.Power Sources*, 1999. **81-82**: p. 416-419.

7. Yoshio, M., H. Noguchi, J.-i. Itoh, M. Okada, and T. Mouri, Preparation and properties of $LiCo_yMn_xNi_{1-x-y}O_2$ as a cathode for lithium ion batteries. *J. Power Sources*, 2000. **90**: p. 176-181.

8. Ohzuku, T. and Y. Makimura, Layered Lithium Insertion Material of $LiCo_{1/3}Ni_{1/3}Mn_{1/3}O_2$ for Lithium-Ion Batteries. *Chem. Lett.*, 2001: p. 642-643.

9. Lu, Z., D.D. MacNeil, and J.R. Dahn, Layered $Li[Ni_xCo_{1-2x}Mn_x]O_2$ Cathode Materials for Lithium Ion Batteries. *Electrochem. Solid-St. Lett.*, 2001. **4**(12): p. A200-A203.

10. Hwang, B.J., Y.W. Tsai, D. Carlier, and G. Ceder, A Combined Computational/Experimental Study on $LiNi_{1/3}Co_{1/3}Mn_{1/3}O_2$. *Chem. Mater.*, 2003. **15**: p. 3676-3682.

11. Rougier, A. and C. Delmas, Non-cooperative Jahn-Teller effect in $LiNiO_2$: an EXAFS study. *Solid State Commun.*, 1995. **94**(2): p. 123-127.

12. MacNeil, D.D., Z. Lu, and J.R. Dahn, Structure and electrochemistry of $Li[Ni_xCo_{1-2x}Mn_x]O_2$ ($0 <= x <= 1/2$). *J. Electrochem. Soc.*, 2002. **149**(10): p. A1332-A1336.

13. Shaju, K.M., G.V.S. Rao, and B.V.R. Chowdari, Performance of layered $Li(Ni_{1/3}Co_{1/3}Mn_{1/3})O_2$ as cathode for Li-ion batteries. *Electrochimica Acta*, 2002. **48**: p. 145-151.

14. Yoon, W.-S., C.P. Grey, M. Balasubramanian, X.-Q. Yang, D.A. Fischer, and J. McBreen, Combined NMR and XAS Study on Local Environments and Electronic Structures of Electrochemcally Li-Ion Deintercalated $Li_{1-x}Co_{1/3}Ni_{1/3}Mn_{1/3}O_2$ Electrode System. *Electrochem. Solid-St. Lett.*, 2004. **7**(3): p. A53-A55.

15. Yoon, W.-S., M. Balasubramanian, K.Y. Chung, X.-Q. Yang, J. McBreen, C.P. Grey, and D.A. Fischer, Investigation of the Charge Compensation Mechanism on the Electrochemically Li-Ion Deintercalated $Li_{1-x}Co_{1/3}Ni_{1/3}Mn_{1/3}O_2$ Electrode System by Combination of Soft and Hard X-ray Absorption Spectroscopy. *J. Am. Chem. Soc.*, 2005. **127**: p. 17479-17487.

16. Yoon, W.-S., S. Iannopollo, C.P. Grey, D. Carlier, J. Gorman, J. Reed, and G. Ceder, Local Structure and Cation Ordering in O3 Lithium Nickel Manganese Oxides with Stoichiometry $Li[Ni_xMn_{(2-x)/3}Li_{(1-2x)/3}]O_2$ -NMR Studies and First Principles Calculations. *Electrochem. Solid-St. Lett.*, 2004. **7**(7): p. A167-A171.

17. Bréger, J., N. Dupré, P.J. Chupas, P.L. Lee, T. Proffen, J.B. Parise, and C.P. Grey, Short- and Long-Range Order in the Positive Electrode Material, $Li(NiMn)_{0.5}O_2$: A Joint X-ray and Neutron Diffraction Pair Distribution Function Analysis and NMR Study. *J. Am. Chem. Soc.*, 2005. **127**: p. 7529-7537.

18. Bréger, J., K. Kang, J. Cabana, G. Ceder, and C.P. Grey, NMR, PDF and RMC study of the positive electrode material $Li(Ni_{0.5}Mn_{0.5})O_2$ synthesized by ion-exchage methods. *J. Mater. Chem.*, 2007. **17**: p. 3167-3174.

19. Cahill, L.S., S.-C. Yin, A. Samoson, I. Heinmaa, L.F. Nazar, and G.R. Goward, ^6Li NMR Studies of Cation Disorder and Transition Metal Ordering in $Li[Ni_{1/3}Mn_{1/3}Co_{1/3}]O_2$ Using Ultrafast Magic Angle Spinning. *Chem. Mater.*, 2005. **17**: p. 6560-6566.

20. Carlier, D., M. Ménétrier, C.P. Grey, C. Delmas, and G. Ceder, Understanding the NMR shifts in paramagnetic transition metal oxides using density functional theory calculations. *Phys. Rev. B*, 2003. **67**: p. 174103.

21. Grey, C.P. and N. Dupré, NMR Studies of Cathode Materials for Lithium-Ion Rechargeable Batteries. *Chem. Rev.*, 2004. **104**: p. 4493-4512.

22. Jouanneau, S. and J.R. Dahn, Preparation, Structure, and THermal Stability of New $Ni_xCo_{1-2x}Mn_x(OH)_2$ ($0 \leqslant x \leqslant 1/2$) Phases. *Chem. Mater.*, 2003. **15**: p. 495-499.

23. Saadoune, I., M. Ménétrier, and C. Delmas, Redox processes in $Li_xNi_{1-y}Co_yO_2$ cobalt-rich phases. *J. Mater. Chem.*, 1997. **7**: p. 2505-2511.

24. Kang, K., D. Carlier, J. Reed, E.M. Arroyo, G. Ceder, L. Croguennec, and C. Delmas, Synthesis and Electrochemical Properties of Layered $Li_{0.9}Ni_{0.45}Ti_{0.55}O_2$. *Chem. Mater.*, 2003. **15**: p. 4503-4507.

25. Bréger, J., M. Jiang, N. Dupré, Y.S. Meng, Y. Shao-Horn, G. Ceder, and C.P. Grey, High-resolution X-ray diffraction, DIFFaX, NMR and first principles study of disorder in the Li_2MnO_3-$Li[Ni_{1/2}Mn_{1/2}]O_2$ solid solution. *J. Solid State Chem.*, 2005. **178**: p. 2575-2585.

26. Rietveld, H.M., A Profile Refinement Method for Nuclear and Magnetic Structures. *J. Appl. Crystallogr.*, 1969. **2**: p. 65.

27. Larson, A.C. and R.B. Von Dreele, *General Structure Analysis System (GSAS), Los Alamos National Laboratory Report LAUR 86-748*. 1987.

28. Toby, B.H., EXPGUI, a graphical user interface for GSAS. *J. Appl. Crystallogr.*, 2001. **34**: p. 210.

29. Peterson, P.F., M. Gutmann, T. Proffen, and S.J.L. Billinge, PDFgetN: a user-friendly program to extract the total scattering structure factor and the pair distribution function from neutron powder diffraction data. *J. Appl. Crystallogr.*, 2000. **33**: p. 1192.

30. Gummow, R.J., M.M. Thackeray, W.I.F. David, and S. Hull, Structure and Electrochemistry of Lithium Cobalt Oxide Synthesised at 400°C. *Mat. Res. Bull.*, 1992. **27**: p. 327-337.

31. Yoon, W.-S., Y. Paik, X.-Q. Yang, M. Balasubramanian, J. McBreen, and C.P. Grey, Investigation of the Local Structure of the $LiNi_{0.5}Mn_{0.5}O_2$ Cathode Material during Electrochemical Cycling by X-Ray Absorption and NMR Spectroscopy. *Electrochem. Solid-St. Lett.*, 2002. **5**(11): p. A263-A266.

32. Pan, C., Y.J. Lee, B. Ammundsen, and C.P. Grey, ^{6}Li MAS NMR Studies of the Local Structure and Electrochemical Properties of Cr-doped Lithium Manganese and Lithium Cobalt Oxide Cathode Materials for Lithium-Ion Batteries. *Chem. Mater.*, 2002. **14**: p. 2289-2299.

33. Carlier, D., K. Kang, G. Ceder, W.S. Yoon, and C.P. Grey. *^{6}Li MAS NMR Study of Lithium Layered Oxides Containing Ni^{2+} Ions: Experiments and DFT Calculations*. in *203rd Meeting of the Electrochemical Society (ECS)*. 2003. Paris.

34. Marichal, C., J. Hirschinger, and P. Granger, ^{6}Li and ^{7}Li NMR in the $LiNi_{1-y}Co_yO_2$ Solid Solution ($0 \leqslant y \leqslant 1$). *Inorg. Chem.*, 1995. **34**: p. 1773-1778.

35. Chazel, C., M. Ménétrier, L. Croguennec, and C. Delmas, $^{6/7}$Li NMR study of the $Li_{1-z}Ni_{1+z}O_2$ phases. *Magn. Reson. Chem.*, 2005. **43**: p. 849-857.

36. Yin, S.-C., Y.-H. Rho, I. Swainson, and L.F. Nazar, X-ray/Neutron Diffraction and Electrochemical Studies of Lithium De/Re-Intercalation in $Li_{1-x}Co_{1/3}Ni_{1/3}Mn_{1/3}O_2$ ($x=0 \rightarrow 1$). *Chem. Mater.*, 2006. **18**: p. 1901-1910.

37. Sears, V.F., Neutron scattering lengths and cross sections. *Neutron News 3*, 1992. **3**: p. 26-37.

38. McGreevy, R.L. and L. Pusztai, Reverse Monte Carlo Simulation: A New Technique for the Determination of Disordered Structures. *Mol. Simul.*, 1988. **1**: p. 359-367.

39. Tucker, M.G., M.T. Dove, and D.A. Keen, Application of the reverse Monte Carlo method to crystalline materials. *J. Appl. Crystallogr.*, 2001. **34**: p. 630.

40. Proffen, T. and R.B. Neder, DISCUS: A program for diffuse scattering and defect-structure simulation. *J. Appl. Crystallogr.*, 1997. **30**: p. 171-175.

41. Koyama, Y., N. Yabuuchi, I. Tanaka, H. Adachi, and T. Ohzuku, Solid-State Chemistry and Electrochemistry of $LiCo_{1/3}Ni_{1/3}Mn_{1/3}O_2$ for Advanced Lithium-Ion Batteries. *J. Electrochem. Soc.*, 2004. **151**(10): p. A1545-A1551.

42. Koyama, Y., I. Tanaka, H. Adachi, Y. Makimura, and T. Ohzuku, Crystal and electronic structures of superstructural $Li_{1-x}[Co_{1/3}Ni_{1/3}Mn_{1/3}]O_2$ ($0 \leqslant x \leqslant 1$). *J. Power Sources*, 2003. **119-121**: p. 644-648.

43. Yabuuchi, N., Y. Koyama, N. Nakayama, and T. Ohzuku, Solid-State Chemistry and Electrochemistry of $LiCo_{1/3}Ni_{1/3}Mn_{1/3}O_2$ for Advanced Lithium-Ion Batteries II. Preparation and Characterization. *J. Electrochem. Soc.*, 2005. **152**(7): p. A1434-A1440.

44. Welberry, T.R., Diffuse X-ray Scattering and Models of Disorder. *Rep. Prog. Phys.*, 1985. **48**: p. 1543.

45. Van der Ven, A., M.K. Aydinol, and G. Ceder, First-Principles Evidence for Stage Ordering in Li_xCoO_2. *J. Electrochem. Soc.*, 1998. **145**(6): p. 2149-2155.

46. Morcrette, M., Y. Chabre, G. Vaughan, G. Amatucci, J.-B. Leriche, S. Patous, C. Masquelier, and J.-M. Tarascon, In situ X-ray diffraction techniques as a powerful tool to study battery electrode materials. *Electrochimica Acta*, 2002. **47**: p. 3137-3149.

Chapter 3 Investigation of the Structural Changes in $Li[Ni_yMn_yCo_{(1-2y)}]O_2$ ($y = 0.05$) upon Electrochemical Lithium Deintercalation

3.1 Introduction

The layered compounds with general formula $LiMO_2$, in which M represents one (or a combination of) transition metal(s) such as Co, Ni, Mn, V etc., have long been considered to be phases with attractive properties for their application as positive electrode materials in rechargeable lithium ion batteries [1-6]. These compounds crystallize in an α-$NaFeO_2$ rock salt structure (adopting an $R\bar{3}m$ space group), with alternating layers formed by edge-sharing LiO_6 and MO_6 octahedra. Among them, those in the series $Li[Ni_yMn_yCo_{(1-2y)}]O_2$ have been shown to have very good electrochemical performance, which has triggered intensive research efforts to understand their structure-properties relationships [7-9]. Previous reports on $LiNi_{0.5}Mn_{0.5}O_2$, one of the end members of this series, have shown that the cation ordering/exchange both in the transition metal and between the transition metal and lithium layers can play a crucial role in determining their electrochemical behavior [10-13]. Thus, the structural characterization of these phases provides essential information with which to understand their electrochemical properties. Recently, a systematic and thorough study using a

variety of techniques, including X-Ray and Neutron Diffraction (XRD/ND), X-ray Absorption Near Edge Spectroscopy (XANES), ^{6}Li Magic Angle Spinning (MAS) Nuclear Magnetic Resonance (NMR) spectroscopy and neutron Pair Distribution Function (PDF) analysis along with Reverse Monte Carlo (RMC) calculations, was performed by us to investigate long and short range structure in this series [14]. The results confirm that they all contain Ni^{2+}, Mn^{4+} and Co^{3+} ions, and that Ni^{2+} and Mn^{4+} have a strong tendency to cluster in the transition metal layers. The electrochemical profiles of the different members of the series indicate that increasing amounts of Ni/Mn induce changes in the mechanism of lithium extraction; the signature of the two-phase process that is generally linked to the insulator-to-metal transition in Li_xCoO_2 [15], at around 3.9 V, gradually disappears, we ascribed in our previous work [14] to a decrease in the size of the $LiCoO_2$-like domains within the structure. Following this work, and with the aim of understanding the changes in mechanism, we selected several representative members with different Ni/Mn contents, and have used XRD, XANES and NMR to probe their structural changes upon electrochemical delithiation.

The results and conclusions presented henceforth focus on one of the members with a low Ni/Mn substitution level, $Li[Ni_{0.05}Mn_{0.05}Co_{0.90}]O_2$ (y = 0.05, denoted as **90Co** in throughout this work). The structure and electrochemical features (e.g., the phase transition at 3.9 V) that resemble to $LiCoO_2$ are largely preserved, while the ^{6}Li NMR spectrum of **90Co**, on the other hand, shows well resolved resonances corresponding to different distinctive Li environments with different numbers of Ni and Mn in the 1st and 2nd cation coordination shells of the Li ions. These resonances were used to follow and

understand how the various lithium local environments evolve upon charging. *In situ* XRD was also performed to investigate the long-range effects of lithium extraction on the compound, and XANES data on all the three transition metal elements were collected during the electrochemical processes to give simultaneous information about the changes in the transition metal oxidation states.

3.2 Experimental

3.2.1 Sample preparation.

The initial phase $^{6}Li[Ni_yMn_yCo_{(1-2y)}]O_2$ (y = 0.05) was synthesized following the procedure from Lu *et al.* by using a mixed-metal hydroxide precursor [7], which was prepared through the dropwise addition of a distilled water solution containing stoichiometric amounts of $Mn(NO_3)_2{\cdot}4H_2O$ (>97.0%, Fluka), $Ni(NO_3)_2{\cdot}6H_2O$ (>98.0%, Fluka), and $Co(NO_3)_2{\cdot}6H_2O$ (98+%, Aldrich) into another one with an excess amount of $LiOH{\cdot}H_2O$ (purified, crystal, Fisher). The resulting precipitate, $(Ni_{0.05}Mn_{0.05}Co_{0.90})(OH)_2{\cdot}nH_2O$, was washed and dried at 180°C overnight, then mixed with a stoichiometric amount of $^{6}Li_2CO_3$ (90-95% ^{6}Li, FW=72.11, Cambridge Isotope Laboratories, Inc.), pelletized, successively heated at 480°C and 900°C for 3 h, with intermediate grinding, and, finally, quenched from 900°C with liquid nitrogen. $^{6}LiCoO_2$ was prepared by successively heat-treating pelletized stoichiometric mixtures of $^{6}Li_2CO_3$ and Co_3O_4 (powder, Aldrich) in air at 450°C for 5 h, and at 900°C for 15 and 24 h with intermediate grinding [15]. The purity of the compounds was characterized by X-ray

diffraction on a Rigaku Miniflex powder diffractometer, which uses Cr Kα radiation (λ = 2.2909 Å).

3.2.2 Electrochemical study.

The positive electrodes consisted of 80 wt% active material, 10 wt% acetylene black (SUPER P Li, TIMCAL), and 10 wt% of poly-vinylidene fluoride (PVDF) (HSV 900, Kynar) binder. The electroactive mixture was dissolved in N-methyl pyrrolidone (NMP) (99.5%, Sigma-Aldrich), cast onto aluminum foil and dried at 80°C. Coin cells (CR2032, Hohsen corp.) were assembled in an argon-filled glove box. Each cell typically contains about 15 mg of active material, separated from a Li disk by two pieces of Celgard separator (Celgard Inc, USA). A 1M solution of $LiPF_6$ in ethylene carbonate:dimethyl carbonate (1:1) was used as the electrolyte (Ferro Co.). Samples at different states of charge (SOC) for the *ex situ* experiments were prepared by stopping batteries being charged at a constant C/50 current density (where C is defined as the theoretical capacity of the compound, 277 mAh/g) to target lithium contents. The cells were opened in an Ar-filled glove box and the cathode films were washed with anhydrous DMC and dried. The resulting samples were either recovered in powder form and packed in rotors for the NMR measurements, or sealed as films with Kapton tape for the XANES experiments. Quasi-open circuit potential data was collected by using the Galvanostatic Intermitent Titration Technique (GITT). Here, a constant current density corresponding to a C/20 rate was applied for 24 min, followed by rest periods of 3 h, until the voltage reached 5 V. All the electrochemical experiments were carried out on an Arbin battery cycler (Arbin Ins., College Station, TX).

3.2.3 *In-situ* X-ray Diffraction. (XRD)

In situ XRD was collected at beamline X18A at the National Synchrotron Light Source (NSLS) at Brookhaven National Laboratory. A radiation wavelength of 1.195 Å and a step size of 0.02º for the 2θ scan were used. A specially designed (for *in situ* measurements) cell [16] with Mylar windows was used to cycle the electrode films prepared as described above.

3.2.4 X-ray Absorption Near-Edge Spectroscopy (XANES)

The XANES spectra were collected at beamline X19A at the NSLS in transmission or fluorescence mode using a Si (111) double-crystal monochromator detuned to 35-45% of its original intensity to eliminate the high order harmonics. Energy calibration was carried out by using the first inflection points in the spectra of Mn, Co and Ni metal foil as references. (Mn K-edge = 6539 eV, Co K-edge = 7709 eV and Ni K-edge = 8333 eV.)

3.2.5 Solid-State Nuclear Magnetic Resonance (NMR)

The ^{6}Li magic angle spinning (MAS) NMR experiments were performed at 29.39 MHz on a Chemagnetics CMX-200 spectrometer (B_0 = 4.7 T) by using a double resonance 1.8 mm probe. Silicon nitride (Si_3N_4) rotors were used and spun at a speed of 38 kHz. All the spectra were acquired following a rotor-synchronized Hahn echo sequence (90°-τ-180°-τ-acquisition). The spectra were referenced to a standard 1M ^{6}LiCl solution at 0 ppm. π/2 pulses of 3.5 μs were used, with a recycle delay time of 0.2 s.

3.3 Results and Discussion

3.3.1 Preliminary electrochemical evaluation.

The voltage-composition profile and the corresponding derivative curve (d*x*/dV) for the first charge to 5 V of a lithium battery containing **90Co** as a positive electrode are plotted in Figure 3.1. The analysis of the derivative profile reveals the existence of several processes, between 3.6 and 3.8 V, at about 3.9 and between 4.5 and 4.7 V, which correspond to a shoulder and two plateau-like regions in the voltage-composition profile. In addition, another process between 4.0 and 4.2 V, accounting for a small amount of capacity, can also be observed. The shoulder around 3.6-3.8 V was previously ascribed to Ni^{2+} oxidation with the amount of Li removed being correlated to the Ni content in the structure [17]. All the other electrochemical signatures are very similar to those observed in Li_xCoO_2[16]; both the 3.9 and 4.5-4.7 V processes are reported to correspond to two-phase regions, whereas the small interval between 4.1 and 4.2 V (at around $x = 0.5$) is ascribed lithium ordering. In stoichiometric $LiCoO_2$, this is associated with a monoclinic distortion, the material returning to hexagonal symmetry upon further lithium deintercalation [18-19]. The close resemblance to $LiCoO_2$ is to be expected, since only 10% of the Co has been substituted by Ni and Mn in **90Co**. Nonetheless, it must be noted here that no distinct plateau is seen at 3.9 V, as for $LiCoO_2$. Correspondingly, the derivative peak is less intense and considerably broader than in $LiCoO_2$, seemingly suggesting some changes in the lithium extraction mechanism. Since the existence of overpotential in a chronoamperometric experiment can smear out plateaus, further

evidence of the order of the oxidation reaction was obtained from quasi-open circuit voltage electrochemical measurements (GITT, Figure 3.2). The absence of a plateau in the region around 3.9 V (see inset in Figure 3.2) is confirmed, suggesting that the transitions taking place at these voltages are single-phase. This possibility will be evaluated in more detail below.

To investigate the structural changes during these processes, both *in situ* and *ex situ* measurements were performed. The different states of charge chosen for the latter are marked in Figure 3.1 with red diamonds. In the following discussion, these samples are denoted as "Li*x*", where *x* indicates the amount of Li remaining in the structure. The sample charged to 5 V has very little lithium left in the structure, so, for reasons of simplicity, it will be denoted as Li0.0, assuming 100% columbic efficiency of the extraction process and ignoring side reactions with the electrolyte that become prominent at these potentials.

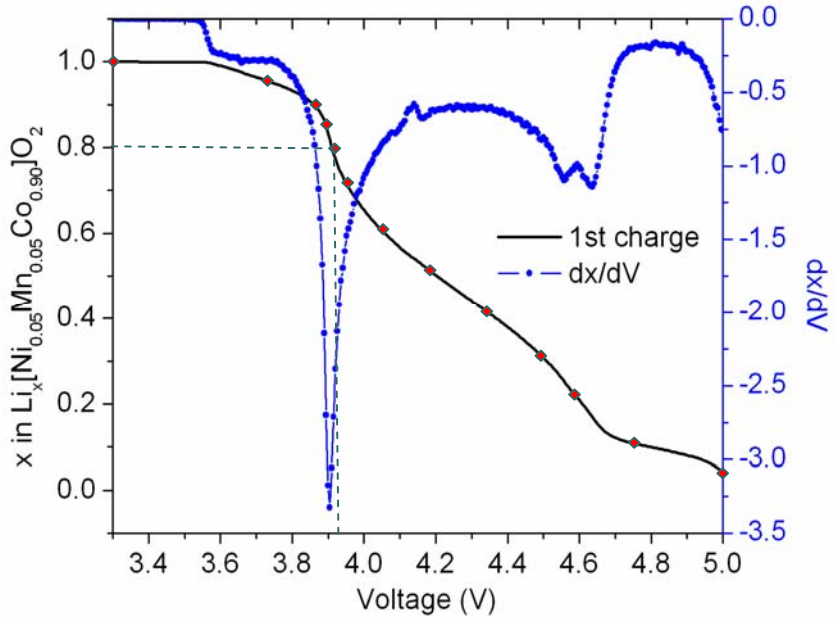

Figure 3.1. Plot of the voltage *vs.* Li content (x in $Li_x[Ni_{0.05}Mn_{0.05}Co_{0.90}]O_2$) (black solid lines) and derivative curves (dx/dV) (blue dotted lines) of a lithium cell containing **90Co** as a positive electrode, charged to 5 V at a C/50 rate. Data points where batteries were stopped for *ex situ* measurements are marked with red diamonds. To enable a clearer discussion, the charged samples are divided into two groups, with SOCs lower and above Li0.8 (20% SOC), as indicated by the dashed line in this figure.

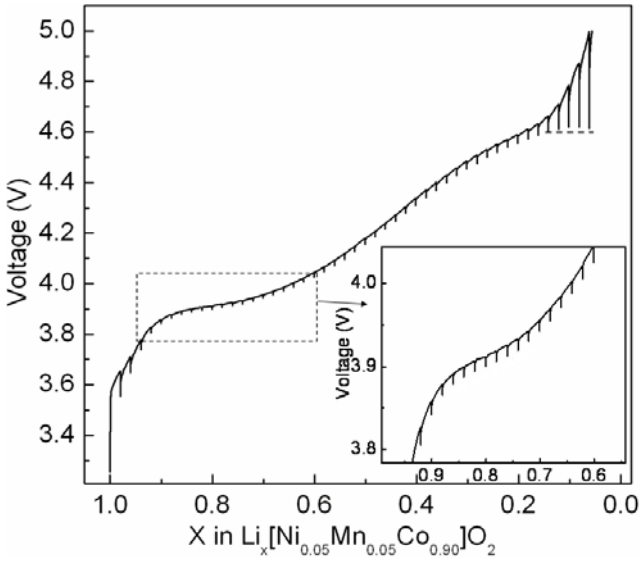

Figure 3.2. Quasi-open circuit voltage curve of the first charge of a Li/ $Li_x[Ni_{0.05}Mn_{0.05}Co_{0.90}]O_2$ cell obtained by the Galvanostatic Intermitent Titration Technique. The battery was charged at a 14 mA/g rate (C/20) for 24 min and then allowed to rest for 3 hrs.

3.3.2 *In situ* XRD study:

Representative XRD patterns of the phases observed at different lithium contents during the first oxidation of **90Co** are plotted in Figure 3.3. As previously reported, pristine **90Co** (sample Li1.0) adopts a layered α-$NaFeO_2$-type structure with O3-type stacking[20] and a $R\bar{3}m$ space group [14]. A smooth and gradual shift of the reflections, without appearance of any new peaks, is observed from the early stages of deintercalation up until 80% of the lithium is removed, which is indicative of a single-phase, solid solution mechanism that preserves the stacking sequence. Close inspection of the (003) reflection (Figure 3.3, bottom), which is directly related to the distance between MO_2 (M=Co, Ni, Mn) layers, reveals that it initially shifts to lower angle, the distance increasing due to the increasing repulsion between negatively charged MO_2 layers upon Li removal [19]. A maximum in interlayer distance is reached at Li0.50. Afterwards, the (003) peak starts moving back to higher 2θ values, which, conversely, is an indication of a decrease in interlayer spacing. This solid solution behavior is in contrast to that of $LiCoO_2$ at similar states of charge; a two-phase transformation associated with an insulator-to-metal transition upon lithium extraction is observed instead [16, 21]. Thus, it can be concluded that the presence of Ni and Mn in the structure has an effect on the structural transitions that occur when lithium is removed, which is in agreement with previous observations of phases in the Ni, Mn-rich part of the $Li[Ni_yMn_yCo_{(1-2y)}]O_2$ series, such as $Li[Ni_{0.5}Mn_{0.5}]O_2$ [13, 22] and $Li[Ni_{1/3}Mn_{1/3}Co_{1/3}]O_2$[23], and in singly-substituted $LiCoO_2$ (e.g. with Mg [21], Mn [24], or Ni [25]).

When the battery is charged to 4.6 V, with only 0.2Li remaining in the structure, the O3 stacking is transformed into O1. The existence of such a two-phase transition is also supported by the clear plateau at 4.6 V in the quasi-OCV profile (Figure 3.2, dashed line), and is in accordance with earlier observations for Li_xCoO_2 [26].

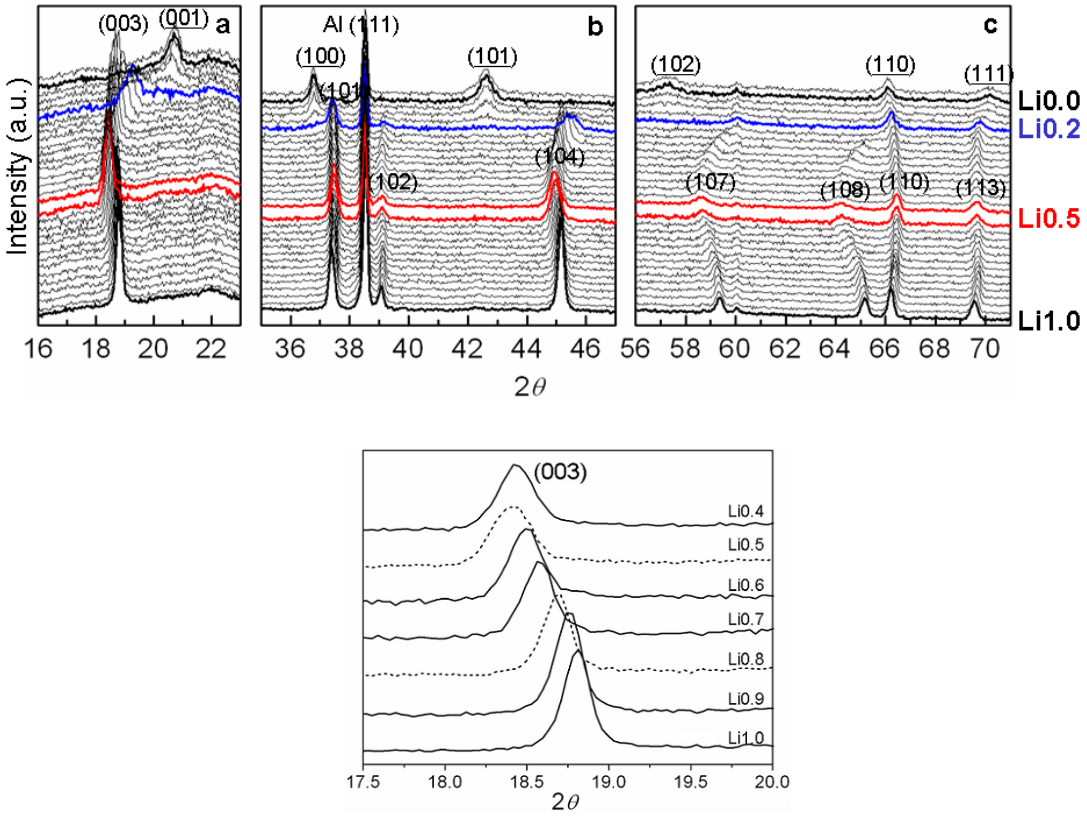

Figure 3.3. *In situ* XRD patterns for a Li/ $Li_x[Ni_{0.05}Mn_{0.05}Co_{0.90}]O_2$ cell charged to 5 V at a C/20 rate. Several stages, labeled as "Li*x*" (where *x* is the Li content in $Li_x[Ni_{0.05}Mn_{0.05}Co_{0.90}]O_2$), are shown as thick lines. Selected 2θ regions are shown in panels (a), (b) and (c) with Miller indices labeled. Indices in brackets correspond to an O3 phase with a $R\bar{3}m$ space group and those underlined in brackets correspond to an O1 phase with a *C*2/*m* space group. The (111) reflection from Al, the current collector, is indicated as well. An expansion of the (003) reflection in samples Li*x* ($1.0 \geq x \geq 0.4$) is shown in the lower panel. The 2θ values correspond to those for copper radiation ($K_{\alpha 1}$: λ = 1.5406 Å). The missing data at around "Li0.5" are due to the interruption of the X-ray beam during the *in situ* experiment.

3.3.3 *Ex situ* XANES.

Figure 3.4 shows the normalized Ni K-edge XANES spectra, and the corresponding first derivative, of **90Co** at different points of the electrochemical lithium deintercalation (SOC), along with that of $Li(Ni_{0.2}Co_{0.8})O_2$, used as a reference for Ni^{3+}. A solid shift of the absorption edge can be observed as early as in sample Li0.95 (5% SOC), which shows an edge position just slightly lower than that of $Li(Ni_{0.2}Co_{0.8})O_2$. The absorption edge further shifts for Li0.90, and a more subtle change is seen in sample Li0.85, which corresponds to a position that is beyond that of the Ni^{3+}-reference and that does not change upon further lithium extraction, thereby suggesting that Ni^{2+} is fully oxidized at this point. It is interesting to note that, although there is only 5% Ni^{2+} in **90Co,** 15% of the lithium has been removed before no solid shift is observed between samples. This suggests that redox reactions involving the other metals in the compound (most likely Co) also contribute to the total capacity obtained in the early stages of the electrode oxidation. When the battery is charged to higher voltages, the absorption edge position does not show significant overall changes. Surprisingly, the only exception is that of the Li0.0 sample; part of the main Ni absorption edge appears at slightly lower energies than Li0.2 while the summit of the absorption curve shifts in the opposite direction, a high voltage behavior that we have recently observed for other layered Ni-Mn compounds [27]. We ascribe this to a change in local structure.

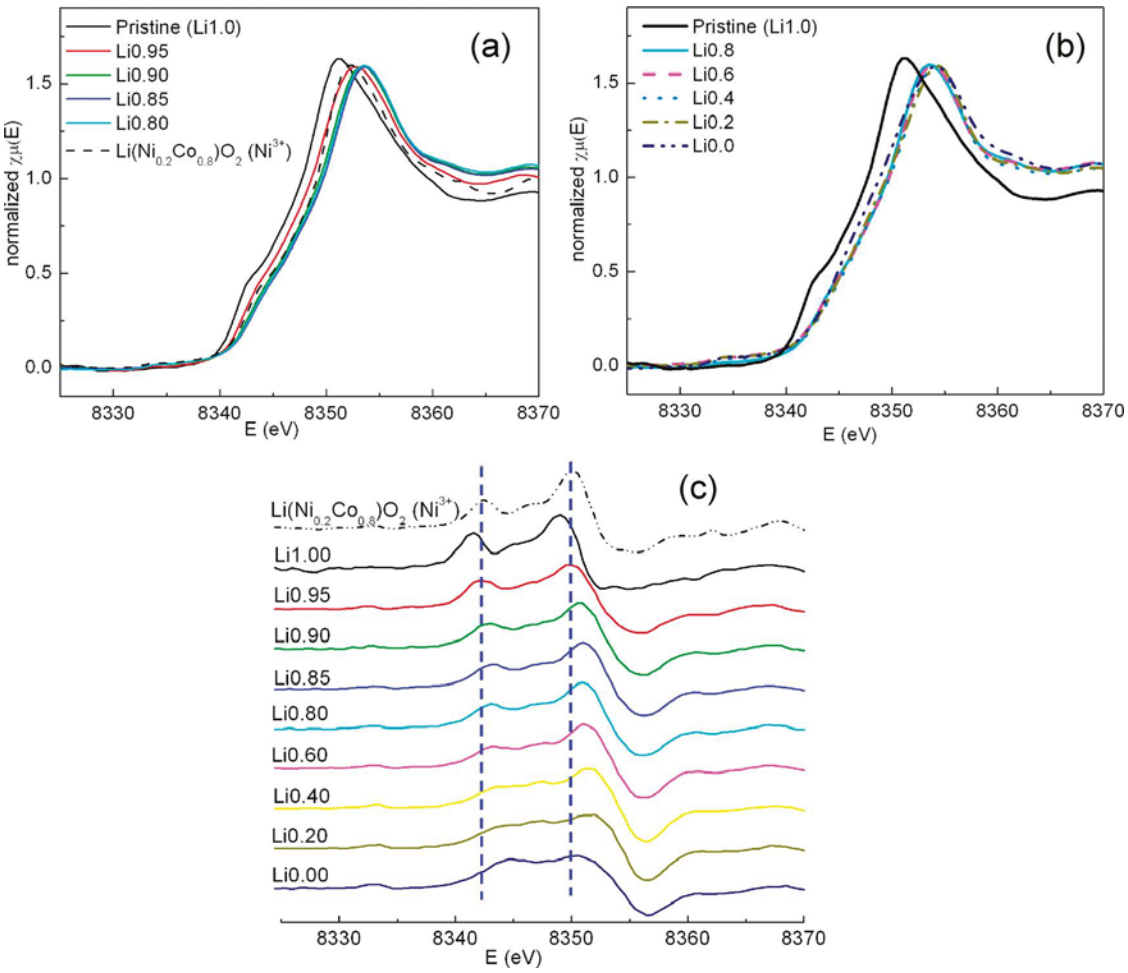

Figure 3.4. Normalized Ni K-edge XANES spectra of **90Co** at different states of charge, $Li_x[Ni_{0.05}Mn_{0.05}Co_{0.90}]O_2$ ("Li*x*"), during the first cycle in a battery; (a) data for x=1.0 to 0.8 and (b) data for x=0.8 to 0.0. (c) Stacked plot of the first derivative. The two dashed lines indicate the energy positions observed for sample Li0.85, and are provided as a guide to the eye. $Li(Ni_{0.2}Co_{0.8})O_2$ is also included as a Ni^{3+} reference.

The Mn K-edge does not show a rigid shift during the oxidation process (Figure 3.5), suggesting that its oxidation state is 4+ throughout. However, the spectra do exhibit visible changes in lineshape. Similar behavior has been reported for $Li_{1.2}Cr_{0.4}Mn_{0.4}O_2$ [28] and $Li(Ni_{1/3}Mn_{1/3}Co_{1/3})O_2$ [29-30], and is ascribed to structural changes in the local geometry of Mn due to lithium extraction, such as those associated to the formation of a the highly oxidized phase with O1 stacking.

Finally, the normalized Co K-edge XANES spectra of electrochemically oxidized **90Co** are shown in Figure 3.6. The absorption edge of Co in the samples at the very initial stages of lithium deintercalation (i.e., between Li1.00 and Li0.95) shows a very slight shift to higher energy, with no visible change in lineshape (Figure 3.6(a)), and, then, stays constant until 15% of the lithium is removed (Li0.85). Such behavior suggests that oxidation of some cobalt ions takes place once the extraction of lithium starts. When more than 15% of the lithium is extracted, a much clearer shift to higher energy, concomitant with an overall change of the spectrum, is seen (Figure 3.6(b)). These changes can be seen more clearly in the first derivative of the spectra plotted in Figure 3.6(c).

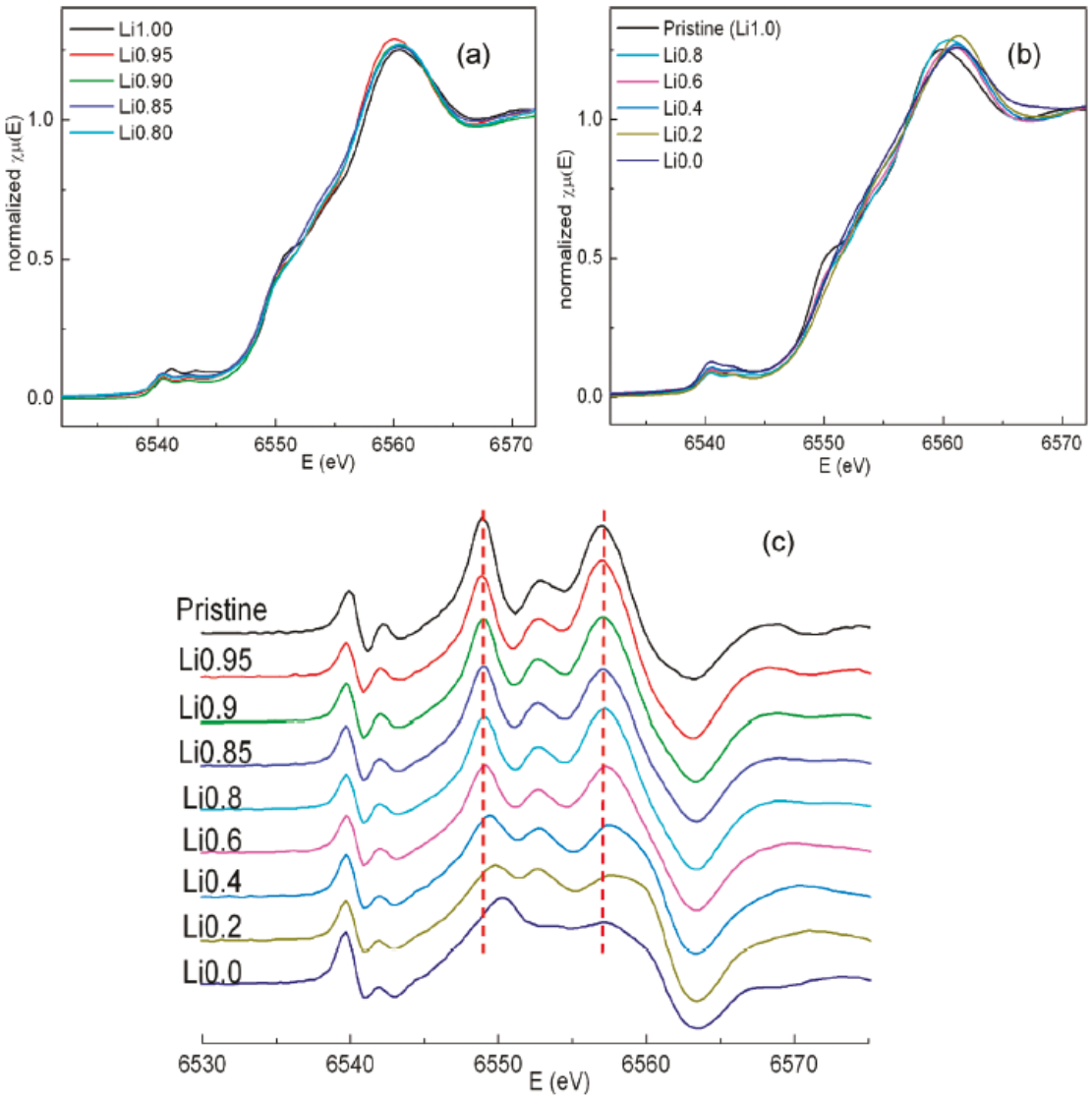

Figure 3.5. Normalized Mn K-edge XANES spectra of **90Co** at different states of charge, $Li_x[Ni_{0.05}Mn_{0.05}Co_{0.90}]O_2$ ("Li*x*"), during the first cycle in a battery; (a) x=1.0 to 0.8 and (b) x=0.8 to 0.0. (c) Stacked plot of the first derivative. The two dashed lines indicate the energy positions observed for pristine **90Co**, and are provided as a guide to the eye.

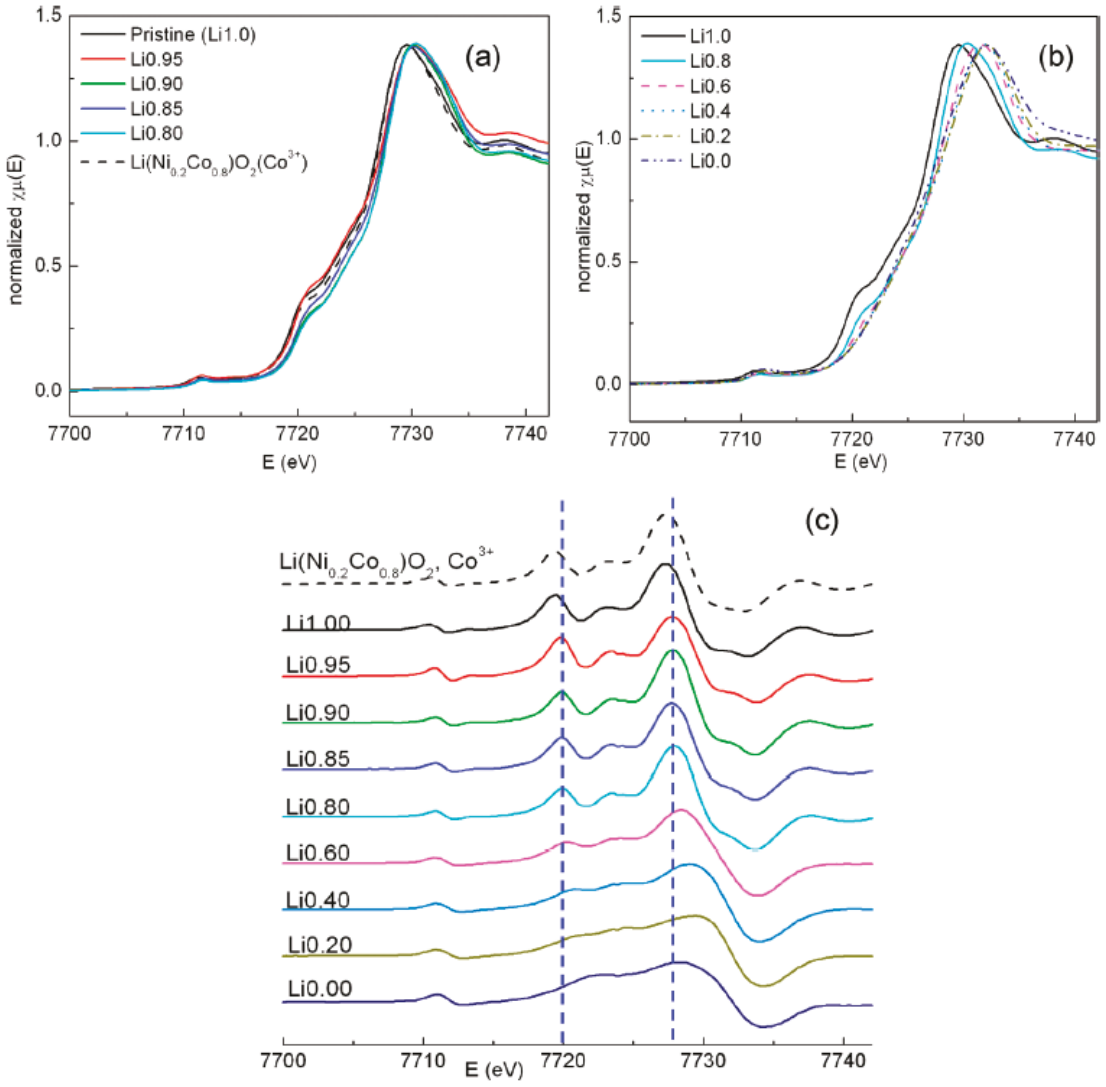

Figure 3.6. Normalized Co K-edge XANES spectra of **90Co** at different states of charge, $Li_x[Ni_{0.05}Mn_{0.05}Co_{0.90}]O_2$ ("Li*x*"), during the first charge; (a) *x*=1.0 to 0.8 and (b) *x*=0.8 to 0.0. (c) Stacked plot of the first derivative. The two dashed lines indicate the energy positions observed for sample Li0.85, and are provided as a guide to the eye. $Li(Ni_{0.2}Co_{0.8})O_2$ is included as a Co^{3+} reference compound.

In summary, the nickel centers play the major role in the charge compensation of the initial lithium extraction (Lix with $x \geq 0.85$). Nonetheless, there appears to be a competing process involving the onset of Co^{3+} oxidation at these voltages. We propose that when some Li in the vicinity of the Ni-Mn clusters are removed (see the NMR part for more detail discussion), Co^{3+} located nearby the Li vacancies may have lower oxidation potentials than the ones in the Co rich regions that are further away. This hypothesis is made based on a recent study on delithiated $LiCoO_2$ phases, in which density functional theory (DFT) calculations indicate an anisotropic charge distribution in the $LiCoO_2$ structure upon delithiation [31], where the charge densities are higher for Co in direct neighborhood of the Li vacancy than those further away. From Li0.8 up to full charged, Li0.0, the charge compensation mainly occurs through Co^{3+} oxidation.

3.3.4 ^{6}Li NMR Spectroscopy.

3.3.4.1 Pristine compound.

A zoom-in of the ^{6}Li MAS NMR spectrum of pristine **90Co** is shown in Figure 3.7(a). In addition to an intense resonance at 0 ppm, due to Li nearby only Co^{3+} diamagnetic ions, in $LiCoO_2$-like local environments, several distinct resonances at 400, 260, 140, -30, -56 and -86 ppm, similar to those previously reported for $Li[Ni_{0.02}Mn_{0.02}Co_{0.96}]O_2$ (**96Co**, Figure 3.7(a)) [14], can be seen. The large shifts of the other signals result from the Fermi contact (hyperfine) interaction between the Li and Ni/Mn paramagnetic ions, which is mediated through the bonds with oxygen [32]. The Fermi-contact shift is a measure of unpaired electron density transferred from the *d*

orbitals of Ni or/and Mn to the Li *s* orbital [33]. The higher the frequency (larger ppm), the greater the extent of electron transfer, and generally the broader the lineshape. In the ideal layered LiMO$_2$ (M = transition metal) structure, each Li^+ ion is surrounded by 12 transition-metal cations, 6 in the first cation coordination shell, forming 90° M–O–Li angles, and 6 in the second cation coordination shell, forming 180° M–O–Li angles (see inset of Figure 3.7(a)). The Fermi contact, and, therefore, the Li NMR shift, is dependent on the geometry of these interactions.

Due to the similarity of the **90Co** and **96Co** spectra, the same Ni/Mn cluster model (Figure 3.9(b)) that was previously used to analyze the **96Co** spectrum [14] is used here as a starting point. In this ideal model, Ni^{2+} and Mn^{4+} ions are located in each other's 1st cation coordination shell in the TM layer forming randomly distributed pairs that are surrounded by only Li and Co. These are termed Type A pairs in this work. Based on this assumption and previous work [34-36], the resonances in **90Co** spectrum can be assigned to Li located in different environments, as labeled in Figure 3.7(a) and Figure 3.9. In comparison to **96Co**, several of the resonances in the **90Co** spectrum, such as those at 260 and 140 ppm, have more complex line shapes containing additional shoulders or resonances that likely result from deviations from the local ordering predicted by this ideal cluster model. New environments may either arise from the existence of extended Ni-Mn clusters, instead of simple pairs, due to the higher Ni and Mn content in **90Co**, or from Li environments with additional Ni and/or Mn ion in their coordination sphere due to the close proximity of two pairs in the same or adjacent TM layers. These environments will generate signals at new shifts or shifts that can be similar to those

observed at high Ni and Mn dilution. For example, Li with one Mn^{4+} in its 2st coordination shell has a shift at around -56 ppm whereas Li with one Ni^{2+} in the 1st coordination shell and one Mn^{4+} in the 2nd coordination shell is associated to a -86 ppm shift. If all are present in a given lithium environment, the new resonance would appear at an overall shift of -56+ (-86) = -142 ppm, which is more distinct in the spectrum of **90Co** than in **96Co**. Another example is Li in environment with two Ni^{2+} ions in its the 2nd coordination shell, which would induce a total shift at around 280 ppm, since each Ni^{2+} in this environment induces a 140 ppm shift. An additional contribution to 280 pppm shoulder arises from the presence of isolated or Type B Mn^{4+} ions (see below for details). Some of the new environments, however, do not generate new resonances: for example, Li with one Mn^{4+} and one Ni^{2+} in its 1st coordination shell (in another TM layer, for example) gives resonance at 230 ppm (this results from the addition of a 260 ppm contribution from $(Mn^{4+})^{1st}$, and a -30ppm contribution from $(Ni^{2+})^{1st}$). Although this environment is already generated by the Ni/Mn pair, the probability that it occurs will increase at higher Ni/Mn concentrations. Consistent with this, the shoulder to lower frequencies of the 260 ppm resonance in the **90Co** spectrum in Figure 3.7(a), is more distinct than that observed in the **96Co** spectrum [14].

Another effect may come from the competing driving forces for clusters vs. disorder, the latter resulting in an increase in the entropy of the system particularly at the temperatures used to synthesize these materials. When Ni and Mn form type A pairs, the MnO_6 and NiO_6 octahedra share two edges, leading to a 90° Ni-O-Mn configuration that has been reported to induce a strong antiferromagnetic (AF) coupling between Ni^{2+} and

Mn^{4+} [37]. Such AF correlations can persist at room temperature, resulting in reduced time-averaged magnetic moments for both the Ni and Mn, and thus smaller spin density transfer to the lithium ions via the intervening oxygens. In contrast, when the MnO_6 and NiO_6 octahedra do not interact, the absence of AF coupling will lead to a larger value of the average magnetic moments and thus a larger Li shift. As a consequence, the magnitude of the shifts induced by an isolated Ni or Mn paramagnet is expected to be larger than from those in a Ni-Mn cluster. The existence of a shoulder at 160 ppm on the 140 ppm ^{6}Li resonance is considered to be the result of this effect; they are assigned to Ni^{2+} in the Li 2nd coordination shell in isolated or Type B pairs (160 ppm) and Type A pairs (140 ppm). Similarly, the contributions to the shoulder at 280 ppm and the resonance at 260 ppm arise from isolated and a clustered Mn^{4+} in its 1st coordination of Li shell, respectively. No fine structure is observed for the resonances at -30 and -56 ppm, corresponding to Li with one Ni^{2+} in the 1st coordination shell and one Mn^{4+} in the 2nd coordination shell, respectively, which could be simply be due to the fact that the differences in the shifts are too small, and the resonances too broad to allow any fine structures to be resolved. The fact that the 140 and 260 ppm resonances are more intense than the 160 and 280 ppm resonances indicates that more Ni^{2+} and Mn^{4+} ions are present in a cluster than are in an isolated form in this compound. The synthesis conditions (e.g. precursors, heating temperature and time, cooling rate) have an effect on the ratio of these two arrangements; the spectrum of a second **90Co** sample prepared using natural abundance $LiOH{\cdot}H_2O$ shows a more symmetric 140 ppm resonance without the 160 ppm shoulder (see Figure 3.8), implying an even stronger tendency of Ni^{2+} and Mn^{4+} to form

clusters in this sample. Slight changes in the distribution of resonances between different samples made by using the same nominal synthesis procedure were also noted in previous work on the 96Co sample [14], showing the high sensitivity of NMR experiment to small experimental variations. Note that the 140 ppm resonance could also arise from Li with one isolated Ni^{2+} in the 2^{nd} coordination shell and an additional Ni^{2+} in a NiMn Type A cluster in the 1^{st} coordination shell, which induces a small negative shift of -30 ppm. However, this "two Ni" theory is less plausible because the 140 ppm resonance is dominant in the spectrum of **96Co**, where the probability that Li has two Ni in the neighboring should be very small, no matter whether a clustered or a random model is considered. Figure 3.7(b) shows a Type B pair which represents a Ni-Mn pair where Ni and Mn are in each others 2^{nd} cation coordination shell. This pair will have similar magnetic interactions as in the isolated case, but will result in $(Ni_1)^{1st}(Mn_1)^{2nd}$ and $(Mn_1)^{1st}(Ni_1)^{2nd}$ resonances which will be difficult to resolve resonances from those from isolated ions in different layers. This pair will have considerably weaker Ni-Mn interactions but may be formed as the system is cooled from a more disordered state and the Ni-Mn start to cluster.

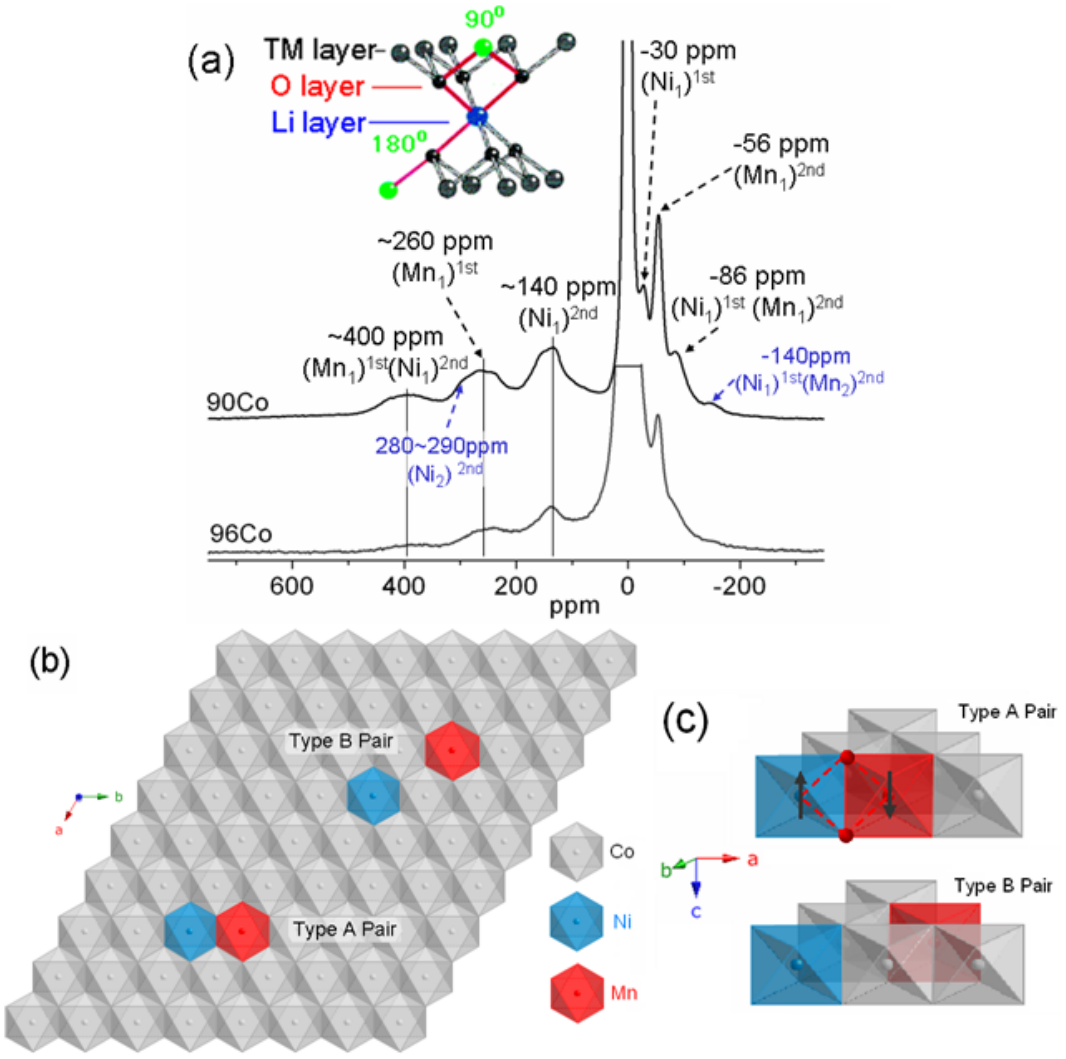

Figure 3.7. (a) ^{6}Li MAS NMR spectra of **90Co** (upper) and **96Co** (lower) acquired at 38 kHz. (Upper left inset): Arrangement of the 12 neighboring TM cations around a central lithium. Selected shifts and the corresponding assignments of the resonances to the Li local environments are indicated. $(Ni_{x1}Mn_{y1})^{1st}(Ni_{x2}Mn_{y2})^{2nd}$ represents the Ni and Mn composition of the two coordination shells for each lithium, where x and y indicate the Ni and Mn contents respectively. The other neighboring cations are all Co^{3+} and Li^{+}, and are omitted for clarity. The 0 ppm $(Co_6)^{1st}(Co)_6{}^{2nd}$ resonance has been truncated in both spectra so as to show the weaker, shifted resonances more clearly. (b) A schematic view of the two types of Ni/Mn pairs (type A and B, as proposed in the text) in the transition metal layers. Cations are represented by colored MO_6 octahedrons (M = Co (grey), Ni (blue) and Mn (red)), and oxygen atoms are omitted for clarity. (c) Illustration of the 90° AF coupling between the type A paired Ni and Mn ions occurs through the intervening oxygen atoms (red balls) (above). The absence of such interactions in type B pairs is shown as well (below).

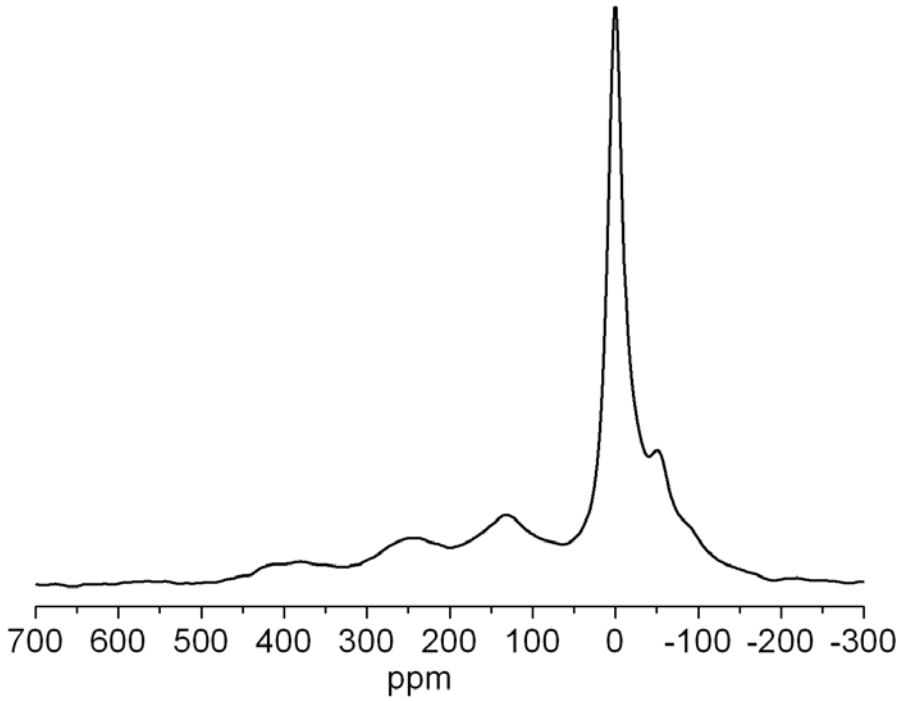

Figure 3.8. A ^{6}Li MAS NMR spectrum of a **90Co** pristine sample made with natural abundance $LiOH \cdot H_2O$, acquired at 4.7 T at a spinning speed of 38 kHz.

3.3.4.2 Ex situ study of charging.

The ^{6}Li MAS NMR results for delithiated **90Co** samples are divided in two groups: those up to Li0.80 are shown in Figure 3.9, whereas those corresponding to higher SOCs are depicted in Figure 3.10. Once Li ions are extracted, as shown in Figure 3.9(a), some general trends are observed. First, upon 10% of Li removal, a pronounced loss of intensity is observed for the 400 and 260 ppm resonances (see solid arrows in Figure 3.9(a)), which are assigned to the Li environments that contain at least one Mn^{4+} in the 1st coordination shell, labeled (1) in the scheme in Figure 3.9(b), indicating that these lithium ions are deintercalated. Extraction from these sites is likely to be driven by the strong Li^{+}-Mn^{4+} Coulombic repulsions，Mn^{4+} being the cation with the highest charge in the structure at this state of charge. While the environment giving rise to the resonance at 400 ppm also contains some nearby Ni ions that will be oxidized to charge-compensate any lithium extraction, this is not the case in the environment corresponding to the 260 ppm resonance which only contains Ni in its 3rd coordination shell. However, it still appears to be favorable to lose a Li^{+} from this environment, presumably due to the large Li^{+}-Mn^{4+} repulsions. It is also possible that some charge compensation occurs via the oxidation of some of the nearby cobalt centers, which could explain why some cobalt oxidation is observed by XANES at the early stages of oxidation.

Another significant decrease in intensity is observed for the resonance at -30 ppm, labeled (1) in Figure 3.9(b) as well, which is ascribed to lithium with Ni^{2+} in the 1st coordination shell. Since Ni^{2+} is the active redox species in the initial delithiation processes, it is not surprising that its oxidation is accompanied by the removal of lithium

in its vicinity. The intensity of the 140 ppm resonance, labeled (2) in Figure 3.9(b), which is assigned to lithium environments in the 2nd coordination shell of Ni^{2+} in a Type A pair, gradually decreases in intensity and shifts toward 100 ppm (see the spectra of Li0.95 and Li0.90 in Figure 3.9(a)). This is ascribed the oxidation of Ni^{2+} to Ni^{3+} since the shifts induced by Ni^{3+} are smaller in magnitude than those due to Ni^{2+}, due to its lower number of unpaired electrons in Ni^{3+} (two as opposed to one) [36]. Interestingly, the intensity of the 160 ppm peak, due to isolated or Type B Ni^{2+} in the 2nd coordination shell remains unchanged. Such observation implies that the lithium ions nearby clustered (Type A) nickel ions are somewhat easier to remove from the structure than the more separated ones. Similar behavior is seen in the **96Co** system (see Figure 3.10), in which the dominant 140 ppm peak loses intensity, uncovering a resonance at 160 ppm, which, initially, cannot be resolved. This is somewhat surprising, since in materials such as $Li[Ni_{0.5}Mn_{0.5}]O_2$, the oxidation potential of Ni^{2+} is even higher than that in $LiNiO_2$, where this is ascribed to the formation of unfavorable Mn^{4+}-Ni^{4+} Coulombic interactions on oxidation of Ni^{2+}.[38] (In $LiNiO_2$ the oxidation of the first Ni^{3+} ions forms only Ni^{4+}-Ni^{3+} interactions). This indicates that Ni-Mn clustering should result in a higher potential for Ni^{2+} oxidation. In contrast, our results suggest that it is the unfavorable Li^{+}-Mn^{4+} interaction that is dominant in controlling delithiation and that in type B or isolated systems, the Ni^{2+} is too far from a Mn^{4+} ion for this to be a relevant factor. Calculations, which may provide further insight into this process, are ongoing to test this hypothesis.

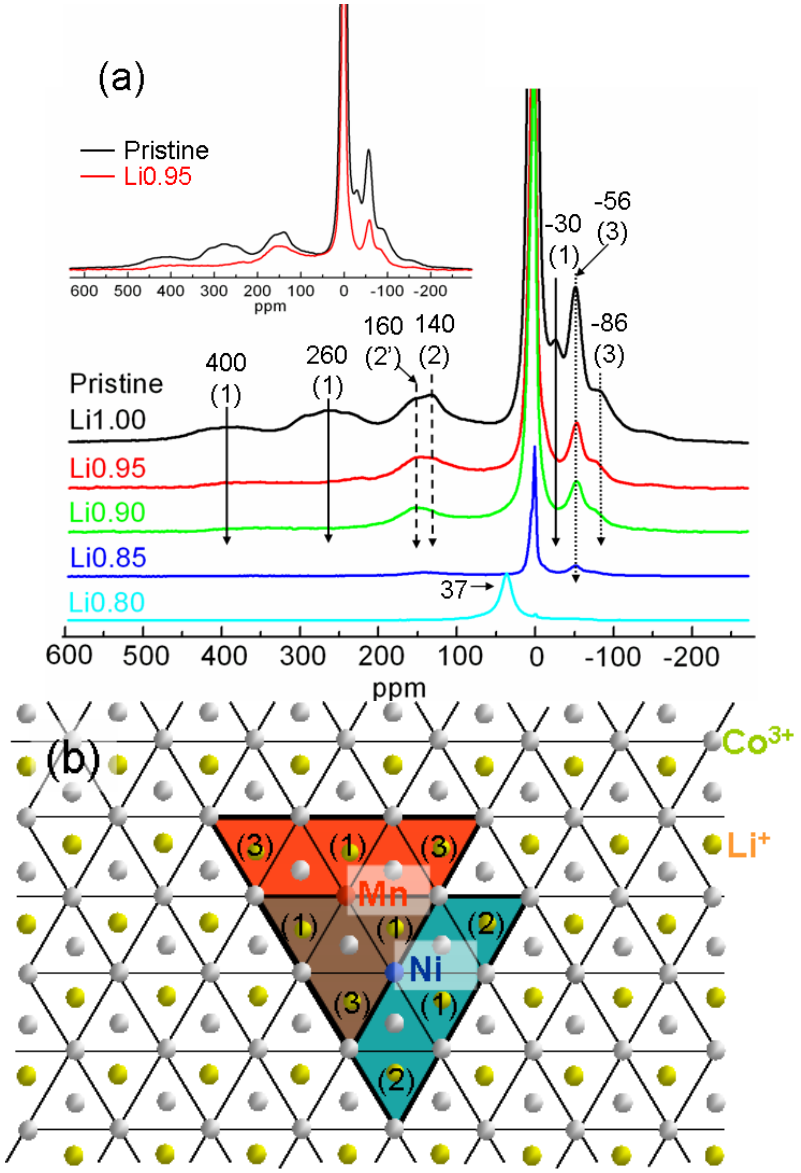

Figure 3.9. (a) Zoom of the ^{6}Li MAS NMR spectra of pristine and partially charged **90Co**, labeled as Lix ($1.00 \geq x \geq 0.80$) and normalized based on the acquisition number and sample mass. The inset shows the superposition of the spectra for Li1.00 and Li0.90. The shift values of major resonances are indicated. Solid, dashed and dotted arrows are provided as a guide to the eye so as to see the evolution of the resonances corresponding to different environments in the structure (see text). (b) Projection along the c axis of the schematic of the layered structure including two transition metal layers and the lithium layer (yellow balls) in between. The white balls denote Co^{3+} ions in the top (crossed by the solid lines) and bottom layer. The oxygen layers are omitted for clarity. One pair of Ni and Mn ions is shown to illustrate the major environments in which the Li are located. The numbers are used to assign the corresponding resonances in Figure 3.9 (a).

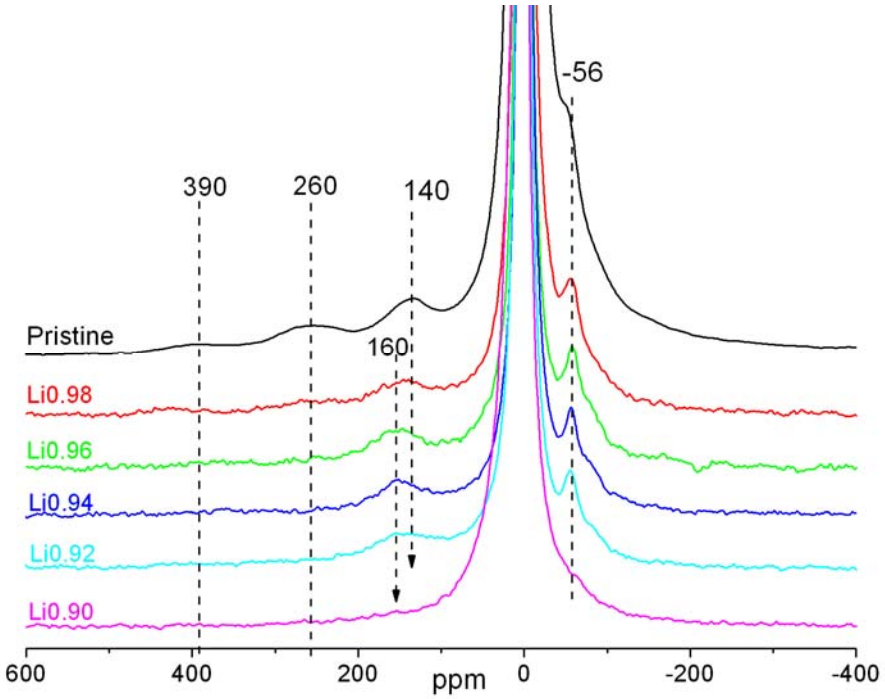

Figure 3.10. A zoom of the ^{6}Li MAS NMR spectra, normalized based on the acquisition number and sample mass, of pristine and partially charged $Li[Ni_{0.02}Mn_{0.02}Co_{0.96}]O_2$ (**96Co**) samples, labeled as Li*x* stand for $Li_x[Ni_{0.02}Mn_{0.02}Co_{0.96}]O_2$ ($1.00 \geq x \geq 0.90$).

The resonances at -56 and -86 ppm, labeled (3) in Figure 3.9(b), and assigned to local lithium environments with, at least, one Mn^{4+} ion in their 2nd coordination shell, remain until higher states of charge (Li0.9), but are largely removed by Li0.85. Unfavorable Li^{+}-Mn^{4+} interactions are not expected to be significant for 2nd coordination shell interactions so there is no strong driving force for Li removal from these sites. The weak -56 ppm resonance that persists at Li0.85 is assigned to Li ions nearby isolated Mn^{4+} ions and those in the Type A cluster that are furthest from Ni^{2+}. Careful examination of the resonance at -86 ppm, generated by environments that also contain one Ni^{2+} ion in the 1st coordination shell, reveals that it gradually shifts to slightly higher frequency and loses intensity upon lithium removal, until it eventually disappears at Li0.85. Such shift is again ascribed to Ni^{2+} to Ni^{3+} oxidation, while the intensity decrease is the result of the progressive extraction of lithium from these environments. The fact that some intensity can still be observed for the resonances at 160 and -86 ppm in Li0.90 is an indication that not all Ni is oxidized at this SOC, consistent with the XANES results above.

From Li0.90 to Li0.85, the 140/160 ppm region also loses intensity, suggesting that the removal of Li located in environments with $Ni^{2+/3+}$ in the 2nd coordination shell, happens at relatively high SOCs. $Ni^{2+/3+}$ has electron(s) in the e_g orbitals, which have been shown, in DFT calculations [39] to stabilize Li ions via 180° Li-O-Ni interactions, the occupied e_g orbitals pointing directly towards the p-orbitals of the intervening oxygen atom and transferring charge into these orbitals.

A pronounced decrease of the intensity of the 0 ppm signal, which is much more than expected from the small change in Li content, is observed between Li0.9 and Li0.85 (Figure 3.9(a)). Similar observations were reported for Li_xCoO_2 [15] and $Li_x[Co_{1-y}Mg_y]O_2$ [21]; the signal intensity was shown to drop a surprising 76% with the extraction of only 0.06 Li per Co in the former case. Such a phenomenon is characteristic of the formation Co^{4+} with localized electron holes, in a diamagnetic Co^{3+} lattice, and the loss of signal has been ascribed to the large Fermi-contact shifts induced by Co^{4+} (resulting in such large Fermi-contact shifts that the signals are no longer readily observed) [15]. However, since low-spin Co^{4+} ions contain only one unpaired electron (and should result in a smaller shift than for example seen for Mn^{4+}), we propose that the loss of signal is not directly due to the Co^{4+} ions, but arises due to electronic fluctuations as the system approaches an insulator-to-metal (MIT) transition. Upon initial oxidation of Co^{3+}, small polarons (holes) are created that are associated with Co^{4+}. As the system approaches the transition and the average separation between the polarons decrease, fluctuations of the electronic spins-states may occur which could result in significant relaxation of the ^7Li nuclei so that they are broadened beyond detection.

The set of well-resolved resonances at lower SOC is almost completely replaced by a single broad peak at positive shifts, e.g., at 37 ppm for Li0.80, when the sample is further oxidized (Figure 3.11(a)). In contrast, the metallic phase $Li_{0.75}CoO_2$ that is formed after the insulator to metallic transition that occurs upon Li extraction from $LiCoO_2$ gives rise to a resonance at 57 ppm [15]. The change to a metallic state, and the corresponding change in the mechanism of electron delocalization, brings about a

modification of the interaction between the Li nuclei and the unpaired electrons on the transition metals, and, therefore, of the mechanism that dominates the NMR shift. The resulting "Knight shift" is a measure of the density of states at the Fermi Level at the nucleus under observation. Since metallic compounds generally show Pauli paramagnetism, i.e., the magnetic susceptibility is temperature-independent, Knight shifts can be differentiated from Fermi contact shifts by their behavior upon a change in temperature; while the former remain more or less constant, the latter generally show a significant (generally Curie-Weiss) dependence on temperature. Another difference between both types of shifts is that Knight shifts typically show spin-lattice relaxation times (T_1) that are substantially longer than Fermi contact shifts, and that can be correlated with the Knight shift via the Korringa relationship [40]. In our particular case, the ^{7}Li shift observed in Li0.8 is small and has a long T_1 of 70 ms, whereas, for instance, the T_1 of the -56 ppm, hyperfine-shifted resonance observed in the same sample was only about 7 ms. The smaller absolute value of the shift in Li0.8 compared to $Li_{0.75}CoO_2$ is ascribed to the difference of the nature of the MIT. For $Li_{0.75}CoO_2$, this transition is of 1st order, involving two-phase coexistance, while solid solution behavior is observed for 90Co. Metallic domains form at lower SOCs (Li0.8 corresponds to the oxidation of only approximately 0.1 Co, assuming that Ni oxidation dominates initially) than in $Li_{0.75}CoO_2$, with fewer holes in the t_{2g} band, and thus smaller Knight shifts. The lack of two-phase behavior, as seen for Li_xCoO_2, strongly suggests that extent of localization of the metallic domains is initially constrained by the presence of Ni and Mn, in a situation that is similar to that reported in Mg-substituted $LiCoO_2$ [21].

Along with a loss of intensity, the peak at 37 ppm in Li0.80 moves to higher frequencies upon further Li removal until Li0.50. The shift towards higher frequency is associated with the increase in the concentration of charge carriers as electrons are removed from the conduction band [15]. The Li shifts for the Li0.6 and Li0.5 samples are similar to those of Li_xCoO_2 (Li0.60; δ 101 ppm and Li0.50; δ 105 ppm), confirming that Co oxidation is occurring in this electrochemical region,

After the maximum at 105 ppm for Li0.50, the Knight-shifted resonance moves back to lower frequency upon further Li deintercalation. Since no data is available in the literature for $LiCoO_2$ at these high states of charge, ^{6}Li MAS NMR measurements for Li_xCoO_2 with $x \leq 0.5$ were performed (Figure 3.11(b)). The decreased signal-to-noise ratio in these spectra is due to the shorter acquisition times used for these samples. It can be clearly seen that the Knight shifted resonances move to lower frequency (from 102 to 85 ppm) upon lithium extraction, mirroring the behavior of the doped samples, and indicating a reduction in the density of states at the Fermi level located at the Li s-orbital. Given that, according to the XRD results, Li0.50 is also the sample at which point the interlayer distance reaches the maximum, the evolution of this shift will be discussed in the framework of the changes in crystal, as well as the electronic structure. Figure 3.12 shows a simplified schematic diagram representing the electronic band structures in pristine and delithiated **90Co**. The narrow band formed from the Ni e_g orbitals is assumed to lie slightly higher in energy than that of Co t_{2g} band. (Note that both these bands will contain small contributions from the O 2*p* orbitials). Note that, since cobalt and nickel can, to some degree, be oxidized simultaneously, some overlap of these bands must occur,

which is similar to the situation that has been proposed in the $LiNi_{0.1}Co_{0.9}O_2$ system [25]. The majority of the O 2*p* states form a band located at lower energies. As Li is progressively removed up until Li0.50, the electrons are first removed from the Ni e_g band, and, then, from Co t_{2g} band. The Fermi level (E_f) consequently shifts to lower energy. The system goes through a solid solution process and neither the crystal nor the electronic band structure change significantly. The density of state (DOS) at E_f increases as E_f shifts to lower energy, causing an increase in the Knight shift from around 40 to 100 ppm (Figure 3.12(a)-(b)). As more Li is removed, the overlap between Co and O orbitals, and, therefore, the covalency of the bond increases [41-42]. This is a result of the increase in the oxidation state of Co, which results in the Co bands dropping in energy, enabling a larger overlap with the O 2p bands. When more than 0.5 Li per formula unit is extracted, this effect starts to dominate. Indeed, increased hybridization between the Co 3d and the O 2p states in delithiated Li_xCoO_2 phases when $x<0.5$ has been very recently reported [31, 43]. At this point, the Co 3d band gets broader (due to increased overlap) and the DOS at E_f decreases (Figure 3.12(c)-(d)). Increased covalency of the Co-O bonds also weakens the Li-O overlap, which makes the Li-O bonds more ionic. Furthermore, when electrons are removed from Co-O hybrid states to compensate the charge loss associated with delithiation, the charge compensation occurs by inducing holes at the oxygen bands, formally decreasing their charge, which will weaken the spin transfer to lithium.

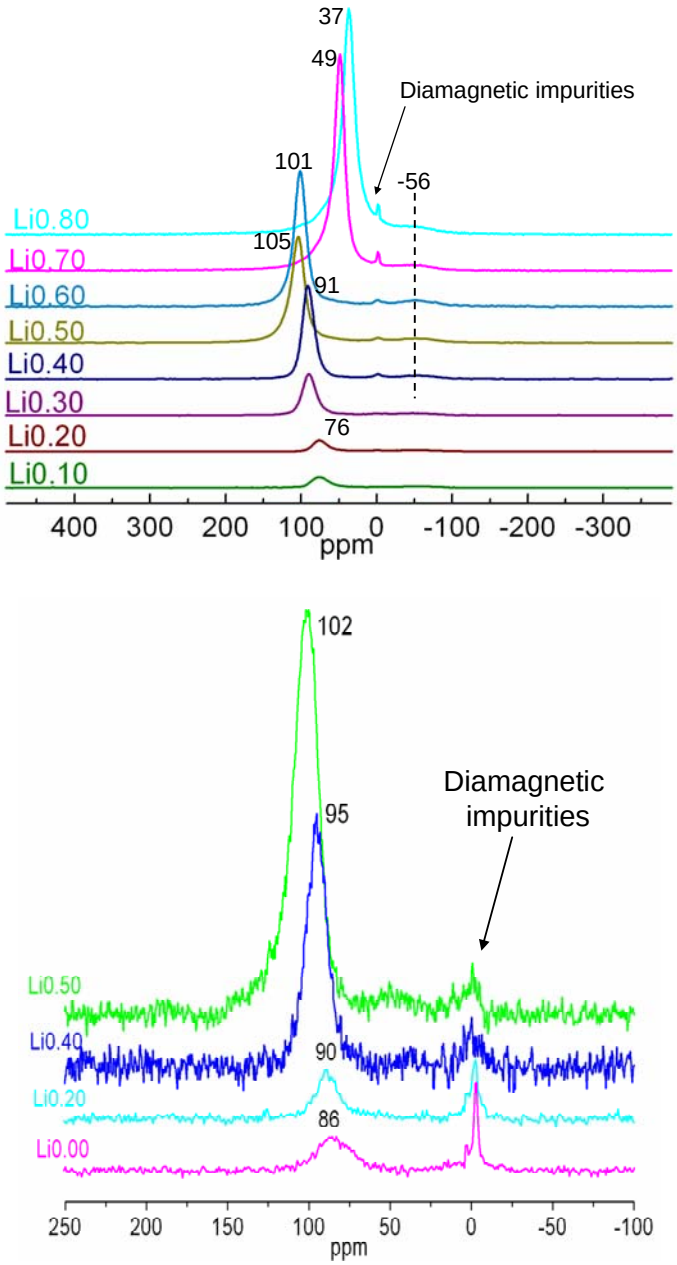

Figure 3.11. ^{6}Li MAS NMR spectra for (a) **90Co** charged to $x \leq 0.80$ in samples Lix, and (b) Li_xCoO_2 with $x \geq$ Li0.50. The isotropic resonances are marked, together with the peak due to the presence of diamagnetic impurities due to unwashed salts of the battery electrolyte and the passivation layer on the electrode.

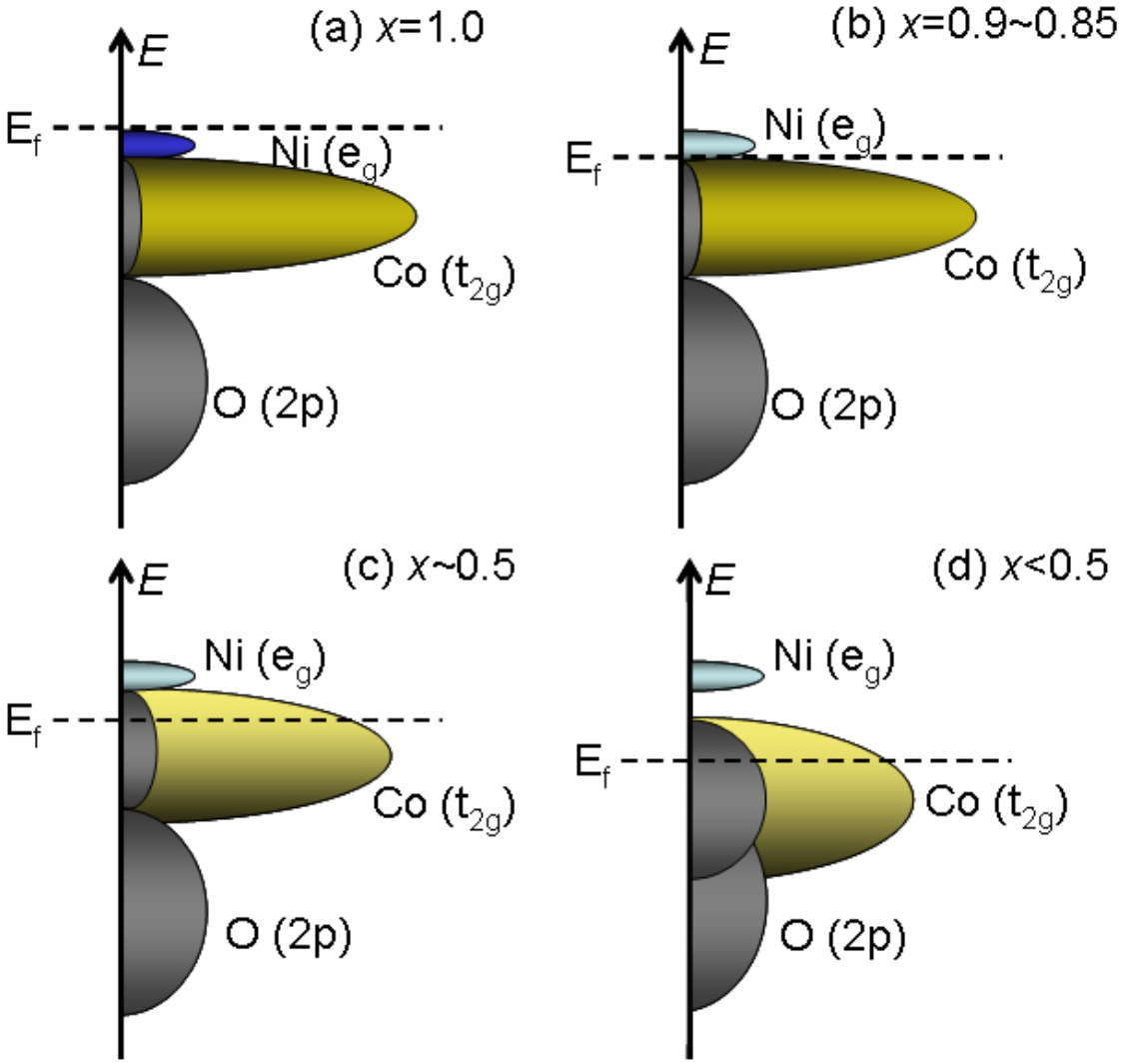

Figure 3.12. A schematic illustration of the band structure diagram showing the changing of Fermi level (E_f) and band structures of the **90Co** phase upon removal of different amount of Li. *x* indicates the remaining amount of Li in the structure. The e_g band of Ni, t_{2g} band of Co and 2p band of O are represented with blue, yellow and grey respectively, and the use of lighter colors (blue and yellow, for Ni and Co respectively) is an indication of the reduced electron density in the corresponding band upon delithiation.

3.4 Conclusions

This study shows the results of electrochemical, *in situ* XRD, *ex situ* XANES and ^{6}Li MAS NMR experiments performed to investigate the evolution of the structure and cation ordering of $Li[Ni_{0.05}Mn_{0.05}Co_{0.90}]O_2$ (**90Co**) upon lithium deintercalation. Two types of Ni-Mn pairs are proposed when exploring the Li local environment in the structure of pristine **90Co**. As Li is removed from the structure for $1.0 \geq x \geq 0.85$ (in $Li_x[Ni_{0.05}Mn_{0.05}Co_{0.90}]O_2$, Li*x*), the Li ions in the 1st coordination shell of the Mn^{4+} and/or Ni^{2+} ions are extracted first, the former being ascribed to the large Coulombic repulsion between Mn^{4+} and Li^{+},. Li ions in the 1st coordination shell of the electrochemically active Ni^{2+} are also removed in this charging regime. Li in the 2nd coordination shell of Ni are stabilized by the electrons in Ni^{2+} and Ni^{3+} e_g orbitals and removed at a later stage. Li removal from the 2nd coordination shell of Mn^{4+}, especially for ions distant from Ni, is more difficult. It also appears that the Co^{3+} nearby Mn^{4+} is not readily oxidized, presumably again because of the formation of unfavorable Co^{4+}-Mn^{4+} interactions, particularly before the insulator-to-metal transition. At these SOCs, both Ni^{2+} and to a lesser degree Co^{3+} are electrochemically active species. Evidence for the oxidation of some of the Ni^{2+} to Ni^{4+} via Ni^{3+} is seen. When 15% of the Li is extracted, features characteristic of the formation of Co^{4+} with localized spins are observed. Metallic behavior is observed at $x \geq 0.80$, as shown by the observation of a Knight shifted resonance in the Li NMR spectrum. However, this insulator-to-metal transition does not result in a phase transition likely due to the presence of Ni-Mn clusters perturbing long-range electronic delocalization. On charging for $0.8 > x \geq 0.50$, the interlayer spacing

keeps increasing, and the Knight shifted resonance gradually moves to higher frequency. The electrochemical profile of **90Co** shows a feature at Li0.50 similar to that observed in $LiCoO_2$, which is a result of lithium ordering at this SOC. Above $x = 05$, the NMR results for **90Co** are similar to those seen for Li_xCoO_2 system, the increased Co-O orbital hybridization (bonding) affecting the band structure, and thus the NMR behavior. Finally, when the battery is charged to even higher voltage (*ca.* 4.6 V), almost all the lithium ions are removed from the structure and the O3 to O1 phase transition occurs.

References

1. Mizushima, K., P.C. Jones, P.J. Wiseman, and J.B. Goodenough, Li_xCoO_2(0<x<-1): A new cathode material for batteries of high energy density. *Mater. Res. Bull.*, 1980. **15**(6): p. 783.

2. Dahn, J.R., U. von Sacken, and C.A. Michal, Structure and electrochemistry of $Li_{1\pm y}NiO_2$ and a new Li_2NiO_2 phase withe the $Ni(OH)_2$ structure *Solid State Ionics*, 1990. **44**(1-2): p. 87-97.

3. Capitaine, F., P. Gravereau, and C. Delmas, A new variety of $LiMnO_2$ with a layered structure. *Solid State Ionics*, 1996. **89**: p. 197-202.

4. De Picciotto, L.A., M.M. Thackeray, and G. Pistoia, An electrochemical study of the systems $Li_{1\pm x}V_2O_4$ and $Li_{1-x}VO_2$ (0<=x<=1). *Solid State Ionics*, 1988. **28-30**(Part 2): p. 1364-1370.

5. Saadoune, I. and C. Delmas, $LiNi_{1-y}Co_yO_2$ positive electrode materials: relationships between the structure, physical properties and electrochemical behaviour. *J. Mater. Chem.*, 1996. **6**: p. 193-199.

6. Rossen, E., C.D.W. Jones, and J.R. Dahn, Structure and electrochemistry of $Li_xMn_yNi_{1-y}O_2$. *Solid State Ionics*, 1992. **57**(3-4): p. 311-318.

7. Lu, Z., D.D. MacNeil, and J.R. Dahn, Layered $Li[Ni_xCo_{1-2x}Mn_x]O_2$ Cathode Materials for Lithium Ion Batteries. *Electrochem. Solid-St. Lett.*, 2001. **4**(12): p. A200-A203.

8. Ohzuku, T. and Y. Makimura, Layered Lithium Insertion Material of $LiCo_{1/3}Ni_{1/3}Mn_{1/3}O_2$ for Lithium-Ion Batteries. *Chem. Lett.*, 2001: p. 642-643.

9. Ohzuku, T. and Y. Makimura, Layered Lithium Insertion Material of $LiNi_{1/2}Mn_{1/2}O_2$: A Possible Alternative to $LiCoO_2$ for Advanced Lithium-Ion Batteries. *Chem. Lett.*, 2001: p. 744-745.

10. Kang, K., Y.S. Meng, J. Bréger, C.P. Grey, and G. Ceder, Electrodes with High Power and High Capacity for Rechargeable Lithium Batteries. *Science*, 2006. **311**: p. 977-980.

11. Bréger, J., K. Kang, J. Cabana, G. Ceder, and C.P. Grey, NMR, PDF and RMC study of the positive electrode material $Li(Ni_{0.5}Mn_{0.5})O_2$ synthesized by ion-exchage methods. *J. Mater. Chem.*, 2007. **17**: p. 3167-3174.

12. Bréger, J., N. Dupré, P.J. Chupas, P.L. Lee, T. Proffen, J.B. Parise, and C.P. Grey, Short- and Long-Range Order in the Positive Electrode Material, $Li(NiMn)_{0.5}O_2$:

A Joint X-ray and Neutron Diffraction Pair Distribution Function Analysis and NMR Study. *J. Am. Chem. Soc.*, 2005. **127**: p. 7529-7537.

13. Bréger, J., Y.S. Meng, Y. Hinuma, S. Kumar, K. Kang, Y. Shao-Horn, G. Ceder, and C.P. Grey, Effect of High Voltage on the Structure and Electrochemistry of $LiNi_{0.5}Mn_{0.5}O_2$: A Joint Experimental and Theoretical Study. *Chem. Mater.*, 2006. **18**: p. 4768-4781.

14. Zeng, D., J. Cabana, J. Bréger, W.-S. Yoon, and C.P. Grey, Cation Ordering in $Li[Ni_xMn_xCo_{(1-2x)}]O_2$ Layered Cathode Materials: A Nuclear Magnetic Resonance (NMR), Pair Distribution Function, X-ray Absorption Spectroscopy, and Electrochemical Study. *Chem. Mater.*, 2007. **19**(25): p. 6277-6289.

15. Ménétrier, M., I. Saadoune, S. Levasseur, and C. Delmas, The insulator-metal transition upon lithium deintercalation from $LiCoO_2$: electronic properties and ^7Li NMR study. *J. Mater. Chem.*, 1999. **9**: p. 1135-1140.

16. Morcrette, M., Y. Chabre, G. Vaughan, G. Amatucci, J.-B. Leriche, S. Patous, C. Masquelier, and J.-M. Tarascon, In situ X-ray diffraction techniques as a powerful tool to study battery electrode materials. *Electrochimica Acta*, 2002. **47**: p. 3137-3149.

17. MacNeil, D.D., Z. Lu, and J.R. Dahn, Structure and electrochemistry of $Li[Ni_xCo_{1-2x}Mn_x]O_2$ ($0 <= x <= 1/2$). *J. Electrochem. Soc.*, 2002. **149**(10): p. A1332-A1336.

18. Reimers, J.N. and J.R. Dahn, Electrochemical and *In situ* X-Ray Diffraction Studies of Lithium Intercalation in Li_xCoO_2. *J. Electrochem. Soc.*, 1992. **139**(8): p. 2091-2097.

19. Amatucci, G.G., J.-M. Tarascon, and L.C. Klein, CoO_2, The End Memeber of the Li_xCoO_2 Solid Solution. *J. Electrochem. Soc.*, 1996. **143**(3): p. 1114-1123.

20. Fouassier, C., C. Delmas, and P. Hagenmuller, Evolution structurale et proprietes physiques des phases A_xMO_2 (A = Na, K; M = Cr, Mn, Co) ($x <= 1$). *Mater. Res. Bull.* **10**(6): p. 443-449.

21. Levasseur, S., M. Ménétrier, and C. Delmas, On the $Li_xCo_{1-y}Mg_yO_2$ system upon deintercalation: electrochemical, electronic properties and Li-7 MAS NMR studies. *J. Power Sources*, 2002. **112**(2): p. 419-427.

22. Yang, X.Q., J. McBreen, W.S. Yoon, and C.P. Grey, Crystal structure changes of $LiMn_{0.5}Ni_{0.5}O_2$ cathode materials during charge and discharge studied by synchrotron based in situ XRD. *Electrochem. Commun.*, 2002. **4**(8): p. 649-654.

23. Yoon, W.-S., K.Y. Chung, J. McBreen, and X.-Q. Yang, A comparative study on structural changes of $LiCo_{1/3}Ni_{1/3}Mn_{1/3}O_2$ and $LiNi_{0.8}Co_{0.15}Al_{0.05}O_2$ during first charge using in situ XRD. *Electrochem. Commun.*, 2006. **8**(8): p. 1257-1262.

24. Waki, S., K. Dokko, T. Itoh, M. Nishizawa, T. Abe, and I. Uchida, High-Speed voltammetry of Mn-doped $LiCoO_2$ using a microelectrode technique. *J. Solid State Electrochem.*, 2000. **4**: p. 205-209.

25. Saadoune, I., M. Ménétrier, and C. Delmas, Redox processes in $Li_xNi_{1-y}Co_yO_2$ cobalt-rich phases. *J. Mater. Chem.*, 1997. **7**: p. 2505-2511.

26. Levasseur, S., M. Menetrier, and C. Delmas, On the dual effect of Mg doping in $LiCoO_2$ and $Li_{1+\delta}CoO_2$: Structural, electronic properties, and Li-7 MAS NMR studies. *Chem. Mater.*, 2002. **14**(8): p. 3584-3590.

27. Jiang, M., B. Key, Y.S. Meng, and C.P. Grey, Electrochemical and Structural Study of Li-excess Materials $Li[Li_{1/9}Ni_{1/3}Mn_{5/9}]O_2$. *Chem. Mater.*, 2009. **21**(13): p. 2733-2745.

28. Yoon, W.-S., Y. Paik, X.-Q. Yang, M. Balasubramanian, J. McBreen, and C.P. Grey, Investigation of the Local Structure of the $LiNi_{0.5}Mn_{0.5}O_2$ Cathode Material during Electrochemical Cycling by X-Ray Absorption and NMR Spectroscopy. *Electrochem. Solid-St. Lett.*, 2002. **5**(11): p. A263-A266.

29. Yoon, W.-S., M. Balasubramanian, K.Y. Chung, X.-Q. Yang, J. McBreen, C.P. Grey, and D.A. Fischer, Investigation of the Charge Compensation Mechanism on the Electrochemically Li-Ion Deintercalated $Li_{1-x}Co_{1/3}Ni_{1/3}Mn_{1/3}O_2$ Electrode System by Combination of Soft and Hard X-ray Absorption Spectroscopy. *J. Am. Chem. Soc.*, 2005. **127**: p. 17479-17487.

30. Tsai, Y.W., B.J. Hwang, G. Ceder, H.S. Sheu, D.G. Liu, and J.F. Lee, In-Situ X-ray Absorption Spectroscopic Study on Variation of Electronic Transitions and Local Structure of $LiNi_{1/3}Co_{1/3}Mn_{1/3}O_2$ Cathode Material during Electrochemical Cycling. *Chem. Mater.*, 2005. **17**: p. 3191-3199.

31. Laubach, S., S. Laubach, P.C. Schmidt, D. Ensling, S. Schmid, W. Jaegermann, A. ThiBen, K. Nikolowski, and H. Ehrenberg, Changes in the crystal and electronic structure of $LiCoO_2$ and $LiNiO_2$ upon Li intercalation and de-intercalation. *Phys. Chem. Chem. Phys.*, 2009. **11**: p. 3278-3289.

32. Grey, C.P. and N. Dupré, NMR Studies of Cathode Materials for Lithium-Ion Rechargeable Batteries. *Chem. Rev.*, 2004. **104**: p. 4493-4512.

33. Lee, Y.J., F. Wang, and C.P. Grey, ^6Li and ^7Li MAS NMR Studies of Lithium Manganate Cathode Materials. *J. Am. Chem. Soc.*, 1998. **120**: p. 12601-12613.

34. Carlier, D., M. Ménétrier, C.P. Grey, C. Delmas, and G. Ceder, Understanding the NMR shifts in paramagnetic transition metal oxides using density functional theory calculations. *Phys. Rev. B*, 2003. **67**: p. 174103.

35. Pan, C., Y.J. Lee, B. Ammundsen, and C.P. Grey, ^{6}Li MAS NMR Studies of the Local Structure and Electrochemical Properties of Cr-doped Lithium Manganese and Lithium Cobalt Oxide Cathode Materials for Lithium-Ion Batteries. *Chem. Mater.*, 2002. **14**: p. 2289-2299.

36. Carlier, D., K. Kang, G. Ceder, W.S. Yoon, and C.P. Grey. *^{6}Li MAS NMR Study of Lithium Layered Oxides Containing Ni^{2+} Ions: Experiments and DFT Calculations*. in *203rd Meeting of the Electrochemical Society (ECS)*. 2003. Paris.

37. Chernova, N.A., M. Ma, J. Xiao, M.S. Whittingham, M. Stanley, J. Bréger, and C.P. Grey, Layered $Li_xNi_yMn_yCo_{1-2y}O_2$ Cathodes for Lithium Ion Batteries: Understanding Local Structure via Magnetic Properties. *Chem. Mater.*, 2007. **19**: p. 4682-4693.

38. Reed, J. and G. Ceder, Charge, potential, and phase stability of layered $Li(Ni_{0.5}Mn_{0.5})O_2$. *Electrochem. Solid State Lett.*, 2002. **5**(7): p. A145-A148.

39. Dompablo, M.E.A.y.d., C. Marianetti, A.V.d. Ven, and G. Ceder, Jahn-Teller mediated ordering in layered Li_xMO_2 compounds. *Phys. Rev. B*, 2001. **63**: p. 144107.

40. Slichter, C.P., *Principles of Magnetic Resonance*. Springer Series in Solid-State Sciences 1. 1990, New York: Springer-Verlag.

41. Graetz, J., A. Hightower, C.C. Ahn, R. Yazami, P. Rez, and B. Fultz, Electronic structure of chemically-delithiated $LiCoO_2$ studied by electron energy-loss spectrometry. *J. Phys. Chem. B*, 2002. **106**(6): p. 1286-1289.

42. Hwang, B.J., Y.W. Tsai, D. Carlier, and G. Ceder, A Combined Computational/Experimental Study on $LiNi_{1/3}Co_{1/3}Mn_{1/3}O_2$. *Chem. Mater.*, 2003. **15**: p. 3676-3682.

43. Dahéron, L., R. Dedryvere, H. Martinez, M. Ménétrier, C. Denage, C. Delmas, and D. Gonbeau, Electron Transfer Mechanisms upon Lithium Deintercalation from $LiCoO_2$ to CoO_2 Investigated by XPS. *Chem. Mater.*, 2008. **20**: p. 583-590.

Chapter 4 Study of the Structural Changes upon Reversible Electrochemical Lithium Insertion in Copper Based Layered Oxysulfides

4.1 Introduction

Material with structures that are capable of lithium insertion/extrusion can function as electrodes in lithium ion batteries (LIBs) system. Nowadays, improving the properties of existing materials or looking for new materials with novel structures are largely motivated by the increase of the technological demands in the LIB market. Most of the positive electrode materials used in today's rechargeable lithium batteries operate by intercalation mechanisms. The intercalation compounds, such as layered $LiCoO_2$, spinel type $LiMn_2O_4$, olivine type $LiFePO_4$, and their doped variants, have one (or more) redox center (often the 3d transition metals) that function as the charge reservoir and a stable framework structure that is capable of reversible lithium intercalation. However, there exist intrinsic capacity limitations as lithium can only be inserted into the vacant sites in the framework structure. The available charge in these systems is limited by the amount and the valence changes of the redox species, e.g., often only one electron per transition metal cation is available. In contrast, conversion or displacement reactions offer the possibility in utilizing multiple electrons of the transition metal cations since they both involve Li-electrochemical driven fully reduction of the transition metals to the

metallic state, and thus, a much larger capacity can be achieved. The conversion reaction is often associated with 3d transition metal binary compounds M_xX_y (M = Fe, Co, Cu etc. and X = F, O, S, N, P etc.). Upon lithiation, the full reduced transition metals are embedded in Li_nX matrices and form the metallic particle/Li_nX nano-composites, the redox reactions are repetitive, and after an initial capacity loss in the 1st cycle, good capacity retention can be achieved. As for the concept of displacement reactions, they have been applied in describing the reactions of some the Cu-Sn and Cu-Sb intermetallic alloys that can function as the negative electrode materials in LIBs [1-3]. The term has been re-introduced to describe reactions that occur in some positive electrode materials for rechargeable LIBs by Tarascon et al. only very recently [4]. This type of reaction, also termed as combination displacement/intercalation (CDI) reactions, has features of both the intercalation and conversion reactions. Namely, materials operating by this mechanism usually have invariant parts in the structure, but the mechanism also involves Li-driven metal extrusion/injection processes. So far, besides $Ag_2V_4O_{11}$ that has been successfully applied in primary lithium batteries for implantable medical devices [5-7], only a few systems operated by this mechanism have been examined as positive electrode materials for rechargeable lithium batteries, and they are all copper based materials [4, 8-11].

$Cu_{2.33}V_4O_{11}$ is the first successfully developed positive electrode material for rechargeable LIBs that operates by the CDI mechanism. It has a layered structure consisted of $[V_4O_{11}]_n$ layers, and Cu cations(Cu^+ and Cu^{2+}) distributed in between the layers. When it electrochemically reacts with Li, a reversible Li-driven process leading to

the growth and disappearance of Cu metal dendrites with a concomitant decomposition and recrystallization of the initial phase is observed, and it shows a sustainable reversible capacity of over 250 mAh/g at a voltage around 2.7 V [4]. Lately, a systematic study on several other Cu-V-O and Cu-V-S systems has revealed that the dimensionality and flexibility of the framework structure, and the Cu mobility in the material, play important roles in governing the CDI reactions [10]. As the Cu is known to be mobile in the spinel structure, a Cu-based thiospinel, $CuTi_2S_4$, has also been examined regarding its electrochemical reactivity toward Li [8]. As $CuTi_2S_4$ is a cation mixed-valance system ($Cu^{+}Ti^{3+}Ti^{4+}\ S_4^{2-}$), another Cu-based thiospinels, $CuCr_2S_4$, an anion mixed system ($Cu^{+}Cr_2^{3+}S_3^{2-}S^{-\bullet}$), was chosen and studied for comparison [8-9]. The results suggest that the $CuTi_2S_4$ system goes through a CDI reaction in the initial stage of the first discharge (not beyond 2 Li insertion), where Li intercalation into the Ti_2S_4 framework is associated with fully reduced Cu extrusion and reduction of Ti^{4+} to Ti^{3+}. This process is fully reversible upon re-oxidation (charging). As for $CuCr_2S_4$, its electrochemical reactivity towards Li initially also occurs through a CDI reaction, with the reduction of Cu and $S^{-\bullet}$, but Cu cannot be totally reduced and extruded (the end of the discharge phase is $Li_{1.75}Cu_{0.25}Cr_2S_4$), and the reaction is partially reversible. The differences between these two thiospinels have been ascribed to the larger Cu mobility in $CuTi_2S_4$ than in $CuCr_2S_4$ [8]. Another class of compounds that shows the CDI reactions towards Li is a novel class of oxysulfides, $Sr_2MnO_2Cu_{2m-\delta}S_{m+1}$ (m = 1, 2 and 3, $\delta \sim 0.5$) [12-13]. These materials consist of alternating Perovskite-type [Sr_2MnO_2] sheets and various thicknesses of antifluorite-type [Cu_2S] sheets. Previous studies have shown that Li can be both

chemically [14] and electrochemically [11] inserted into the structure, and these reactions are reversible. The neutron diffraction data for the chemical lithiated phases [14] and Li NMR data for the electrochemical lithiated phases [11] have confirmed that the inserted Li ions, in both cases, replace the Cu in the MS_4 tetrahedral sites in the framework structure, and the elemental Cu is extruded. The electrochemical capacity of the oxysulfides is proportional to the thickness of the sulfide layers where the m=3 member has the largest capacity, and this indicate that the Perovskite-type oxide layers seem inert in the electrochemical reactions. The cycleability of these materials in LIBs has been tested within a voltage window of 1.1 to 2.7 V, and the results have shown that the capacity retentions of these oxysulfides largely depend on the thickness of the Cu_2S layer in each member as well, and higher capacity retentions were observed for the ones with thinner sulfide layers. This indicates that the rigid Perovskite-type [Sr_2MnO_2] layers in the structure, although seem with no capacity contribution, provide the structural stability and are beneficial to the cycleability.

Understanding the involved electrochemical processes from a fundamental point of view can provide valuable insight in recognizing the structure-properties relationship of the material and help design or search for new functional systems with desired performance features. The studies summarized above have provided valuable information in understanding the CDI reactions and some of the crucial parameters in determining the electrochemical performance. However, there still remain pieces of the puzzle to fully understand the CDI mechanism, and clearly more studies are needed to provide further information. At this point, not only exploring the CDI reactions to other systems, but

conducting further studies on the known systems, will be very useful. To pursue a deeper understanding of the CDI reactions in the oxysulfide systems, a representative member, $Sr_2MnO_2Cu_{4-\delta}S_3$ (when m = 2), which has a double thickness of the $[Cu_2S]$ layered motif in the structure (crystal structure shown in Figure 4.1, denoted as MnCu(II) in the following), has been chosen as a representative case and its electrochemical behavior as positive electrode in LIBs and the structural changes during the (dis)charge processes are investigated intensively. In this paper, the electrochemical behavior of MnCu(II) will be discussed in detail first, and the crystal structural changes during (dis)charge will then be evaluated by *in situ* XRD data. After that, the *ex situ* XANES data on Cu, Mn and S will be provided to examine the changes of their oxidation states and some local environment variations, and finally, the *ex situ* ^{7}Li NMR results will be presented to analyze the changes of the Li surrounding environments. The overall information regarding each electrochemical process, such as the phase transitions and involved redox species etc, will be summarized at the end.

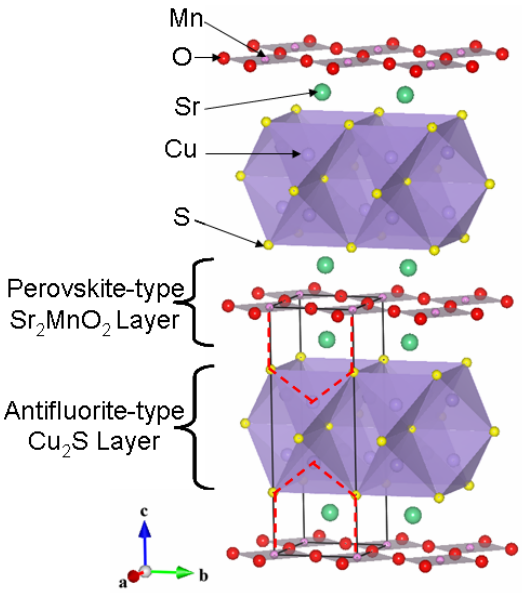

Figure 4.1. The crystal structure diagram of $Sr_2MnO_2Cu_{3.5}S_3$ (MnCu(II)). The unit cell is indicated with black solid lines and the "MnO_2" square planes and "CuS_4" tetrahedras are shown in translucent pink and blue respectively. Colors used: Sr: green, Mn: pink, O: red, Cu: blue, and S: yellow. The environment around the tetrahedral site, e.g., interactions between the cation/vacancy and two Mn (above or below) through the bonds with S, are highlighted with red dashed lines in the diagram.

4.2 Experimental Section

4.2.1 Sample Preparation.

Electrochemical (de)lithiated samples of MnCu(II) were prepared by using coin cells of $Sr_2MNO_2Cu_{3.5}S_{3.5}$ as the active material for the positive electrode. The positive electrode mixture consisted of 80 wt% of the active material, 10 wt% of acetylene black, and 10 wt% of poly-vinylidene fluoride (PVDF) binder in N-methyl pyrrolidone (NMP). Coin cells (CR2032, Hohsen corp.) were assembled in an argon-filled glove box. Each cell typically contains about 15 mg of active material, separated from Li foil as negative electrode by two pieces of Celgard separator (Celgard Inc, USA). A 1M solution of $LiPF_6$ in ethylene carbonate:dimethyl carbonate (1:1) has been used as the electrolyte. The electrochemical experiments were carried out on a battery cycler (Arbin Instrument, College Station, TX) in galvanostatic mode at a C/20 rate. Batteries stopped at desired stage of (dis)charge were open in an Ar-filled glove box and the cathode films were washed with DMC and dried. The resulting samples were either recovered in powder form and packed in rotors for *ex situ* NMR measurements, or sealed as films with Kapton and Mylar tapes for *ex situ* XANES experiments.

4.2.2 *In-situ* X-ray Diffraction. (XRD)

In situ XRD data were collected in beamline X18A at the National Synchrotron Light Source (NSLS) at Brookhaven National Laboratory. The radiation wavelength is 1.195 Å and a step size of 0.02º for 2θ scan was used. A specially designed cell (for *in*

situ measurements) [15] with Mylar windows was used to cycle the electrode films prepared as described above.

4.2.3 X-ray Absorption Near-Edge Spectroscopy (XANES)

The XANES spectra were collected in beamline X19A at the NSLS at Brookhaven National Laboratory. The measurements were performed in transmission or fluorescence mode using a Si (111) double-crystal monochromator detuned to 35-45% of its original intensity to eliminate the high order harmonics. Energy calibration was carried out by using the first inflection points in the spectra of Mn and Cu metal foil as references. (Mn K-edge = 6539 eV, Cu K-edge = 8979 eV.) The S K-edge XANES spectra were calibrated against the native sulfur K-edge at 2472 eV.

4.2.4 Solid-State Nuclear Magnetic Resonance (NMR)

The ^{7}Li magic angle spinning (MAS) NMR experiments were performed at 77.8 MHz on a Chemagnetics CMX-200 spectrometer (B_0 = 4.7 T) by using a double resonance 1.8 mm probe. Silicon nitride (Si_3N_4) rotors were used and spun at a speed of 38 kHz. All the spectra were acquired following a rotor-synchronized Hahn echo sequence (90°-τ-180°-τ-acquisition). The spectra were referenced to a standard 1M ^{7}LiCl solution at 0 ppm. π/2 pulses of 2 μs were typically used, with a delay time of 1 s.

4.3 Results and Discussion

4.3.1 Electrochemistry Studies

Figure 4.2 shows the voltage-composition curves of lithium batteries using MnCu(II) as positive electrodes and cycled between 1.1 and 2.75 and between 1.1 and 3.75 V. MnCu(II) has around 3.5 mol of Cu^+ and 0.5 mol of vacancies per formula unit ($Sr_2MnO_2Cu_{3.5}S_3$) at the tetrahedral sites in the [Cu_2S] layers [13], and Li^+ can be inserted topotactically into the structure by replacing the Cu^+ under chemical reductive ion exchange conditions [14]. After a small process at around 2.1 to 2.2 V, accounting for about 10 mAh/g (0.25 Li) of the capacity, the 1st discharge curve of MnCu(II) displays a long process at around 1.5 V, and reaches the capacity equivalent to about 4 mol of Li insertion per formula unit (187 mAh/g), indicating that this process corresponds to the Li-Cu (or vacancy) exchange. Since the inserted Li ions replace the Cu and also take the vacant tetrahedral sites, Mn in the structure is reduced in addition to the reduction of Cu (see detailed information in the following section). Even for the same cutoff voltage of 1.1 V, the exact amount of Li insertion varies slightly from cell to cell. This is most likely due to the differences in the electrode construction for each individual cell and that may cause differences in the over potential and affect the obtained discharge capacity. As shown in Figure 4.2(a), during the following charge, two processes, at around 1.8 and 2.5 V, are seen when the battery was charged to 2.75 V, where 80% of the capacity is restored. Results from quasi-open circuit voltage electrochemical measurements (GITT, see Figure 4.3(a)) indicate that the equilibrium potential for the 1.8 V process is around 1.7 V, and is the same as the potential of the 2nd half of the 1.5 V process during the 1st

discharge, suggesting the involved redox species may be the same. The subsequent 2nd discharge curve, however, shows different features from the 1st one, and a much more pronounced feature at around 2.2 V is now observed. The GITT results (see Figure 4.3(b)) show that the equilibrium voltage of this process is around 2.3 V, and is the same as the 2.5 V process during the 1st charge, indicating similar reaction mechanisms may be involved in these two processes. Other than the 2.2 V process, the 2nd process of this discharge almost overlaps with the second half of the 1st discharge curve, which indicates this part may involve the same mechanism. These two features are largely preserved during the following extended cycles and associated with the good cycleability observed for this material within the voltage window of 1.1 to 2.7 V [11]. Note that, the discharge curve shows different features in the 2nd and following cycles from the 1st one, suggesting the structure of MnCu(II) that has been charged to 2.75 V is different from the pristine material and lithium reinsertion processes change consequently. Interestingly, these two processes are similar to the two plateaus at around 2.1 and 1.7 V observed for CuS in its 1st discharge process [16] [17], except the capacity corresponding to each plateau is much smaller than in the case of CuS due to the much lower molecular weight of CuS. CuS contains both Cu^{+} and Cu^{2+} cations and both S^{2-} and S_2^{2-} anions, and the structure of CuS is different from the [Cu_2S] motif in the MnCu(II) structure. Nonetheless, the similarity of the electrochemical profiles between these two systems indicates that there may involve similar electrochemical processes.

In contrast, when the battery was charged further to a higher voltage at 3.75 V, e.g., higher than the oxidation potential of Cu metal (~ 3.56 V), there is an additional

short process at around 3.3 V (Figure 4.2(b)), and extra capacity is obtained as well. In this case, the overall capacity obtained in charge is larger than the capacity obtained during the 1st discharge by approximately 30 mAh/g. This extra capacity could be due to the oxidation of Cu^0 to Cu^+ and either exchanging with Li ion in the structure or migrate in the electrolyte. Detail analysis will be discussed in later sections.

This additional process is believed to involve further oxidation of residual Cu, as a similar process has been described before in the $Li_xCuTi_2S_4$ system, where the electrochemical profile displays a short process at around 3.3 V when the battery is charged to 3.7 V. This 3.3 V process has been ascribed to complete Cu re-insertion into the structure according to the XRD results [14].

The following discharge curve has a very similar shape to the 1st discharge, indicating that the structure of this material at the 3.75 V state is largely restored to its pristine state. Nonetheless, when carefully comparing the curves during the 2nd discharge to that during the 1st, we notice that the 2.2 V process is slightly enhanced and the overall capacity of the 2nd discharge is smaller (a drop of around 8%). Although the capacity drop is less than for the sample charged to 2.75 V, the cycling performance of MnCu(II) within the larger voltage window, e.g., 1.1 to 3.75 V, is not as good and the capacity fades very quick upon cycling (see Figure 4.4). This may indicate that the framework of the pristine MnCu(II) is not as stable as the phase that is formed on being charged to 2.75 V when it is subject to reversible lithium intercalation.

To enable a detailed study of all the processes, samples at different discharge/charge levels during the 1st cycle and the two 2nd discharges, marked with red

dots and labeled with letters a to k in Figure 4.2, were prepared for *ex situ* measurements. Information regarding each sample, e.g., the (dis)charge stage, the Li content and/or voltage, etc., is summarized in Table 4.1. Since the 1st discharge only shows a long process, the *ex situ* samples during the 1st discharge (samples a to d) were prepared by controlling the Li contents and labeled accordingly. During the following charge and two different subsequent discharges, there are several processes in each (dis)charge. To study each process, samples at the onset or after a certain process were prepared by controlling the cutoff voltages, and labeled accordingly (samples e to m).

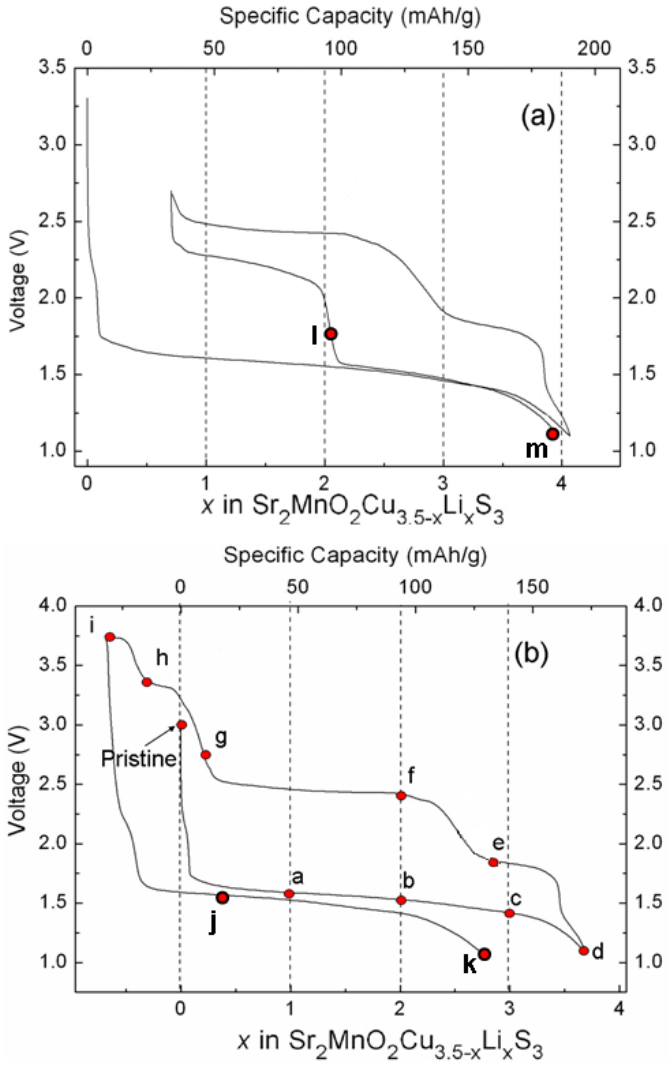

Figure 4.2. Plot of the voltage *vs.* Li content and specific capacity of lithium batteries with MnCu(II) as the positive electrodes cycled at a C/20 rate. The curves shown here include the complete 1st cycle (discharge and charge) and the 2nd discharge for a battery cycled between: (a) 1.1 to 2.75 V, and (b) 1.1 to 3.75 V. Points labeled at desired stages of (dis)charge correspond to samples that were subjected to *ex situ* measurements.

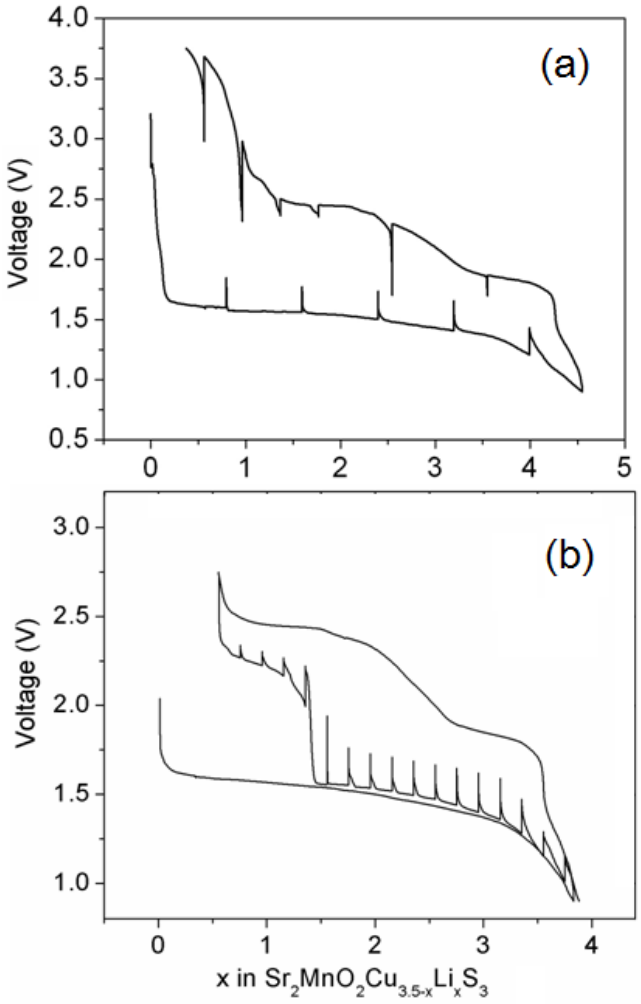

Figure 4.3. Quasi-open circuit voltage curve of MnCu(II)|Li batteries during (a) the 1st cycle, and (b) the 2nd discharge after being charged to 2.75 V, obtained by the galvanostatic intermittent titration technique (GITT). The batteries were both operated at a C/20 rate. The battery shown in (a) was (dis)charged for 4 h and then allowed to rest for 8 h, and the one shown in (b) was discharged for 1 h and then rest for 8 h.

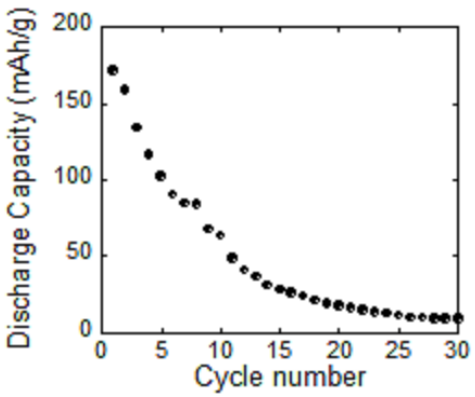

Figure 4.4. The cycle performance of MnCu(II) within the 1.1 to 3.75 V window. The applied current rate is C/20.

Table 4.1. Summary of the sample descriptions during each process.

	Sample label & name	**Descriptions**
The 1st discharge	a: Li1.0	Partially lithiated sample obtained following insertion of 1.0 mol of Li per formula unit.
	b: Li2.0	Partially lithiated sample obtained following insertion of 2.0 mol of Li per formula unit.
	c: Li3.0	Partially lithiated sample obtained following insertion of 3.0 mol of Li per formula unit.
	d: Li4.0	Sample discharged to 1.1 V. The lithium content for this fully lithiated sample should be around 4.0 mol but may vary slightly from different batteries. It is denoted as "Li4.0" for consistency with other discharged samples during the 1st discharge.
The 1st charge (after the 1st discharge to 1.1 V)	e: Ch1.8V	Sample charged back to 1.8 V after being discharged to 1.1 V during the 1st discharge. It is after the 1st process at ~ 1.8 V of the charge.
	f: Ch2.5V	Sample charged back to 2.5 V after being discharged to 1.1 V during the 1st discharge. It is the onset of the 2nd process at ~ 2.5 V of the charge.
	g: Ch2.75V	Sample charged back to 2.75 V after being discharged to 1.1 V during the 1st discharge. It is after the 2nd process at ~ 2.5 V of the charge.
	h: Ch3.3V	Sample charged back to 3.3 V after being discharged to 1.1 V during the 1st discharge. It is during the 3rd process at ~ 3.3 V of the charge.
	i: Ch3.75V	Sample charged back to 3.75 V after being discharged to 1.1 V during the 1st discharge. It is after the 3rd process at ~ 3.3 V of the charge.
The 2nd discharge (after the 1st charge to 3.75 V)	j: (H)2ndDis_1.5V	Sample at an early stage of the 2nd discharge after the 1st charge to 3.75 V. The Li content in this sample is comparable with that in sample a: Li1.0 during the 1st discharge.
	k: (H)2ndDis_1.1V	Sample at the end of the 2nd discharge (discharged to 1.1 V) after the 1st charge to 3.75 V. This sample resembles to the fully discharged sample d: Li4.0 during the 1st discharge.
The 2nd discharge (after the 1st charge to 2.75 V)	l: (L)2ndDis_1.7V	Sample at a middle stage of the 2nd discharge after the 1st charge to 2.75 V. It is after the 1st process at ~2.2 V during the 2nd discharge.
	m: (L)2ndDis_1.1V	Sample at the end of the 2nd discharge (discharged to 1.1 V) after the 1st charge to 2.75 V.

4.3.2 XRD measurements

Representative *in situ* XRD patterns of the phases observed during the 1st cycle of MnCu(II) between 1.1 and 2.8 V are plotted in Figure 4.5. A previous study has reported that the pristine MnCu(II) adopts a *P*4/mmm space group [13]. During the 1st discharge, at the early stage of lithium intercalation (before the insertion of 1 Li, Li1.0) there is no significant change in the XRD pattern. When more Li is inserted into the structure, the reflections coming from Cu metal (2θ = 43° and 51°, as indicated in the figure) start to appear. The intensity of the Cu reflections increase as the battery is discharged further，indicating the gradual extrusion of Cu from the framework structure does not occur from the very beginning but rather after some amount of Li insertion (e.g., Li1.0). Along with the formation of Cu metal, the intensity change of a reflection at low angle, the (001) reflection at 2θ = 7.7°, is also observed. In a previous study of the chemical lithiation of MnCu(II), this reflection has been regarded as a characteristic reflection from the fully lithiated phase [14]. It does not arise from Cu metal directly, but instead it reflects a contrast of the electron density between the layers of the framework structure and is an indirect indication of Cu metal formation. In the pristine MnCu(II) structure, this reflection is accidently absent due to similar electron density of Mn and Cu. However, when Li is inserted into the structure and replaces Cu, contrast of the electron density between layers increases as Li has a much lower electron density than Cu. The presence of this reflection is then observed, with the intensity increasing as more Li-Cu exchange occurs. Another change of this reflection is that it shifts slightly to the lower angle upon lithiation (see Figure 4.5, the right panel). This indicates an increase of the *c* parameter of

the unit cell and also the expansion of the framework along the axial direction. In addition to the Cu metal related reflections, a new phase (marked with triangles in the figure) is present after 2.0 moles of Li insertion, and is dominant at the end of the 1st discharge. This phase is the fully lithiated form of MnCu(II) and can be indexed to the same space group, *P*4/mmm, as the chemically lithiated form reported previously [14]. Since the XRD pattern of the electrochemically lithiated form (d: Li4.0) is very similar to that reported for the chemically lithiated one [14], it indicates that both chemical and electrochemical lithiation of MnCu(II) have the same structure.

During the following charge, lithium is removed from the lithiated phase and the system goes through a two-phase reaction region first (mainly the 1st process at 1.8 V and the initial part of the 2nd process at 2.5 V) and then a solid-solution region (the rest of the 2.5 V process). The (001) reflection now clearly moves to higher 2θ angle, but to a slightly lesser extent than during the 1st discharge (see Figure 4.5, where the apex of the peak does not cross the dashed line). This suggests that some contraction of the framework along the *c* direction occurs upon the Li removal. The Cu metal content decreases accordingly as well, as indicated by the reduced intensity of the Cu metal reflections and the (001) reflection of the framework structure. However, the change of the Cu metal content does not occur at a constant rate. Since the reflections coming from Cu metal are broad, the intensity change of the (001) reflection is used here as an indicator to evaluate the change of Cu metal content in the electrode composite. More specifically, a decrease of the intensity of the (001) reflection is observed shortly after the charge starts and throughout the 1st discharge process at around 1.8 V, e.g., between the

points d and e, while a more significant intensity change of this reflection occurs during the 2nd process at around 2.5 V, e.g., between the points f and g. This indicates that more significant Cu re-insertion into the structure takes place during the 2nd process rather than the 1st one. Nonetheless, Cu-reinsertion is not complete at the point where the battery is charged to 2.8 V, as evidenced by the non-zero intensity of the Cu metal reflections, which also indicates that there remains some Cu metal in the composite electrode at this stage of charge. The intensity of the (001) reflection is near zero at the 2.8 V state, and this indicates that most of the Cu has been re-inserted into the framework structure and the amount of remaining Cu metal should be very small.

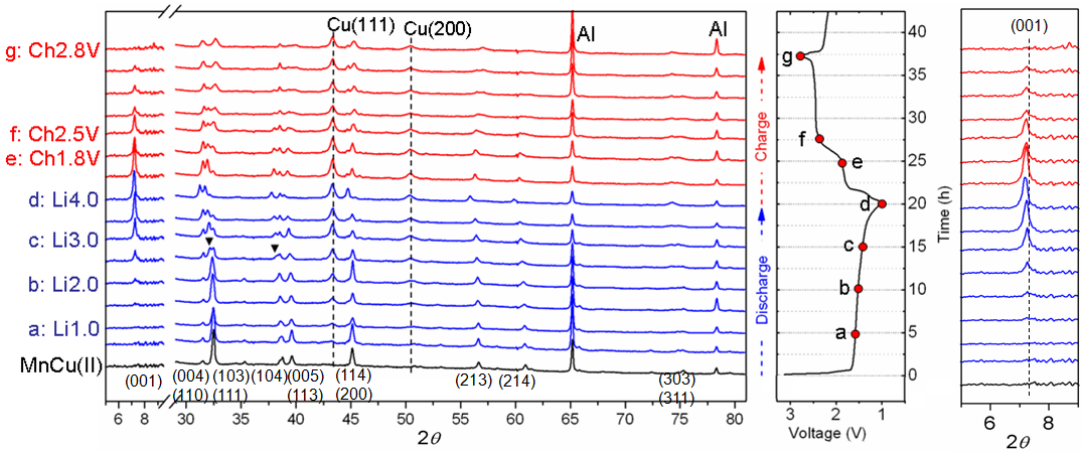

Figure 4.5. Representative *in situ* XRD patterns (left panel) and corresponding electrochemical profile (middle panel) for a Li/MnCu(II) cell cycled between 1.1 and 2.8 V at a C/20 rate. Selected spots at different stages of discharge/charge are marked with letters a to g in the electrochemical profile (same as the set of letters that used for *ex situ* samples). Each corresponding XRD pattern is labeled with the same letter and a brief description, for example, "Li1.0" indicates insertion of 1.0 mole of Li per formula into the structure, and "Ch1.8V" indicates the battery is charged to 1.8 V after the 1st discharge. Indices in brackets correspond to the pristine MnCu(II) phase that adopts a *P*4/mmm space group. Reflections due to Cu metal are indicated with dashed lines and labeled with the appropriate index. The right panel is a zoomed view of the region of 2θ between 5° and 9°, and the dashed line indicates the highest 2θ angle reached by the (001) reflection during the experimental period and is provided as a guide of the eye. The region of 2θ between 9° and 29° is not shown here due to large background. Reflections coming from the Al foil in the *in situ* cell are marked as well.

4.3.3 *Ex situ* XANES analysis

In the following discussion regarding the XANES results (Cu, Mn and S K-edges) for the cycled MnCu(II) phases, the individual process will be addressed separately: (i) the 1st discharge (down to 1.1 V), (ii) the 1st charge (up to 3.75 V), and (iii) two 2nd discharges (down to 1.1 V after charging to 2.75 V and to 3.75 V).

4.3.3.1 The 1st discharge

The normalized Cu K-edge XANES spectra of lithiated MnCu(II) phases during the 1st discharge and their corresponding 1st derivative curves are shown in Figure 4.6. The change of the absorption edge position is subtle and a clearer view is provided by the 1st derivative curves where the absorption edge position is indicated by an inflection peak at the corresponding energy (Figure 4.6(b)). Comparing the peak positions of the pristine and lithiated samples, no significant shift is observed from pristine MnCu(II) to the sample Li1.0, but the peak clearly shifts to lower energy in the sample Li2.0 and in samples thereafter. This indicates that the Cu ions are reduced during the 1st discharge and the reduction is more significant after the insertion of around one mole of Li into the structure than at the very beginning. This is consistent with the *in situ* XRD results where the reflections coming from Cu metal start to appear and become more intense after Li1.0.

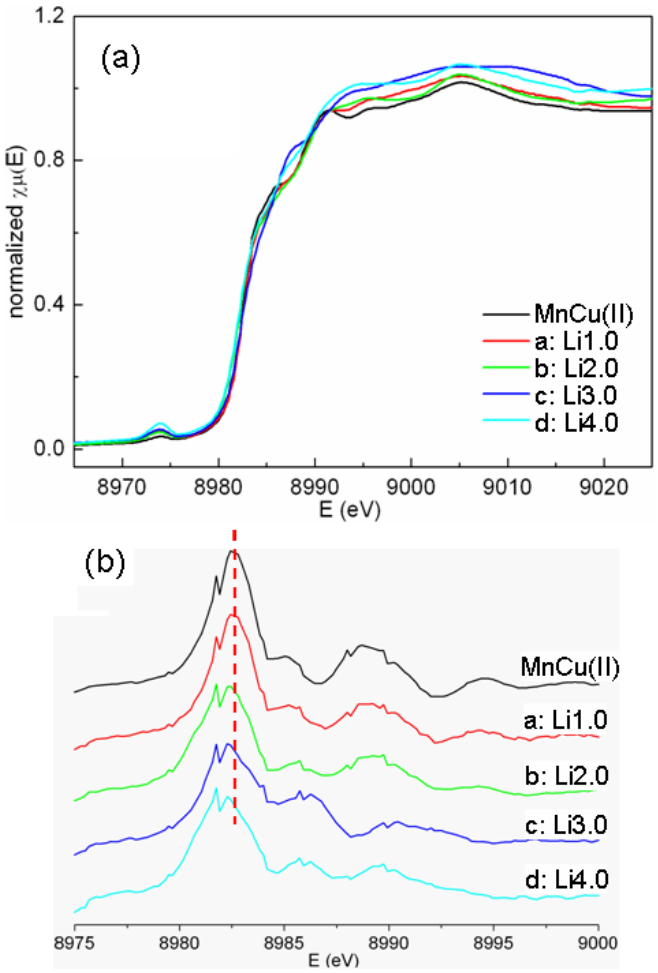

Figure 4.6. (a) Normalized Cu K-edge XANES spectra of pristine and lithiated MnCu(II) phases during the 1st discharge, and (b) a stacked plot of the corresponding first derivative curves. The dashed line in (b) indicates the energy position observed for the pristine sample MnCu(II), and is provided as a guide to the eye.

Figure 4.7 shows the normalized Mn K-edge XANES spectra. The Mn environment in the layered structure is shown in the figure as well. In pristine MnCu(II), it has been reported that the oxidation state of Mn is +2.5, and the Mn K-edge absorption edge of pristine MnCu(II) was found to be located between those of the Mn^{2+} and Mn^{3+} reference compounds. [13] Upon Li insertion, Mn is reduced during the discharge, as indicated by a clear shift of the absorption edge to lower energy. However, most of the absorption edge shift occurs from pristine MnCu(II) to sample Li2.0, the absorption edge remaining at a similar position thereafter, suggesting that the majority of the Mn ions in the structure are reduced by Li = 2.0. The edge positions of these samples are very similar to that of MnO (not shown here), indicating that the Mn is fully reduced to 2+ in samples Li2.0 to Li4.0. In addition to the displacement of the absorption edge, drastic changes of the line shape of the absorption curve are also observed. This is ascribed to structural changes in the local geometry of Mn since the line shape of the Mn XANES spectrum is very sensitive to the surrounding environment of Mn. In pristine MnCu(II), Mn is located in an elongated octahedral site where four oxygen sit on the corners of the square plane and two sulfur atoms are located above and below on the axial positions. Upon the lithium insertion and replacing Cu in the "Cu_2S" layer, there are very likely subtle changes to the sulfur environments, which will have a direct effect on the symmetries and surrounding environment of Mn. For example, as seen in Figure 4.7, the pre-edge peak is more intense in sample Li2.0 and samples thereafter, and this indicates the inversion symmetry of Mn environment is reduced upon lithium insertion. Although it is not clear how exactly the Mn environment changes, the asymmetric displacement of the sulfur above and below

and Mn moving slightly off its original position may be one reason accounting for the loss of the inversion symmetry.

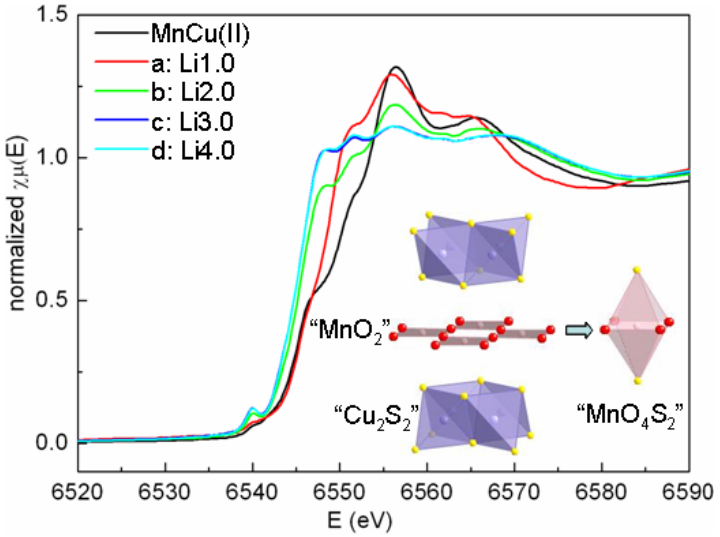

Figure 4.7. Normalized Mn K-edge XANES spectra of the pristine and lithiated MnCu(II) phases during the 1st discharge. The lower corner inset is a schematic showing the elongated octahedral environment around Mn (represented as "MnO_4S_2" in the figure) in the structure. The "MnO_2" like sheet and the "Cu_2S" like motif are labeled in the MnCu(II) structure, and Sr is omitted for clarity.

Since S is the species that is directly connected to both of the two active redox cations (Cu and Mn) in the structure, the sulfur environment was investigated by performing the S K-edge XANES measurements on pristine MnCu(II) and two discharged samples, Li2.0 and Li4.0, shown in Figure 4.8. Several features, labeled with letters *I* to *V* in the figure, can be identified, and which are due to different electronic transitions. Regarding the spectrum of pristine MnCu(II) compound, feature *II* at around 2475 eV is the main absorption, and a weak absorption *I* can be observed at lower energy at around 2471 eV. A doublet featured absorption *IV* and a broad absorption *V* can also be seen at higher energy levels. The spectrum has been compared to those of several reference mineral compounds, chalcocite (Cu_2S), covellite (CuS), pyrite (FeS_2) and elemental sulfur (see Figure 4.9). Tentative assignments of the observed features in the MnCu(II) spectra have been made based on the studies from Li *et al.* on some copper sulfide minerals [18] and Pattrick *et al.* on amorphous copper sulfides [19]. Feature *II*, *IV* and *V* are attributed to the transitions of S 1*s*- to S *p*-like states, and feature *I* is assigned to the transitions of the S 1*s*- electrons to S 3*p*-like states hybridized with the Cu 3*d* band in tetrahedral CuS_4 clusters. In pristine MnCu(II), it has been demonstrated that the Cu-3d/S-3p valence band is full [13] and this may be the reason for the weak feature of absorption *I.* Further detailed analysis of the spectrum will not be discussed here since it is beyond the scope of this study.

Upon lithiation, the intensity of absorption *II* gradually decreases and intensity of absorption *IV* increases. However, no significant shift of the energy positions is observed for all the absorption features, indication the oxidation state of S remains the same. The

changes of the intensities are very similar to those observed in the Li_xTiS_2 system [20], and it is most likely due to the elongation of Mn-S bond in the structure, which can be a result of the reduction of Mn (2.5+) to Mn (2+) [13]. In addition to this, a new absorption feature *III* at around 2477 eV clearly emerges and gradually becomes more intense as more lithium is intercalated into the structure. A peak at a similar energy has been observed for the anti-fluorite structure Li_2S [21], and thus we assign this peak to the "Li_2S" anti-fluorite double layer in MnCu(II) formed by replacing Cu^+ by Li^+.

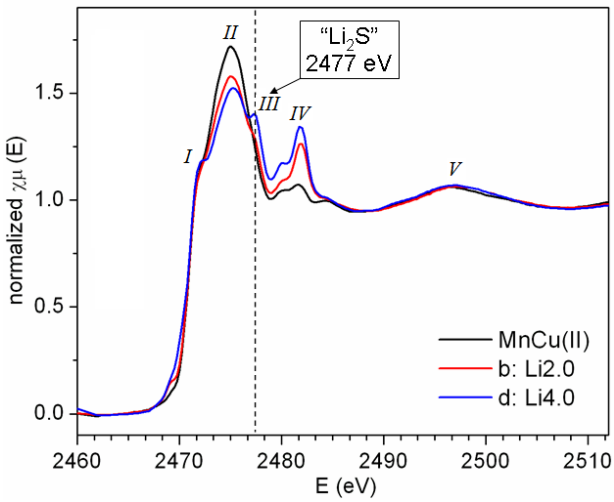

Figure 4.8. Normalized S K-edge XANES spectra of pristine and lithiated MnCu(II) phases during the 1st discharge. The absorption features are labeled with numbers *I* to *V*. The energy of feature *III* (due to sulfur in a Li_2S, anti-fluorite arrangement) is indicated with a dash line.

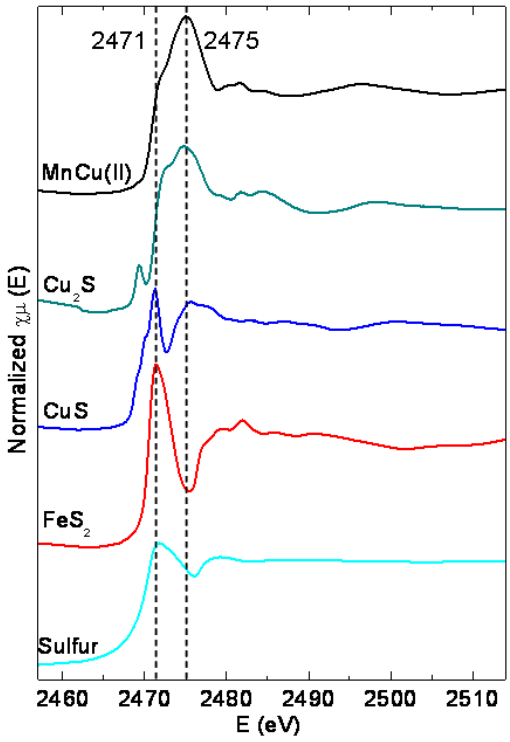

Figure 4.9. S K-edge XANES spectra of the pristine MnCu(II) and several mineral reference compounds: chalcocite (Cu_2S), covellite (CuS), pyrite (FeS_2) and elemental sulfur. The two energy positions of the features at the absorption edge for pristine MnCu(II) are indicated and labeled with two dash lines.

In summary, during the 1st discharge, the metal K-edge XANES results for both Cu and Mn show shift to lower energy of the absorption edge positions, indicating the reduction of Cu and Mn during the discharge process. The edge shift for Cu is more significant in samples after Li1.0 than before, while for Mn, most of the reduction occurs before Li2.0. This indicates that Mn is reduced first upon lithium intercalation and Cu is then reduced and extruded as copper metal, which is consistent with the *in situ* XRD results. In part, the fact that Mn is reduced prior to Cu may be ascribed to Li insertion into the vacant tetrahedral sites, (which may account for the small process at around 2.1 to 2.2 V in the electrochemical profile), a process which will be accompanied by Mn reduction to balance the charge. After this initial stage, further Li insertion may take place to both the vacant site and the site occupied by Cu, and during this stage, in addition into the Mn reduction, the Cu is also reduced and extruded as Cu metal.

Regarding the S XANES results, an increase of the bond length (presumably Mn-S) with the reduction of Mn is observed. Also, formation of Li_2S-like structure upon lithiation is indicated by the presence of a characteristic absorption at 2477 eV and this provides direct evidence for Li-Cu exchange.

4.3.3.2 The 1st charge

The normalized Cu K-edge XANES spectra for MnCu(II) phases during the following charge and their 1st derivative curves are shown in Figure 4.10. Note that sample e, g, and i (see Table 4.1) are at the end of the 1.8, 2.5 and 3.3 V process, respectively. Comparing the peak positions of the 1st derivative curves (Figure 4.10(b)),

there is no significant change from the fully discharged sample (d) to the end of the 1.8 V process (sample e), and at the onset of the 2.5 V process (sample f), indicating the change of the oxidation state of Cu during the 1.8 V process is negligible. These results do not contradict the *in situ* XRD results, where only a small intensity change of the (001) reflection during the 1.8 V process is observed, since the amount of oxidized Cu is clearly so small that the change of the average oxidation state of Cu is too small to be detected in the XANES measurements.

However, the 1st derivative inflection peak for samples charged to higher voltages, e.g., sample g charged to 2.75 V (after the 2.5 V process) and sample i charged to 3.75 V (after the 3.3 V process), shows a clear and continuous shift to higher energy levels, suggesting the oxidation of Cu during both processes. During the 2.5 V process, the observation is consistent with the *in situ* XRD results, where a significant amount of Cu is reinserted into the structure, as indicated by a distinct intensity decrease of the (001) reflection when the battery was charged from point f to point g. No *in situ* XRD data is available to evaluate the Cu content changes during the 3.3 V process, since the measurement was stopped at 2.8 V. However, preliminary *ex situ* neutron diffraction results do indicate that there are remaining Cu metal reflections in the sample charged to 2.75 V while the Cu metal peaks of the sample charged to 3.75 V have completely vanished. Furthermore, comparing the edge positions of sample i and pristine MnCu(II), the former is clearly at a higher energy, suggesting a partial oxidation of Cu to a higher oxidation state than in the pristine phase, which can be a reason for the extra capacity obtained during the 3.3 V process.

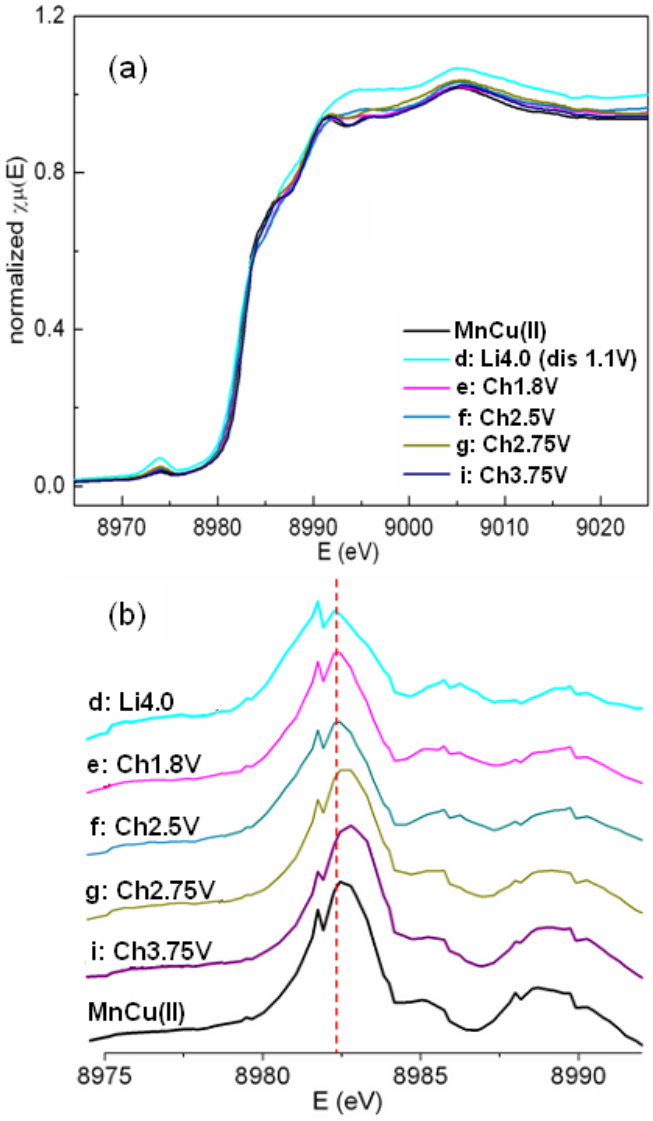

Figure 4.10. (a) Normalized Cu K-edge XANES spectra of MnCu(II) phases during the 1st charge, and (b) a stacked plot of the corresponding first derivative curves. The spectra of pristine MnCu(II) and the fully lithiated form (d: Li4.0) are also included as references. The dashed line in (b) indicates the energy position observed for the fully lithiated phase (d: Li4.0), and is provided as a guide to the eye.

The normalized Mn K-edge XANES spectra of pristine MnCu(II) and phases at different stages of charge are shown in Figure 4.11. From the fully lithiated sample d to sample f, only a very small shift of the absorption edge is observed, indicating the change of the Mn oxidation state during the 1.8 V process is minor. Nonetheless, the change of the line shape is distinct, indicating a change in the Mn surrounding environment. The major displacement of the absorption edge towards the higher energy level, however, takes place between sample f and sample g, which are before and after the 2nd process at 2.5 V respectively, suggesting the oxidation of Mn during this process. After sample g, the absorption edge does not move further upon further charging, indicating that no further Mn oxidation occurs during the 3.3 V process. In fact, the absorption edge for sample i, the one charged to 3.75 V, is even at a slightly lower energy level than those of sample g and the pristine MnCu(II). (The spectrum of sample g is nearly identical to that of the pristine MnCu(II).) The change of the lineshape, although dramatic, more or less traces back to the lineshape changes observed during the 1st discharge process: the absorption curve of sample f (charged to 2.5 V) is similar to that of sample b (Li2.0) and the spectra of sample g and i are similar to the pristine one. This indicates delithiation from the structure restores both the oxidation state and surrounding environment of Mn to its pristine like.

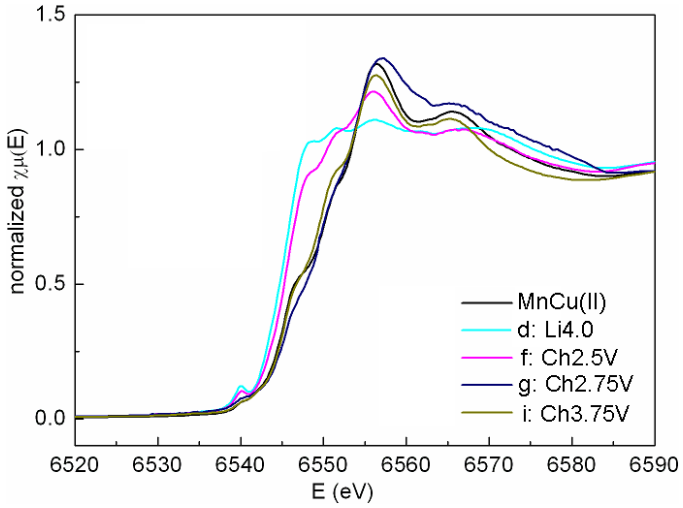

Figure 4.11. Normalized Mn K-edge XANES spectra of MnCu(II) phases during the 1st charge. The spectra of pristine MnCu(II) and the fully lithiated form (d: Li4.0) are also included as references.

Figure 4.12 shows the S XANES results for MnCu(II) phases during the 1st charge process, as well as a comparison among the pristine MnCu(II) and two samples charged to 2.75 and 3.75 V. The features of the absorption curves are labeled as *I* to *V* as described in previous section. Upon the removal of lithium from the fully lithiated phase d (Li4.0), a gradual decrease of the absorption feature *III* at around 2477 eV, the characteristic feature of the Li_2S-like structure, is clearly observed, indicating the reduction of this environment during the charge. A closer examination (see the inset of Figure 4.12(a)), however, reveals that the Li_2S-like environment is not present in samples charged to 2.75 (g) and 3.75 V (i), the ones after the 2.5 V process. This suggests that the Li_2S-like structure is diminished mostly during the 1.8 and 2.5 V processes, and the 3.3 V process does not involve the Li_2S-like environment. Besides the *III* absorption feature, a noticeable increase of the intensity of feature *II* and a decrease of partial of the feature *IV* are observed from sample e to g, where the 2.5 V process occurs. The change of the intensities, is opposite to those observed during the 1st discharge, and is now ascribed to the shortening of the Mn-S bonds resulting from the oxidation of Mn. This is consistent with the Mn XANES results where the majority of Mn oxidation is only observed during the 2.5 V process.

The absorption curves for sample g and i are nearly identical (see Figure 4.12(b)), only the intensity of feature *II* for sample i being slightly higher. However, they are not exactly the same as the spectrum of pristine MnCu(II) phase, indicating the sulfur environment is not totally restored to its pristine like even when the battery was charged to 3.75 V. Besides the intensity differences, a new absorption peak appears at around

2470 eV in the spectra for both sample g and i (see the inset of Figure 4.12(b)). This peak has been ascribed to transitions involving the S_2^{2-}-groups [18-19], and the presence of this peak indicates some S^{2-} is oxidized to the S_2^{2-} ion during the charge process, and this may also rationalize part of the extra capacity obtained during charge.

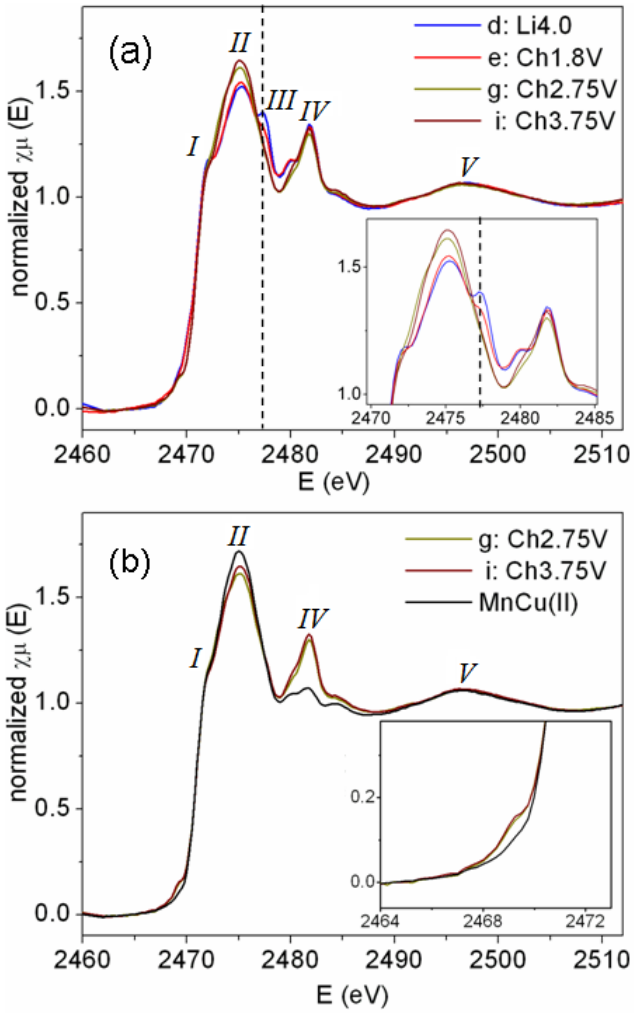

Figure 4.12. Normalized S K-edge XANES spectra of (a) MnCu(II) phases during the 1st charge , and (b) the pristine MnCu(II) and two samples charged to 2.75 and 3.75 V, respectively. The insets show zoomed views of the spectra: (a) between 2470 to 2485 eV, and (b) between 2464 to 2473 eV. The absorption features are labeled with letter *a* to *e* (see text).

In summary, during the charge, the three processes, at 1.8, 2.5 and 3.3 V, respectively, involve different redox species. During the 1.8 V process, Li is removed from the structure and the "Li_2S" environment reduces, as indicated by the S XANES results. Some of the Cu is oxidized and reinserted into the structure, but the amount of reinserted Cu is small and some of the tetrahedral sites are vacant. The 2.5 V process involves further reducing of the intensity of the Li_2S-like environment and the oxidation of both Cu and Mn. A small amount of S_2^{2-} anion formation is also observed during this region. The formation of these S_2^{2-} groups could be driven by (or made more energetically favorable) shortening of the S-S distance resulting from the vacant sites generated during the 1.8 V process. As there are no more Li_2S-like environments but clearly un-reinserted Cu remains, more tetrahedral sites must be vacant in the structure as compared to the pristine MnCu(II) phase, which may result shorter separations between some neighboring S atoms and a small portion of them even forming S-S bonds. Presence of more vacant tetrahedral sites in the sulfide layer is also the most distinct difference of the structure at 2.75 V state from that of the pristine MnCu(II) phase. Finally, the 3.3 V process involves the oxidation of Cu, and the Cu is further oxidized to an average oxidation state that slightly higher than Cu(I). At the 3.75 V state, the occupancy of the Cu in the tetrahedral site is comparable to that of the pristine phase. However, the structure of the phase at this voltage slightly differs from the pristine phase by the presence of the small amount of the S_2^{2-} group, the slightly reduced Mn, and Cu at a slightly higher oxidation state than Cu(I).

4.3.3.3 The 2nd discharge

As described in the electrochemical section, the behavior of MnCu(II) during the 2nd discharge largely depends on the cut off voltage applied for the 1st charge, e.g., whether it is relatively high (3.75 V) or low (2.75 V). The samples at selected stages of discharge during these two 2nd discharge are labeled with (H), for those being charged to 3.75 V, or (L), for those being charged to 2.75 V, accordingly.

The Cu XANES results are shown in Figure 4.13. When the battery was charged to 3.75 V, the following discharge profile is similar to the 1st discharge. It is then not very surprising to see a similar behavior of the Cu absorption edge during this 2nd discharge. A significant variation of the absorption edge to lower energy level, i.e., the reduction of Cu, is only observed, again, after the battery was discharged to 1.5 V with around 1.0 Li insertion per formula unit (sample j) but not from the very beginning. On the other hand, when the battery was charged to 2.75 V and then discharged, two processes, at 2.2 and 1.5 V respectively, are now present, and a continuous shift is observed during the whole discharge, e.g., both of the two processes involve the reduction of Cu. Note that, right after the rising step of the absorption edge, the absorption curve at higher energy levels shows drastic changes of the line shape, and some part appears move to higher energy. However, these changes are most likely due to the variations of the structural configurations but not directly related to the valence state of Cu, and therefore they are not used here to evaluate the oxidation state of Cu.

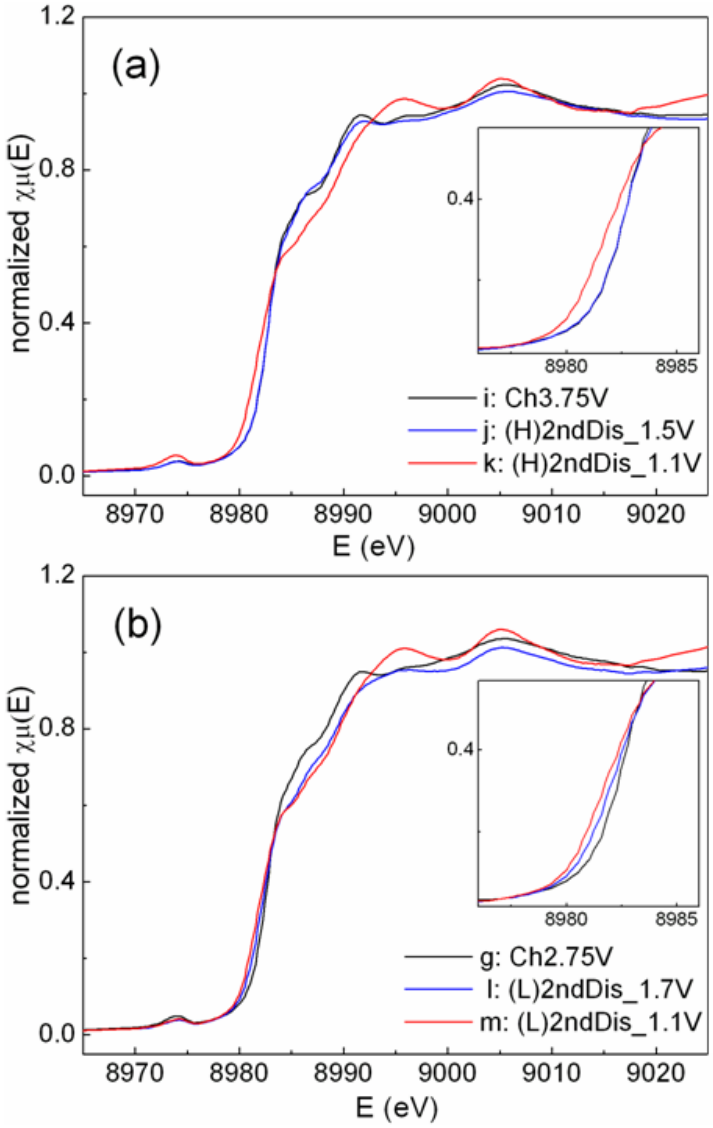

Figure 4.13. Normalized Cu K-edge XANES spectra of MnCu(II) phases during the two 2nd discharge processes after the 1st charge. The cut off voltage of the 1st charge is (a) 3.75 V, and (b) 2.75 V, respectively. The insets in (a) and (b) are zooms of the absorption edge regions.

Similarly, the Mn XANES results, shown in Figure 4.14, are also different depending on the cut off voltage applied to the 1st charge. In the 3.75 V case, the spectra largely resemble the ones for samples during the 1st discharge at similar stages of discharge, e.g., sample a: Li1.0 and sample d: Li4.0. The absorption edge clearly moves to lower energy level upon lithium insertion, indicating the reduction of Mn during the 2nd discharge. Besides the displacement between sample i and j, the absorption edge shifts further to lower energy in the fully discharged sample k. Due to the absence of samples at intermediate stages, it is not possible to tell when the absorption edge reaches the lowest energy between sample j and k. However, since the electrochemical behavior of this 2nd discharge is similar to the 1st one, it is very likely that Mn is fully reduced in the middle of the discharge and reduction of Mn does not extend the whole discharge.

When the cut off voltage applied to the 1st charge is low (2.75 V), the Mn XANES results clearly show that, despite the changes of the line shape that are caused by the surrounding environment of Mn, the absorption edge moves to lower energy only from sample g to l, but stays the same position thereafter. This suggests that the Mn reduction only takes place during the 1st process at 2.2 V, and the 2nd process at lower voltage does not involve further reduction of Mn.

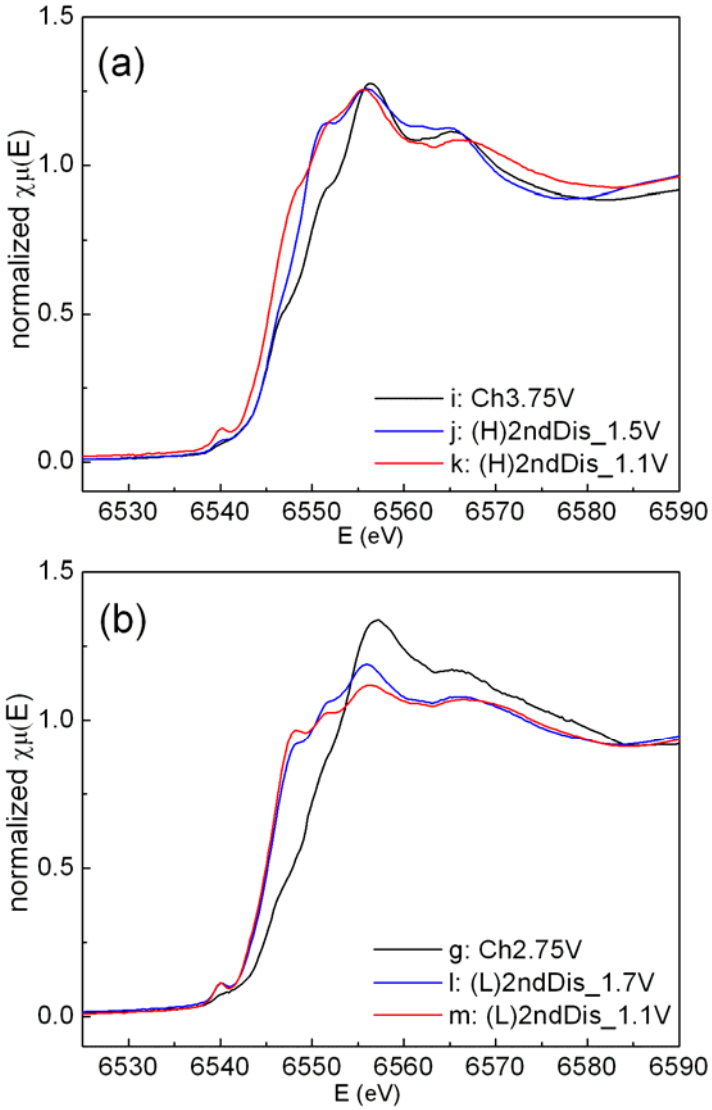

Figure 4.14. Normalized Mn K-edge XANES spectra of MnCu(II) phases during the two 2nd discharge processes after the 1st charge. The cut off voltage of the 1st charge is (a) 3.75 V, and (b) 2.75 V, respectively.

The S XANES results for samples during the two 2nd discharge processes are shown in Figure 4.15. At a first glance, it is obvious that the variations of the spectra in Figure 4.15(a) are much larger than those in Figure 4.15(b), indicating the S framework must have undergone more dramatic changes during the 2nd discharge after being charged to 3.75 V than that to 2.75 V. As discussed in previous part, the intensity changes of different parts of the absorption curve are most likely due to the change of bond distances, for example, the Mn-S bond and S-S bond etc. A detailed analysis of these changes will not be performed here, however, the information obtained in the preliminary observation clearly indicates that after being charged to 2.75 V, the redox reactions taking place during the 2nd discharge result in less distortion of the S framework and this may rationalize the better cycling performance of MnCu(II) within the smaller voltage window, 1.1 to 2.75 V, than that within the larger one to 3.75 V. The S behavior of the 2nd discharge after being charged to 3.75 V is significantly different from its behavior during the 1st discharge, for example, the "Li_2S"-like environment is not seen to form at the early stage of the discharge (sample j) and a much larger variation of the absorption curve for sample j than that for sample a is observed. These different behaviors can be accounted for by the small variation of the Cu content and its oxidation state at the 3.75 V state from pristine MnCu(II) and the 2.75 V state, and the different oxidation state of Mn. Although these variations are very small, they may have significant effects in determining the structure of the S framework, which is directly related to the Li (de)intercalation reaction processes.

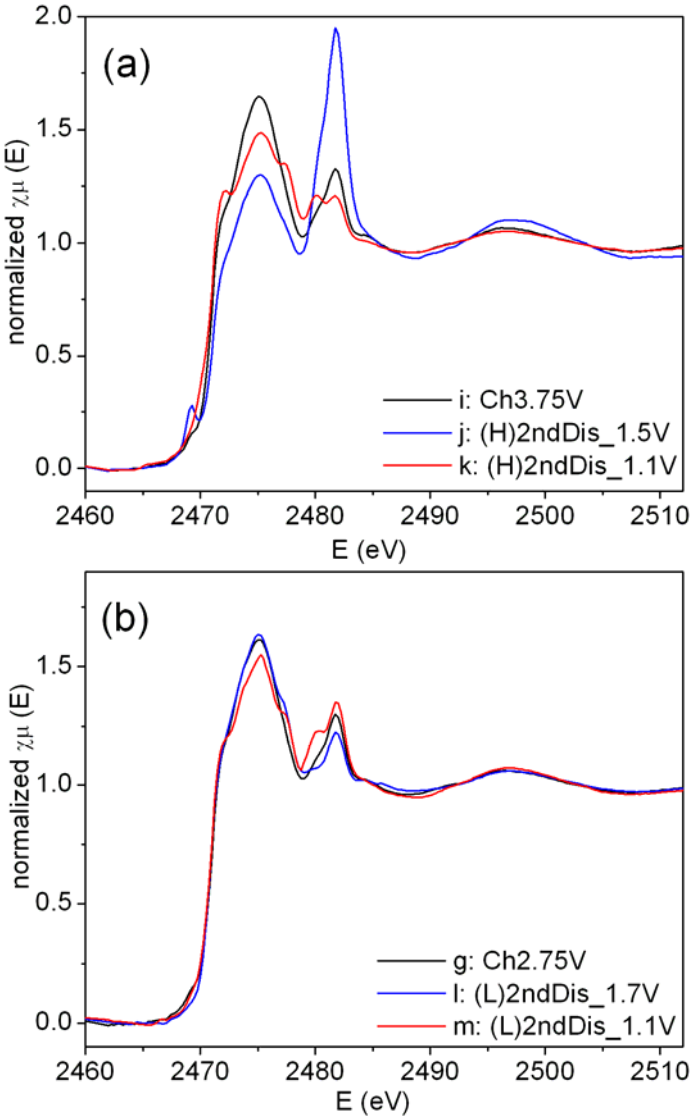

Figure 4.15. Normalized S K-edge XANES spectra of MnCu(II) phases during the two 2nd discharge processes after the 1st charge. The cut off voltage of the 1st charge is (a) 3.75 V, and (b) 2.75 V, respectively.

In summary, during the 2nd discharge after the 3.75 V state, both Cu and Mn are reduced, and they behave similarly to their behavior during the 1st discharge. However, the S framework experiences drastic changes and the variation is largely different from that during the 1st discharge. As in the case where the applied cut off voltage of the 1st charge is 2.75 V, the enhanced 2.2 V process involves the fully reduction of Mn and partial reduction of Cu, and Cu is reduced further during the 2nd process at 1.5 V until the end of the discharge. The S environment, however, does not show large variations throughout the whole 2nd discharge process, and this may rationalize the good cycleability of MnCu(II) within this voltage window.

4.3.4 ^{7}Li NMR Results

The *ex situ* ^{7}Li NMR spectra for different MnCu(II) phases (lithiated / delithiated) during the 1st discharge and charge processes are shown in Figure 4.16. Besides an intense resonance at 0 ppm, which arises from diamagnetic impurities, all the spectra show a group of resonances between the 200 and 270 ppm region, resulting from the Fermi contact interaction between paramagnetic Mn and Li through bonds with S, via a similar mechanism to that of a Li-O-Mn interaction [22].

During the 1st discharge, the spectrum of the initially lithiated sample Li1.0 shows two distinct resonances at 210 and 265 ppm, and upon further Li intercalation, only the 210 ppm resonance remains in the spectra of sample Li2.0, Li3.0 and Li4.0. The intensity of the 210 ppm resonance increases as a result of the increasing Li content in the structure. To assign these resonances, the environment around the inserted Li has been examined.

As mentioned in previous part, Li in the framework of MnCu(II) is in the tetrahedral site within the "Cu_2S" layer and can interact with two Mn from the "Sr_2MnO_2" layer above or below. According to the Mn XANES results, the average oxidation state of Mn in the pristine phase is 2.5+, indicating the presence of 50 % Mn^{2+} and 50 % Mn^{3+}. As Li is inserted into the framework, the XANES results indicate that Mn^{3+} is gradually reduced, and in sample Li1.0, approximately half of the Mn^{3+} is reduced to Mn^{2+}, resulting in approximately 75% of Mn^{2+} and 25% of Mn^{3+} in the structure at this stage. Fully reduction to Mn^{2+} is obtained in sample Li2.0. Therefore, the 210 ppm resonance has been assigned to Li interacting with only Mn^{2+} (two Li-S-Mn^{2+} interactions) and the 265 ppm resonance has been assigned to Li environment containing Mn^{3+} (one Li-S-Mn^{3+} interaction and one Li-S-Mn^{2+} interaction). An environment with Li interacting with two Mn^{3+} ions is not considered here since this configuration is not energetically favorable due to the large Columbic repulsion between the two neighboring highly charged Mn^{3+} cations. In addition, the amount of Mn^{3+} is small at the Li1.0 stage and the probability of Li in such environment is expected to be low. Since the NMR shifts are additive, it can be deduced from above assignments that each Li-S-Mn^{2+} interaction in this structure results in an around 210 / 2 = 105 ppm shift in the ^{7}Li NMR spectrum and each Li-S-Mn^{3+} induces around a 265 – 105 = 160 ppm shift. The value for the Li-S-Mn^{2+} interaction is consistent with the shifts observed for the other lithiated oxysulfides in the same series as MnCu(II) [11]. These results, however, appear contradictory to the expectation that Mn^{2+} (d^5) with more unpaired electrons would induce larger shift than Mn^{3+} (d^4), since the shift in Li NMR is usually proportional to the transferred electron density from the

paramagnetic species to the studied Li. However, this contradiction may be rationalized by the following explanations. As Mn in the MnCu(II) structure is located in the center of an elongated octahedral MnO_4S_2, both Mn^{2+} and Mn^{3+} are in a axially distorted environment even though Mn^{2+} is not a Jahn-Teller cation. In such a circumstance, dz^2 and $d(x^2-y^2)$ orbitals are not degenerate in energy but the dz^2 orbital has lower energy, and thus, both Mn^{2+} and Mn^{3+} have one electron occupying this orbital. Therefore, the resulting electronic configurations (high spin) for these two cations are Mn^{2+}: $(dxz,dyz)^2(dxy)^1(dz^2)^1(dx^2-y^2)^1$ and Mn^{3+}: $(dxz,dyz)^2(dxy)^1(dz^2)^1(dx^2-y^2)^0$. However, when considering the interactions between the Mn and S, which are directly related to the electron transfer from Mn to S, not all the orbitals are directly involved. More specifically, the S-$3p_x/p_y$ orbitals can overlap with the Mn-$3d_{xz}/d_{yz}$ orbitals in a π-interaction and the S-$3p_z$ orbital can form a σ-overlap with the Mn-$3dz^2$ orbital [13]. The involved orbitals, $3dxz/dyz$ and $3dz^2$, contain the same number of electrons for both Mn^{2+} and Mn^{3+}, indicating the electron contributions from Mn^{2+} and Mn^{3+} are similar. However, since the Mn^{3+} is a higher charged cation, the Mn^{3+}-S bond is expected to be shorter than the Mn^{2+}-S bond, which enables a better overlap between the Mn^{3+} and S orbitals. Therefore, a more efficient electron density transfer from Mn to S is expected and this results the larger Li NMR shift observed for Li in environment containing Mn^{3+} than in the ones containing Mn^{2+} only.

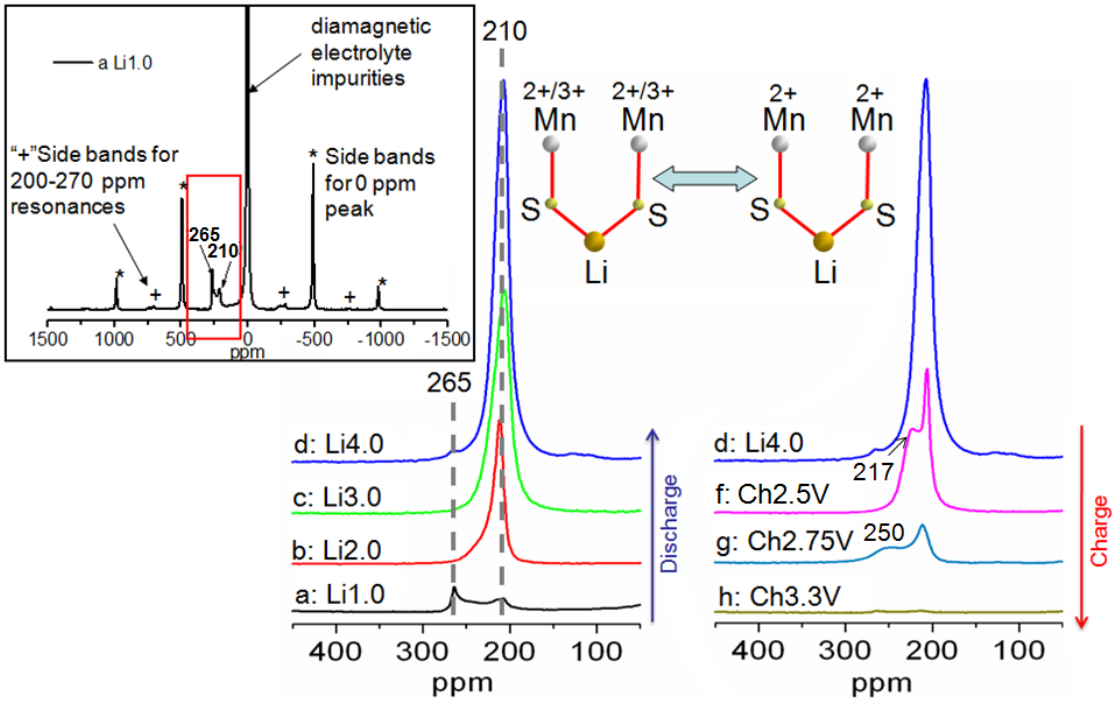

Figure 4.16. Zoomed view of the ^{7}Li NMR spectra of MnCu(II) phases during the 1st discharge (left) and charge (right) processes. The spectra have been normalized based on the acquisition number and sample mass. The inset at the left up corner is the full spectrum of sample a: Li1.0 shown as an example. The zoomed region is indicated by a red rectangle box. A schematic picture showing the Li environments in the MnCu(II) structure during the discharge/charge cycle is also included.

During the following charge, when lithium is gradually removed from the structure, the intensity of the 210 ppm resonance reduces, and new resonances at around 217 and 250 ppm emerge in charged sample f and g, respectively. These changes are due to the decrease of the Li content and reduction of Mn in the structure. The new resonances, however, are not distinct peaks but rather have broad line shapes, and the shifts are not at 265 ppm but somewhere in between 210 and 265 ppm. These features very likely imply some disordering existing in the structure, which may result in a continuous distribution of different environments and thus a broad resonance line shape. The Mn XANES results indicate the change of surrounding environment, not the oxidation state, of Mn during the 1.8 V process, and mainly reduction of Mn during the 2.5 V process. This provides some clue in determining the environments that contribute to the 217 and 250 ppm resonances. Since Mn is mainly Mn^{2+} at the end of the 1.8 V process, the 217 ppm resonance is also assigned to Li in environment containing two Mn^{2+}, and the variation of the shift may due to the distortion of the surrounding environment of Mn that may affect the effective electron transfer from Mn to Li. Similarly, the 250 ppm resonance is assigned to Li in a distorted environment containing both Mn^{3+} and Mn^{2+}. Another possibility to rationalize the shifts is the solid-solution behavior of the system during this region (after sample f to g), as shown in the in situ XRD results. The Li may distributed over environments where a continuous range of bond length (Mn-S, S-Li) and bond angles (Li-S-Mn) are present, resulting in a continuous distribution of shifts in the spectra. The 217 and 250 ppm broad resonances are intermediate between the 210 and 265 ppm resonances. Finally, in the spectra of the

sample charged to 3.3 V (sample h) and 3.75 V (see Figure 4.17), the resonances have nearly zero intensity, indicating that only a little amount of Li remains in the structure at this stage. This is consistent with the S XANES results, where the Li_2S-like environment is not seen any more in samples charged to higher than 2.75 V.

The ^{7}Li NMR results for samples during the two 2^{nd} discharge processes are shown in Figure 4.17 in two groups. Note that, the small displacement of the shift in the spectrum for sample m is not intrinsic but very likely caused by the small temperature variations during the MAS experiment. Nonetheless, comparing these two groups of spectra, it is clear that the intensities of the resonances for samples being charged to 3.75 V are significantly lower than the ones being charged to 2.75V. This is consistent with the electrochemical profiles shown in Figure 4.2, where the Li contents in sample j and k are smaller than those in sample l and m. Despite the intensity difference, the spectra of two samples at the end of each discharge, sample k and m, have very similar line shapes: an intense resonance at around 210 ppm with a shoulder at its higher frequency side. This is different from the line shape observed for the sample at the end of the 1^{st} discharge (sample d:Li4.0), where a symmetric resonance at 210 ppm is present. This implies that the intercalated Li at these states are not in a single environment but are distributed over some distorted environments. However, the distribution of Li over these environments is similar for these two samples.

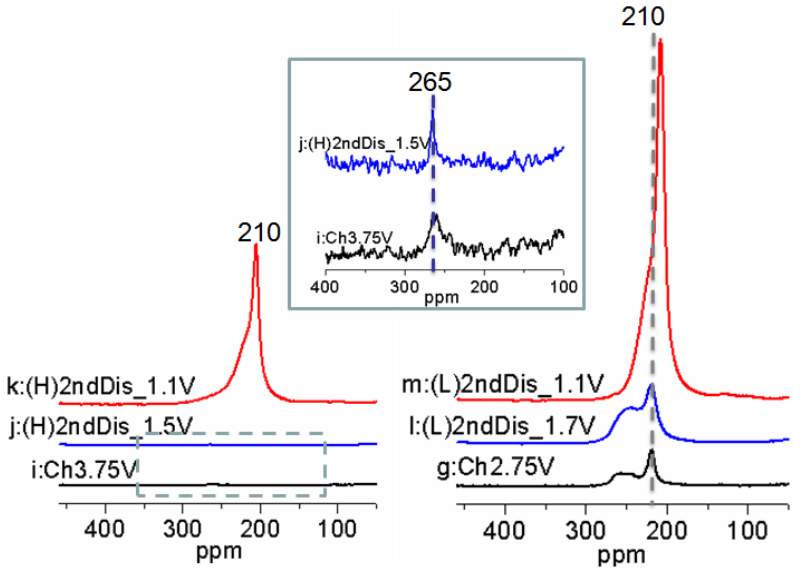

Figure 4.17. Zoomed view of the ^{7}Li NMR spectra of MnCu(II) phases during the 2nd discharge after being charged to 3.75 V (left), and 2.75 V (right). The spectra have been normalized based on the acquisition number and sample mass and the two groups of spectra are shown at the same scale. The inset shows the spectra for sample i and j (indicated by a gray rectangle box in the left) with a 20 times amplified magnitude.

4.3.5 Discussion

To provide a clear view, information regarding the involved redox species and phase transitions for each process during the 1st cycle is summarized in Figure 4.18. To rationalize the order of the redox processes, the structure of MnCu(II) has been examined carefully. The MnCu(II) structure contains rigid Perovskite-type oxide (Sr_2MnO_2) layers and relatively flexible antifluorite-type sulfide layers (Cu_2S). As a result of the interactions between the oxide and sulfide layers, the separation between the two neighboring S within the xy plane in the Cu_2S layer is the same as the Mn-Mn distance within the Perovskite layer. According to previous study, in pristine MnCu(II) phase, the Mn-Mn distance is 4.015 Å, i.e., twice the Mn-O bond length (2.0076Å) [13]. This distance, however, is slightly longer than the S-S distance within a close packed ideal Cu_2S framework, which is 3.94 Å [23]. This is consistent with the presence of 0.5 mole vacancy per formula unit, e.g., 1/8 vacant tetrahedral sites, and partial oxidation of the Mn^{2+} to Mn^{3+}. In this way, on one hand, accommodation of some vacancy allows the slight variation (increase) of the S-S distance within the sulfide layer, and on the other hand, oxidation of some Mn will result shortening of the Mn-O bond (as well as the Mn-Mn distance) in the oxide layer. The best match is then obtained with 1/8 vacancies. Consequently, the tetrahedral site in the sulfide layer in MnCu(II) is larger than that of Cu_2S, and considerable mobility of Cu at this site is observed [13]. When Li is inserted into the structure, it enters the vacancy or extrudes Cu from the tetrahedral site and forms the "Li_2S"-like environment. Since the shortest S-S distance in a close packed antifluorite type Li_2S structure is 4.036 Å, larger than the 4.015 Å S-S distance in the pristine

MnCu(II) phase, it requires an expansion of the S framework in the sulfide layers. Therefore, Mn reduction occurs and the Mn-O bond length increases, allowing the adjustment of the Perovskite framework to maintain a match (i.e., minimize the strain) between the oxide and sulfide layers. During this region, a solid-solution behavior is observed, indicating the continuous change of the parameters of the framework. As Mn reduction takes place prior to the reduction of Cu, it is very likely due to Li entering some of the vacant tetrahedral site first. At this stage, presumably the small feature at 2.2 V in the electrochemical profile, where no Cu is extruded (& reduced) and therefore, Mn is reduced to balance the charge. However, the stage is short, as the length of the 2.2 V feature is less than 0.5 Li, indicating that after this short stage, Li does not go into the vacant site exclusively but also takes the site occupied by Cu, and reduction of both Cu and Mn is then observed. After Mn is fully reduced, Cu is the only species that Is reduced, which means that the framework cannot accommodate more variations upon further Li insertion, and therefore a 2nd phase (the fully lithiated phase) starts to form.

During the following charge process, the delithiation processes and changes of the framework are more complicated. During the 1st process at around 1.8 V, as Li is removed from the structure, the "Li_2S"-like environment reduces notably. The re-insertion (oxidation) of Cu during this process, however, is not very significant. This may due to the lower diffusivity of Cu^+ than that of the Li^+, and when Li^+ is removed easily from the structure, Cu^+ cannot migrate into the structure and take the evacuated tetrahedral site immediately. Although there is no direct evidence at this point, it is very likely that considerable amount of vacancies are generated during this process, and

contraction of the S framework may occur. Although a formal $2S^{2-} \rightarrow S_2^{2-}$ reaction is not observed during this process, some electrons may be depleted from S and result a small increase of the overall oxidation state of S. Therefore, the charge compensation during this process may contribute from partial oxidation of both Cu and S. The contraction of the S framework may also explain the rising voltage for the following process (~2.5 V), since the energy required for further Li removal may increase as the tetrahedral site contracts.

During the 2.5 V process, "Li_2S"-like environment is further reduced and almost diminished at the end of this process. Although the S XANES results imply the vanishing of the "Li_2S" structure at the 2.75 V state, NMR results show there that still exists a small amount of Li in the structure, presumably due to the higher sensitivity of NMR than the XANES technique. The majority of Mn is oxidized during this process, as well as the Cu. The oxidation of Mn results in a reduction of the Mn-O bond length and, similar to the circumstances during the 1st discharge, a solid-solution behavior is observed during this region. As Cu is oxidized, it re-enters the structure and takes over the tetrahedral site from removed Li. In addition, formation of a small portion of S_2^{2-}-group is observed, indicating the oxidation of some S during this process. It is worth pointing out that after this process, e.g., at the 2.75 V state, insertion of Cu is not complete and there are very likely present more vacant tetrahedral sites than in the pristine phase. Discharging from this state, the process where Li enters the vacant tetrahedral site is expected to be more pronounced than in the pristine phase. In fact, the following 2nd discharge profile does show a more pronounced 2.2 V process than during the 1st discharge. In addition, the

oxysulfide framework at this state adopts a configuration which seems at an optimized point and is largely preserved during the following discharge/charge cycles.

Upon further charging, the 3.3 V process involves removal of the remaining small amount of Li and further oxidation (reinsertion) of Cu. Mn, however, is not oxidized to higher oxidation state even when the battery is charged to 3.75 V. The restriction on the Mn oxidation may come the same limitations for the structure of the framework in the pristine phase, that oxidation of Mn to higher oxidation state will result in the shortening of Mn-O bonds and the Mn-Mn (or O-O) distance, inducing too much strain between the two types of layers. At the 3.75 V state, the observed Cu oxidation state is even higher than that in the pristine phase, implying that some of the Cu is oxidized to Cu(II). This may result a contraction of the sulfide layer within the structure. In the following discharge from this point, since Li insertion requires an expansion of the sulfide layer, a larger variation of the S framework is expected. In fact, the S XANES results do indicate that the variations of the S framework during the 2^{nd} discharge after the 3.75 V state are much more significant than that from either the pristine phase or the 2.75 V state. The following discharge curve also shows a slightly more pronounced 2.2 V feature than during the 1^{st} discharge, which seems to imply the presence of more vacant tetrahedral site than in the pristine phase. This phenomenon may due to the reduced amount of Cu being re-inserted, as some Cu may dissolve in the electrolyte during the cycle. The loss of Cu may rationalize part of the capacity fading upon cycling.

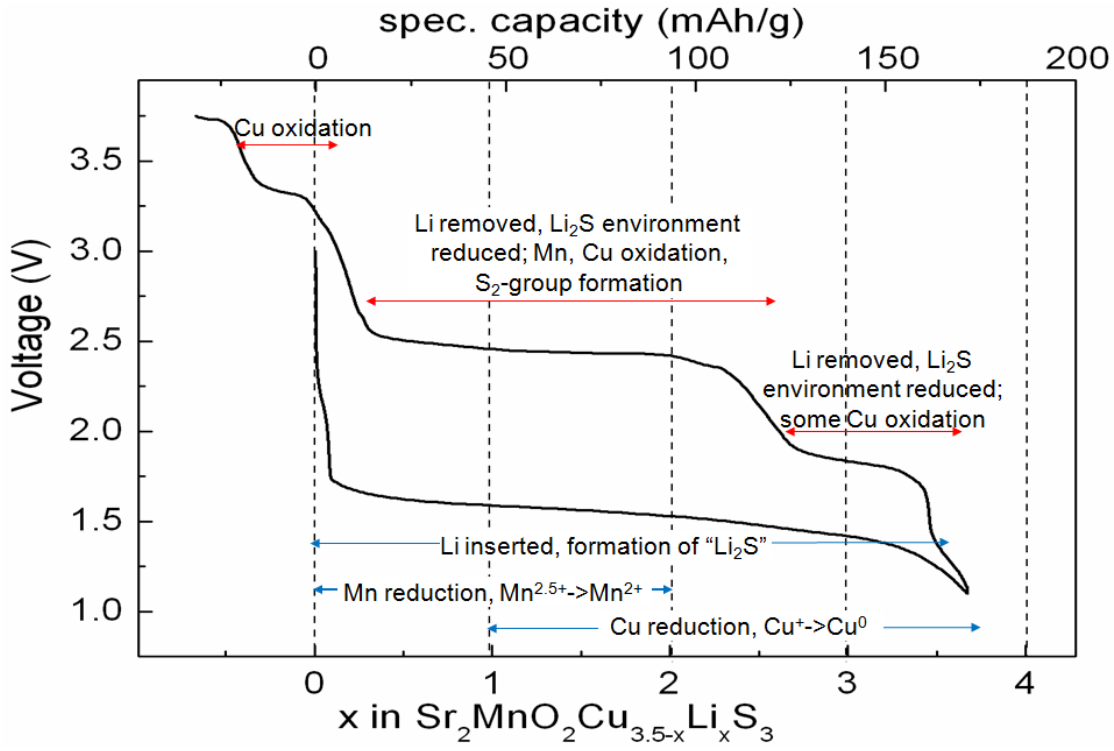

Figure 4.18. Summary of the redox reactions involved for each process during the 1st cycle of a MnCu(II)|Li battery within the voltage window 1.1 to 3.75 V. The discharge and charge processes are labeled with blue and red arrows respectively.

4.4 Conclusions

Layered oxysulfides $Sr_2MnO_2Cu_{2m-\delta}S_{m+1}$ (m = 1, 2 and 3, $\delta \sim 0.5$) consist of alternating Perovskite-type [Sr_2MnO_2] layer and antifluorite-type [Cu_2S] layer in the structure, and show reversible reactivity towards Li via a displacement mechanism. This paper presents the results of an intensive study on $Sr_2MnO_2Cu_{4-\delta}S_3$ (MnCu(II)), a representative member from this series, regarding to its electrochemical behavior and structural variations upon the (de)lithiation processes. The 1st discharge of MnCu(II) down to 1.1 V enables the insertion of about 4 Li into the structure, and exhibits a long pseudo-plateau feature. During this process, first, reduction of Mn from the oxide layer is observed, and then reduction of Cu from the sulfide layer and further reduction of Mn both take place, meanwhile the extrusion of Cu metal is observed, along with an expansion of the framework structure. The gradual formation of Li_2S-like structure is observed upon lithium insertion. The following charge (up to 3.75V), however, has a staircase-like voltage profile with three distinct processes at around 1.8, 2.5 and 3.3 V. The 1.8 V process involves the removal of Li and reduction of Li_2S-like structure, and a small amount of Cu metal is oxidized and re-inserted into the framework structure. Further removal of Li and oxidation of Cu occur during the 2.5 V process, along with the oxidation of Mn back to its valence state in pristine phase. As there still remains some un-oxidized Cu metal after the 2.5 V process, some of the tetrahedral sites in the sulfide layer are vacant, and the phase at this stage has more vacant tetrahedral sites than the pristine MnCu(II) phase. When the applied cutoff voltage to charge is 2.75 V, the following discharge curve shows different feature from the 1st discharge and a staircase-

like profile with two plateaus at 2.1 and 1.7 V are observed. The GITT results indicate that OCVs of these two processes at 2.1 and 1.7 V are the same as the 2.5 and 1.8 V processes in charge respectively, and within the voltage window of 1.1 to 2.75 V, good reversibility is observed. The 3.3 V process, which accounts for a small amount of capacity, shows up when the battery is charged to 3.75 V, and it has been ascribed to the oxidation of the residual Cu. As the average oxidation state of Cu at this stage is slightly higher than in the pristine phase, a small amount of Cu may be oxidized further to Cu(II). The structure of the MnCu(II) phase that charged to 3.75 V is largely restored to the pristine-like, and the following discharge curve displays a long pseudo-plateau very similar to the 1st one. However, the cycleability of MnCu(II) within the 1.1 to 3.75 V voltage window is much worse than in the 1.1 to 2.75 V range, and this indicates that the structure of the phase that is charged to 2.75 V has better structural stability than the 3.75 V phase. As the 2.75 V phase has more vacancies in the sulfide layer, the sulfur framework is thought to be more flexible and readily to accommodate structural changes upon (de)lithiation, while the sulfur framework in the 3.75 V state phase undergoes much more drastic changes during cycles.

In this study, we have examined the CDI reaction mechanism in a new system, the layered oxysulfide compounds containing anti-fluorite type Cu_2S motifs. At first glance, the oxide layers were expected to be inactive during the (de)lithiation processes and the copper sulfide layers to be directly involved. However, the results from this study have indicated that the involved processes are much more complicated than just the Li/Cu exchange within the copper sulfide layers. The transition metals in the other part of the

structure, for example, Mn in the studied system, may also play an important role. This work demonstrates the complexity of the displacement reactions in these layered oxysulfides. The valuable information obtained in this study may provide further insight in studying other structural related compounds, e.g., compounds containing copper sulfide layers, regarding their function in the lithium ion batteries.

References

1. Kepler, K.D., Vaughey, J.T., and Thackeray, M.M., Copper-tin anodes for rechargeable lithium batteries: an example of the matrix effect in an intermetallic system. *J.Power Sources*, 1999. **81**: p. 383-387.

2. Kepler, K.D., Vaughey, J.T., and Thackeray, M.M., $Li_xCu_6Sn_5$ ($0 < x < 13$): An intermetallic insertion electrode for rechargeable lithium batteries. *Electrochem. Solid State Lett.*, 1999. **2**(7): p. 307-309.

3. Thackeray, M.M., Vaughey, J.T., Johnson, C.S., Kropf, A.J., Benedek, R., Fransson, L.M.L., and Edstrom, K., Structural considerations of intermetallic electrodes for lithium batteries. *J. Power Sources*, 2003. **113**(1): p. 124-130.

4. Morcrette, M., Rozier, P., Dupont, L., Mugnier, E., Sannier, L., Galy, J., and Tarascon, J.M., A reversible copper extrusion-insertion electrode for rechargeable Li batteries. *Nat. Mater.*, 2003. **2**(11): p. 755-761.

5. Leising, R.A. and Takeuchi, E.S., Solid-state cathode materials for lithium batteries: effect of synthesis temperature on the physical and electrochemical properties of silver vanadium oxide. *Chem. Mater.*, 1993. **5**(5): p. 738-742.

6. Leising, R.A. and Takeuchi, E.S., Solid-State Synthesis and Characterization of Silver Vanadium Oxide for Use as a Cathode Material for Lithium Batteries. *Chem. Mater.*, 1994. **6**(4): p. 489-495.

7. Leising, R.A., Thiebolt, W.C., and Takeuchi, E.S., Solid-State Characterization of Reduced Silver Vanadium Oxide from the Li/SVO Discharge Reaction. *Inorg. Chem.*, 1994. **33**(25): p. 5733-5740.

8. Bodenez, V., Dupont, L., Morcrette, M., Surcin, C., Murphy, D.W., and Tarascon, J.M., Copper extrusion/reinjection in Cu-based thiospinels by electrochemical and chemical routes. *Chem. Mater.*, 2006. **18**(18): p. 4278-4287.

9. Bodenez, V., Dupont, L., Laffont, L., Armstrong, A.R., Shaju, K.M., Bruce, P.G., and Tarascon, J.M., The reaction of lithium with $CuCr_2S_4$ - lithium intercalation and copper displacement/extrusion. *J. Mater. Chem.*, 2007. **17**(30): p. 3238-3247.

10. Rozier, P., Morcrette, M., Szajwaj, O., Bodenez, V., Dolle, M., Surcin, C., Dupont, L., and Tarascon, J.M., Li-Driven Copper Extrusion/Re-injection in Various Cu-based Oxides and Sulfides. *Isr. J. Chem.*, 2008. **48**(3-4): p. 235-249.

11. Indris, S., Cabana, J., Rutt, O.J., Clarke, S.J., and Grey, C.P., Layered Oxysulfides $Sr_2MnO_2Cu_{2m-0.5}S_{m+1}$ (m=1, 2, and 3) as Insertion Hosts for Li ion batteries. *J. Am. Chem. Soc.*, 2006. **128**(41): p. 13354-13355.

12. Zhu, W.J. and Hor, P.H., Unusual layered transition-metal oxysulfides: $Sr_2Cu_2MO_2S_2$ (M=Mn, Zn). *J. Solid State Chem.*, 1997. **130**(2): p. 319-321.

13. Gal, Z.A., Rutt, O.J., Smura, C.F., Overton, T.P., Barrier, N., Clarke, S.J., and Hadermann, J., Structural chemistry and metamagnetism of an homologous series of layered manganese oxysulfides. *J. Am. Chem. Soc.*, 2006. **128**(26): p. 8530-8540.

14. Rutt, O.J., Williams, G.R., and Clarke, S.J., Reversible lithium insertion and copper extrusion in layered oxysulfides. *Chem. Commun.*, 2006(27): p. 2869-2871.

15. Morcrette, M., Chabre, Y., Vaughan, G., Amatucci, G., Leriche, J.-B., Patous, S., Masquelier, C., and Tarascon, J.-M., In situ X-ray diffraction techniques as a powerful tool to study battery electrode materials. *Electrochimica Acta*, 2002. **47**: p. 3137-3149.

16. Chung, J.-S. and Sohn, H.-J., Electrochemical behaviors of CuS as a cathode material for lithium secondary batteries. *J. Power Sources*, 2002. **108**: p. 226-231.

17. Yamakawa, N., Jiang, M., and Grey, C.P., Investigation of the Conversion Reaction Mechanisms for Binary Copper (II) Compunds by Solid-State NMR Spectroscopy and X-ray Diffraction. *Chem. Mater.*, 2009. **21**: p. 3162-3176.

18. Li, D., Bancroft, G.M., Kasrai, M., Fleet, M.E., Feng, X.H., Yang, B.X., and Tan, K.H., S K-Edge and L-Edge Xanes and Electronic-Structure of Some Copper Sulfide Minerals. *Phys. Chem. Minerals*, 1994. **21**(5): p. 317-324.

19. Pattrick, R.A.D., Mosselmans, J.F.W., Charnock, J.M., England, K.E.R., Helz, G.R., Garner, C.D., and Vaughan, D.J., The structure of amorphous copper sulfide

precipitates: An X-ray absorption study. *Geochimica et Cosmochimica Acta*, 1997. **61**(10): p. 2023-2036.

20. Wu, Z.Y., Ouvrard, G., Lemaux, S., Moreau, P., Gressier, P., Lemoigno, F., and Rouxel, J., Sulfur K-edge x-ray-absorption study of the charge transfer upon lithium intercalation into titanium disulfide. *Phys. Rev. Lett.*, 1996. **77**(10): p. 2101-2104.

21. Branci, C., Sarradin, J., Olivier-Fourcade, J., and Jumas, J.C., Lithium Insertion Mechanism in Tin-Based Spinel Sulfides. *Chem. Mater.*, 1999. **11**: p. 2846-2850.

22. Grey, C.P. and Dupré, N., NMR Studies of Cathode Materials for Lithium-Ion Rechargeable Batteries. *Chem. Rev.*, 2004. **104**: p. 4493-4512.

23. Vajenine, G.V. and Hoffmann, R., Compounds Containing Copper-Sulfur Layers: Electronic Structure, Conductivity, and Stability. *Inorg. Chem.*, 1996. **35**: p. 451-457.

Chapter 5 Conclusions

Two types of layered material, the oxides $Li[Ni_xMn_xCo_{(1-2x)}]O_2$ ($0 < x \leq 1/3$) series, and the oxysulfides $Sr_2MnO_2Cu_{2m-\delta}S_{m+1}$ (m = 1, 2 and 3, $\delta \sim 0.5$), have investigated regarding their applications as the positive electrode materials for rechargeable lithium ion batteries.

Several members of the $Li[Ni_xMn_xCo_{(1-2x)}]O_2$ ($0.01 \leq x \leq 1/3$) series, isostructural with layered $LiCoO_2$ (space group $R\bar{3}m$, No. 166), were synthesized. The XANES measurements show that these compounds contain Ni^{2+}, Mn^{4+} and Co^{3+} ions. The ^6Li MAS NMR spectra of the compounds show some common features. Several well resolved resonances can be observed in the compounds with low Ni/Mn contents, and when the amount of Ni and Mn increases, those resonances start to merge and finally form a broad resonance. The chemical environments of the resonances in the spectra for low Ni/Mn contents ($x \leq 0.10$) were assigned using prior NMR analyses of paramagnetic materials, based in the hyperfine shift due to each type of transition metal cation in the 1st and 2nd coordination shells. In the very dilute sample, $^6Li[Ni_{0.02}Mn_{0.02}Co_{0.96}]O_2$, analysis of the ^6Li MAS NMR spectra indicates the formation of Ni^{2+}/Mn^{4+} clusters in the predominantly Co^{3+} TM layers. Moreover, it has been found that the oxidation state of Ni in this high Co content sample is highly dependent on the starting Li/Transition Metal ratio, the NMR spectrum of a sample containing 5% Li excess showing peaks associated to the presence of Ni^{3+}. Neutron PDF analysis of $Li[Ni_{1/3}Mn_{1/3}Co_{1/3}]O_2$ shows a non-

random distribution of Ni and Mn cations in the TM layers, with Ni closer to Mn in the 1st coordination shell (resembling the $\left[\sqrt{3}\times\sqrt{3}\right]$ R30º-type superlattice structure model) but a more random distribution of Co. The ^{6}Li NMR spectrum of this compound and an analysis of the resonance due to Co^{3+} rich regions, for the whole $Li[Ni_xMn_xCo_{(1-2x)}]$ series, is also consistent with the PDF results, indicating a non-random distribution of transition metal cations in the TM layers that Ni and Mn show a strong tendency for clustering. The local ordering was correlated with variations in the mechanism of lithium intercalation with increased Ni/Mn content. The most significant change was the conversion of two-phase reaction due to an insulator to metal transition, as reported for stoichiometric $LiCoO_2$, first into a broader process and then the total disappearance of this process for $x \geq 0.20$. The decrease in the concentration of Co-rich clusters in the pristine materials as seen by NMR, tracked closely with these changes.

The structural changes of $Li[Ni_{0.05}Mn_{0.05}Co_{0.90}]O_2$ (**90Co**) upon lithium deintercalation has been investigated intensively. Two types of Ni-Mn pairs are proposed when exploring the Li local environment in the structure of pristine **90Co**. As Li is removed from the structure for $1.0 \geq x \geq 0.85$ (in $Li_x[Ni_{0.05}Mn_{0.05}Co_{0.90}]O_2$, Li*x*), the Li ions in the 1st coordination shell of the Mn^{4+} and/or Ni^{2+} ions are extracted first, the former being ascribed to the large Coulombic repulsion between Mn^{4+} and Li^{+},. Li ions in the 1st coordination shell of the electrochemically active Ni^{2+} are also removed in this charging regime. Li in the 2nd coordination shell of Ni are stabilized by the electrons in Ni^{2+} and Ni^{3+} e_g orbitals and removed at a later stage. Li removal from the 2nd coordination shell of Mn^{4+}, especially for ions distant from Ni, is more difficult. It also

appears that the Co^{3+} nearby Mn^{4+} is not readily oxidized, presumably again because of the formation of unfavorable Co^{4+}-Mn^{4+} interactions, particularly before the insulator-to-metal transition. At these SOCs, both Ni^{2+} and to a lesser degree Co^{3+} are electrochemically active species. Evidence for the oxidation of some of the Ni^{2+} to Ni^{4+} via Ni^{3+} is seen. When 15% of the Li is extracted, features characteristic of the formation of Co^{4+} with localized spins are observed. Metallic behavior is observed at $x \geq 0.80$, as shown by the observation of a Knight shifted resonance in the Li NMR spectrum. However, this insulator-to-metal transition does not result in a phase transition likely due to the presence of Ni-Mn clusters perturbing long-range electronic delocalization. On charging for $0.8 > x \geq 0.50$, the interlayer spacing keeps increasing, and the Knight shifted resonance gradually moves to higher frequency. The electrochemical profile of **90Co** shows a feature at Li0.50 similar to that observed in $LiCoO_2$, which is a result of lithium ordering at this SOC. Above x = 05, the NMR results for **90Co** are similar to those seen for Li_xCoO_2 system, the increased Co-O orbital hybridization (bonding) affecting the band structure, and thus the NMR behavior. Finally, when the battery is charged to even higher voltage (*ca.* 4.6 V), almost all the lithium ions are removed from the structure and the O3 to O1 phase transition occurs.

Layered oxysulfides $Sr_2MnO_2Cu_{2m-\delta}S_{m+1}$ (m = 1, 2 and 3, $\delta \sim 0.5$) consist of alternating Perovskite-type [Sr_2MnO_2] layer and antifluorite-type [Cu_2S] layer in the structure, and show reversible reactivity towards Li via a displacement mechanism. The electrochemical behavior of a representative member, $Sr_2MnO_2Cu_{4-\delta}S_3$ (MnCu(II)), and its structural variations during the (de)lithiation processes, have been studied intensively.

The 1st discharge of MnCu(II) down to 1.1 V enables the insertion of about 4 Li into the structure, and exhibits a long pseudo-plateau feature. During this process, first, reduction of Mn from the oxide layer is observed, and then reduction of Cu from the sulfide layer and further reduction of Mn both take place, meanwhile the extrusion of Cu metal is observed, along with an expansion of the framework structure. The gradual formation of Li_2S-like structure is observed upon lithium insertion. The following charge (up to 3.75V), however, has a staircase-like voltage profile with three distinct processes at around 1.8, 2.5 and 3.3 V. The 1.8 V process involves the removal of Li and reduction of Li_2S-like structure, and a small amount of Cu metal is oxidized and re-inserted into the framework structure. Further removal of Li and oxidation of Cu occur during the 2.5 V process, along with the oxidation of Mn back to its valence state in pristine phase. As there still remains some un-oxidized Cu metal after the 2.5 V process, some of the tetrahedral sites in the sulfide layer are vacant, and the phase at this stage has more vacant tetrahedral sites than the pristine MnCu(II) phase. When the applied cutoff voltage to charge is 2.75 V, the following discharge curve shows different feature from the 1st discharge and a staircase-like profile with two plateaus at 2.1 and 1.7 V are observed. The GITT results indicate that OCVs of these two processes at 2.1 and 1.7 V are the same as the 2.5 and 1.8 V processes in charge respectively, and within the voltage window of 1.1 to 2.75 V, good reversibility is observed. The 3.3 V process, accounts for a small amount of capacity, shows up when the battery is charged to 3.75 V, and it has been ascribed to the oxidation of the residual Cu. As the average oxidation state of Cu at this stage is slightly higher than in the pristine phase, a small amount of Cu may be oxidized further

to Cu(II). The structure of the MnCu(II) phase that charged to 3.75 V is largely restored to the pristine-like, and the following discharge curve displays a long pseudo-plateau very similar to the 1st one. However, the cycleability of MnCu(II) within the 1.1 to 3.75 V voltage window is much worse than in the 1.1 to 2.75 V range, and this indicates that the structure of the phase that is charged to 2.75 V has better structural stability than the 3.75 V phase. As the 2.75 V phase has more vacancies in the sulfide layer, the sulfur framework is thought to be more flexible and readily to accommodate structural changes upon (de)lithiation, while the sulfur framework in the 3.75 V state phase undergoes much more drastic changes during cycles.

Understanding the involved electrochemical processes from a fundamental point of view can provide valuable insight in recognizing the structure-properties relationship of the material and help design or search for new functional systems with desired performance features. The studies described in this dissertation have provided valuable information in understanding the intercalation and displacement reactions, and provide further insight into the structural features of these compounds.

References

Chapter 1

1. *BP Statistical Review of World Energy (June 2009)*. 2009.

2. *International Energy Outlook 2009*. 2009, Energy Information Administration, U.S. Department of Energy.

3. *Emissions of Greenhouse Gases in the United States 2008*, U.S.E.I. Administration, Editor. 2009, U.S. Department of Energy.

4. Winter, M. and R.J. Brodd, What Are Batteries, Fuel Cells, and Supercapacitors? *Chem. Rev.*, 2004. **104**: p. 4245-4269.

5. Tarascon, J.-M. and M. Armand, Issues and challenges facing rechargeable lithium batteries. *Nature*, 2001. **414**: p. 359-367.

6. Whittingham, M.S., Electrical Energy-storage and intercalation chemistry. *Science*, 1976. **192**(4244): p. 1126-1127.

7. Mohri, M., N. Yanagisawa, Y. Tajima, H. Tanaka, T. Mitate, S. Nakajima, M. Yoshida, Y. Yoshimoto, T. Suzuki, and H. Wada, Rechargeable lithium battery based pyrolytic carbon as a negative electrode. *J. Power Sources*, 1989. **26**(3-4): p. 545-551.

8. Mizushima, K., P.C. Jones, P.J. Wiseman, and J.B. Goodenough, Li_xCoO_2(0<x<-1): A new cathode material for batteries of high energy density. *Mater. Res. Bull.*, 1980. **15**(6): p. 783.

9. Nishi, Y., The Development of Lithium Ion Secondary Batteries. *Chem. Rec.*, 2001. **1**(5): p. 406-413.

10. Nagaura, T. and K. Tozawa, Lithium ion rechargeable battery. *Prog. Batteries Solar Cells*, 1990. **9**: p. 209-217.

11. Thackeray, M.M., W.I.F. David, P.G. Bruce, and J.B. Goodenough, Lithium insertion into manganese spinels. *Mat. Res. Bull.*, 1983. **18**(4): p. 461-472.

12. Amatucci, G. and J.M. Tarascon, Optimization of insertion compounds such as $LiMn_2O_4$ for Li-ion batteries. *J. Electrochem. Soc.*, 2002. **149**(12): p. K31-K46.

13. Johnson, C.S., J.S. Kim, C. Lefief, N. Li, J.T. Vaughey, and M.M. Thackeray, The significance of the Li_2MnO_3 component in 'composite' xLi_2MnO_3 •(1-x)$LiMn_{0.5}Ni_{0.5}O_2$ electrodes. *Electrochem. Commun.*, 2004. **6**(10): p. 1085-1091.

14. Johnson, C.S., N. Li, J.T. Vaughey, S.A. Hackney, and M.M. Thackeray, Lithium-manganese oxide electrodes with layered-spinel composite structures xLi_2MnO_3 •(1-x)$Li_{1+y}Mn_{2-y}O_4$ ($0 < x < 1$, $0 <= y <= 0.33$) for lithium batteries. *Electrochem. Commun.*, 2005. **7**(5): p. 528-536.

15. Thackeray, M.M., C.S. Johnson, J.T. Vaughey, N. Li, and S.A. Hackney, Advances in manganese-oxide 'composite' electrodes for lithium-ion batteries. *J. Mater. Chem.*, 2005. **15**(23): p. 2257-2267.

16. Padhi, A.K., K.S. Nanjundaswamy, and J.B. Goodenough, Phospho-olivines as positive-electrode materials for rechargeable lithium batteries. *J. Electrochem.Soc.*, 1997. **144**(4): p. 1188-1194.

17. Chung, S.Y., J.T. Bloking, and Y.M. Chiang, Electronically conductive phospho-olivines as lithium storage electrodes. *Nat. Mater.*, 2002. **1**(2): p. 123-128.

18. Herle, P.S., B. Ellis, N. Coombs, and L.F. Nazar, Nano-network electronic conduction in iron and nickel olivine phosphates. *Nat. Mater.*, 2004. **3**(3): p. 147-152.

19. Ravet, N., Y. Chouinard, J.F. Magnan, S. Besner, M. Gauthier, and M. Armand, Electroactivity of natural and synthetic triphylite. *J. Power Sources*, 2001. **97-8**: p. 503-507.

20. Yamada, A., S.C. Chung, and K. Hinokuma, Optimized $LiFePO_4$ for lithium battery cathodes. *J. Electrochem. Soc.*, 2001. **148**(3): p. A224-A229.

21. Arnold, G., J. Garche, R. Hemmer, S. Strobele, C. Vogler, and A. Wohlfahrt-Mehrens, Fine-particle lithium iron phosphate $LiFePO_4$ synthesized by a new low-cost aqueous precipitation technique. *J. Power Sources*, 2003. **119**: p. 247-251.

22. Kwon, S.J., C.W. Kim, W.T. Jeong, and K.S. Lee, Synthesis and electrochemical properties of olivine $LiFePO_4$ as a cathode material prepared by mechanical alloying. *J.Power Sources*, 2004. **137**(1): p. 93-99.

23. Dominko, R., J.M. Goupil, M. Bele, M. Gaberscek, M. Remskar, D. Hanzel, and J. Jamnik, Impact of $LiFePO_4$/C composites porosity on their electrochemical performance. *J. Electrochem. Soc.*, 2005. **152**(5): p. A858-A863.

24. http://www.a123systems.com/.

25. Thackeray, M., Lithium-ion batteries - An unexpected conductor. *Nat. Mater.*, 2002. **1**(2): p. 81-82.

26. Malini, R., U. Uma, T. Sheela, M. Ganesan, and N.G. Renganathan, Conversion reactions: a new pathway to realise energy in lithium-ion battery-review. *Ionics*, 2009. **15**(3): p. 301-307.

27. Poizot, P., S. Laruelle, S. Grugeon, L. Dupont, and J.M. Tarascon, Nano-sized transition-metaloxides as negative-electrode materials for lithium-ion batteries. *Nature*, 2000. **407**(6803): p. 496-499.

28. Amatucci, G.G. and N. Pereira, Fluoride based electrode materials for advanced energy storage devices. *J. Fluorine Chem.*, 2007. **128**(4): p. 243-262.

29. Bervas, M., F. Badway, L.C. Klein, and G.G. Amatucci, Bismuth fluoride nanocomposite as a positive electrode material for rechargeable lithium batteries. *Electrochem. Solid State Lett.*, 2005. **8**(4): p. A179-A183.

30. Badway, F., A.N. Mansour, N. Pereira, J.F. Al-Sharab, F. Cosandey, I. Plitz, and G.G. Amatucci, Structure and electrochemistry of copper fluoride nanocomposites utilizing mixed conducting matrices. *Chem. Mater.*, 2007. **19**(17): p. 4129-4141.

31. Kepler, K.D., J.T. Vaughey, and M.M. Thackeray, $Li_xCu_6Sn_5$ ($0 < x < 13$): An intermetallic insertion electrode for rechargeable lithium batteries. *Electrochem. Solid State Lett.*, 1999. **2**(7): p. 307-309.

32. Kepler, K.D., J.T. Vaughey, and M.M. Thackeray, Copper-tin anodes for rechargeable lithium batteries: an example of the matrix effect in an intermetallic system. *J.Power Sources*, 1999. **81**: p. 383-387.

33. Thackeray, M.M., J.T. Vaughey, C.S. Johnson, A.J. Kropf, R. Benedek, L.M.L. Fransson, and K. Edstrom, Structural considerations of intermetallic electrodes for lithium batteries. *J. Power Sources*, 2003. **113**(1): p. 124-130.

34. Morcrette, M., P. Rozier, L. Dupont, E. Mugnier, L. Sannier, J. Galy, and J.M. Tarascon, A reversible copper extrusion-insertion electrode for rechargeable Li batteries. *Nat. Mater.*, 2003. **2**(11): p. 755-761.

35. Tarascon, J.M., S. Grugeon, M. Morcrette, S. Laruelle, P. Rozier, and P. Piozot, New concepts for the search of better electrode materials for rechargeable lithium batteries. *Comptes Rendus Chimie*, 2005. **8**: p. 9-15.

36. Leising, R.A. and E.S. Takeuchi, Solid-state cathode materials for lithium batteries: effect of synthesis temperature on the physical and electrochemical properties of silver vanadium oxide. *Chem. Mater.*, 1993. **5**(5): p. 738-742.

37. Leising, R.A., W.C. Thiebolt, and E.S. Takeuchi, Solid-State Characterization of Reduced Silver Vanadium Oxide from the Li/SVO Discharge Reaction. *Inorg. Chem.*, 1994. **33**(25): p. 5733-5740.

38. Leising, R.A. and E.S. Takeuchi, Solid-State Synthesis and Characterization of Silver Vanadium Oxide for Use as a Cathode Material for Lithium Batteries. *Chem. Mater.*, 1994. **6**(4): p. 489-495.

39. Bodenez, V., L. Dupont, M. Morcrette, C. Surcin, D.W. Murphy, and J.M. Tarascon, Copper extrusion/reinjection in Cu-based thiospinels by electrochemical and chemical routes. *Chem. Mater.*, 2006. **18**(18): p. 4278-4287.

40. Indris, S., J. Cabana, O.J. Rutt, S.J. Clarke, and C.P. Grey, Layered Oxysulfides $Sr_2MnO_2Cu_{2m-0.5}S_{m+1}$ (m=1, 2, and 3) as Insertion Hosts for Li ion batteries. *J. Am. Chem. Soc.*, 2006. **128**(41): p. 13354-13355.

41. Rozier, P., M. Morcrette, O. Szajwaj, V. Bodenez, M. Dolle, C. Surcin, L. Dupont, and J.M. Tarascon, Li-Driven Copper Extrusion/Re-injection in Various Cu-based Oxides and Sulfides. *Isr. J. Chem.*, 2008. **48**(3-4): p. 235-249.

42. Bodenez, V., L. Dupont, L. Laffont, A.R. Armstrong, K.M. Shaju, P.G. Bruce, and J.M. Tarascon, The reaction of lithium with $CuCr_2S_4$ - lithium intercalation and copper displacement/extrusion. *J. Mater. Chem.*, 2007. **17**(30): p. 3238-3247.

43. Armand, M. and J.M. Tarascon, Building better batteries. *Nature*, 2008. **451**(7179): p. 652-657.

44. Palacin, M.R., Recent advances in rechargeable battery materials: a chemist's perspective. *Chem. Soc. Rev.*, 2009. **38**(9): p. 2565-2575.

45. Winter, M., J.O. Besenhard, M.E. Spahr, and P. Novak, Insertion electrode materials for rechargeable lithium batteries. *Adv. Mater.*, 1998. **10**(10): p. 725-763.

46. Amatucci, G.G., J.-M. Tarascon, and L.C. Klein, CoO_2, The End Memeber of the Li_xCoO_2 Solid Solution. *J. Electrochem. Soc.*, 1996. **143**(3): p. 1114-1123.

47. Ozawa, K., Lithium-ion rechargeable batteries with $LiCoO_2$ and carbon electrodes - the $LiCoO_2$ C system. *Solid State Ionics*, 1994. **69**(3-4): p. 212-221.

48. Wang, H.F., Y.I. Jang, B.Y. Huang, D.R. Sadoway, and Y.T. Chiang, TEM study of electrochemical cycling-induced damage and disorder in $LiCoO_2$ cathodes for rechargeable lithium batteries. *J. Electrochem. Soc.*, 1999. **146**(2): p. 473-480.

49. Reimers, J.N. and J.R. Dahn, Electrochemical and *In situ* X-Ray Diffraction Studies of Lithium Intercalation in Li_xCoO_2. *J. Electrochem. Soc.*, 1992. **139**(8): p. 2091-2097.

50. Morcrette, M., Y. Chabre, G. Vaughan, G. Amatucci, J.-B. Leriche, S. Patous, C. Masquelier, and J.-M. Tarascon, In situ X-ray diffraction techniques as a powerful tool to study battery electrode materials. *Electrochimica Acta*, 2002. **47**: p. 3137-3149.

51. Ménétrier, M., I. Saadoune, S. Levasseur, and C. Delmas, The insulator-metal transition upon lithium deintercalation from $LiCoO_2$: electronic properties and ^7Li NMR study. *J. Mater. Chem.*, 1999. **9**: p. 1135-1140.

52. Mukai, K., Y. Ikedo, H. Nozaki, J. Sugiyama, K. Nishiyama, D. Andreica, A. Amato, P.L. Russo, E.J. Ansaldo, J.H. Brewer, K.H. Chow, K. Ariyoshi, and T. Ohzuku, Magnetic phase diagram of layered cobalt dioxide Li_xCoO_2. *Phys. Rev. Lett.*, 2007. **99**.

53. Van der Ven, A., M.K. Aydinol, and G. Ceder, First-Principles Evidence for Stage Ordering in Li_xCoO_2. *J. Electrochem. Soc.*, 1998. **145**(6): p. 2149-2155.

54. Alcántara, R., P. Lavela, J.L. Tirado, R. Stoyanova, and E. Zhecheva, Structure and electrochemical properties of boron-doped $LiCoO_2$. *J. Solid State Chem.*, 1997. **134**(2): p. 265-273.

55. Antonijevic, S. and S. Wimperis, Refocussing of chemical and paramagnetic shift anisotropies in H-2 NMR using the quadrupolar-echo experiment. *J. Magn. Reson.*, 2003. **164**(2): p. 343-350.

56. Levasseur, S., M. Ménétrier, and C. Delmas, On the $Li_xCo_{1-y}Mg_yO_2$ system upon deintercalation: electrochemical, electronic properties and Li-7 MAS NMR studies. *J. Power Sources*, 2002. **112**(2): p. 419-427.

57. Myung, S.T., N. Kumagai, S. Komaba, and H.T. Chung, Effects of Al doping on the microstructure of $LiCoO_2$ cathode materials. *Solid State Ionics*, 2001. **139**(1-2): p. 47-56.

58. Castro-Garcia, S., A. Castro-Couceiro, M.A. Senaris-Rodriguez, F. Soulette, and C. Julien, Influence of aluminum doping on the properties of $LiCoO_2$ and $LiNi_{0.5}Co_{0.5}O_2$ oxides. *Solid State Ionics*, 2003. **156**(1-2): p. 15-26.

59. Aurbach, D., B. Markovsky, A. Rodkin, E. Levi, Y.S. Cohen, H.J. Kim, and M. Schmidt, On the capacity fading of $LiCoO_2$ intercalation electrodes: the effect of cycling, storage, temperature, and surface film forming additives. *Electrochimica Acta*, 2002. **47**(27): p. 4291-4306.

60. Cho, J., Y.J. Kim, and B. Park, Novel $LiCoO_2$ cathode material with Al_2O_3 coating for a Li ion cell. *Chem. Mater.*, 2000. **12**(12): p. 3788-3791.

61. Cho, J., Y.J. Kim, and B. Park, $LiCoO_2$ cathode material that does not show a phase transition from hexagonal to monoclinic phase. *J. Electrochem. Soc.*, 2001. **148**(10): p. A1110-A1115.

62. Chen, Z.H. and J.R. Dahn, Studies of $LiCoO_2$ coated with metal oxides. *Electrochem. Solid State Lett.*, 2003. **6**(11): p. A221-A224.

63. Cho, J., T.J. Kim, Y.J. Kim, and B. Park, High-performance ZrO_2-coated $LiNiO_2$ cathode material. *Electrochem. Solid State Lett.*, 2001. **4**(10): p. A159-A161.

64. Chen, Z.H. and J.R. Dahn, Effect of a ZrO_2 coating on the structure and electrochemistry of Li_xCoO_2 when cycled to 4.5 V. *Electrochem. Solid State Lett.*, 2002. **5**(10): p. A213-A216.

65. Kannan, A.M., L. Rabenberg, and A. Manthiram, High capacity surface-modified $LiCoO_2$ cathodes for lithium-ion batteries. *Electrochem. Solid State Lett.*, 2003. **6**(1): p. A16-A18.

66. Mladenov, M., R. Stoyanova, E. Zhecheva, and S. Vassilev, Effect of Mg doping and MgO-surface modification on the cycling stability of $LiCoO_2$ electrodes. *Electrochem. Commun.*, 2001. **3**(8): p. 410-416.

67. Wang, Z.X., X.J. Huang, and L.Q. Chen, Performance improvement of surface-modified $LiCoO_2$ cathode materials - An infrared absorption and X-ray photoelectron spectroscopic investigation. *J. Electrochem. Soc.*, 2003. **150**(2): p. A199-A208.

68. Sun, Y.K., J.M. Han, S.T. Myung, S.W. Lee, and K. Amine, Significant improvement of high voltage cycling behavior AlF_3-coated $LiCoO_2$ cathode. *Electrochem. Commun.*, 2006. **8**(5): p. 821-826.

69. Dahn, J.R., U. von Sacken, and C.A. Michal, Structure and electrochemistry of $Li_{1\pm y}NiO_2$ and a new Li_2NiO_2 phase withe the $Ni(OH)_2$ structure *Solid State Ionics*, 1990. **44**(1-2): p. 87-97.

70. Saadoune, I. and C. Delmas, $LiNi_{1-y}Co_yO_2$ positive electrode materials: relationships between the structure, physical properties and electrochemical behaviour. *J. Mater. Chem.*, 1996. **6**: p. 193-199.

71. Capitaine, F., P. Gravereau, and C. Delmas, A new variety of $LiMnO_2$ with a layered structure. *Solid State Ionics*, 1996. **89**: p. 197-202.

72. Rossen, E., C.D.W. Jones, and J.R. Dahn, Structure and electrochemistry of $Li_xMn_yNi_{1-y}O_2$. *Solid State Ionics*, 1992. **57**(3-4): p. 311-318.

73. Ohzuku, T. and Y. Makimura, Layered Lithium Insertion Material of $LiNi_{1/2}Mn_{1/2}O_2$: A Possible Alternative to $LiCoO_2$ for Advanced Lithium-Ion Batteries. *Chem. Lett.*, 2001: p. 744-745.

74. Liu, Z., A. Yu, and J.Y. Lee, Synthesis and characterization of $LiNi_{1-x-y}Co_xMn_yO_2$ as the cathode materials of secondary lithium batteries. *J.Power Sources*, 1999. **81-82**: p. 416-419.

75. Yoshio, M., H. Noguchi, J.-i. Itoh, M. Okada, and T. Mouri, Preparation and properties of $LiCo_yMn_xNi_{1-x-y}O_2$ as a cathode for lithium ion batteries. *J. Power Sources*, 2000. **90**: p. 176-181.

76. Ohzuku, T. and Y. Makimura, Layered Lithium Insertion Material of $LiCo_{1/3}Ni_{1/3}Mn_{1/3}O_2$ for Lithium-Ion Batteries. *Chem. Lett.*, 2001: p. 642-643.

77. Lu, Z., D.D. MacNeil, and J.R. Dahn, Layered $Li[Ni_xCo_{1-2x}Mn_x]O_2$ Cathode Materials for Lithium Ion Batteries. *Electrochem. Solid-St. Lett.*, 2001. **4**(12): p. A200-A203.

78. Shaju, K.M., G.V.S. Rao, and B.V.R. Chowdari, Performance of layered $Li(Ni_{1/3}Co_{1/3}Mn_{1/3})O_2$ as cathode for Li-ion batteries. *Electrochimica Acta*, 2002. **48**: p. 145-151.

79. Hwang, B.J., Y.W. Tsai, D. Carlier, and G. Ceder, A Combined Computational/Experimental Study on $LiNi_{1/3}Co_{1/3}Mn_{1/3}O_2$. *Chem. Mater.*, 2003. **15**: p. 3676-3682.

80. Koyama, Y., I. Tanaka, H. Adachi, Y. Makimura, and T. Ohzuku, Crystal and electronic structures of superstructural $Li_{1-x}[Co_{1/3}Ni_{1/3}Mn_{1/3}]O_2$ ($0 \leqslant x \leqslant 1$). *J. Power Sources*, 2003. **119-121**: p. 644-648.

81. Koyama, Y., N. Yabuuchi, I. Tanaka, H. Adachi, and T. Ohzuku, Solid-State Chemistry and Electrochemistry of $LiCo_{1/3}Ni_{1/3}Mn_{1/3}O_2$ for Advanced Lithium-Ion Batteries. *J. Electrochem. Soc.*, 2004. **151**(10): p. A1545-A1551.

82. Kang, K., Y.S. Meng, J. Bréger, C.P. Grey, and G. Ceder, Electrodes with High Power and High Capacity for Rechargeable Lithium Batteries. *Science*, 2006. **311**: p. 977-980.

83. MacNeil, D.D., Z. Lu, and J.R. Dahn, Structure and electrochemistry of $Li[Ni_xCo_{1-2x}Mn_x]O_2$ ($0 <= x <= 1/2$). *J. Electrochem. Soc.*, 2002. **149**(10): p. A1332-A1336.

84. Jouanneau, S., D.D. MacNeil, Z. Lu, S.D. Beattie, G. Murphy, and J.R. Dahn, Morphology and Safety of $Li[Ni_xCo_{1-2x}Mn_x]O_2$ ($0 \leqslant x \leqslant 1/2$). *J. Electrochem. Soc.*, 2003. **150**(10): p. A1299-A1304.

85. Yoon, W.-S., C.P. Grey, M. Balasubramanian, X.-Q. Yang, D.A. Fischer, and J. McBreen, Combined NMR and XAS Study on Local Environments and Electronic Structures of Electrochemcally Li-Ion Deintercalated $Li_{1-x}Co_{1/3}Ni_{1/3}Mn_{1/3}O_2$ Electrode System. *Electrochem. Solid-St. Lett.*, 2004. **7**(3): p. A53-A55.

86. Yoon, W.-S., M. Balasubramanian, K.Y. Chung, X.-Q. Yang, J. McBreen, C.P. Grey, and D.A. Fischer, Investigation of the Charge Compensation Mechanism on the Electrochemically Li-Ion Deintercalated $Li_{1-x}Co_{1/3}Ni_{1/3}Mn_{1/3}O_2$ Electrode System by Combination of Soft and Hard X-ray Absorption Spectroscopy. *J. Am. Chem. Soc.*, 2005. **127**: p. 17479-17487.

87. Spahr, M.E., P. Novak, B. Schnyder, O. Haas, and R. Nesper, Characterization of layered lithium nickel manganese oxides synthesized by a novel oxidative coprecipitation method and their electrochemical performance as lithium insertion electrode materials. *J. Electrochem. Soc.*, 1998. **145**(4): p. 1113-1121.

88. Bréger, J., N. Dupré, P.J. Chupas, P.L. Lee, T. Proffen, J.B. Parise, and C.P. Grey, Short- and Long-Range Order in the Positive Electrode Material, $Li(NiMn)_{0.5}O_2$: A Joint X-ray and Neutron Diffraction Pair Distribution Function Analysis and NMR Study. *J. Am. Chem. Soc.*, 2005. **127**: p. 7529-7537.

89. Bréger, J., K. Kang, J. Cabana, G. Ceder, and C.P. Grey, NMR, PDF and RMC study of the positive electrode material $Li(Ni_{0.5}Mn_{0.5})O_2$ synthesized by ion-exchage methods. *J. Mater. Chem.*, 2007. **17**: p. 3167-3174.

90. Zhu, W.J. and P.H. Hor, Unusual layered transition-metal oxysulfides: $Sr_2Cu_2MO_2S_2$ (M=Mn, Zn). *J. Solid State Chem.*, 1997. **130**(2): p. 319-321.

91. Gal, Z.A., O.J. Rutt, C.F. Smura, T.P. Overton, N. Barrier, S.J. Clarke, and J. Hadermann, Structural chemistry and metamagnetism of an homologous series of layered manganese oxysulfides. *J. Am. Chem. Soc.*, 2006. **128**(26): p. 8530-8540.

92. Rutt, O.J., G.R. Williams, and S.J. Clarke, Reversible lithium insertion and copper extrusion in layered oxysulfides. *Chem. Commun.*, 2006(27): p. 2869-2871.

93. Grey, C.P. and N. Dupré, NMR Studies of Cathode Materials for Lithium-Ion Rechargeable Batteries. *Chem. Rev.*, 2004. **104**: p. 4493-4512.

94. Levitt, M.H., *Spin dynamics: basics of nuclear magnetic resonance* 2001: John Wiley & Sons Ltd.

95. Kittel, C., *Introduction to Solid State Physics*. 6th ed. 1986: John Wiley & Sons, New York.

96. Carrington, A. and A.D. McLachlan, *Introduction to Magnetic Resonance*. 1967, Harper and Row: New York.

97. Andrew, E.R., A. Bradbury, and R.G. Eades, Nuclear Magnetic Resonance Spectra from a Crystal Roatated at High Speed. *Nature*, 1958. **182**(4650): p. 1659-1659.

98. Yoon, W.-S., Y. Paik, X.-Q. Yang, M. Balasubramanian, J. McBreen, and C.P. Grey, Investigation of the Local Structure of the $LiNi_{0.5}Mn_{0.5}O_2$ Cathode Material during Electrochemical Cycling by X-Ray Absorption and NMR Spectroscopy. *Electrochem. Solid-St. Lett.*, 2002. **5**(11): p. A263-A266.

99. Pan, C., Y.J. Lee, B. Ammundsen, and C.P. Grey, ^{6}Li MAS NMR Studies of the Local Structure and Electrochemical Properties of Cr-doped Lithium Manganese and Lithium Cobalt Oxide Cathode Materials for Lithium-Ion Batteries. *Chem. Mater.*, 2002. **14**: p. 2289-2299.

100. Carlier, D., M. Ménétrier, C.P. Grey, C. Delmas, and G. Ceder, Understanding the NMR shifts in paramagnetic transition metal oxides using density functional theory calculations. *Phys. Rev. B*, 2003. **67**: p. 174103.

Chapter 2

1. Dahn, J.R., U. von Sacken, and C.A. Michal, Structure and electrochemistry of $Li_{1\pm y}NiO_2$ and a new Li_2NiO_2 phase withe the $Ni(OH)_2$ structure *Solid State Ionics*, 1990. **44**(1-2): p. 87-97.

2. Saadoune, I. and C. Delmas, $LiNi_{1-y}Co_yO_2$ positive electrode materials: relationships between the structure, physical properties and electrochemical behaviour. *J. Mater. Chem.*, 1996. **6**: p. 193-199.

3. Capitaine, F., P. Gravereau, and C. Delmas, A new variety of $LiMnO_2$ with a layered structure. *Solid State Ionics*, 1996. **89**: p. 197-202.

4. Rossen, E., C.D.W. Jones, and J.R. Dahn, Structure and electrochemistry of $Li_xMn_yNi_{1-y}O_2$. *Solid State Ionics*, 1992. **57**(3-4): p. 311-318.

5. Ohzuku, T. and Y. Makimura, Layered Lithium Insertion Material of $LiNi_{1/2}Mn_{1/2}O_2$: A Possible Alternative to $LiCoO_2$ for Advanced Lithium-Ion Batteries. *Chem. Lett.*, 2001: p. 744-745.

6. Liu, Z., A. Yu, and J.Y. Lee, Synthesis and characterization of $LiNi_{1-x-y}Co_xMn_yO_2$ as the cathode materials of secondary lithium batteries. *J.Power Sources*, 1999. **81-82**: p. 416-419.

7. Yoshio, M., H. Noguchi, J.-i. Itoh, M. Okada, and T. Mouri, Preparation and properties of $LiCo_yMn_xNi_{1-x-y}O_2$ as a cathode for lithium ion batteries. *J. Power Sources*, 2000. **90**: p. 176-181.

8. Ohzuku, T. and Y. Makimura, Layered Lithium Insertion Material of $LiCo_{1/3}Ni_{1/3}Mn_{1/3}O_2$ for Lithium-Ion Batteries. *Chem. Lett.*, 2001: p. 642-643.

9. Lu, Z., D.D. MacNeil, and J.R. Dahn, Layered $Li[Ni_xCo_{1-2x}Mn_x]O_2$ Cathode Materials for Lithium Ion Batteries. *Electrochem. Solid-St. Lett.*, 2001. **4**(12): p. A200-A203.

10. Hwang, B.J., Y.W. Tsai, D. Carlier, and G. Ceder, A Combined Computational/Experimental Study on $LiNi_{1/3}Co_{1/3}Mn_{1/3}O_2$. *Chem. Mater.*, 2003. **15**: p. 3676-3682.

11. Rougier, A. and C. Delmas, Non-cooperative Jahn-Teller effect in $LiNiO_2$: an EXAFS study. *Solid State Commun.*, 1995. **94**(2): p. 123-127.

12. MacNeil, D.D., Z. Lu, and J.R. Dahn, Structure and electrochemistry of $Li[Ni_xCo_{1-2x}Mn_x]O_2$ ($0 <= x <= 1/2$). *J. Electrochem. Soc.*, 2002. **149**(10): p. A1332-A1336.

13. Shaju, K.M., G.V.S. Rao, and B.V.R. Chowdari, Performance of layered $Li(Ni_{1/3}Co_{1/3}Mn_{1/3})O_2$ as cathode for Li-ion batteries. *Electrochimica Acta*, 2002. **48**: p. 145-151.

14. Yoon, W.-S., C.P. Grey, M. Balasubramanian, X.-Q. Yang, D.A. Fischer, and J. McBreen, Combined NMR and XAS Study on Local Environments and Electronic Structures of Electrochemcally Li-Ion Deintercalated $Li_{1-x}Co_{1/3}Ni_{1/3}Mn_{1/3}O_2$ Electrode System. *Electrochem. Solid-St. Lett.*, 2004. **7**(3): p. A53-A55.

15. Yoon, W.-S., M. Balasubramanian, K.Y. Chung, X.-Q. Yang, J. McBreen, C.P. Grey, and D.A. Fischer, Investigation of the Charge Compensation Mechanism on the Electrochemically Li-Ion Deintercalated $Li_{1-x}Co_{1/3}Ni_{1/3}Mn_{1/3}O_2$ Electrode System by Combination of Soft and Hard X-ray Absorption Spectroscopy. *J. Am. Chem. Soc.*, 2005. **127**: p. 17479-17487.

16. Yoon, W.-S., S. Iannopollo, C.P. Grey, D. Carlier, J. Gorman, J. Reed, and G. Ceder, Local Structure and Cation Ordering in O3 Lithium Nickel Manganese Oxides with Stoichiometry $Li[Ni_xMn_{(2-x)/3}Li_{(1-2x)/3}]O_2$ -NMR Studies and First Principles Calculations. *Electrochem. Solid-St. Lett.*, 2004. **7**(7): p. A167-A171.

17. Bréger, J., N. Dupré, P.J. Chupas, P.L. Lee, T. Proffen, J.B. Parise, and C.P. Grey, Short- and Long-Range Order in the Positive Electrode Material, $Li(NiMn)_{0.5}O_2$: A Joint X-ray and Neutron Diffraction Pair Distribution Function Analysis and NMR Study. *J. Am. Chem. Soc.*, 2005. **127**: p. 7529-7537.

18. Bréger, J., K. Kang, J. Cabana, G. Ceder, and C.P. Grey, NMR, PDF and RMC study of the positive electrode material $Li(Ni_{0.5}Mn_{0.5})O_2$ synthesized by ion-exchage methods. *J. Mater. Chem.*, 2007. **17**: p. 3167-3174.

19. Cahill, L.S., S.-C. Yin, A. Samoson, I. Heinmaa, L.F. Nazar, and G.R. Goward, ^6Li NMR Studies of Cation Disorder and Transition Metal Ordering in $Li[Ni_{1/3}Mn_{1/3}Co_{1/3}]O_2$ Using Ultrafast Magic Angle Spinning. *Chem. Mater.*, 2005. **17**: p. 6560-6566.

20. Carlier, D., M. Ménétrier, C.P. Grey, C. Delmas, and G. Ceder, Understanding the NMR shifts in paramagnetic transition metal oxides using density functional theory calculations. *Phys. Rev. B*, 2003. **67**: p. 174103.

21. Grey, C.P. and N. Dupré, NMR Studies of Cathode Materials for Lithium-Ion Rechargeable Batteries. *Chem. Rev.*, 2004. **104**: p. 4493-4512.

22. Jouanneau, S. and J.R. Dahn, Preparation, Structure, and THermal Stability of New $Ni_xCo_{1-2x}Mn_x(OH)_2$ ($0 \leqslant x \leqslant 1/2$) Phases. *Chem. Mater.*, 2003. **15**: p. 495-499.

23. Saadoune, I., M. Ménétrier, and C. Delmas, Redox processes in $Li_xNi_{1-y}Co_yO_2$ cobalt-rich phases. *J. Mater. Chem.*, 1997. **7**: p. 2505-2511.

24. Kang, K., D. Carlier, J. Reed, E.M. Arroyo, G. Ceder, L. Croguennec, and C. Delmas, Synthesis and Electrochemical Properties of Layered $Li_{0.9}Ni_{0.45}Ti_{0.55}O_2$. *Chem. Mater.*, 2003. **15**: p. 4503-4507.

25. Bréger, J., M. Jiang, N. Dupré, Y.S. Meng, Y. Shao-Horn, G. Ceder, and C.P. Grey, High-resolution X-ray diffraction, DIFFaX, NMR and first principles study of disorder in the Li_2MnO_3-$Li[Ni_{1/2}Mn_{1/2}]O_2$ solid solution. *J. Solid State Chem.*, 2005. **178**: p. 2575-2585.

26. Rietveld, H.M., A Profile Refinement Method for Nuclear and Magnetic Structures. *J. Appl. Crystallogr.*, 1969. **2**: p. 65.

27. Larson, A.C. and R.B. Von Dreele, *General Structure Analysis System (GSAS), Los Alamos National Laboratory Report LAUR 86-748*. 1987.

28. Toby, B.H., EXPGUI, a graphical user interface for GSAS. *J. Appl. Crystallogr.*, 2001. **34**: p. 210.

29. Peterson, P.F., M. Gutmann, T. Proffen, and S.J.L. Billinge, PDFgetN: a user-friendly program to extract the total scattering structure factor and the pair distribution function from neutron powder diffraction data. *J. Appl. Crystallogr.*, 2000. **33**: p. 1192.

30. Gummow, R.J., M.M. Thackeray, W.I.F. David, and S. Hull, Structure and Electrochemistry of Lithium Cobalt Oxide Synthesised at 400°C. *Mat. Res. Bull.*, 1992. **27**: p. 327-337.

31. Yoon, W.-S., Y. Paik, X.-Q. Yang, M. Balasubramanian, J. McBreen, and C.P. Grey, Investigation of the Local Structure of the $LiNi_{0.5}Mn_{0.5}O_2$ Cathode Material during Electrochemical Cycling by X-Ray Absorption and NMR Spectroscopy. *Electrochem. Solid-St. Lett.*, 2002. **5**(11): p. A263-A266.

32. Pan, C., Y.J. Lee, B. Ammundsen, and C.P. Grey, ^{6}Li MAS NMR Studies of the Local Structure and Electrochemical Properties of Cr-doped Lithium Manganese and Lithium Cobalt Oxide Cathode Materials for Lithium-Ion Batteries. *Chem. Mater.*, 2002. **14**: p. 2289-2299.

33. Carlier, D., K. Kang, G. Ceder, W.S. Yoon, and C.P. Grey. *^{6}Li MAS NMR Study of Lithium Layered Oxides Containing Ni^{2+} Ions: Experiments and DFT Calculations*. in *203rd Meeting of the Electrochemical Society (ECS)*. 2003. Paris.

34. Marichal, C., J. Hirschinger, and P. Granger, ^{6}Li and ^{7}Li NMR in the $LiNi_{1-y}Co_yO_2$ Solid Solution ($0 \leqslant y \leqslant 1$). *Inorg. Chem.*, 1995. **34**: p. 1773-1778.

35. Chazel, C., M. Ménétrier, L. Croguennec, and C. Delmas, $^{6/7}$Li NMR study of the $Li_{1-z}Ni_{1+z}O_2$ phases. *Magn. Reson. Chem.*, 2005. **43**: p. 849-857.

36. Yin, S.-C., Y.-H. Rho, I. Swainson, and L.F. Nazar, X-ray/Neutron Diffraction and Electrochemical Studies of Lithium De/Re-Intercalation in $Li_{1-x}Co_{1/3}Ni_{1/3}Mn_{1/3}O_2$ ($x=0 \rightarrow 1$). *Chem. Mater.*, 2006. **18**: p. 1901-1910.

37. Sears, V.F., Neutron scattering lengths and cross sections. *Neutron News 3*, 1992. **3**: p. 26-37.

38. McGreevy, R.L. and L. Pusztai, Reverse Monte Carlo Simulation: A New Technique for the Determination of Disordered Structures. *Mol. Simul.*, 1988. **1**: p. 359-367.

39. Tucker, M.G., M.T. Dove, and D.A. Keen, Application of the reverse Monte Carlo method to crystalline materials. *J. Appl. Crystallogr.*, 2001. **34**: p. 630.

40. Proffen, T. and R.B. Neder, DISCUS: A program for diffuse scattering and defect-structure simulation. *J. Appl. Crystallogr.*, 1997. **30**: p. 171-175.

41. Koyama, Y., N. Yabuuchi, I. Tanaka, H. Adachi, and T. Ohzuku, Solid-State Chemistry and Electrochemistry of $LiCo_{1/3}Ni_{1/3}Mn_{1/3}O_2$ for Advanced Lithium-Ion Batteries. *J. Electrochem. Soc.*, 2004. **151**(10): p. A1545-A1551.

42. Koyama, Y., I. Tanaka, H. Adachi, Y. Makimura, and T. Ohzuku, Crystal and electronic structures of superstructural $Li_{1-x}[Co_{1/3}Ni_{1/3}Mn_{1/3}]O_2$ ($0 \leqslant x \leqslant 1$). *J. Power Sources*, 2003. **119-121**: p. 644-648.

43. Yabuuchi, N., Y. Koyama, N. Nakayama, and T. Ohzuku, Solid-State Chemistry and Electrochemistry of $LiCo_{1/3}Ni_{1/3}Mn_{1/3}O_2$ for Advanced Lithium-Ion Batteries II. Preparation and Characterization. *J. Electrochem. Soc.*, 2005. **152**(7): p. A1434-A1440.

44. Welberry, T.R., Diffuse X-ray Scattering and Models of Disorder. *Rep. Prog. Phys.*, 1985. **48**: p. 1543.

45. Van der Ven, A., M.K. Aydinol, and G. Ceder, First-Principles Evidence for Stage Ordering in Li_xCoO_2. *J. Electrochem. Soc.*, 1998. **145**(6): p. 2149-2155.

46. Morcrette, M., Y. Chabre, G. Vaughan, G. Amatucci, J.-B. Leriche, S. Patous, C. Masquelier, and J.-M. Tarascon, In situ X-ray diffraction techniques as a powerful tool to study battery electrode materials. *Electrochimica Acta*, 2002. **47**: p. 3137-3149.

Chapter 3

1. Mizushima, K., P.C. Jones, P.J. Wiseman, and J.B. Goodenough, Li_xCoO_2($0<x<-1$): A new cathode material for batteries of high energy density. *Mater. Res. Bull.*, 1980. **15**(6): p. 783.

2. Dahn, J.R., U. von Sacken, and C.A. Michal, Structure and electrochemistry of $Li_{1\pm y}NiO_2$ and a new Li_2NiO_2 phase withe the $Ni(OH)_2$ structure *Solid State Ionics*, 1990. **44**(1-2): p. 87-97.

3. Capitaine, F., P. Gravereau, and C. Delmas, A new variety of $LiMnO_2$ with a layered structure. *Solid State Ionics*, 1996. **89**: p. 197-202.

4. De Picciotto, L.A., M.M. Thackeray, and G. Pistoia, An electrochemical study of the systems $Li_{1\pm x}V_2O_4$ and $Li_{1-x}VO_2$ (0<=x<=1). *Solid State Ionics*, 1988. **28-30**(Part 2): p. 1364-1370.

5. Saadoune, I. and C. Delmas, $LiNi_{1-y}Co_yO_2$ positive electrode materials: relationships between the structure, physical properties and electrochemical behaviour. *J. Mater. Chem.*, 1996. **6**: p. 193-199.

6. Rossen, E., C.D.W. Jones, and J.R. Dahn, Structure and electrochemistry of $Li_xMn_yNi_{1-y}O_2$. *Solid State Ionics*, 1992. **57**(3-4): p. 311-318.

7. Lu, Z., D.D. MacNeil, and J.R. Dahn, Layered $Li[Ni_xCo_{1-2x}Mn_x]O_2$ Cathode Materials for Lithium Ion Batteries. *Electrochem. Solid-St. Lett.*, 2001. **4**(12): p. A200-A203.

8. Ohzuku, T. and Y. Makimura, Layered Lithium Insertion Material of $LiCo_{1/3}Ni_{1/3}Mn_{1/3}O_2$ for Lithium-Ion Batteries. *Chem. Lett.*, 2001: p. 642-643.

9. Ohzuku, T. and Y. Makimura, Layered Lithium Insertion Material of $LiNi_{1/2}Mn_{1/2}O_2$: A Possible Alternative to $LiCoO_2$ for Advanced Lithium-Ion Batteries. *Chem. Lett.*, 2001: p. 744-745.

10. Kang, K., Y.S. Meng, J. Bréger, C.P. Grey, and G. Ceder, Electrodes with High Power and High Capacity for Rechargeable Lithium Batteries. *Science*, 2006. **311**: p. 977-980.

11. Bréger, J., K. Kang, J. Cabana, G. Ceder, and C.P. Grey, NMR, PDF and RMC study of the positive electrode material $Li(Ni_{0.5}Mn_{0.5})O_2$ synthesized by ion-exchage methods. *J. Mater. Chem.*, 2007. **17**: p. 3167-3174.

12. Bréger, J., N. Dupré, P.J. Chupas, P.L. Lee, T. Proffen, J.B. Parise, and C.P. Grey, Short- and Long-Range Order in the Positive Electrode Material, $Li(NiMn)_{0.5}O_2$: A Joint X-ray and Neutron Diffraction Pair Distribution Function Analysis and NMR Study. *J. Am. Chem. Soc.*, 2005. **127**: p. 7529-7537.

13. Bréger, J., Y.S. Meng, Y. Hinuma, S. Kumar, K. Kang, Y. Shao-Horn, G. Ceder, and C.P. Grey, Effect of High Voltage on the Structure and Electrochemistry of $LiNi_{0.5}Mn_{0.5}O_2$: A Joint Experimental and Theoretical Study. *Chem. Mater.*, 2006. **18**: p. 4768-4781.

14. Zeng, D., J. Cabana, J. Bréger, W.-S. Yoon, and C.P. Grey, Cation Ordering in $Li[Ni_xMn_xCo_{(1-2x)}]O_2$ Layered Cathode Materials: A Nuclear Magnetic Resonance (NMR), Pair Distribution Function, X-ray Absorption Spectroscopy, and Electrochemical Study. *Chem. Mater.*, 2007. **19**(25): p. 6277-6289.

15. Ménétrier, M., I. Saadoune, S. Levasseur, and C. Delmas, The insulator-metal transition upon lithium deintercalation from $LiCoO_2$: electronic properties and ^7Li NMR study. *J. Mater. Chem.*, 1999. **9**: p. 1135-1140.

16. Morcrette, M., Y. Chabre, G. Vaughan, G. Amatucci, J.-B. Leriche, S. Patous, C. Masquelier, and J.-M. Tarascon, In situ X-ray diffraction techniques as a powerful tool to study battery electrode materials. *Electrochimica Acta*, 2002. **47**: p. 3137-3149.

17. MacNeil, D.D., Z. Lu, and J.R. Dahn, Structure and electrochemistry of $Li[Ni_xCo_{1-2x}Mn_x]O_2$ ($0 <= x <= 1/2$). *J. Electrochem. Soc.*, 2002. **149**(10): p. A1332-A1336.

18. Reimers, J.N. and J.R. Dahn, Electrochemical and *In situ* X-Ray Diffraction Studies of Lithium Intercalation in Li_xCoO_2. *J. Electrochem. Soc.*, 1992. **139**(8): p. 2091-2097.

19. Amatucci, G.G., J.-M. Tarascon, and L.C. Klein, CoO_2, The End Memeber of the Li_xCoO_2 Solid Solution. *J. Electrochem. Soc.*, 1996. **143**(3): p. 1114-1123.

20. Fouassier, C., C. Delmas, and P. Hagenmuller, Evolution structurale et proprietes physiques des phases A_xMO_2 (A = Na, K; M = Cr, Mn, Co) ($x <= 1$). *Mater. Res. Bull.* **10**(6): p. 443-449.

21. Levasseur, S., M. Ménétrier, and C. Delmas, On the $Li_xCo_{1-y}Mg_yO_2$ system upon deintercalation: electrochemical, electronic properties and Li-7 MAS NMR studies. *J. Power Sources*, 2002. **112**(2): p. 419-427.

22. Yang, X.Q., J. McBreen, W.S. Yoon, and C.P. Grey, Crystal structure changes of $LiMn_{0.5}Ni_{0.5}O_2$ cathode materials during charge and discharge studied by synchrotron based in situ XRD. *Electrochem. Commun.*, 2002. **4**(8): p. 649-654.

23. Yoon, W.-S., K.Y. Chung, J. McBreen, and X.-Q. Yang, A comparative study on structural changes of $LiCo_{1/3}Ni_{1/3}Mn_{1/3}O_2$ and $LiNi_{0.8}Co_{0.15}Al_{0.05}O_2$ during first charge using in situ XRD. *Electrochem. Commun.*, 2006. **8**(8): p. 1257-1262.

24. Waki, S., K. Dokko, T. Itoh, M. Nishizawa, T. Abe, and I. Uchida, High-Speed voltammetry of Mn-doped $LiCoO_2$ using a microelectrode technique. *J. Solid State Electrochem.*, 2000. **4**: p. 205-209.

25. Saadoune, I., M. Ménétrier, and C. Delmas, Redox processes in $Li_xNi_{1-y}Co_yO_2$ cobalt-rich phases. *J. Mater. Chem.*, 1997. **7**: p. 2505-2511.

26. Levasseur, S., M. Menetrier, and C. Delmas, On the dual effect of Mg doping in $LiCoO_2$ and $Li_{1+\delta}CoO_2$: Structural, electronic properties, and Li-7 MAS NMR studies. *Chem. Mater.*, 2002. **14**(8): p. 3584-3590.

27. Jiang, M., B. Key, Y.S. Meng, and C.P. Grey, Electrochemical and Structural Study of Li-excess Materials $Li[Li_{1/9}Ni_{1/3}Mn_{5/9}]O_2$. *Chem. Mater.*, 2009. **21**(13): p. 2733-2745.

28. Yoon, W.-S., Y. Paik, X.-Q. Yang, M. Balasubramanian, J. McBreen, and C.P. Grey, Investigation of the Local Structure of the $LiNi_{0.5}Mn_{0.5}O_2$ Cathode Material during Electrochemical Cycling by X-Ray Absorption and NMR Spectroscopy. *Electrochem. Solid-St. Lett.*, 2002. **5**(11): p. A263-A266.

29. Yoon, W.-S., M. Balasubramanian, K.Y. Chung, X.-Q. Yang, J. McBreen, C.P. Grey, and D.A. Fischer, Investigation of the Charge Compensation Mechanism on the Electrochemically Li-Ion Deintercalated $Li_{1-x}Co_{1/3}Ni_{1/3}Mn_{1/3}O_2$ Electrode System by Combination of Soft and Hard X-ray Absorption Spectroscopy. *J. Am. Chem. Soc.*, 2005. **127**: p. 17479-17487.

30. Tsai, Y.W., B.J. Hwang, G. Ceder, H.S. Sheu, D.G. Liu, and J.F. Lee, In-Situ X-ray Absorption Spectroscopic Study on Variation of Electronic Transitions and Local Structure of $LiNi_{1/3}Co_{1/3}Mn_{1/3}O_2$ Cathode Material during Electrochemical Cycling. *Chem. Mater.*, 2005. **17**: p. 3191-3199.

31. Laubach, S., S. Laubach, P.C. Schmidt, D. Ensling, S. Schmid, W. Jaegermann, A. ThiBen, K. Nikolowski, and H. Ehrenberg, Changes in the crystal and electronic structure of $LiCoO_2$ and $LiNiO_2$ upon Li intercalation and de-intercalation. *Phys. Chem. Chem. Phys.*, 2009. **11**: p. 3278-3289.

32. Grey, C.P. and N. Dupré, NMR Studies of Cathode Materials for Lithium-Ion Rechargeable Batteries. *Chem. Rev.*, 2004. **104**: p. 4493-4512.

33. Lee, Y.J., F. Wang, and C.P. Grey, ^6Li and ^7Li MAS NMR Studies of Lithium Manganate Cathode Materials. *J. Am. Chem. Soc.*, 1998. **120**: p. 12601-12613.

34. Carlier, D., M. Ménétrier, C.P. Grey, C. Delmas, and G. Ceder, Understanding the NMR shifts in paramagnetic transition metal oxides using density functional theory calculations. *Phys. Rev. B*, 2003. **67**: p. 174103.

35. Pan, C., Y.J. Lee, B. Ammundsen, and C.P. Grey, ^6Li MAS NMR Studies of the Local Structure and Electrochemical Properties of Cr-doped Lithium Manganese and Lithium Cobalt Oxide Cathode Materials for Lithium-Ion Batteries. *Chem. Mater.*, 2002. **14**: p. 2289-2299.

36. Carlier, D., K. Kang, G. Ceder, W.S. Yoon, and C.P. Grey. *^6Li MAS NMR Study of Lithium Layered Oxides Containing Ni^{2+} Ions: Experiments and DFT Calculations*. in *203rd Meeting of the Electrochemical Society (ECS)*. 2003. Paris.

37. Chernova, N.A., M. Ma, J. Xiao, M.S. Whittingham, M. Stanley, J. Bréger, and C.P. Grey, Layered $Li_xNi_yMn_yCo_{1-2y}O_2$ Cathodes for Lithium Ion Batteries:

Understanding Local Structure via Magnetic Properties. *Chem. Mater.*, 2007. **19**: p. 4682-4693.

38. Reed, J. and G. Ceder, Charge, potential, and phase stability of layered $Li(Ni_{0.5}Mn_{0.5})O_2$. *Electrochem. Solid State Lett.*, 2002. **5**(7): p. A145-A148.

39. Dompablo, M.E.A.y.d., C. Marianetti, A.V.d. Ven, and G. Ceder, Jahn-Teller mediated ordering in layered Li_xMO_2 compounds. *Phys. Rev. B*, 2001. **63**: p. 144107.

40. Slichter, C.P., *Principles of Magnetic Resonance*. Springer Series in Solid-State Sciences 1. 1990, New York: Springer-Verlag.

41. Graetz, J., A. Hightower, C.C. Ahn, R. Yazami, P. Rez, and B. Fultz, Electronic structure of chemically-delithiated $LiCoO_2$ studied by electron energy-loss spectrometry. *J. Phys. Chem. B*, 2002. **106**(6): p. 1286-1289.

42. Hwang, B.J., Y.W. Tsai, D. Carlier, and G. Ceder, A Combined Computational/Experimental Study on $LiNi_{1/3}Co_{1/3}Mn_{1/3}O_2$. *Chem. Mater.*, 2003. **15**: p. 3676-3682.

43. Dahéron, L., R. Dedryvere, H. Martinez, M. Ménétrier, C. Denage, C. Delmas, and D. Gonbeau, Electron Transfer Mechanisms upon Lithium Deintercalation from $LiCoO_2$ to CoO_2 Investigated by XPS. *Chem. Mater.*, 2008. **20**: p. 583-590.

Chapter 4

1. Kepler, K.D., Vaughey, J.T., and Thackeray, M.M., Copper-tin anodes for rechargeable lithium batteries: an example of the matrix effect in an intermetallic system. *J.Power Sources*, 1999. **81**: p. 383-387.

2. Kepler, K.D., Vaughey, J.T., and Thackeray, M.M., $Li_xCu_6Sn_5$ ($0 < x < 13$): An intermetallic insertion electrode for rechargeable lithium batteries. *Electrochem. Solid State Lett.*, 1999. **2**(7): p. 307-309.

3. Thackeray, M.M., Vaughey, J.T., Johnson, C.S., Kropf, A.J., Benedek, R., Fransson, L.M.L., and Edstrom, K., Structural considerations of intermetallic electrodes for lithium batteries. *J. Power Sources*, 2003. **113**(1): p. 124-130.

4. Morcrette, M., Rozier, P., Dupont, L., Mugnier, E., Sannier, L., Galy, J., and Tarascon, J.M., A reversible copper extrusion-insertion electrode for rechargeable Li batteries. *Nat. Mater.*, 2003. **2**(11): p. 755-761.

5. Leising, R.A. and Takeuchi, E.S., Solid-state cathode materials for lithium batteries: effect of synthesis temperature on the physical and electrochemical properties of silver vanadium oxide. *Chem. Mater.*, 1993. **5**(5): p. 738-742.

6. Leising, R.A. and Takeuchi, E.S., Solid-State Synthesis and Characterization of Silver Vanadium Oxide for Use as a Cathode Material for Lithium Batteries. *Chem. Mater.*, 1994. **6**(4): p. 489-495.

7. Leising, R.A., Thiebolt, W.C., and Takeuchi, E.S., Solid-State Characterization of Reduced Silver Vanadium Oxide from the Li/SVO Discharge Reaction. *Inorg. Chem.*, 1994. **33**(25): p. 5733-5740.

8. Bodenez, V., Dupont, L., Morcrette, M., Surcin, C., Murphy, D.W., and Tarascon, J.M., Copper extrusion/reinjection in Cu-based thiospinels by electrochemical and chemical routes. *Chem. Mater.*, 2006. **18**(18): p. 4278-4287.

9. Bodenez, V., Dupont, L., Laffont, L., Armstrong, A.R., Shaju, K.M., Bruce, P.G., and Tarascon, J.M., The reaction of lithium with $CuCr_2S_4$ - lithium intercalation and copper displacement/extrusion. *J. Mater. Chem.*, 2007. **17**(30): p. 3238-3247.

10. Rozier, P., Morcrette, M., Szajwaj, O., Bodenez, V., Dolle, M., Surcin, C., Dupont, L., and Tarascon, J.M., Li-Driven Copper Extrusion/Re-injection in Various Cu-based Oxides and Sulfides. *Isr. J. Chem.*, 2008. **48**(3-4): p. 235-249.

11. Indris, S., Cabana, J., Rutt, O.J., Clarke, S.J., and Grey, C.P., Layered Oxysulfides $Sr_2MnO_2Cu_{2m-0.5}S_{m+1}$ (m=1, 2, and 3) as Insertion Hosts for Li ion batteries. *J. Am. Chem. Soc.*, 2006. **128**(41): p. 13354-13355.

12. Zhu, W.J. and Hor, P.H., Unusual layered transition-metal oxysulfides: $Sr_2Cu_2MO_2S_2$ (M=Mn, Zn). *J. Solid State Chem.*, 1997. **130**(2): p. 319-321.

13. Gal, Z.A., Rutt, O.J., Smura, C.F., Overton, T.P., Barrier, N., Clarke, S.J., and Hadermann, J., Structural chemistry and metamagnetism of an homologous series of layered manganese oxysulfides. *J. Am. Chem. Soc.*, 2006. **128**(26): p. 8530-8540.

14. Rutt, O.J., Williams, G.R., and Clarke, S.J., Reversible lithium insertion and copper extrusion in layered oxysulfides. *Chem. Commun.*, 2006(27): p. 2869-2871.

15. Morcrette, M., Chabre, Y., Vaughan, G., Amatucci, G., Leriche, J.-B., Patous, S., Masquelier, C., and Tarascon, J.-M., In situ X-ray diffraction techniques as a powerful tool to study battery electrode materials. *Electrochimica Acta*, 2002. **47**: p. 3137-3149.

16. Chung, J.-S. and Sohn, H.-J., Electrochemical behaviors of CuS as a cathode material for lithium secondary batteries. *J. Power Sources*, 2002. **108**: p. 226-231.

17. Yamakawa, N., Jiang, M., and Grey, C.P., Investigation of the Conversion Reaction Mechanisms for Binary Copper (II) Compunds by Solid-State NMR Spectroscopy and X-ray Diffraction. *Chem. Mater.*, 2009. **21**: p. 3162-3176.

18. Li, D., Bancroft, G.M., Kasrai, M., Fleet, M.E., Feng, X.H., Yang, B.X., and Tan, K.H., S K-Edge and L-Edge Xanes and Electronic-Structure of Some Copper Sulfide Minerals. *Phys. Chem. Minerals*, 1994. **21**(5): p. 317-324.

19. Pattrick, R.A.D., Mosselmans, J.F.W., Charnock, J.M., England, K.E.R., Helz, G.R., Garner, C.D., and Vaughan, D.J., The structure of amorphous copper sulfide precipitates: An X-ray absorption study. *Geochimica et Cosmochimica Acta*, 1997. **61**(10): p. 2023-2036.

20. Wu, Z.Y., Ouvrard, G., Lemaux, S., Moreau, P., Gressier, P., Lemoigno, F., and Rouxel, J., Sulfur K-edge x-ray-absorption study of the charge transfer upon lithium intercalation into titanium disulfide. *Phys. Rev. Lett.*, 1996. **77**(10): p. 2101-2104.

21. Branci, C., Sarradin, J., Olivier-Fourcade, J., and Jumas, J.C., Lithium Insertion Mechanism in Tin-Based Spinel Sulfides. *Chem. Mater.*, 1999. **11**: p. 2846-2850.

22. Grey, C.P. and Dupré, N., NMR Studies of Cathode Materials for Lithium-Ion Rechargeable Batteries. *Chem. Rev.*, 2004. **104**: p. 4493-4512.

23. Vajenine, G.V. and Hoffmann, R., Compounds Containing Copper-Sulfur Layers: Electronic Structure, Conductivity, and Stability. *Inorg. Chem.*, 1996. **35**: p. 451-457.